

The University of Nottingham

Deformation and Collapse Of Orthogonal 3D Woven Composites: Quasi-static and Impact Loading

By

Paul Turner, MEng

Thesis submitted to the University of Nottingham for the degree of Doctor of Philosophy

July, 2016

PREFACE

This thesis is submitted for the degree of Doctor of Philosophy at the University of Nottingham. The research work was conducted at the University of Nottingham Engineering department during the period from October 2012 to October 2015 under the supervision of Dr Tao Liu.

The research was funded by the EPSRC accounts EPSRC EP/P505658/1 and EP/K503101/1 and supported by the Early Career Research and Knowledge Transfer Awards from the University of Nottingham. The numerical calculations were undertaken with the High Performance Computing facility at the University of Nottingham.

This dissertation is a result of my own work and incudes nothing of which is the outcome of work done in collaboration except where mentioned within the text.

This document, in whole or in part, has not been previously submitted for any other degree, diploma or qualification.

The thesis contains approximately 57,200 words, 83 figures and 6 tables.

Paul Turner
Nottingham, U.K
November 2015

DEDICATION

TO MY FAMILY AND
TO MY WIFE OLYA

ABSTRACT

This thesis presents an experimental and numerical investigation undertaken in order to develop the understanding of the behaviour of orthogonal 3D woven composites under quasi-static tension/compression, out-of-plane bending and dynamic soft and multi-hit ballistic impact load cases. Focus is given to the deformed configuration of samples, and to the initiation and propagation of damage within the material. The damage mitigation properties of the through-the-thickness (TTT) reinforcement are highlighted throughout.

A pressurised gas gun test system was developed at the University of Nottingham in order to undertake the soft and ballistic impact tests upon 3D woven composite samples. Experimental and numerical comparisons are made to similar UD-laminate composite materials.

An established continuum damage mechanics framework is employed for numerical modelling of the quasi-static and dynamic load cases, allowing for further insights into the experimental results. A review of the efficacy of the numerical modelling strategy is presented, alongside a study on the influence of the TTT reinforcement on the out-of-plane static and dynamic response of the material.

The numerical modelling strategy is then adapted for ballistic impact events. A numerical study is conducted on the multi-hit ballistic impact properties of orthogonal 3D woven composites, the first of its kind. Comparisons are made between numerical calculations both with and without the presence of the TTT reinforcement. A parameter study is also conducted on the effect of the inter-laminar shear strength on the ballistic limit of laminate composite plates.

ACKNOWLEDGEMENTS

I would like to express my sincere gratitude to my supervisor Dr Tao Liu, for his guidance, knowledge, and support during the undertaking of this research. I am also extremely grateful for the support and supervision of Dr Xuesen Zeng.

I would also like to express my thanks to the extensive technical support provided at the University of Nottingham. Without the tireless efforts of these people, the research output of the University would be dramatically reduced. This includes James Meakin, Steve Gange, Steve Lawton, Bal Loyla, Graham Malkinson, Gary Davies, Nigel Rook, Craig Cox, Mike Langford, Tom Buss, Paul Johns, Ben Jennison, Roger Smith and Rory Screaton.

LIST OF NOTATIONS

Roman Symbols

A_{tow}^{warp}	Average transverse cross sectional area of warp tow
A_{tow}^{weft}	Average transverse cross sectional area of weft tow
A_x	Area of cross section of composite along warp direction
A_y	Area of cross section of composite along weft direction
d	Roller diameter
D	Damage variable
d_f^c	Fibre compression damage variable
d_m^c	Matrix compression damage variable
d_p	Diameter of projectile
d_s	Shear damage variable
d_f^t	Fibre tensile damage variable
d_m^t	Matrix tensile damage variable
$\widetilde{E}_1$	Equivalent UD-laminate longitudinal Young's modulus
$\overline{E}_1$	Tow longitudinal Young's modulus
$\overline{E}_2$	Tow transverse Young's modulus
E_f	Young's Modulus of fibre reinforcement
G_{12f}	In-plane shear modulus of fibre reinforcement
$\overline{G}_{12}$	Tow in-plane shear modulus
G_C^i	Mode *i* Fracture Energy
$\widetilde{G}_{12}$	Equivalent UD-laminate shear modulus
G_{xy}	Composite in-plane shear stiffness
$\hbar$	Cohesive contact damage variable
I_0	Projectile momentum per unit area
J	Fracture energy
$\overline{J}_1^c$	Tow longitudinal compressive fracture energy
$\overline{J}_1^t$	Tow longitudinal tensile fracture energy

J_m	Matrix fracture energy
$\widetilde{J}_1^c$	Equivalent UD-laminate longitudinal compressive fracture energy
$\widetilde{J}_1^t$	Equivalent UD-laminate longitudinal tensile fracture energy
k_n, k_s, k_t	Normal and shear stiffness
L	Sample length
l_p	Length of projectile
n_x	Number of weft tows in sample
n_y	Number of warp tows in sample
P_m	Average overpressure
P_c	Collapse load
P_{peak}	Peak overpressure
s	Stand-off
S_c	Shear strength
t_e	Effective traction
t_e^0	Effective traction at damage initiation
tn, ts, tt	Normal and shear tractions
u	DOF of node
v_0	Projectile exit velocity
V_I	Primary impact velocity
V_{II}	Secondary Impact velocity
V_{tow}^{warp}	Warp tow volume fraction
V_{tow}^{weft}	Weft tow volume fraction
w	Width of sample
W_e	Strain energy
$\overline{X}^C$	Tow longitudinal compressive strength
$\overline{X}^T$	Tow longitudinal tensile strength
$\widetilde{X}^C$	Equivalent UD-laminate longitudinal compressive strength
$\widetilde{X}^T$	Equivalent UD-laminate longitudinal tensile strength
X^C	Composite longitudinal compressive strength
X_r	Longitudinal strength of fibre reinforcement
X^T	Composite longitudinal tensile strength

$\overline{Y}$	Tow transverse strength
Y_e	Energy released per volume due to damage progression
Y^T	Transverse tensile strength

Greek Letters

α	Ratio of deviatoric strength to hydrostatic strength
γ	Shear strain
δ	Deflection
δ_b	Displacement of post-impact clamped beam
δ_e	Effective separation
$\delta_{e,max}$	Maximum value of separation for cohesive contact
δ_e^0	Effective separation at damage initiation
δ_n, δ_s, δ_t	Normal and shear separations
ε_c	Critical strain
ε_D	Densification Strain
ε_f	Matrix fracture strain
ε_{pl}	von Mises effective plastic strain
ε_{xx}	Longitudinal strain along the x(warp) direction
ε_{yy}	Longitudinal strain along the y(weft) direction
η	Viscosity coefficient
η_t	Relaxation time of system
$\hat{\rho}$	Matrix density
$\overline{\rho}$	Relative density
ρ_p	Density of projectile
ρ_{tow}	Density of tow
ρ^{UD}	Density of effective UD laminate ply
$\sigma_{kk,c}^0$	Initial yield stress in hydrostatic compression
σ_c^0	Initial yield stress in uniaxial compression
σ_{22}	Transverse stress
σ_e	Von Mises effective stress
σ_k	Critical stress within yarn for kink band formation

σ_{xx}	Longitudinal stress along the x(warp) direction
σ_y	Plateau stress
σ_{yy}	Longitudinal stress along the y(weft) direction
τ_y	Critical stress for shear flow
$\overline{\upsilon}_{12}$	Tow Poisson's ratio
υ_p	Plastic Poisson's ratio
φ	Fibre misalignment angle
ϕ	Metal foam material yield function
ω	Damage variable

Acronyms

2D	Two-Dimensional
3D	Three Dimensional
AAM	Air-to-Air missile
BK	Benzeggagh-Kenane
BVID	Barely Visible Impact Damage
CAI	Compression After Impact
CDM	Continuum Damage Mechanics
CFRPs	Carbon fibre reinforced polymers
CT	Computed tomography
DCB	Double Cantilever Beam
DIC	Digital Image Correlation
DNS	Direct numerical simulation
DoF	Degrees of freedom
ELS	End-Loaded Split
ENF	End-Notched Flexure
FE	Finite Element
FSI	Fluid Structure Interaction
HMMWV	High Mobility Multipurpose Wheeled Vehicle
IEDs	Improvised Explosive Devices
LEFM	Linear elastic fracture mechanics
NDE	Non-Destructive Evaluation

OA	Orientation averaging
PBO	Poly(p-phenylene-2,6-benzobisoxazole)
RVE	representative volume element
SAM	Surface-to-air
SEM	Scanning electron microscope
SHPB	Split Hopkinson pressure bar
TNT	Trinitrotoluene
TTAIL	Through-Thickness Angle Interlock
TTT	Through-the-thickness
UD	Uni-directional
UHMWPE	Ultra-High Molecular Weight Polyethelene
VCCT	Virtual crack closure technique
XFEM	Extended finite element method

LIST OF FIGURES

Figure 1.1. Delamination damage of a Diamond DA20-C1 aircraft vertical fin..... 2
Figure 1.2(a) Orthogonal and (b) layer-interlock woven fibre preforms. 4
Figure 1.3. General Electric GE9x turbo fan engine 5
Figure 1.4. High Mobility Multipurpose Wheeled Vehicle (HMMWV), ... 6
Figure 2.1 Literature review route map 12
Figure 2.2. Edge view of a quasi-isotropic glass reinforced epoxy composite material post drop-weight impact test 13
Figure 2.3. Delamination due to inter-laminar stresses 15
Figure 2.4. Out-of-plane loading of laminate composites which can cause sufficient inter-laminar stresses to induce delamination damage 15
Figure 2.5. Sources of delamination in laminate composites due to discontinuities 16
Figure 2.6. Ply-by-ply and inter-ply damage at 90% failure load, for a central notch under pure tensile loading 17
Figure 2.7(a) Sketch of TTAIL composite material (b) C-scan of sample after quasi-static indentation test of deflection 7 mm. 19
Figure 2.8. Bearing failure damage around a bolt hole within a graphite /epoxy laminate. 20
Figure 2.9. Cross sections of 3D woven fabrics 22
Figure 2.10. Sketch of “crimping” fibre distortion common to 3D woven composites. 23
Figure 2.11. Plastic tow straightening stress as a function of fibre waviness 24
Figure 2.12. (a) Example R-curve for layer-to-layer 3D woven composite material. 26
Figure 2.13. Collated tensile Young’s modulus data for cross-ply, 2D woven and 3D woven composites. 28
Figure 2.14. Collation of compressive strength data of 0/90°, 2D woven, and 3D woven composites 31
Figure 2.15. Effect of z-binder content on the normalised compressive strength of 3D woven composites 32

Figure 2.16. Collated post impact compressive strength (%) of cross-ply, 2D woven, and 3D woven composite materials. 35
Figure 2.17. Comparison of post-impact flexural strength between 2D and 3D woven composite materials. 35
Figure 2.18. Sketch of a mobile vehicle resisting the impact of soil ejecta 38
Figure 2.19(a) High speed photographic sequence of an Alporas metal foam projectile impacting a Kolsky pressure bar at v_0 = 381 ms^{-1}. (b) The measured contact pressure histories of Alporas foam of relative density $\overline{\rho} = 0.11$ and length L = 100 mm of two different velocity impacts during a direct impact Kolsky bar experiment (c) The measured contact pressure histories of Alporas foam of two lengths, relative density $\overline{\rho} = 0.11$ and impact velocity v_o = 380 ms^{-1}. (d) The measured peak and mean contact pressures of Alporas metal foams as a function of impact velocity v_0. 41
Figure 2.20. Ladeveze fibrous composite laminate meso-scale modelling strategy 45
Figure 2.21. Laminar failure planes. 47
Figure 2.22. Three general modes of fracture 49
Figure 3.1(a) 3D orthogonal woven carbon composites showing Full through-the-thickness (TTT) reinforcement on the left and Half TTT reinforcement on the right. 65
Figure 3.2. Typical stress-strain curves during quasi-static uni-axial material coupon tests of the full TTT 3D woven composites 68
Figure 3.3. (a) Sketch of cantilever beam test, showing front surface painted for DIC analysis. (b) Sketch of composite beam orientated along the x-direction (warp). 69
Figure 3.4(a) Force applied by the roller against normalised roller deflection along the z-direction for a range of beam lengths. Beams orientated along the warp direction (Full TTT material). (b) The collapse load for a range of beam lengths orientated along the warp direction Full TTT. 71
Figure 3.5. Long (40 mm) cantilever beam tests results 73
Figure 3.6. μCT image of long (40 mm) cantilever beam test along the x-direction (warp) 74
Figure 3.7. Short (8 mm) cantilever beam test results..... 76

Figure 3.8. μCT images of short beam failure modes of the Full TTT 3D woven composites 77
Figure 3.9. Long (40mm) cantilever beam test of a UD laminate material..... 78
Figure 3.10. Short (8mm) beam cantilever beam test of UD laminate material. .. 80
Figure 3.11(a) Finite element modelling strategy employed within this study..... 83
Figure 3.12. Comparison between the finite element predictions and the experimental data of uni-axial quasi-static compressive and tensile stress-strain responses 97
Figure 3.13. Finite element simulation of uni-axial compression test along weft direction..... 99
Figure 3.14. Finite element simulation of uni-axial tension test along weft direction..... 101
Figure 3.15. Finite element simulation of uni-axial compression test along warp direction..... 103
Figure 3.16. Experimental data and FE prediction of force applied by the roller against vertical roller displacement relationship during long cantilever beam bending test (40 mm) along x-direction (warp)..... 105
Figure 3.17(a) and (b) Experimental data and FE predictions of the force applied by the roller against vertical roller displacement relationship during short cantilever beam bending tests (8 mm) along for x-direction (warp) and y-direction (weft), respectively..... 107
Figure 3.18(a) Finite element prediction of the load resisted against vertical roller displacement of long beam cantilever tests (40 mm) along the x-direction (warp) with cohesive contact removed 109
Figure 3.19(a) Finite element prediction of load resisted against vertical roller displacement of short beam cantilever tests (8 mm) orientated along the x-direction (warp) with cohesive contact removed 110
Figure 4.1. Quasi-static uniaxial compression stress-strain curve for the Alporas aluminium foam projectile. 116
Figure 4.2. Sketch of experimental set up of dynamic soft impact tests on orthogonal 3D woven composite panels. 118
Figure 4.3. Finite element model for the simulation of orthogonal 3D woven carbon composites undergoing soft impact. 121

Figure 4.4. Comparison of experimental results for Full TTT material and FE prediction for normalised back-face deflection $\hat{\delta} \equiv \delta / l_0$ as a function of normalised time $\hat{t} \equiv t\, v_0 / l_p$. 130
Figure 4.5. Deformation montage of 3D orthogonal woven carbon-fibre composites under soft impact of impulse $I_0 = 2.64$ kPa s 131
Figure 4.6. Comparison of the normalised maximum back face deflection $\overline{\delta}_{\max}$ during soft impact as a function of normalised impact impulse $\bar{I}_0$ upon 3D woven carbon composites 132
Figure 4.7. Maximum normalised back-face deflection $\hat{\delta} \equiv \delta / 2l_0$ against normalised time after impact $\hat{t} \equiv tv_0 / l_p$ 133
Figure 4.8. Deformation montage of carbon-fibre composites under soft impact 134
Figure 4.9. Photographic images and FE predictions of damage modes exhibited by Half TTT 3D woven carbon composite undergoing soft impact..... 136
Figure 4.10(a) and (b) Finite element simulations of the predicted compressive damage initiation on the front surface of orthogonal 3D woven composite beams undergoing a soft impact event $I_0 = 3.33$ kPa s for Full TTT and Half TTT material 138
Figure 4.11. Sketch showing the experimental setup of the clamped beam quasi-static bending test. 140
Figure 4.12. Load imposed by the roller P against roller vertical displacement δ_p for post-impact clamped-clamped beam tests for Full TTT material..... 141
Figure 4.13 (a) Summary of the peak load during post-impact clamped beam testing verses the velocity of impact v_0. 142
Figure 4.14. Finite element predicted deformation of an orthogonal 3D woven carbon composite undergoing a soft impact event $I_0 = 4.03$ kPa s 143
Figure 4.15. Montage of finite element simulations of a soft impact event of impulse $I_0 = 2.96$ kPa s with cohesive contact removed..... 144
Figure 5.1. (a) Sketch of experimental set up for ballistic impact of 3D woven composite beams 154

Figure 5.2. Validation of the numerical modelling strategies via the simulation of rigid impact upon orthogonal 3D woven composite beams 156
Figure 5.3 FE predicted and experimentally recorded transient deformation of (a) Half TTT beam during impact $v_0 = 76\,\mathrm{ms}^{-1}$, (b) Full TTT beam during impact $v_0 = 110\,\mathrm{ms}^{-1}$ and (c) Half TTT beam during impact $v_0 = 190\,\mathrm{ms}^{-1}$. 157
Figure 5.4. Comparison between experimentally observed and predicted damage mechanisms for a lower velocity projectile $v_0 = 76\,\mathrm{ms}^{-1}$ impacting upon Half TTT material beam orientated along the x-direction (warp). 158
Figure 5.5 Optical microscopic images of cross-sectioned sample of lower velocity projectile $v_0 = 76\,\mathrm{ms}^{-1}$ impacting upon Half TTT material beam orientated along the x-direction (warp). Cross section corresponds to location in Figure 5.4..... 159
Figure 5.6. Comparison between experimentally observed and predicted damage mechanisms for a medium velocity projectile $v_0 = 110\,\mathrm{ms}^{-1}$ impacting upon Full TTT material..... 160
Figure 5.7. Comparison between experimentally observed and predicted damage mechanisms for a high velocity projectile $v_0 = 190\,\mathrm{ms}^{-1}$ impacting upon a Half TTT composite beam. 161
Figure 5.8. Meshed geometry for singular-hit ballistic impact simulations upon 3D woven composite circular plates. 163
Figure 5.9. Predicted transient longitudinal tensile stress field on back-face of plate impacted by a singular rigid spherical projectile of velocity $v_0 = 110\ \mathrm{ms}^{-1}$ 165
Figure 5.10(a) Sketch of penetration mechanisms demonstrated by FE predictions of ballistic penetration event v_0 = 155 ms^{-1} 168
Figure 5.11(a) Predicted mechanisms of deformation and penetration of orthogonal 3D woven composite material undergoing impact v_0 = 170 ms^{-1} 171
Figure 5.12(a) and (b) Predicted tensile fibre damage initiation on the front-face of composite laminate beams undergoing ballistic impact of v_0 = 110 ms^{-1} at time after impact t = 225 μs..... 172

Figure 5.13. The predicted coefficient of restitution *e* as a function of the normalised impact velocity $\bar{v}_0 \equiv v_0 / V_L$ for the 3D woven composite and equivalent UD-laminate material. ..... **Error! Bookmark not defined.**
Figure 5.14(a) Meshed geometry of impact simulations on UD-laminate carbon fibre composite material. (b) validation of multi-hit modelling strategy via a comparison of FE predicted ballistic limit surface and experimentally recorded ballistic limit surface 177
Figure 5.15 Meshed geometry for multi-hit ballistic impact simulations upon 3D woven composite circular plates. 178
Figure 5.16(a) FE prediction of the multi-hit ballistic limit surface of Half TTT 3D woven composite material and equivalent UD-laminate..... 179
Figure 5.17. Isometric and cross-sectional views of predicted damage and deformed configuration of composite plates for an equi-velocity multi-hit event $V_I = V_{II} = 125 \text{ ms}^{-1}$ 181
Figure 5.18. Numerically predicted deformed configuration of plate at the moment of secondary impact..... 183
Figure 5.19. Predicted ballistic limit as a function of inter-laminar shear strength for a uni-directional laminate plate. 186

LIST OF TABLES

Table 3.1. Material parameters for the cohesive contact between matrix slices ... 90
Table 3.2. Tow material properties calculated from manufacturer's data and material testing. ... 94
Table 3.3 Material properties of matrix and tows for the composite material used in the constitutive model in the FE calculations. ... 95
Table 4.1. Equivalent UD-laminate properties (modified values) ... 127
Table 5.1. The material properties of each uni-directional ply of laminate composite material employed within the constitutive model of the multi-hit validation FE model. ... 176
Table 5.2. The material parameters for the cohesive interface between the surfaces of each ply of laminate model within the multi-hit validation FE calculations. . 176

Table of Contents

CHAPTER 1 ..... **1**

1.1 3D WOVEN COMPOSITE MATERIALS 2

1.2 NUMERICAL MODELLING 4

1.3 IMPACT MECHANICS 5

1.4 THESIS OBJECTIVES 6

1.5 THESIS OUTLINE 8

CHAPTER 2 ..... **11**

2.1 DELAMINATION 12

2.1.1 Delamination due to impact loading *12*

2.1.2 Delamination due to free edge effect *14*

2.1.3 Delamination due to out-of-plane loading *15*

2.1.4 Delamination due to discontinuities *16*

2.1.5 Detecting delamination damage *17*

2.2 3D WOVEN COMPOSITES 21

2.2.1 Fibre architecture *21*

2.2.2 Toughening *24*

2.2.3 Young's modulus *27*

2.2.4 Tensile strength *28*

2.2.5 Compressive strength *29*

2.2.6 High strain rate properties ($\dot{\varepsilon} > 100$) *32*

2.2.7 Impact Resistance *33*

2.2.8 Bending of 3D woven composite materials *35*

2.3 SOFT IMPACT 37

2.4 MULTI-HIT IMPACT UPON COMPOSITE STRUCTURES 42

2.5 FE MODELLING OF FIBROUS COMPOSITES 44

2.5.1 Continuum Damage Mechanics (CDM) 44

2.5.2 Modelling fracture 48

2.6 3D WOVEN COMPOSITES MODELLING STRATEGIES 51

2.7 RATE DEPENDENCY OF FIBRE REINFORCED COMPOSITE MATERIALS 55

2.8 NUMERICAL MODELLING OF 3D WOVEN COMPOSITES UNDER IMPACT LOADING 57

CHAPTER 3 61

3.1 INTRODUCTION 62

3.2 3D WOVEN COMPOSITE MATERIAL DESCRIPTION AND MANUFACTURING PROCESS 63

3.2.1 Composite manufacturing 66

3.3 IN-PLANE TENSION AND COMPRESSION COUPON TESTS 66

3.4 CANTILEVER BEAM BENDING TESTS - 3D WOVEN COMPOSITE 68

3.4.1 Long cantilever bending tests 72

3.4.2 Short cantilever bending tests 74

3.5 UD LAMINATE CANTILEVER BEAM BENDING 77

3.5.1 UD laminate long beam 77

3.5.2 UD laminate short beam 78

3.6 FINITE ELEMENT ANALYSIS 80

3.6.1 FE model of orthogonal 3D woven composites 80

3.6.2 Description of the constitutive laws employed for FE simulation 83

3.6.3 The damage model for warp and weft tows and TTT-reinforcement 85

3.6.4 Matrix material damage model 87

3.6.5 Cohesive law for interface between layers through the thickness 88

3.7 CALIBRATION OF MATERIAL PROPERTIES EMPLOYED IN FE SIMULATIONS 91

3.7.1 Weft tows, warp tows and TTT-reinforcement as shell elements 91

3.7.2 Matrix material as solid elements 96

3.8 FE SIMULATION RESULTS FOR IN-PLANE COUPON TESTS 97

3.9 FE SIMULATIONS OF CANTILEVER BEAM TESTS 104

3.9.1 Long beam 104

3.9.2 Short beam 105

3.10 PRE-DELAMINATED COMPOSITE CANTILEVER BEAMS 108

3.11 CONCLUDING REMARKS 110
CHAPTER 4 113
4.1 INTRODUCTION 114
4.2 MATERIALS AND PROPERTIES 115
4.3 SOFT IMPACT TESTING 116
4.3.1 Dynamic soft impact response 116
4.3.2 Test protocol 116
4.4 SOFT IMPACT FINITE ELEMENT ANALYSIS 118
4.4.1 FE analysis of orthogonal 3D woven composites 118
4.4.2 Soft impact FE constitutive model 122
4.4.3 Rate dependency of tow and matrix material 122
4.4.4 Constitutive model for the metal foam projectile 123
4.4.5 Matrix material 125
4.4.6 Equivalent UD-laminate material 126
4.5 RESULTS AND DISCUSSION 127
4.5.1 Transient deflection of beams 128
4.5.2 Effect of Through-the-thickness reinforcement density on back-face deflection 131
4.5.3 Damage during soft impact 132
4.6 POST IMPACT QUASI-STATIC BENDING RESPONSE 139
4.7 THE ROLE OF THE TTT REINFORCEMENT 142
4.8 CONCLUDING REMARKS 145
CHAPTER 5 147
5.1 INTRODUCTION 149
5.2 FINITE ELEMENT MODELLING 151
5.3 BALLISTIC IMPACT UPON 3D WOVEN COMPOSITE BEAMS 152
5.3.1 Deformation and damage mechanisms during clamped-beam ballistic impact loading 154
5.4 3D WOVEN SINGULAR-HIT IMPACT SIMULATIONS 162
5.4.1 Deformed configuration and stress distribution 163
5.4.2 UD-laminate clamped plate deformation and penetration mechanisms 165

5.4.3 3D woven composite plates deformation and penetration mechanisms..... 169

5.4.4 Fibre damage distribution 171

*5.4.5 Coefficient of restitution ..... **Error! Bookmark not defined.***

5.5 MULTI-HIT BALLISTIC IMPACT MODELLING VALIDATION (UD-LAMINATE)..... 173

5.6 CLAMPED CIRCULAR PLATE MULTI-HIT BALLISTIC IMPACT PREDICTIONS 177

5.6.1 Multi-hit ballistic limit surface 178

5.6.2 Multi-hit damage mechanisms 180

5.6.3 Projectile off-set..... 182

5.7 INTER-LAMINAR SHEAR STRENGTH ON THE BALLISTIC LIMIT OF UD-LAMINATE COMPOSITE PLATES 183

5.7.1 Numerically predicted ballistic limit 185

5.8 CONCLUDING REMARKS 186

5.9 DISCUSSION AND RECOMMENDATIONS FOR FUTURE WORK 189

CHAPTER 6..... 191

6.1 CONCLUSIONS 191

6.1.1 Quasi-static collapse of 3D woven carbon fibre composites 191

6.1.2 Soft impact of orthogonal 3D woven composites..... 192

6.1.3 Multi-hit ballistic impact characterisation of 3D woven composites 193

6.2 LIMITATION OF CURRENT STUDY AND FUTURE WORKS 196

6.2.1 Quasi-static collapse of 3D woven carbon fibre composites 196

6.2.2 Soft impact of orthogonal 3D woven composites..... 196

6.2.3 Multi-hit ballistic impact characterisation of 3D woven composites 197

6.3 PUBLISHED WORK..... 198

APPENDIX 223

CHAPTER 1

INTRODUCTION

Within the last 30 years. the use of composite materials, in particular fibre reinforced composites, saw a large-scale increase of use within the marine [1], aerospace [2, 3], and automotive sectors [4]. The main benefits of fibre reinforced composite materials which helped to increase their usage are their remarkably high specific stiffness and strength, excellent fatigue resistance, and the ability to tailor weave types and lay-ups to optimise component design.

Nowadays, composite materials have advanced a great deal, and have become integral to the design of high-performance automotive, aeronautical, and aerospace engineering structures. Carbon fibre reinforced polymers (CFRPs) are becoming increasingly attractive for commercial use as production methods become cheaper, and processing techniques allow complex net shapes to be formed. For example, the current generation of commercial aircraft consist of approximately 50% composite materials by weight. This allows for a vast reduction in the overall weight of structures, without sacrificing the rigidity or strength of a structure. CFRPs exhibit high levels of heterogeneity, given rise due to their highly orientation-dependent fibre structures. Certain high-end applications of carbon fibre reinforced composites utilise a simple structural configuration in the form of uni-directional (UD) laminate composites. UD-laminate composites can be extremely useful materials in themselves, however, are marred with early-onset damage issues. A common cause of damage with UD-laminate composites is inter-laminar crack propagation. This is effectively a splitting apart of the layers of the material, and is referred to as delamination. A prominent example of which occurred in the U.S.A, where a non-routine inspection of an Airbus A300 aircraft led to the chance discovery of composite delamination caused by leaking hydraulic fluid. This damage was reported to be significant enough that failure could have occurred during regular flight. A similar

damage source was cited for the rudder failure of an Airbus A310, and gave particular concerns to the often-undetectable nature of delamination damage [5]. Figure 1.1 presents a photograph of delamination damage sustained on the vertical fin of a Diamond DA20-C1 aircraft after being blown into hanger doors by strong winds.



Figure 1.1. Delamination damage of a Diamond DA20-C1 aircraft vertical fin. (Image reproduced from http://www.mansbergeraircraft.com/Images/gallery%20xbjry/xbjry-3f.jpg)

1.1 3D woven composite materials

Woven textile composites have seen extensive development in the last decade due to their inherent protection against inter-laminar crack propagation [6, 7] and their ease of manufacturing of complex shapes [8]. In particular, nearly net-shape 3D woven composite textiles have generated much interest within industry. The 3D weaving process, not too dissimilar to older loom-based textile weaving, has the potential for high automation and speed. Inter-laminar fracture toughness values have been reported in the literature up to values as high as 7000 J/m^2 [9], with far less reductions of in-plane material properties as is common with 2D woven structures. Research into 3D woven composite materials undertaken over the past

decade has revealed the following advantages of 3D woven composites in comparison to UD-laminate composites [8]:

- The ability to produce complex, almost net-shape preforms
- Cheaper and easier to manufacture
- Customisation of through-thickness properties
- Higher delamination and impact resistance
- Potential for higher strain-to-failure values
- Increased inter-laminar fracture toughness properties

It should, however, be noted that some distortion and crimping of yarns is present within the material and this can lead to a reduction of in-plane properties with respect to analogous UD-laminates [8].

The general manufacturing method for woven composites involves feeding warp yarns into a weaving loom from the yarn source. The yarn source can consist of either of a singular package of yarn (referred to as a creel), or a number of cylindrical beams of which the warp yarns have been pre-wound. A lifting mechanism is used to lift the warp yarns and create space in between them (referred to as the shed). The weft yarns are then inserted into this space at right angles to the direction of the warp yarns. A reed, of which is similar to a comb, is used to ensure the correct spacing of warp yarns throughout the width of the fabric, and to compress the fabric after weft yarn insertion. The through-the-thickness reinforcement can then be inserted and the path controlled by the sequence of yarn lifting. A wide variety of fibre preform architectures can be manufactured by variations on the shed and weaving patterns. Two of the most common weave patterns, orthogonal and layer interlock weaves, are shown in Figure 1.2(a) and (b), respectively. Although the in-plane properties of 3D woven composites have been well documented within the literature, there are still gaps in the form of under-investigated load cases. These include quasi-static out-of-plane bending, soft impact, and multi-hit ballistic impact. The work presented within this thesis will address these gaps.

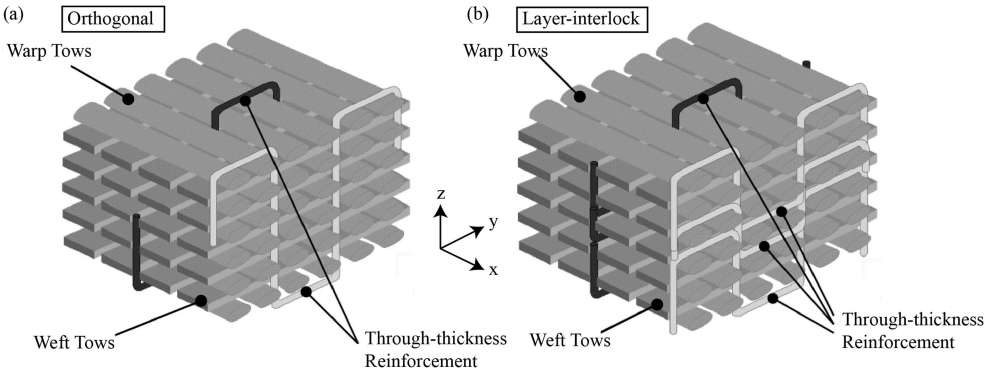


Figure 1.2(a) Orthogonal and (b) layer-interlock woven fibre preforms. Reproduced from Mouritz, Bannister [8].

1.2 Numerical modelling

Numerous finite element modelling strategies have been developed for the prediction of the elastic properties of 3D woven composites. However, for damage initiation and propagation within such complicated materials, numerical predictions have often been semi-empirical or reliant upon published data of material properties. In order for 3D woven composite materials to reach maturity and enter wide-spread use within industry, further development of numerical modelling strategies must be completed. This will allow vastly reduced costs for the design and development of composite structures which could benefit from the use of 3D woven materials, such as turbo fan engine fan blades and fan cases.

Components must be designed to withstand extreme loading conditions, significantly complicating analysis in comparison with simple material coupon tests. Reliable and computationally efficient non-linear numerical simulation methodologies of full-scale 3D woven composite components still remain a “holy grail” for engineers.

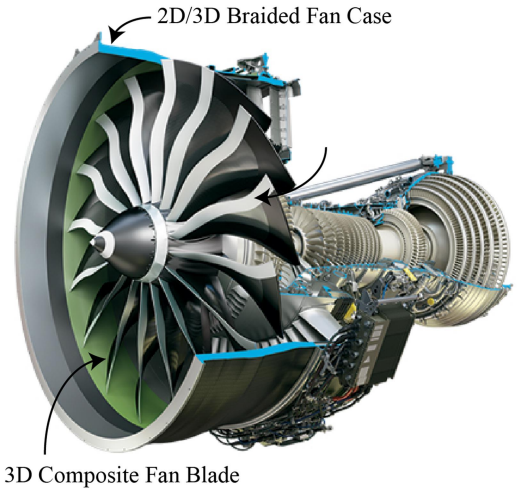


Figure 1.3. General Electric GE9x turbo fan engine with 3D composite fan blade and 2D/3D braided fan case. Image reproduced from http://www.ge.com/stories/aviation-ge9x.

1.3 Impact mechanics

The high specific stiffness and strength of composites naturally lend themselves for use in highly mobile vehicles, for example jet aircraft and troop carriers. In regards to the military applications, the ability of a material to protect against impact loading is often the critical design criteria for the structure. One prominent example of this is the use of small arm bullets and Improvised Explosive Devices (IEDs) targeting troop carrying vehicles on and behind the front line of conflict zones. IED is a broad term that includes buried mines, roadside explosives, and charges placed within vehicles. These devices can pose significant threats to both civilian and military targets due to the creation of high velocity fragmentation, soil ejecta, shock waves, and thermal radiation.

The threat can broadly be classified into two categories, namely, ballistic impact and blast loading. Ballistic impacts are characterised by hard projectiles or fragments travelling at high velocities to impact upon a structure. Ballistic impact is also referred to as “hard impact”. Blast loading, on the other hand, is characterised by the interaction of shock waves upon a structure. These shock waves can be present in various mediums such as air, water, sand, or soil. The

interaction of the shock waves upon a structure is referred to as the fluid-structure interaction (FSI), and the behaviour changes significantly for different fluid mediums. This type of loading is referred to as "soft impact". Protective structures should be designed to resist both types of threat, or even combinations of the two. For example, a buried road-side land mine imposes both hard impact from fragmentation, and soft impact from the accelerated sand ejecta. Figure 1.4 shows a photograph of a High Mobility Multipurpose Wheeled Vehicle (HMMWV), commonly referred to as a Humvee, demonstrating severe front-side damage after the nearby detonation of an IED. The high specific stiffness and strength, combined with inherent impact damage mitigation properties, make 3D woven composite materials a natural choice for blast resistance.



Figure 1.4. High Mobility Multipurpose Wheeled Vehicle (HMMWV), commonly known as a Humvee, demonstrating damage from an IED blast. (Image reproduced from http://www.precious-testimonies.com/images/j/JOE_5217.jpg)

1.4 Thesis objectives

This thesis provides an in-depth examination of carbon fibre composite materials under quasi-static tension, compression, and out-of-plane bending, dynamic soft impact, and ballistic impact loading. It incorporates mechanical coupon testing,

quasi-static and dynamic structural testing and finite element numerical simulation to provide a comprehensive understanding of the response of 3D woven composite materials.

The main objectives of the work presented here are:

1. to develop the understanding of the collapse mechanisms of orthogonal 3D woven composites under quasi-static in-plane tension and compression and quasi-static out-of-plane bending,
2. to characterise the response of orthogonal 3D woven carbon fibre composites during dynamic soft impact loading,
3. to understand the influence of fibre architecture and inter-laminar shear strength on the response of fibre reinforced composites undergoing singular and multi-hit ballistic impact loading.

This work makes the following novel contributions to the field in order to accomplish the above mentioned objectives. The first objective was achieved by quasi-static in-plane and out-of-plane cantilever bending experimental tests of two orthogonal 3D woven composite materials varying only by density of through-thickness reinforcement. Cantilever beam bending experiments were used to demonstrate two distinct collapse mechanisms. The two damage modes were investigated in depth via Digital Image Correlation (DIC) and post-test μCT scans. This was supplemented by a full-scale embedded element finite element modelling strategy, employed to provide further insights into the experimental results. The numerical model employs an established continuum damage mechanics framework. The study demonstrates the areas in which this modelling strategy is shown to be effective, and suggests areas in which greater detailing are necessary. The second objective was realised by the design and construction of a pressurised gas gun material test system at the University of Nottingham. The gas gun was employed to conduct high speed soft impact experiments upon orthogonal 3D woven composite beams. A description of the design of the test system is presented in Appendix A to this thesis. The modelling strategy presented previously for quasi-static load cases was modified and employed to aid

in the analysis of the experimental results. The soft impact response of 3D orthogonal woven composite materials has not previously been covered experimentally or numerically within the literature. The third objective utilised the previously developed and validated finite element modelling strategy to conduct numerical calculations of single and multi-hit ballistic impact simulations on both 3D woven composite material, and an equivalent UD-laminate material. It used full scale simulations to discuss in detail the global response of plates during singular penetrative events, and multi-hit impact events. This again is a novel contribution to the literature, highlighting the ways in which through-the-thickness reinforcement can modify the multi-hit response of fibre reinforced composite materials. A novel parameter study on the effect of the inter-laminar shear strength on the ballistic limit of composite laminate plates is then presented. It is the first study to utilise a numerical model to attempt to provide a mechanistic interpretation of the response of laminate composites of varying inter-laminar properties.

1.5 Thesis Outline

Chapter 2 in this thesis presents a literature review which examines the current state of affairs regarding CFRPs undergoing out-of-plane bending, soft impact, and ballistic impact. It discusses the nature and causes of delamination damage, and the ways in which 3D woven composites can protect against this damage mode. It also introduces the current FE modelling strategies regarding fibre reinforced composites, highlighting the difficulties faced during modelling of complex woven composites.

As it will be shown in Chapter 2, 3D woven carbon composite materials can provide enhanced out-of-plane properties due to the presence of fibre reinforcement orientated through-the-thickness of the material. The collapse response of 3D woven composite materials is studied through the use of quasi-static in-plane tension and compression and out-of-plane cantilever beam bending experiments in **Chapter 3**. Results are compared to a similar UD-laminate composite material. A meso-scale finite element modelling strategy for 3D woven

carbon composites is then introduced and validated via uni-axial quasi-static mechanical testing. The FE method is then utilised to further investigate the collapse response of the samples, and how the through-thet-thickness reinforcement influences the response of the beams.

3D woven carbon fibre composite materials have the ability to not only provide significant enhancements during quasi-static loading conditions, but also during dynamic load cases. A high-speed soft impact experimental and numerical investigation is undertaken in **Chapter 4**. The role of the through-the-thickness reinforcement is addressed via the examination of the back-face deflection and damage sustained within beam samples throughout the loading event. Comparisons are made between two different materials of varying densities of through-the-thickness reinforcement. The internal damage sustained during the test is then investigated via the use of post-impact clamped-clamped beam bending experiments. Experimental tests are supplemented with a variation of the finite element modelling strategy presented in Chapter 3.

The finite element modelling strategy presented in Chapter 4 for the impact of orthogonal 3D woven carbon composites is expanded in **Chapter 5** by experimental validation of ballistic impact tests on composite beams. The model is then used to investigate the multi-hit ballistic impact characterisation of 3D woven carbon composite panels. Comparisons are made with uni-directional laminate composite panels, and metallic panels. Characterisation and ranking of the ballistic limit of fibrous composite materials is often achieved by the calculation of the materials so called Cunniff velocity. The Cunniff velocity has been proven to successfully rank glass fibre, carbon fibre aramid fibre, ultra-high molecular weight polyethelene (UHMWPE), and Poly (p-phenylene-2,6-benzobisoxazole) (PBO) fibre composites. However, the Cunniff velocity is entirely focused on fibre properties. It has been shown within the literature that the matrix properties of composites can cause significant variations in the ballistic limit. Chapter 5 concludes with a parameter study investigating the effect of inter-laminar shear strength on the targets ballistic limit.

Finally, **Chapter 6** contains a summary of all of the conclusions and contributions made within this thesis and provides recommendations for future studies to progress on from this work.

CHAPTER 2

LITERATURE REVIEW

Summary

As discussed in Chapter 1, composite materials can provide a multitude of benefits for structures under a variety of loading conditions. This literature review provides an overview of test methods, material response, and modelling strategies for carbon fibre reinforced epoxy matrix composites, focusing on delamination damage, advanced 3D woven composite materials, out-of-plane loading, soft impact, multi-hit impact load cases, and modelling strategies.

The first part of this review gives an extensive overview of delamination damage within composite materials, and highlights the current testing methods for out-of-plane bending of carbon fibre composites, with particular focus on 3D woven carbon composite materials. It goes on to discuss soft impact and multihit impact of composite materials. The second part discusses the finite element (FE) modelling approaches which are commonly employed for fibre reinforced composites, proceeding to highlight the methodologies used for 3D woven composite structures, and modelling of impact events. Figure 2.1 presents a flow chart which summarises the logical sequencing of this literature review. It is not intended as an entirely exhaustive review on the subjects in question, but as a selection of the most relevant sources for each topic. Readers are suggested to follow citations within the review for further information.

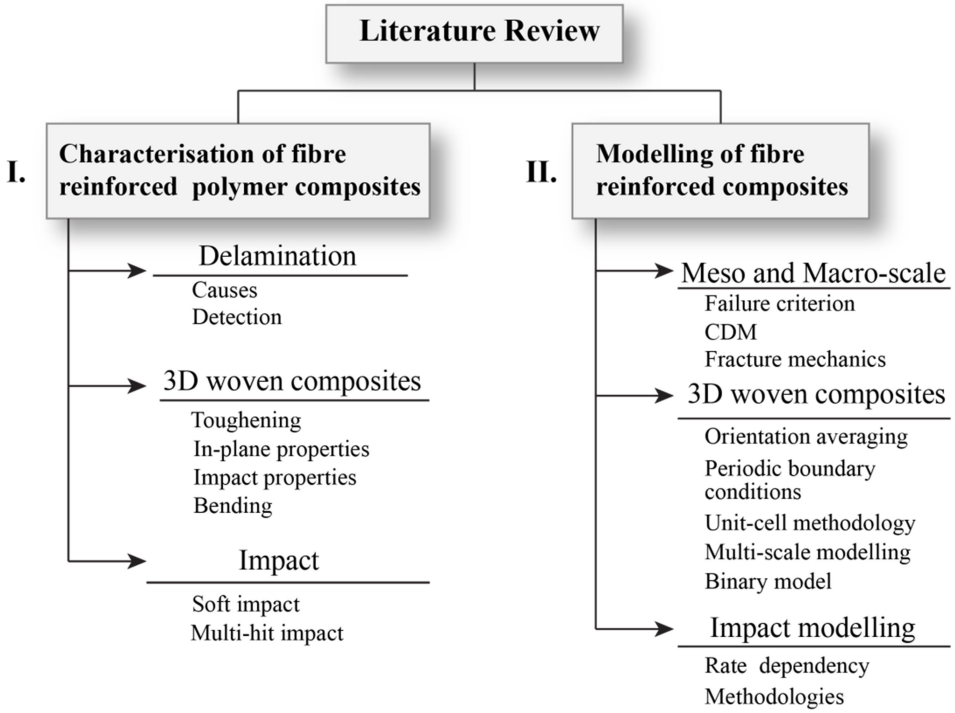


Figure 2.1 Literature review route map

2.1 Delamination

Delamination is one of the most critical failure mechanisms presented by fibre-reinforced laminate composite materials. The influence that delamination has upon the design of composite structures is perhaps one of the largest differences in behaviour between composite and metallic structures. The most common sources of delamination will be reviewed here.

2.1.1 Delamination due to impact loading

Delamination damage can be particularly insidious because the damage is not necessarily visible during surface inspect of structures [10-12]. Upon viewing of surface, the material has undergone no damage. However, underneath the surface there can be extensive inter-laminar cracking causing large reductions in strength. This is particularly an issue during impact loading, as demonstrated by a photograph of the edge of a quasi-isotropic glass reinforced epoxy composite post drop-weight impact test, shown in Figure 2.2. The material presents no visible

surface damage, but demonstrates extensive delamination throughout the internal structure.

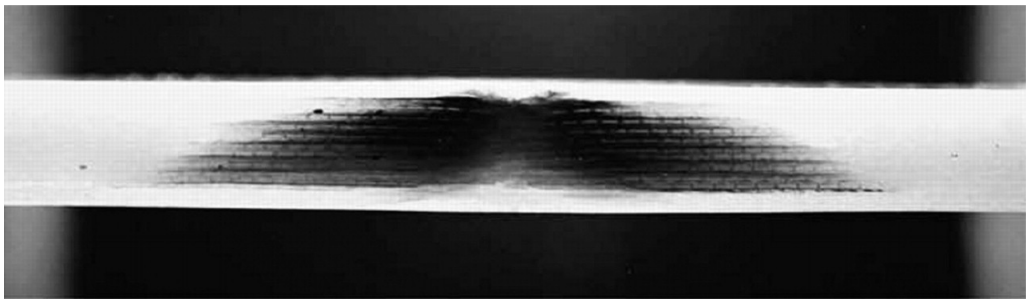


Figure 2.2. Edge view of a quasi-isotropic glass reinforced epoxy composite material post drop-weight impact test demonstrating extensive internal delamination damage. From Shyr and Pan [13].

The majority of wide-spread delamination presented during impact loading is localised to the resin-rich interface between plies. Delamination occurs at this position due to a combination of inherently weak through-thickness properties of composite materials combined with highly concentrated inter-laminar stresses present during impact events. This delamination often occurs at mid-plane, reducing away from the impact point [14]. Initial compressive stresses acting through the thickness of the composite plate can lead to localised suppression of delamination [15]. However, this benefit may be short-lived due to through-thickness stress-wave reflection off the free surface distal to strike location.

An often overlooked effect, delamination damage induced by impact loading can cause reductions of the residual tensile strength of composite materials. Studies such as Ogi, Kim [16] and Balasubramani and Boopathy [17] have been conducted to investigate tensile strength after impact. However, they do not distinguish the reduction in properties by delamination damage or that of fibre fracture. It is assumed that the majority of the reduction in tensile strength after impact is due to fibre damage, and not of delamination. The overall response may be due to a combination of these effects.

Compression after impact (CAI) testing is of great importance due to the large influence that delamination has upon the compressive material properties. The compressive properties are often significantly reduced as the delaminated plies no longer act as composite but begin to buckle individually. Delaminated composites undergoing compressive loading often undergo progressive out-of-plane local buckling of plies. This was investigated via the measurement of out-of-plane displacement fields by Guedra-Degeorges [18]. An alternative mechanism, in which delamination causes a reduction the CAI properties of composites, was demonstrated by Soutis and Curtis [19]. They showed that during buckling of delaminated plies, load redistribution can cause stress concentrations leading to fibre fracture. Pavier and Clarke [20] used finite element analysis to identify the superposition of bending and compressive stresses within the un-delaminated part of the laminate causing final failure of 0° plies.

2.1.2 Delamination due to free edge effect

Inter-laminar stresses can arise due to the geometry of a composite structure. Figure 2.3 presents three examples of delamination due to the presence of inter-laminar stresses owing to the geometric change of a composite structure. Potential delamination locations are highlighted on the figure in red. The first case, Figure 2.3(a), is that of a curved laminate subjected to bending. A bending moment acting to reduce the curvature will cause tensile normal inter-laminar stresses to develop. This can be combined with inter-laminar stresses that develop due to out-of-plane loading [21]. Delamination begins at the location of the highest radial stress in the curved region [22].

The second case, Figure 2.3(b), shows a step and scarf laminate taper. Both inter-laminar normal and shear stresses are caused due to the change in composite thickness influencing the distribution of stress. The third case shows a laminate composite experiencing distortion due to residual curing stresses, which can lead to matrix cracking and delamination damage [23].

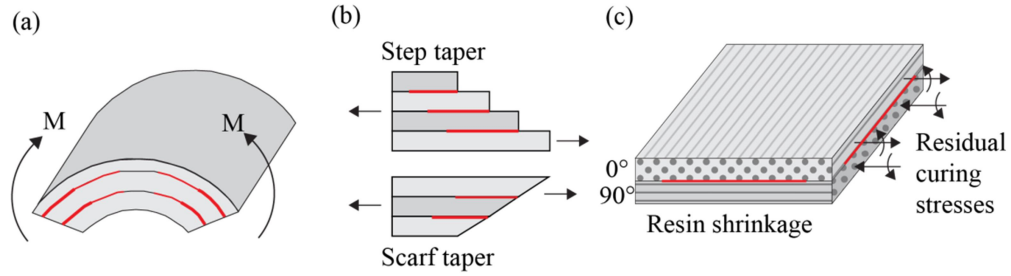


Figure 2.3. Delamination due to inter-laminar stresses (a) curved geometry under bending (b) taper geometry under tensile loading (c) residual curing stresses causing distortion. Adapted from Wisnom [14].

2.1.3 Delamination due to out-of-plane loading

Inevitably, due to the widespread proliferation of composite materials in primary and secondary aerospace and automotive structures, laminates will undergo a wide variety of load cases, including out-of-plane loading. Figure 2.4 demonstrates two load cases in which high inter-laminar stresses caused by out-of-plane loading may induce delamination damage. The first is a T-piece in which compressive loading upon the top surface of the web results in high inter-laminar shear stresses around the gusset, resulting in delamination [24]. The second is a laminate cantilever beam under-going out-of-plane bending loading. Regions of potential delamination damage are highlighted on Figure 2.4 in red.

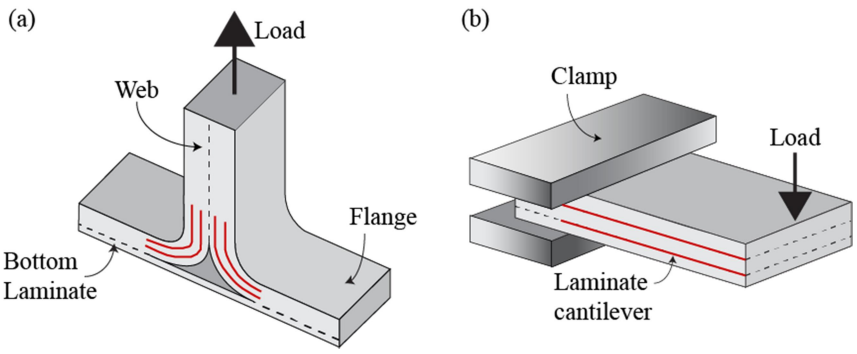


Figure 2.4. Out-of-plane loading of laminate composites which can cause sufficient inter-laminar stresses to induce delamination damage (a) T-piece (b) cantilever beam bending. Regions of potential delamination are marked in red.

2.1.4 Delamination due to discontinuities

Discontinuities arise in many different forms, and can lead to increases in local stress states. A localised increase of stress, combined with sufficient strain energy within the material, results in the propagation of cracking. Simply dropping tools upon laminate composites can cause cracks within the material [25, 26]. These cracks can lead to increased strain energy release rates and a localised Mode I component near free edges [27].

Dropping-off plies for thickness tapering are also prone to delaminations [28-30]. This is predominantly caused by the introduction of discontinuities or free edges at the cut locations [31, 32]. Surface ply drop-offs and stacked plies of the same orientation have increased susceptibility delamination [33].

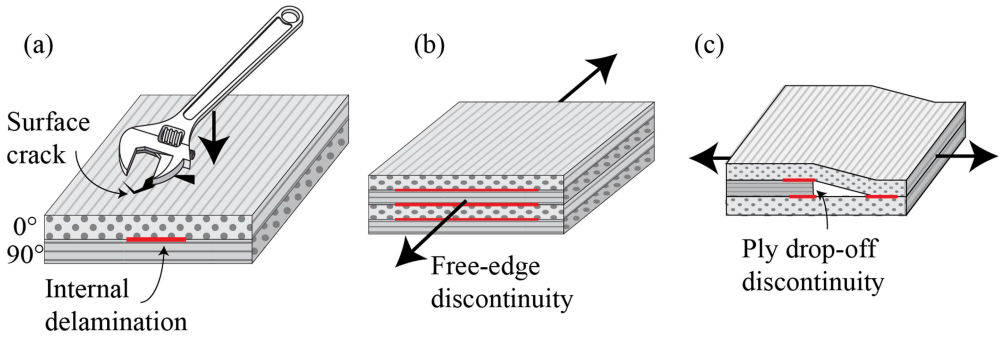


Figure 2.5. Sources of delamination in laminate composites due to discontinuities (a) crack discontinuities due to dropped tools, (b) free edge discontinuities, (c) ply drop-off discontinuity. Potential locations of delamination are marked in red.

Other sources of delamination include off-axis loading of quasi-isotropic laminates [34], tensile loading of thick laminates [35], tensile loading of notched laminates [36-41] open hole tensile loading [42-44], notched compressive testing [44-48], and notched combined loading [44]. An example of delamination damage due to notched tensile loading is presented in Figure 2.6. For a more detailed account of the sources and effects of delamination, readers are referred to Garg [49] and more recently, Wisnom [14].

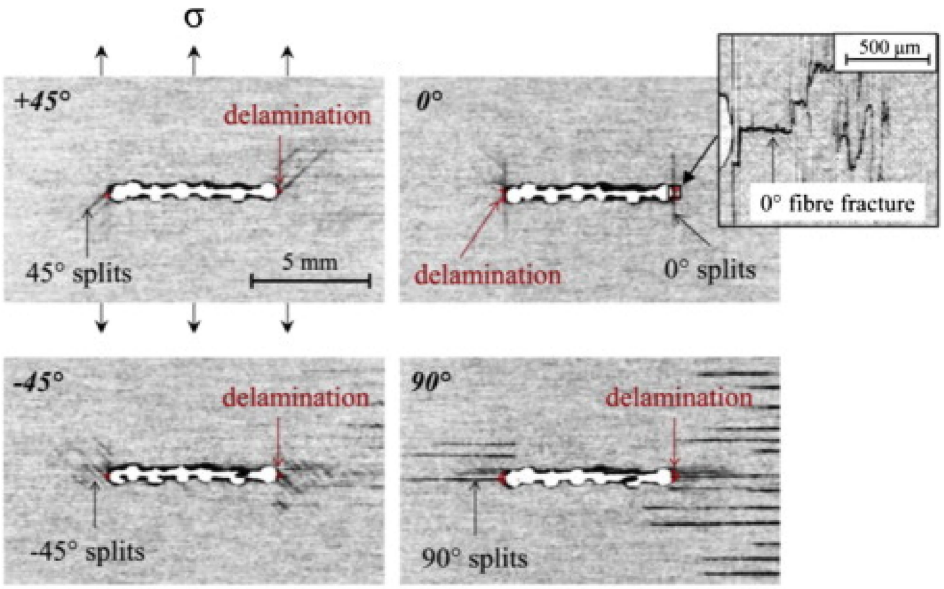


Figure 2.6. Ply-by-ply and inter-ply damage at 90% failure load, for a central notch under pure tensile loading adapted from Tan, Deshpande [44].

2.1.5 Detecting delamination damage

Due to the potentially negative consequences of an un-detected delamination damage mode in composite structures, there has been a large quantity of research focusing on non-destructive evaluation (NDE) of composite materials in order to detect delamination. NDE allows for the detection of damage prior to catastrophic events, reducing the down time required for structural maintenance.

One method utilised for the detection of matrix cracks and delamination damage is by embedding optical fibre sensors with the composite. Modifications to the magnitude and distribution of the reflection spectrum are used to determine the location and nature of damage within the composite. This method has been proved useful for mapping the growth of damage regions [50-52], in particular delamination [53-57]. However, issues include the inability to embed fibre optic sensors in already-built structures, the inherent strength decrease due to the insertion of fibres, and the difficulty in repairing them if damaged [58, 59].

A technique for in-situ damage classification of composite materials which can be applied to systems in service without any strength decrease and with improved ease of sensor repair is the electric potential method. Delamination damage can be detected by changes in the through-thickness electrical resistivity [59-62]. As each composite material can vary from its constitutive components and ply lay-up, it is necessary to calibrate the equipment for each material type [59].

Other detection methods include the introduction of a diagnostic layer consisting of either an electrical grid [63] or actuators and sensors [64, 65] and vibration-based structural health monitoring. For vibration-based delamination detection, readers are referred to the review by Zou, Tong [66].

C-scans can prove useful in the detection of matrix cracking, delamination, or other damage modes which are commonly incurred by the impact loading of composite structures [67-71]. A comparison of the areas of damage can used in order to rank materials by their ability to resist damage. Researchers note that the presence of through-thickness reinforcement within composite structures can reduce the area of delamination damage [72]. Gerlach, Siviour [72] also goes on to note that studies of delamination damage of UD-laminate composites propagates relatively evenly in the in-plane directions, whilst for through-thickness angle interlock (TTAIL) composites, damage is often oval shaped, progressing further in the weft direction than the warp. Figure 2.7(a) and (b) presents a sketch of the TTAIL composite material showing binder orientation, and C-scan of a TTAIL plate specimen centrally loaded quasi-static to an out-of-plane displacement of 7mm (adapted from Gerlach, Siviour [72]).

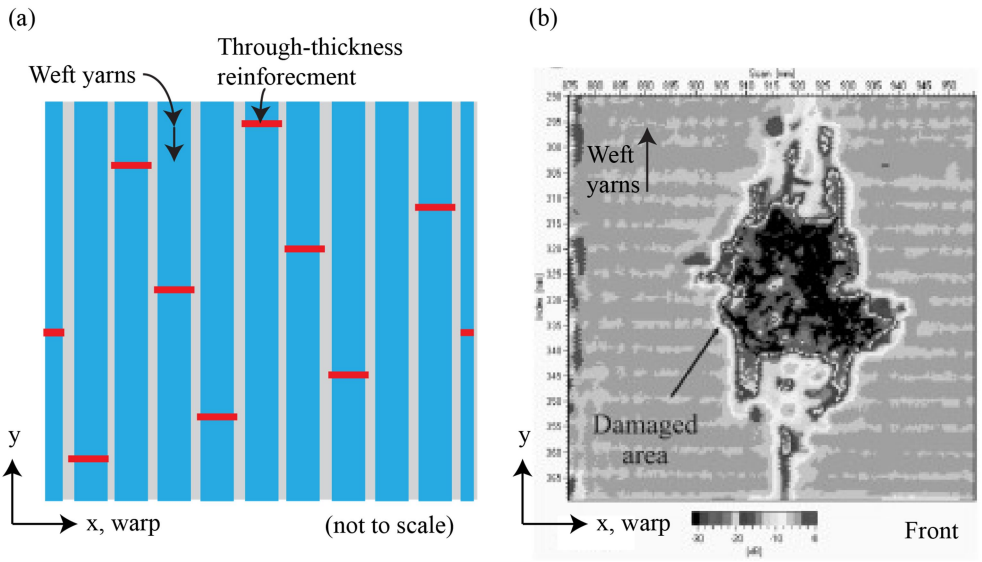


Figure 2.7(a) Sketch of TTAIL composite material (b) C-scan of sample after quasi-static indentation test of deflection 7 mm. (Adapted from Gerlach, Siviour [72]).

The C-scan methodology can be used to rapidly scan large areas of composite structures. However, it has been noted that it is not particularly effective at detecting barely visible impact damage (BVID). The reasoning behind this is that BVID does not necessarily induce discontinuities within the material at the scale required for detection [73]. Also, the C-scan method only gives information regarding the projected damage, and cannot resolve over-lapping delaminations [74].

CT-scanning of samples can provide excellent 3D visualisations of damage modes within composite structures. The development of several commercial systems have made x-ray microtomography (micro-CT) more accessible for use within laboratories. Micro-CT scanning has been proved to be useful in the characterisation of the internal damage of fibre reinforced composites such as fatigue crack growth [75], delamination [76, 77], fibre breakage [75, 76, 78] and fibre pull-out [79]. This level of characterisation is often superior to that which can be provided by post-impact material testing, or even C-scans. Figure 2.8 presents images of a three-dimensionally reconstructed model using micro-CT

data of a bearing failure around a bolt hole within a graphite/epoxy laminate, from Schilling, Karedla [77]. It demonstrates the level of detail that can be achieved by utilising a CT scanning methodology, and how delamination lengths can be measured without extensive sectioning of the sample.

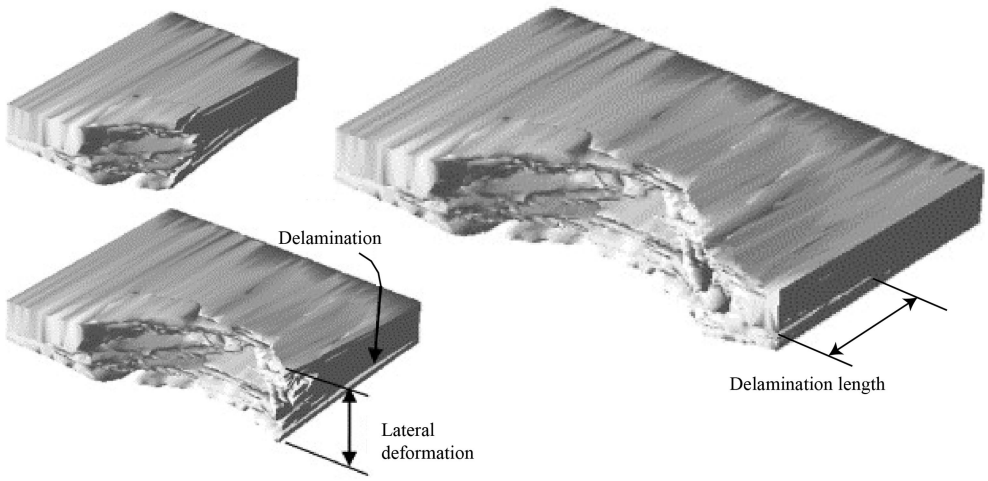


Figure 2.8. Bearing failure damage around a bolt hole within a graphite /epoxy laminate. Reconstructed volumes using X-ray microtomography. (Adapted from Schilling, Karedla [77]).

Difficulties, however, can arise during the CT scanning of carbon fibre reinforced epoxy matrix composites, due to the similar levels of impedance between the fibres and the matrix. This can be improved with the use of a zinc-iodide x-ray opaque dye in order to improve contrast within the images and aid visualisation [77, 80]. However, for constrained samples, with only small quantities of damage (for example after low velocity impact of 3D woven composite materials), penetration and absorption of the dye into the microscopic damage regions proves difficult.

Other methodologies include vibrational analysis [81-83], which operates on the principal that changes to a structure's physical properties brought on by damage, such as mass, damping, and stiffness, effects its modal properties and dynamic responses.

2.2 3D woven composites

3D woven composites offer a combination of reasonable manufacturing cost with the delamination resistance without a large-scale reduction of in-plane properties which is common with traditional 2D weaves. The majority of this thesis focuses on 3D woven composites, and the contribution of the through-the-thickness yarns to the response of composite materials undergoing various load cases.

3D woven composites are fibre reinforced composite materials that are manufactured with the use of woven fibre preforms which contain fibres orientated in all three dimensions. The process of weaving a 3D preform typically involves inserting nominally straight weft yarns between layers of warp yarns. 3D woven preforms can be manufactured using the majority of commercial weaving looms, although Jacquard looms are the most common due to their high levels of automation and good management of the final fibre structure [84, 85]. The warp yarns are held parallel to the direction of the weaving process (0°), which is commonly referred to as the x-axis. They travel through a series of bars or rollers to maintain their relative positions and apply a small tensile force onto the yarns. A lifting machine then raises the warp yarns to create a gap (the shed) into which the weft yarns (90°). Variation in the lifting and weft yarn insertion process can allow for multiple sheds to be formed, therefore allowing many simultaneous weft yarns to be inserted. This allows for a much faster preform production rate and is what is often regarded as true three-dimensional weaving [85]. Furthermore, 3D weaves offer much higher permeability than stacked 2D preforms, allowing for an increase in the rate of matrix infusions; giving the potential for toughened matrix materials [86].

2.2.1 Fibre architecture

Variations to the weaving path of the though-thickness reinforcement, or "z-binder yarn", can give rise to different 3D weave architectures. These are angle interlock, orthogonal weaves (which both can be either through-the-thickness or layer-to-layer) and multilayer weaves. Although angle interlock weaves offer

enhanced properties in regard to delamination resistance, impact resistance, damage resistance and geometrical stability with respect to laminate composites [87], superior through-the-thickness elastic and strength properties can often be achieved by using orthogonal woven composites [88].

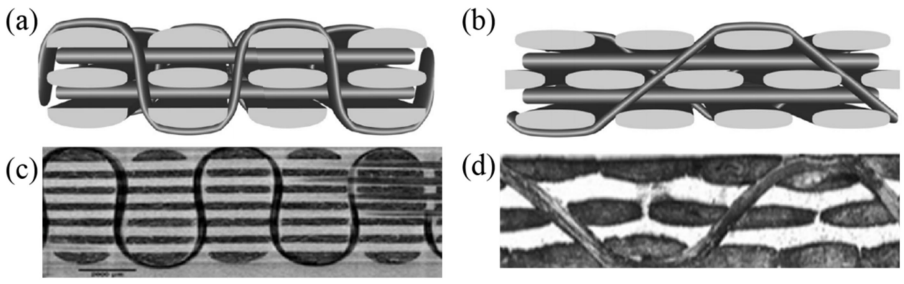


Figure 2.9. Cross sections of 3D woven fabrics : geometric models (a) orthogonal and (b) angle-interlock fabrics; μCT scans (c) orthogonal and (d) angle-interlock [89].

The introduction of the through-the-thickness causes displacement and distortion of the in-plane warp and weft yarns [90-92]. One of the main effects the binder has is the compressive force it has upon the in-plane fibre architecture, compressing the yarns and causing localised changes in angle of the top and bottom yarns. This effect is referred to as “crimping” [93, 94], and is most prominent at the position of wrap-around of the through-thickness reinforcement [95]. Figure 2.10 presents a sketch of crimping of tows.

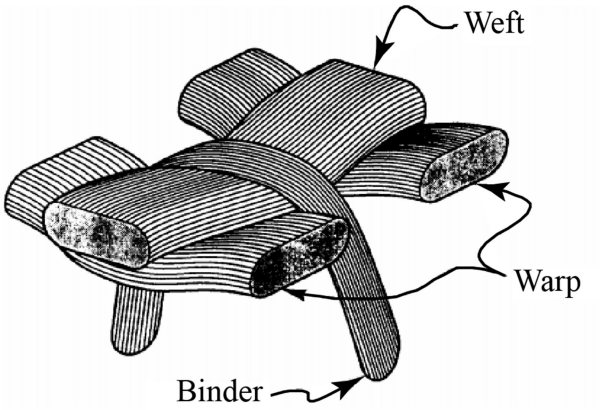


Figure 2.10. Sketch of "crimping" fibre distortion common to 3D woven composites. (After Cox, Dadkhah [96]).

Crimping is present in other composite materials such as 2D woven and even UD-laminate; however, to a much smaller extent. The two predominant methodologies for quantifying the amount of crimp in a composite material is to either simply measure the crimp angle from parallel to the plane or reporting the ratio between the length of the crimped yarn to the length of the specimen from which it resides within. This ratio is known as the "crimp factor" [95, 97, 98]. Tong, Mouritz [85] collated published data regarding the crimp angle and the plastic tow straightening stress and is presented in Figure 2.11. It is useful for relating the fibre crimp angles for different fibre architectures.

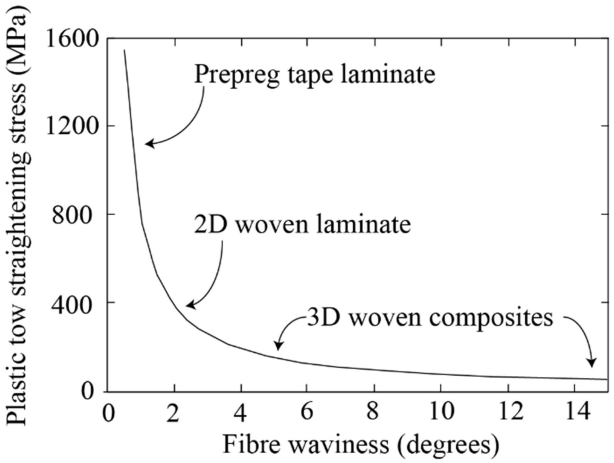


Figure 2.11. Plastic tow straightening stress as a function of fibre waviness from Tong, Mouritz [85]

The compressive forces from the binder yarns also cause a grouping effect of in-plane yarns referred to as "collimation"[90]; this can lead to alternating fibre groupings and resin-rich areas within the composite [90, 92]. The effects of the binder on the in-plane fibre architecture has been well covered within the literature. However, isolating the exact role in which it plays during bending or impact loading can be difficult when attempting to find analogous non-crimp or UD-laminate materials for a direct comparison [99]. This thesis uses the finite element method and a comparison between 3D woven composites and a specifically generated "equivalent UD-laminate" material, identical in all aspects except the through-thickness reinforcement, in order to address this issue.

2.2.2 Toughening

The main reasoning behind the inclusion of through-thickness reinforcement in 3D woven composites is the poor inter-laminar fracture toughness of laminate composites. A brief over-view of the issue and theory is reported here, followed by a description of the enhancement provided by through-thickness reinforcement.

The quantity of energy required for the propagation of a Mode I crack (tensile) is given by the fracture toughness of the resin matrix, G_{IC}. This fracture toughness

can effectively be enhanced by toughening mechanisms induced by fibre bridging or crack branching [100-102]. Fibre bridging can even occur in UD-laminate composites, when fibres cross over into the plane of an adjacent ply, forcing the crack to fracture the bridging fibres before propagation can continue. This was recoded to have increased the tensile fracture toughness of a composite by up to four times [103].

The presence of fibres within a composite material can also act to increase the fracture toughness by crack branching. This is where a propagating crack is forced to deflect from the longitudinal axis, increasing the travel path, and therefore increasing the energy required for delamination to occur [102].

The double cantilever beam (DCB) test is commonly employed to composite materials in order to determine the Mode I fracture energy. The test employs a pre-initiated crack located at the mid-plane of the free end. A constant displacement is applied to the crack, and the applied force and crack length are recorded throughout the test. This allows for the calculation of the energy required for crack growth (G_{IC}). Interpretation of the data allows for the generation of a resistance curve (R-curve). The R-curve demonstrates the energy at which crack-growth transitions to become stable, i.e. self-propagating. Figure 2.12(a) presents an example R-curve for a layer-to layer woven composite demonstrating a definitive bridging zone, where the crack growth resistance values increase with increasing crack size. The material then reaches a steady state value of fracture toughness. This value represents the stage in which the progression of the crack resulted in the same number of through-thickness tows added to the crack-bridge zone as those which were fractured through crack progression [104]. Figure 2.12(b) presents a sketch of a typical fibre bridging zone during Mode I crack propagation within 3D woven composites. 3D woven composites can increase Mode I fracture toughness by around 10-20 times that of a similar UD-laminate material [105], with orthogonal through-the-thickness weaves performing better than angle-interlock weaves [104]. The dominant mechanisms of energy absorption by the bridging of through-thickness tows have been attributed to [106, 107]:

1. Elastic stretching of yarns
2. Debonding between yarns and matrix
3. Fracture of through-thickness reinforcement
4. Pull-out of through-thickness reinforcement

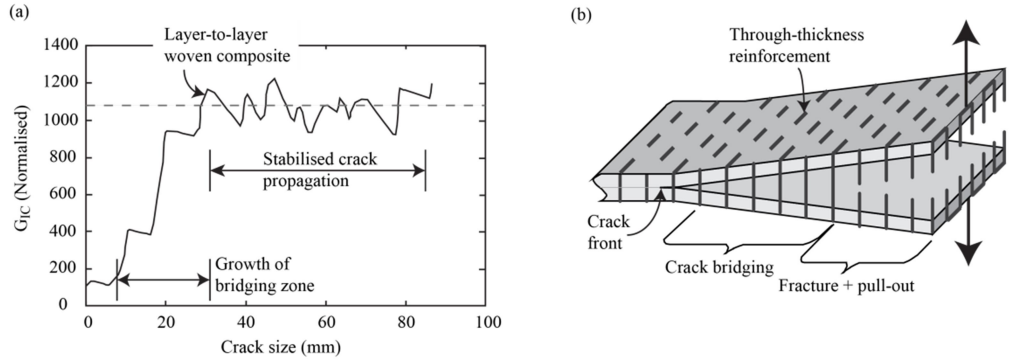


Figure 2.12. (a) Example R-curve for layer-to-layer 3D woven composite material. The values are normalised for commercial sensitivity reasons. (After Fishpool, Rezai [104]) (b) Sketch of a through-thickness reinforcement bridging zone (After Tong, Mouritz [85]).

Generally, the measurement of Mode II fracture of materials is a more complicated procedure due in part to frictional forces between delaminated surfaces, inducing variability with recorded values of G_{IIC} [108]. The standard methodologies for measuring the Mode II fracture of composite materials is the end-loaded split (ELS) method [109, 110], and the four-point end-notched flexure (ENF) tests [111, 112]. The original testing methodology, the three-point ENF test [113], had certain disadvantages as it generated an unstable crack growth and yields only initiation values of G_{IIC} [114]. The same authors then go on to note the disadvantage of the stabilised ENF test, highlighting the complexities of requiring real-time controlling of the test specimen.

The standard four-point ENF test has the disadvantage of inducing compressive stress across the delaminated interface in the region of the load and support pins, potentially increasing the apparent fracture toughness by up to 5% [115]. Studies have made improvements to the test method by modifying the loading pattern in

order to reduce the effects of friction [116]. The ELS test has been shown to produce a stable crack growth. However, researchers have commented on difficulties in recording the exact length of delamination throughout the test [115], as distinguishing between crack growth and other damage sources is not trivial with Mode II testing [114]. Blackman, Brunner [114] introduced a "crack length independent" approach in order to avoid such difficulties.

2.2.3 Young's modulus

Previous investigations into the Young's modulus of 3D woven composites in comparison with 2D composites yield varying outcomes. Some have claimed that 3D woven composites have a reduced Young's modulus [117, 118], whilst others have claimed the opposite to hold true [119, 120]. In order to clarify this apparent contradiction, a consistent definition of yarn types and volume fractions must be applied to a collection of data within the literature [105]. The collated data set of Young's modulus of each composite as a function of the product of Young's modulus of pristine fibre reinforcement (E_f) and the warp fibre volume fraction is presented in Figure 2.13. Although troubled by large material data scatter, particularly for carbon fibre composites, Rudov-Clark [105] concludes that the Young's moduli of 3D woven composites are comparable to that of cross-ply and 2D woven composites.

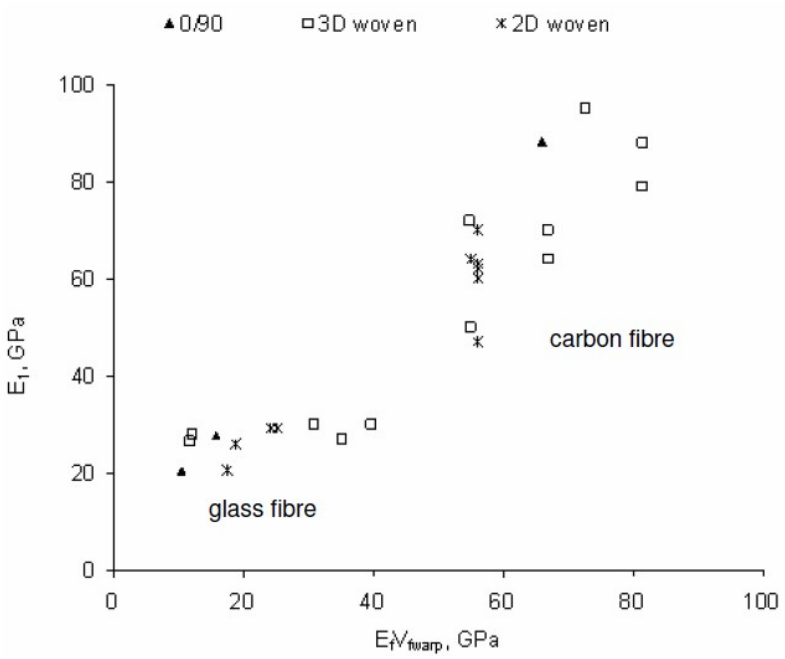


Figure 2.13. Collated tensile Young's modulus data for cross-ply, 2D woven and 3D woven composites. From Rudov-Clark [105] PhD Thesis. Original data from [95, 97, 121-123].

Various researchers have ascertained that the actual physical presence of the through-thickness reinforcement has no influence on the Young's modulus of the composite [97, 118], and that only by the introduction of fibre crimping is the Young's modulus lowered [118]. Rudov-Clark [105] presented collated data of the Young's modulus of layer interlock, angle interlock, and orthogonal 3D woven composites as a function of the product of the Young's modulus of individual fibres and volume fraction along the warp direction. No significant differences between the three fibre architectures were noted.

2.2.4 Tensile strength

As with Young's modulus, individual investigations have led to different conclusions regarding the effect of the binder on the tensile strength of composites with some studies reporting unchanged properties [6, 124] and others reporting a reduction in strength [117]. Attempts at data collation of previously published literature also lead to different conclusions with Mouritz and Cox [99], suggesting

a modest decrease in tensile strength and the review presented in Rudov-Clark [105] PhD thesis indicating no significant difference with or without the binder. The primary reasoning behind the disparities within the published literature is the frequent large scattering of results and the difficulty of standardising equivalent UD-laminates or 2D woven composites for comparisons. This thesis will present a finite element method that can be utilised for elucidating the exact role of the through-thickness reinforcement during in-plane mechanical tests.

Reductions of the tensile strength of 3D woven composites have been attributed to fibre crimping or fibre damage which have been recorded during the weaving process [6, 121, 125]. A study on the damage of in-plane and through-thickness yarns during the weaving process by Rudov-Clark [105] revealed a reduction of strength in the yarns by up to 30% due to ultra-small scratches on the fibres caused by abrasion of fibres during weaving. No mechanisms have been reported for the increase of tensile strength due to the presence of though-thickness reinforcement [99].

2.2.5 Compressive strength

Compressive loading of fibre reinforced composites is often compared to that of an end-loaded column undergoing buckling. For optimal load resistance in compression, the fibres require precise alignment to the loading direction and high levels of lateral support provided primarily by the matrix material. Marissen and Brouwer [126] summarised the properties required for a fibre reinforced composite to exhibit good performance during compression loading as: good fibre alignment, large fibre diameter, high fibre stiffness, high matrix stiffness and yield stress, minimal manufacturing related defects, i.e. good fibre impregnation and excellent bond strength between fibre and matrix.

The inherent fibre waviness induced by the weave process can be the limiting factor for woven composite materials. The generalised form of critical stress within a yarn for kink band instigation is given as:

$$\sigma_k = \frac{\tau_r}{\phi} \tag{2.1}$$

where ϕ is the angle of misalignment of the fibres, and τ_r is the critical stress for shear flow within the resin [127]. The compressive strength of 2D woven composites is lower than that of UD-laminates due to increased fibre waviness, and compressive strength decreases with increasing fibre waviness [128]. With 3D woven composites, this fibre misalignment is primarily located on the top and bottom edges of the composite; removal of these layers can lead to an improved compressive strength in these materials [129].

The standard equation for kink band prediction was expanded upon by Cox, Dadkhah [130] to account for the random distribution of fibre angles within a composite, arguing that kink bands will form first in the most highly crimped yarn regions and utilised in the creation of a finite element modelling strategy referred to as the Binary Model [131], discussed in greater detail later in this literature review. It has been determined that 3D woven composites can exhibit superior performance in compression compared with 2D laminate materials due to better alignment of in-plane yarns, and the suppression of delamination by the binder. This effect was seen to increase for composites with a higher density of through-thickness reinforcement [132].

Figure 2.14 presents a collation of compressive strength of cross-ply laminates, 2D woven, and 3D woven composites. The results are plotted against the theoretical strength of 0° plies within the composite. Detailed comparisons between the materials prove difficult due to large degrees of scattering within the results.

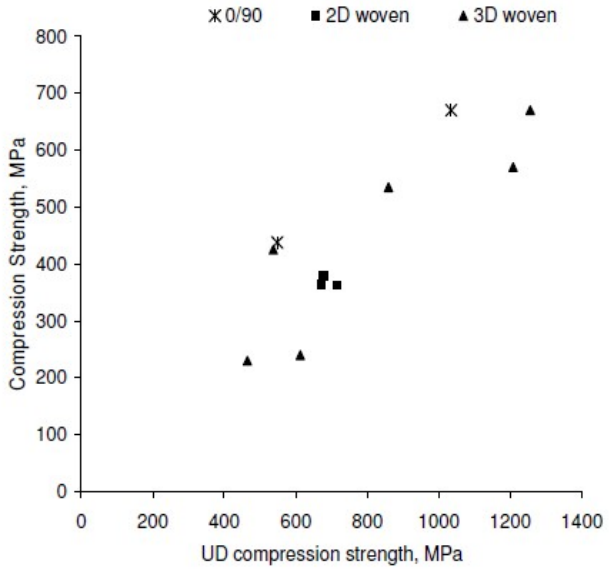


Figure 2.14. Collation of compressive strength data of 0/90°, 2D woven, and 3D woven composites from Rudov-Clark [105] PhD thesis.

Mouritz and Cox [99] present a collation of results within the literature regarding the normalised compressive strength (normalised against "equivalent UD-laminate") as a function of z-binder percentage in order to attempt to ascertain the effective of the through-thickness reinforcement. These results are presented here in Figure 2.15. The data shows large scatter and no statistically significant trend regarding the z-binder content. Issues arise in regard to the normalisation of the results, and the difficulty of finding a true "equivalent UD-laminate" material with identical in-plane fibre architecture and volume fraction as the 3D woven composite.

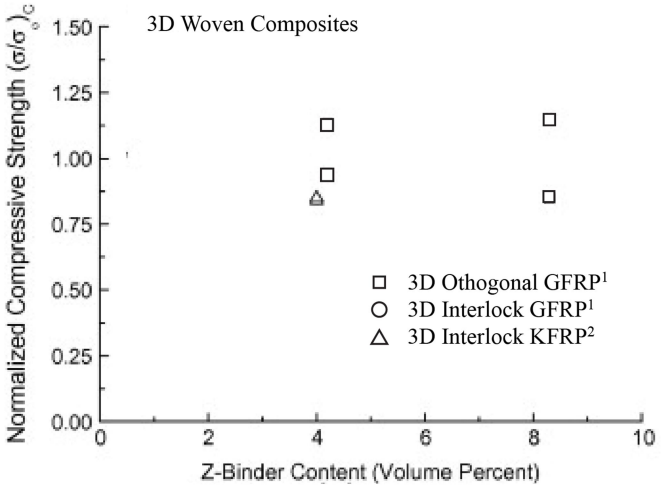


Figure 2.15. Effect of z-binder content on the normalised compressive strength of 3D woven composites [99].

The dominant mechanism for compressive strength enhancement inclusive of through-thickness reinforcement is the suppression of delamination and enhancement of the buckling resistance. However, the introduction of geometrical defects due to the introduction of the binder also acts to lower the compressive strength. This thesis utilises experimental compressive tests on a 3D woven composite material, combined with full-scale numerical modelling of the sample with and without through-thickness reinforcement, in order to elucidate the exact nature of the progression of the compressive collapse event within 3D woven composites.

2.2.6 High strain rate properties ($\dot{\varepsilon} > 100$)

Generally, within a carbon fibre reinforced polymer matrix composite, the matrix material displays strain-rate sensitivity [133] whilst the carbon fibres themselves do not [134, 135]. This can lead to some strain-rate sensitivity in the composite response, in particular compressive response, as the localised buckling of fibres can be delayed due to the strain rate sensitivity of the matrix, increasing strain to failure and thus, peak stress.

Even though one of the main reasons behind the development of 3D woven composite materials is due to their enhanced impact resistance, the literature is sparsely populated with data regarding the rate sensitivity of 3D woven composites, in particular carbon fibre reinforced polymers. Gerlach, Siviour [72] present an investigation into the in-plane and through-thickness response of two non-crimp through thickness interlock of binder volume fractions 3% and 6% subjected to high-strain rate loading. They conclude that the through-the-thickness reinforcement volume fraction has only a small effect on the in-plane stiffness of the composite. However, the through-thickness reinforcement does provide significant delamination resistance during plate bending tests. During three-point bending tests, they note a greater drop-off of load resisted for beams orientated along the weft direction than the warp direction. This is attributed to the orientation of the through-thickness reinforcement. The study only focuses on one material fibre architecture, with 3D orthogonal through-the-thickness composites remaining un-investigated.

2.2.7 Impact Resistance

As previously mentioned, impact resistance of composites is critical to their continued use. Impact loading is typically a critical load case for fibre reinforced composites as damage can occur without any visible signs, causing large reductions in compressive strength.

A useful system of judging the relative performance of composites structures under impact loading is the recording of energy absorbed with minimal reduction of structural performance, a common measurement being compression after impact tests. During impact, composites exhibit the following energy-absorbing damage modes [136]:

- Out-of-plane shear stresses due to the impacting force causes matrix cracking, potentially leading to delamination.
- During the impact event, bending of the structure causes inter-laminar stresses, and thus, the propagation of delamination.

- Penetration of the projectile causes fibre pull-out and tensile fracture.

In comparison with 2D composites, 3D woven composites often absorb a greater amount of energy, with reduction in damage area [137], particularly the suppression of delamination. [85, 138].

Even inclusive of any in-plane property reductions due to the presence of the through-thickness reinforcement, 3D woven composite exhibit far superior compressive and flexural performance for post-impact testing than their 2D counterparts due to the suppression of delamination and containment of impact damage area [85]. Figure 2.16 presents a collation of results presented by Rudov-Clark [105] showing a comparison of the post-impact compressive strength between cross-ply laminates, 2D woven, and 3D woven materials [96, 123, 128]. Figure 2.17 presents a comparison of the post-impact flexural strength between cross-ply laminates, 2D woven, and 3D woven composite materials, after Tong, Mouritz [85]. There is, however, only a limited amount of data available 2D woven and 0/90 laminates. Combined with the large degree of scatter present, definitive conclusions are difficult to be drawn.

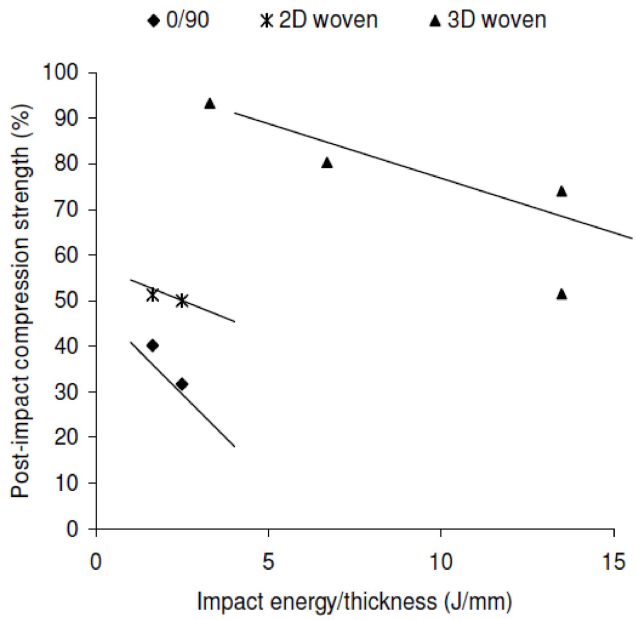


Figure 2.16. Collated post impact compressive strength (%) of cross-ply, 2D woven, and 3D woven composite materials. From Rudov-Clark [105]. Original sources [96, 123, 128].

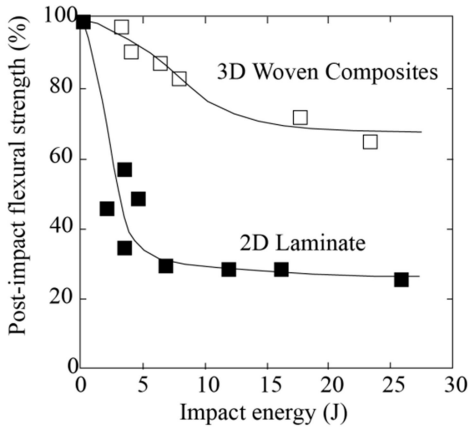


Figure 2.17. Comparison of post-impact flexural strength between 2D and 3D woven composite materials. After Tong, Mouritz [85].

2.2.8 Bending of 3D woven composite materials

Bending deformation is common for structural applications of composite materials. It can arise as direct out-of-plane loading, such as the case of composite skins or face-sheets in light-weight sandwich panels in which these structures are specifically designed to resist bending. It can also occur within curved composite structures due to the variation of thermal expansion coefficients both in the plane and through the thickness of the material. With structures in constrained states, this can lead to inter-laminar normal stresses. Bending is of particular importance to composites inclusive of through-thickness reinforcement, as the principal reasoning behind the addition of the reinforcement is to improve inter-laminar properties. In spite of this, there is still relatively sparse coverage in the literature regarding the bending response of 3D woven composite materials.

The bending properties of woven composite materials are generally investigated with the use of three different test methods. These are: plate bending tests [72], long beam three-point bending tests [95] and short beam three-point bending tests [139]. Three-point bending is the commonly accepted test method used for the out-of-plane testing 3D woven composites. However, three-point bending tests often have difficulties in the activation of the delamination damage mode. Also, for composite materials with high levels of orthotropy, the regular flexural curvature is combined with a twisting curvature throughout the beam length, complicating analysis [140].

Generally, the flexural properties of 3D woven composites have been found to be inferior to that of 2D composites [12, 95, 117]. The reduction in flexural properties has been attributed to misalignment of fibres; for example, by crimping [95]. Fibre kinking, commonly isolated to the top and bottom surfaces of a composite material, is of significant importance during flexure due to premature buckling of fibres and formation of kink-bands on the compression side [126].

The out-of-plane properties of a through-the-thickness angle interlock 3D woven composite material were classified via a three-point bending test and plate bending test by Gerlach, Siviour [72]. The results gave an indication into how the density of the through-thickness reinforcement influences the lengths of delamination damage. However, these tests are highly dependent on support conditions and loader geometry. A layer-to-layer interlock composite was investigated by Gras, Leclerc [141] under three point bending testing, with the Digital Image Correlation (DIC) technique used to determine the out-of-plane shear modulus of the beam. DIC image analysis can only capture the surface strain field, and care must be taken not to confuse local strains present on the front surface of a composite beam with that of representative values throughout the beam thickness.

Three point bending tests of a layer-to-layer orthogonal interlock textile composite were employed by Zhang, Pankow [142], also utilising DIC to capture local increases in crease and microcracking. Due to the localised damage initiation

experienced by fibre reinforced composites, interpretation of beam collapse may be complicated by asymmetric failure. For example, damage can initiate underneath the leading nose, or within either or both of the two arms of a three-point bending testing. This can lead to complications during analysis of damage development [143].

In order to avoid such difficulties, Liu, Thouless [144] applied a cantilever beam bending test to Dyneema© material. The cantilever test proved to be effective at simplifying the analysis of beam collapse. The cantilever beam bending test has yet to be applied to the out-of-plane collapse of 3D woven composite materials, and will be investigated in this thesis. The effect of through-thickness reinforcement on the out-of-plane stiffness and collapse mechanisms of 3D woven composite beams will be investigated within this thesis; an issue which is yet to be covered within the literature.

2.3 Soft Impact

The search for materials with enhanced protection against impact loading such as air blast or sand impact is of major concern in the design of military vehicles. Both rapidly expanding radial shockwaves and sand ejecta from shallow buried landmines or Improvised Explosive Devices (IEDs) can cause widespread damage of structures. Figure 2.18 presents a sketch of a typical critical load case experienced by protective systems for mobile vehicular systems.

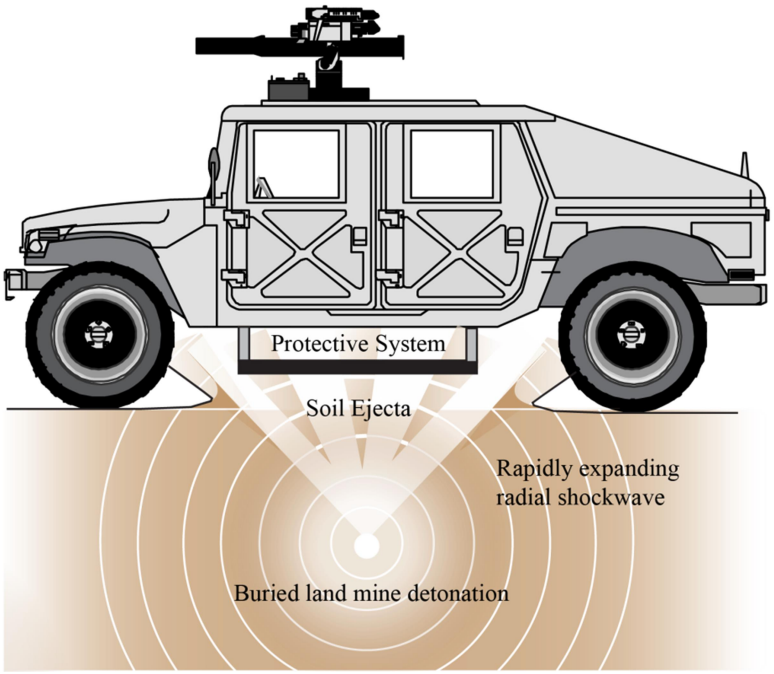


Figure 2.18. Sketch of a mobile vehicle resisting the impact of soil ejecta from the detonation of a shallow-buried land mine.

There have been several experimental methodologies developed for blast-loading of structures. The first methodology was that of using explosives to load structures. This technique has the benefit of having the same loading profiles of actual dynamic loading likely to be experienced by structures. However, it adds difficulties, as the wave fronts are spherical and the complex pressure signatures generated are difficult to model. Another experimental technique developed to enable the reproduction of shock waves in the laboratory, but moving away from the use of explosives, is the shock tube [145, 146]. It provides the advantage of plane wave-front generation and easily controlled experimental parameters. However, it requires large bespoke equipment, with calibration required that is unique for each shock tube system [145].

A more economical and simplistic method to load structures with a well-defined dynamic distributed impulse was introduced by Radford, Deshpande [147], in which cylindrical metallic foam projectiles are accelerated into samples by a laboratory scale pressurised gas gun. This method has often been referred to as

"soft impact" loading. The projectiles are highly compressible, exerting pressure pulses on structures in the order of 100 MPa for the duration of approximately 200 μs. The pressure pulses have characteristics remarkably similar to that observed in fluid shock loading, almost instantaneously rising pressure peaks diminishing with a rough exponential shape [147]. For comparison a charge weight of 100 kg of TNT at a standoff of 14 m causes a peak overpressure of approximately 250 KPa in air [148], and 2.7 MPa in water [149]. An underwater blast of a charge of 10 kg of TNT at a standoff of 1m, following the analytical formulation provided by Cole [150], exerts a peak overpressure in the order of 100 MPa.

Figure 2.19 presents a group of four figures adapted from Radford, Deshpande [147] aimed at giving the reader an understanding of the general characteristics of a soft impact event utilising aluminium foam projectiles. Figure 2.19(a) presents a high speed photographic sequence of an Alporas metal foam projectile impacting a Kolsky pressure bar at v_0 = 381 ms^{-1}, demonstrating progressive projectile densification. Figure 2.19(b) presents the measured contact pressure histories of an Alporas foam projectile of relative density $\overline{\rho} = 0.11$ and length L = 100 mm of two different velocity impacts during a direct impact Kolsky bar experiment. The pressure histories demonstrate a rapid increase, with a rough exponential decay. Higher velocity impacts produce a higher peak pressure and higher average pressure. The measured contact pressure histories of Alporas foam projectiles of two different lengths, L = 100 mm and L = 50 mm, relative density $\overline{\rho} = 0.11$ and impact velocity v_o = 380 ms^{-1} are presented in Figure 2.18(c). Increasing the length of projectile increases the duration of pressure pulse exerted upon a structure. Generally, the pressure pulse duration is measured from the time the pressure has obtained ½ of the initial peak value, until the pressure has dropped halfway down the trailing edge of the pressure history [147]. The measured peak and mean contact pressures of Alporas metal foams as a function of impact velocity v_0. The theoretical peak pressure and best fit-curve for the mean pressure are also included. The theoretical predictions for the peak pressure P_{peak} [147] is given simply by:

$$p_{peak} = \sigma_Y + \frac{\rho v_0^2}{\varepsilon_D} \tag{2.2}$$

with σ_Y as the plateau stress and ε_D as the densification strain of the aluminium foam material. The experimental data for the mean is empirically fit via the relationship [147]:

$$p_m = \sigma_Y + 0.66\frac{\rho v_0^2}{\varepsilon_D} \tag{2.3}$$

Discrepancies between the theoretical prediction and experimental data are attributed to omitting the exact nature of the shock and rate sensitivity of the base material. For a more detailed discussion of the mechanisms of blast loading, the readers are referred to Smith and Hetherington [151] for air blasts and Liu, Fleck [152] for sand impact.

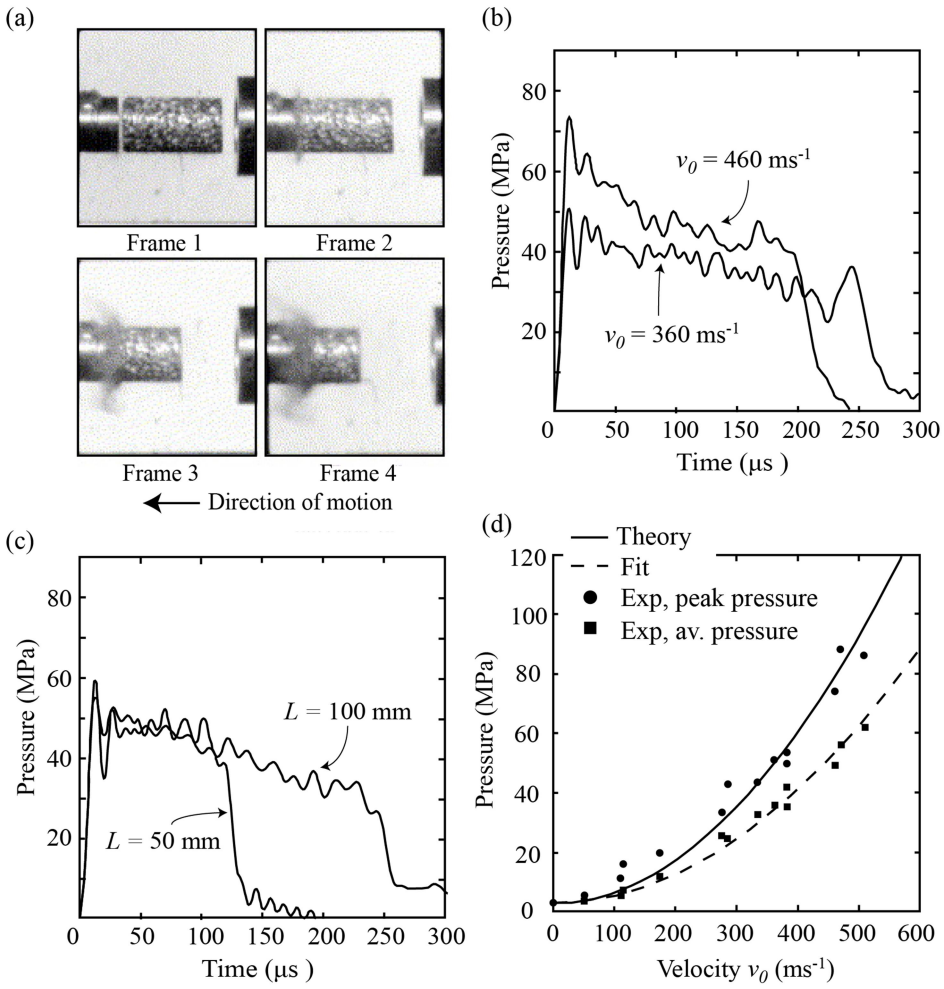


Figure 2.19(a) High speed photographic sequence of an Alporas metal foam projectile impacting a Kolsky pressure bar at v_0 = 381 ms^{-1}. (b) The measured contact pressure histories of Alporas foam of relative density $\overline{\rho} = 0.11$ and length L = 100 mm of two different velocity impacts during a direct impact Kolsky bar experiment (c) The measured contact pressure histories of Alporas foam of two lengths, relative density $\overline{\rho} = 0.11$ and impact velocity v_o = 380 ms^{-1}. (d) The measured peak and mean contact pressures of Alporas metal foams as a function of impact velocity v_0. Theoretical peak pressure and best fit-curve for mean pressure also included. (Figures adapted from Radford, Deshpande [147]).

The dynamic inertial response of a variety of monolithic and sandwich panels of composite and metal materials have been investigated via the metallic foam

projectile methodology by Radford, Fleck [153], Radford, McShane [154], McShane, Radford [155] and more recently Russell, Liu [156] and Kandan, Russell [157]. Monolithic carbon fibre laminate beams have been shown to provide superior performance with regards to the back-face deflection during dynamic shock loading than that of stainless steel beams of equal areal mass [156]. Evidence was also presented that composites with lower strength matrix can exhibit increased performance whilst undergoing dynamic soft impact loading, for both carbon fibre reinforced polymer composites and ultra-high molecular weight polyethylene (UHMWPE) composites [157]. However, laminated composites have been shown to exhibit delamination damage, even when no catastrophic longitudinal fibre fracture is observed [156]. This is a performance-limiting quality inherent within all laminate composites and will become more exaggerated if the composite matrix strength is reduced.

2.4 Multi-hit impact upon composite structures

In reality, dynamic impact events do not necessarily occur as singular isolated events. Fragment cluster impact (FCI) is a common scenario which arises from the ejection of multiple high velocity projectiles accelerated from the fragmentation of a metallic case containing high explosive (HE) charges. Predominant examples of such are surface-to-air (SAM) or air-to-air missiles (AAM). The majority of the current literature focuses on the singular-point ballistic impact load cases, with little consideration for multi-point impacts or multi-hit singular point impacts.

During a singular impact, the structural response of laminate composite materials is governed by the interaction of multiple longitudinal and transverse stress waves [158] generated from the impact location and travelling to, and reflecting off, clamped or free edges. During multi-impact events, the constructive and deconstructive interference of stress waves, wave scattering effects, and cumulative damage progression can change the response of composite structures.

Qian, Qu [159] and Qian and Qu [160] conducted an analytical and numerical study into the multi-site impact (fragmentation) of metallic armour systems. They

reported on the cumulative damage of the plate, noting that fragment density is more sensitive than the interval between impacts on the damage pattern. They also note the complexity of the problem and the limitations of size of simulated regions during numerical modelling.

Deka, Bartus [161] conducted an experimental and numerical investigation into the response of an S2-glass/epoxy composite laminate subjected to high velocity, multi-site impacts. They pay particular attention to the stress wave interaction of multi-site impacts, and how stress wave attenuation can influence the distribution of damage within composite plates. They conclude that sequential impacts resulted in a 23.0% and 14.2% increase in delamination damage over simultaneous impact for two and three impacts, respectively. They report on the residual velocity of projectile, but make no mention to how sequential impacts influence the ballistic limit of the material.

Kandan, Russell [162] proposed a method in which multi-hit singular-point characterisation of materials is realised through a ballistic limit interaction map between primary and secondary impact events. It was proven to be a useful technique in determining the influence of primary impacts on the response of a secondary impact for a wide range of impact velocities. The initial impact V_I causes damage within the plate and modifies the response during a secondary impact event V_{II}. A combination of the primary and secondary impacts results in either penetration or rebound of the projectile. The shape of the boundary surface between these two binary events is related to inherent material properties. The methodology was then employed for a numerical study of the multi-hit damage characterisation of 304 stainless steel plates by Russell [163].

The literature is yet to address the influence of through-thickness reinforcement on the multi-hit response of fibre reinforced composite materials. This thesis will conduct a numerical study of the multi-hit impact response of an orthogonal 3D woven carbon fibre reinforced epoxy matrix composite material in order to begin to fill the gap within the current published studies.

2.5 FE modelling of fibrous composites

Complexities during the numerical modelling of fibre reinforced composites stem from the complex microstructure of the material, high levels of anisotropy and heterogeneity, and a wide variety of damage modes exhibited. This literature review will now present and discuss the challenges and solutions presented with the modelling of complex composite materials. It begins by introducing general methodologies which are relevant to the modelling of a wide range of composite materials, then, a greater focus will be given for 3D woven composite materials.

2.5.1 Continuum Damage Mechanics (CDM)

Earlier composite material failure models [164-166] had the ability to predict failure, for example as predicted by a critical stress-state surface, and subsequently reduced the relevant elastic properties to zero over a fixed number of time steps. This is not an ideal solution, as the post-failure behaviour of the material is completely neglected. In order to model the propagation of damage within a material, continuum constitutive laws were developed.

There are numerous different mechanical damage models that have been developed and utilised within FE analysis. Often cited as the pioneers of damage mechanics [167, 168] proposed that the state of damage within a material could be represented by a variable of which characterises damage evolution. Damage variables tend to be vector variables for composite materials, as unlike metals, damage modes are highly dependent on direction. The approach introduced by Kachanov [167] and Talreja [168] was initially applied to composite materials by Frantziskonis [169] and Frantziskonis and Joshi [170]. This tensor form of damage variable, taking into account the common damage modes exhibited by composite materials (matrix cracking, fibre breakage, and fibre-matrix debonding), formed the basic principal of composite damage mechanics which has been utilised by many researchers.

A meso-scale damage model based on continuum damage mechanics was introduced by Ladeveze and LeDantec [171]. It modelled fibrous composite

laminate matrix cracking and fibre/matrix debonding at the ply-scale, introducing damage variables for reduction of material stiffness. The model was formulated under plane-stress assumptions, the behavioural differences between the tensile and compressive responses along the fibre direction were taken into account.

This methodology was then updated to include the simulation of multiple plies, and interfaces between them [172-174]. The interface is a two dimensional entity, acting to transfer forces and displacements between adjacent layers. This allowed for the prediction of delamination damage. The model operated under the hypothesis that the behaviour of any laminate can be described by elementary mesoconstituents; namely, the singular plies and the interfaces between them. One of the underlying principal assumptions within this methodology is that damage is assumed to be uniform within the thickness of each mesoconstituent. However, the state of damage can vary from one ply to the next within the laminate structure. Figure 2.20 presents a sketch of the fibrous composite laminate modelling strategy inclusive of individual plies, and the interfaces joining them together (adapted from Ladeveze and Lubineau [175]).

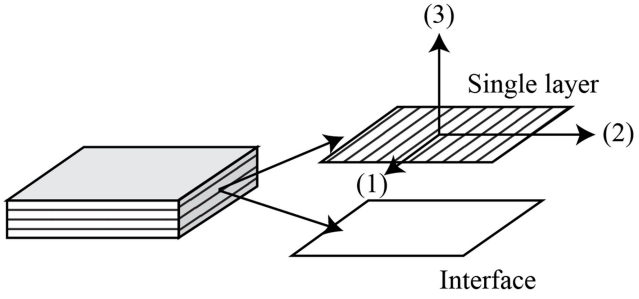


Figure 2.20. Ladeveze fibrous composite laminate meso-scale modelling strategy ; showing a singular layer, and interface. (Adapted from Ladeveze and Lubineau [175]).

Comparisons were made with micromechanical damage mechanisms. They note that the mesomodel can actually be interpreted as homogenised results from micromechanical damage mechanisms such as microcracking, delamination at the tips of microcracks and fibre-matrix debonding [172]. The modelling

methodology has shown satisfactory results with comparisons to experimental results, and had been the basis for numerous models within the literature, for example, Coutellier and Rozycki [176] and Johnson, Pickett [177]. However, if employed for the FE modelling of large-scale components such as fan blades, a meso-model can prove computationally expensive.

Another model, by Matzenmiller, Lubliner [178], incorporates a damage growth law based upon a Weibull distribution of strengths. The Matzenmiller et al. model utilises the failure criteria developed by Hashin [165], which introduces the concept of failure planes to separate the failure space into four distinct criteria.

-Mode I: Fibre rupture $(\sigma_{11} \geq 0)$:

$$\left(\frac{\sigma_{11}}{X_t}\right)^2 - 1 \begin{cases} \geq 0 \text{ failed} \\ > 0 \text{ elastic} \end{cases} \qquad (2.4)$$

Primarily caused by tensile stresses along the fibre direction σ_{11}, failure is initiated by a number of fibre breaks in the vicinity of one another. Strain localisation occurs at these break locations.

-Mode II: Fibre buckling and kinking $(\sigma_{11} < 0)$:

$$\left(\frac{\sigma_{11}}{X_c}\right)^2 - 1 \begin{cases} \geq 0 \text{ failed} \\ > 0 \text{ elastic} \end{cases} \qquad (2.5)$$

Failure caused due to compressive stresses along the fibre direction ($-\sigma_{11}$). Damage initiation begins as the buckling of single fibres [127], and propagates to the formation of a kink band, reducing the load-carrying capability of the material. Composites with a stiff matrix material exhibit little to no non-linearity before kink band formation.

-Mode III: Matrix cracking under transverse tension and shearing

$$\left(\frac{\sigma_{22}}{Y_t}\right)^2 + \left(\frac{\tau}{S_c}\right)^2 - 1 \begin{cases} \geq 0 \text{ failed} \\ > 0 \text{ elastic} \end{cases} \qquad (2.6)$$

Microcracking within the matrix material is modelled as continuously distributed defects within a narrow damage zone. Failure due to microcracking is dependent on the tensile strength and shear strength of the laminar. Microcrack growth is unstable under load-control, with few microcracks rapidly expanding for ultimate failure. However, if the loading is strain controlled, stiffness reduction is gradual.

-Mode IV: Matrix crushing under transverse compression and shearing

$$\left(\frac{\sigma_{22}}{Y_c}\right)^2 + \left(\frac{\tau}{S_c}\right)^2 - 1 \begin{cases} \geq 0 \text{ failed} \\ > 0 \text{ elastic} \end{cases} \qquad (2.7)$$

In-plane shear or transverse compression loading causes microcracking of the resin. Local tensile stresses are formed within the matrix due to mismatches between the fibre and matrix Poisson ratios. Fragmentation of the resin causes a reduction in stiffness parallel to the fibre orientation. Failure is related to the compressive strength and shear strength of the composite laminate material.

The failure planes of the matrix modes III and IV are normal to the fibres, and the failure planes of the fibre modes I and II are associated with planes perpendicular to the fibres. Figure 2.21 presents a sketch of the laminar failure planes.

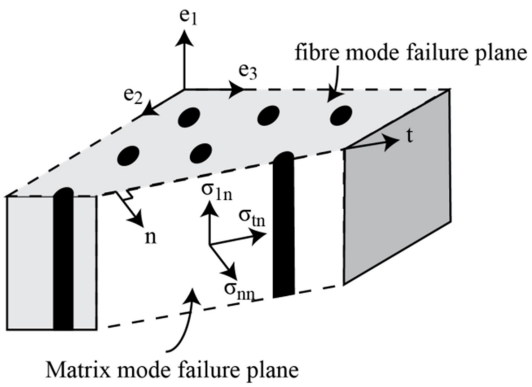


Figure 2.21. Laminar failure planes. After [178].

After the onset of damage, it introduces three damage parameters: ω_{11}, ω_{22}, and ω_{12}. The longitudinal and transverse damage parameters assume different values for tension and compression, whilst the shear damage parameter is independent of

the sign of shear stress τ. The damaged laminar has an assumed linear constitutive law, with the influence of the damage on the elastic response represented as functions of ω and the undamaged material property. This is different to methods employed previously, which take the elasticity constants themselves as unknowns to be solved for [179-181]. The Matzenmiller et al. model utilises principles from thermodynamics in order to relate the energy released per volume due to the progression of damage Y_e to the strain energy W_e and damage variable ω:

$$Y_e = -\frac{\partial W_e}{\partial \omega} \tag{2.8}$$

The model has proven effective during simulation of fibre reinforced composites under impact loading [156, 182]. However, a common criticism of the method is that the material parameters are based on unrealistic, non-physical values, and requires correct determination of fracture toughness for all modes of failure.

Another criticism of this relatively simple modelling strategy is the lack of interaction between damage modes. In reality, the formation of microcracks within the matrix due to transverse loading may lead to degradation of stiffness in the longitudinal direction.

CDM has been extensively utilised in the literature for the modelling of both low velocity impact [182-187] and ballistic impact [188-190]. For a more detailed review on the implementation of CDM modelling strategies on the impact damage of composite materials, readers are referred to Williams and Vaziri [182].

2.5.2 Modelling fracture

Early modelling strategies for predicting laminate composite failure were divided into those predicting in-plane failures and those predicting out-of-plane failures. For in-plane failure, it was common to employ property degradation models utilising damage criteria calibrated from experimental data and stress states calculated from classical laminate theories [191, 192].

For out-of-plane failure, for example delamination, traditional methodologies include linear elastic fracture mechanics (LEFM) [193]. LEFM assumes the existence of a singular stress field positioned around a crack tip and often utilises a failure criterion based on a critical fracture toughness. This energy-based criterion can be a constant for a given material. However, this is true for only a fixed mode ratio. This restricts LEFM to cases of more simplified geometry and singular fracture modes.

Expanding upon LEFM, for use within more complicated structures, Rybicki and Kanninen [194], Shivakumar, Tan [195], and Raju, Hivakumar [196] developed the Virtual Crack Closure Technique (VCCT). The VCCT involves the introduction of specifically deigned crack-tip elements. Nevertheless, the use of specific crack-tip elements can induce numerical instabilities as well as high levels of mesh-dependency [197]. Also, inherent within the VCCT formulation is an assumption of self-similar crack growth. This is commonly a false assumption [198], and other methods which take into account mixed-mode fractures are necessary. Also, elements behind and ahead of the crack front must be of the same size. This imposes strong requirements on the mesh, so much so that an adaptive meshing technique should be utilised; this is computationally expensive [199]. The three modes of fracture are: opening (Mode I), in-plane shearing (Mode II), and tearing (Mode III). They are demonstrated visually in Figure 2.22.

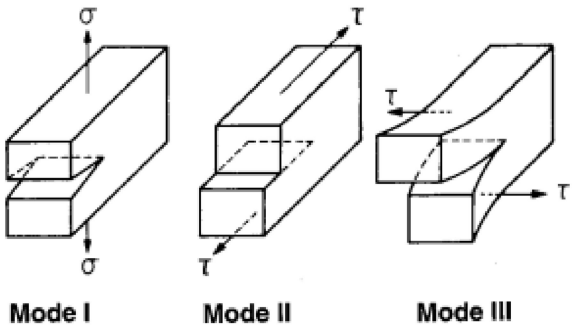


Figure 2.22. Three general modes of fracture [200].

Another more recent method for modelling the propagation of fractures within a material is the extended finite element method (XFEM). The XFEM enriches

specific regions of the domain with level set functions, allowing the modelling of geometries that are independent of the mesh. The additional terms for the displacement field follows the form:

$$u_{XFEM}(x) = \sum_{i \in I} N_i u_i(x) + \sum_{j \in J} N_j H(x)\, a_j(x) + \sum_{k \in K} N_k \left(\sum_{\alpha=1}^{4} F_\alpha(x) b_{k\alpha} \right) \quad (2.9)$$

where *i* is the set of all the nodes within the mesh, $N_i(x)$ is the nodal shape function, u_i is the standard DOF of node *i*, a_j and $b_{k\alpha}$ are the DOF of nodes from set J and K, enriched with the Heaviside function $H(x)$, and crack-tip function $F_\alpha(x)$, respectively. For a more detailed discussion about the implementation of XFEM, readers are directed towards Dolbow and Belytschko [201].

The concept of field enrichment was first introduced by Gifford and Hilton [202], but has since become a very popular tool for the modelling of crack propagation at anticipated regions with a domain [203-206]. Issues of XFEM include the knowledge a priori of the location of fractures, and the need for special treatment of blending elements between enriched and regular elements [207]. Also, the FE domain can contain only a single crack, or non-interacting cracks, and parallel processing is unavailable.

A popular technique for the modelling of fracture processes includes the insertion of cohesive elements or interfaces at areas in which composites are prone to extensive matrix cracking, for example in between plies. The basic premise for such models is the relation between tractions and displacements at crack interfaces. This is a popular strategy for both laminate composites [208, 209] and woven composites [210]. Models utilising a traction-separation interface can specify independent cohesive laws for the three crack opening modes, so that the toughness of the three modes can be different. Cohesive zone models are effective at tackling issues such as free-edge delamination initiation and propagation, and damage and delamination around pinned holes [193]. However, as discussed by Dávila, Rose [211], describing the softening mechanism of a cohesive interaction

or element can prove difficult due to the combination of mechanisms acting on different length scales inherent within fibre reinforced composites such as fibre tensile fracture, fibre-matrix pull-out, matrix cracking and fibre bridging. They suggest a super-imposed bi-linear softening law in order to capture the post damage initiation behaviour across the interface.

2.6 3D woven composites modelling strategies

The analysis of 3D woven composites is significantly complicated by the intricate fibre geometry and high levels of heterogeneity. A few of the most prominent modelling strategies employed for the analysis of 3D woven composites will now be introduced and discussed, with particular focus on orthogonal 3D woven composites.

Analytical models of woven composite structures, such as the orientation averaging approach [212], mosaic models [213], and the Mori-Tanaka method for knitted textile composites, can often give an efficient first-estimation for the elastic properties of complex composite materials. However, due to the over-simplification of the geometry, accurate predictions of the stress-strain field are difficult to achieve.

The orientation averaging (OA) method is a popular modelling strategy. It attempts to characterise the heterogeneity of composite materials by finding an appropriate scale of representative body at which the material acts homogenously. The composite geometry is discretised into small volume elements, in which all fibres are aligned and orientated in one direction. Each of these volume elements can therefore be treated as transversely isotropic uni-directional lamina. The composite is discretised into small volume elements, with each volume element being treated as a unidirectional laminar with transversely isotropic properties. The technique has been extensively utilised throughout the literature [214-217]. The OA method was expanded to take into account the effect of material variability such as tow waviness by Cox and Dadkhah [212]. A knock-down factor η_f $\left(\eta_f \leq 1\right)$, estimated from the stochastic distribution of out-of-plane tow

waviness, is utilised to reduce the in-plane tow stiffness of tows. The model chose to neglect in-plane tow waviness as it was deemed insignificant. Macroscopic averages of composite stiffness were calculated under either iso-stress or iso-strain assumptions. This leads to a significant improvement to the accuracy of the prediction of the elastic constants of the material. The OA method has been proven to be effective in predicting the elastic properties of a composite material.

A common strategy exploiting the periodicity of the geometry of woven composite structures is to employ a unit-cell methodology. This method attempts to reduce the complicated material geometry to the smallest size repeating unit. Periodic boundary conditions can then be employed in order to simulate the entire test coupon. Li [218] presented a comprehensive review of the formulation of correct boundary conditions, taking the microstructure of the composite into consideration. Composite simulation via the use of unit cells and periodic boundary conditions is demonstrated within Zeng, Brown [219], Green, Matveev [220], Wang, Wang [221], and Xia, Zhou [222]. This modelling strategy again is effective for the prediction of the elastic response of composite materials, but suffers from problems during the onset and propagation of damage when the assumption of periodicity becomes invalid. This is because the nature of damage initiation and progression with a composite sample is inherently localised. Also, periodic boundary conditions may have reduced accuracy in the through-thickness direction due to the finite number of layers within a composite, and that in reality there may be geometric variations within the fibre reinforcement due to layer shift (lateral displacement of layers due to composite manufacturing).

A structural analysis model for predicting the strength of orthogonal 3D woven composites based on the micro-mechanical FE analysis of unit-cells was presented by Nagai, Yokoyama [223]. Here, the material was discretised into homogenous volumes with assumed anisotropic non-linear material properties. The material properties were previously determined from micro-mechanical FE analysis utilising a unit cell consisting of beam elements for fibre components and beam and rod elements for matrix components. The non-linear material properties are applied to the elements within the model, and strength analysis conducted for

tensile, compression and shear loading. Experiments were utilised for model validation.

Huang and Waas [224] conducted a 3D multi-unit cell FE simulation in order to investigate the compressive strength and failure mechanisms of woven textile composites. They found that only by composing a model of at least 16 unit cells gave good agreement to experimental results [224]. Kink band formation was determined as the main compressive strength limit factor [225].

Naik, Azad [88] presented a 3D strength model for the prediction of the tensile strength of an orthogonal 3D woven composite. The model was based on volume averaging for stress and failure analysis, discretising the composite structure first into sections perpendicular to the loading axis, then into sections perpendicular to the loading axis. Each element was assumed to consist of either transversely isotropic lamina, each orientated along the fibre direction, or pure matrix material. An iso-stress assumption was used to translate global material strains to section-strains, and an iso-strain assumption was utilised to transfer this to element strains. Stresses are thus calculated from the element strains, with a maximum stress criterion utilised for element failure. The model did not incorporate shear deformations.

Tan, Tong [227] conducted an investigation into the prediction of the failure strength of orthogonal 3D woven composite with a multi-level 3D FE macro/micro model. An assembly of many RVEs were used to create a macro-scale structural model a quarter scale of a specimen. The RVE was created at the yarn level, incorporating stuffer, filler, and z-yarns, the cross-sections of which were assumed to be rectangular. The global level mesh used eight-node brick elements, the local level mesh was generated using Strand6 software. The boundary conditions within the micro-FE model were determined from average displacements obtained from the macro-model and a maximum stress failure criterion utilised for microcracking or failure identification. The predicted transverse failure strength was shown to be slightly different to experimental results, attributed to waviness of filler tows. Also, assumptions of symmetry

within composite coupon samples could lead to erroneous results due to localised progression of damage within the material.

Bogdanovich [228] attempts to model the response of 3D woven composites through the introduction of a "meso-volume": a homogenous, anisotropic block with effective properties determined from volumetrically averaged 3D stress and strain fields computed at a smaller scale. The meso-volume can represent large sections of a structural component down to singular fibres. Therefore, the methodology is useful for conducting numerical analyses on a wide variety of problems. For example loading, either displacement controlled or stress controlled, applied at the macro level is transferred to individual pure matrix and composite lamina blocks through iso-strain and iso-stress conditions. A maximum stress failure criteria was used, and post-failure a degradation factor was employed to reduce model stiffness based on different failure modes. A review of the multi-scale modelling methodology is presented by Bogdanovich [86].

The finite element Binary Model [131, 229, 230] is a modelling strategy that attempts to remove any assumptions of periodicity within the material. It was used for simulation of relatively large, three-dimensional models of textile composites, whilst paying particular attention to the induced stochastic flaws within the material developed during the manufacturing process. The model uses beam elements to represent fibre tows, which are then embedded within a solid effective medium that represents the matrix. The Binary Model can incorporate non-linearity in both the reinforcing tow and matrix easily, and was shown to reproduce well the qualitative features of stress-strain curves for uni-axial tests on a 3D woven angle interlock material. However, the model requires a variable referred to as a "knock-down factor" when calculating the effective Young's Modulus of the cuboidal effective medium elements; which is only available through extensive mechanical testing. The Binary Model utilises beam elements to represent tows, which has its limitation in geometrical detailing of fibre architecture.

2.7 Rate dependency of fibre reinforced composite materials

The relative importance of the rate-dependent behaviour of fibre reinforced composite materials has been discussed in depth within the literature. Several experimental studies have been carried out demonstrating the strain rate dependent effects of fibre reinforced polymer composites [231-233], with Welsh and Harding [234] and Pankow, Salvi [235] focusing on woven composite materials. Gerlach, Siviour [72] provide an experimental study on the failure modes, damage and delamination of two 3D woven carbon fibre composites subjected to high rates of loading. Whilst carbon fibres themselves are generally considered to exhibit little to no rate dependency the viscoplasticity of the polymer matrix will often lead to rate dependency of the composite material. Polymers are known to exhibit rate-dependent rupture strength at various strain-rates [236-238].

During compression testing at increased strain rates, CFRPs have been shown to supress the typical failure mechanism of kink band formation, and for the material to undergo complete disintegration. This is due to the increased shear resistance of the highly rate-dependent matrix material. The change in damage mechanism leads to an increase of the initial Young's modulus, ultimate strength, and energy absorption within the material. [239]. Groves, Sanchez [240] conducted a study on a CFRP composite under tensile and compressive loading of strain rates ranging from 0-3000s^{-1}, utilising high energy drop-tower and the split Hopkinson bar testing methods. They report the tensile and compressive strength and modulus increasing with increasing loading rate. The transverse modulus and strength of CFRPs have been demonstrated to show low-levels of increase with increasing strain rate [241, 242]. A more comprehensive overview of the literature in regards to the rate-dependency of fibre reinforced composites was provided by Jacob, Starbuck [242].

A common methodology of testing the high-strain rate material properties is through the use of a Split Hopkinson Pressure Bar. This allows for the direct

testing of compression, tensile, and shear composite material properties up to strain rates of approximately 10,000 s^{-1}. However, the differences in testing procedures and specimen sizes within the literature can lead to contradictory conclusions within the literature [243].

An example of a commonly used function for attempting to model the strain-rate dependent material behaviour is the power-law function. It can be used to model relatively low-levels of rate dependency, with a logarithmic increase in properties such as yield stress or UTS with increasing strain rates. It takes the following form:

$$g(\dot{\varepsilon}) = g_0\left[m \log\left(\frac{\dot{\varepsilon}}{\dot{\varepsilon}_0}\right)+1\right] \tag{2.10}$$

where $g(\dot{\varepsilon})$ is a rate dependent function such as Young's modulus or strength, m is a material constant, g_o and $\dot{\varepsilon}_0$ are the reference function and reference strain rate, respectively.

Wei, de Vaucorbeil [243] introduced a novel finite element fluid-structure interaction model which incorporates strain-rate effects for the simulation of a UD-laminate composites subjected to underwater blast loading. A user-defined material subroutine was introduced to modify the Hashin fibre failure criterion and modified Tsai-Wu matrix failure criterion with rate dependency. In order to limit the complexity of the model, rate dependency of the material's modulus was ignored. Attention was focused on the rate dependency of the strength and therefore, via the assumption of the rate dependency of the failure strain exhibiting the same behaviour as the strength, the toughness. They obtained the reference fibre tensile strength, fibre compressive strength, matrix tensile strength, and matrix compressive strength from Daniel, Ishai [244]. The corresponding rate-dependent material parameters were extracted from dynamics tests undertaken by Daniel, Luo [245]. They demonstrated an improved prediction of the spatial distribution and magnitude of damage under impact loading compared with previous models.

Pankow, Waas [246] attempts to incorporate rate dependency of both matrix material and transversely isotropic tow components of their finite element model. For the tow material model, the Cowper-Symonds power-law was also utilised. Split Hopkinson pressure bar (SHPB) material tests were conducted on pure epoxy resin to determine the power-law material constants. The model demonstrated acceptable predictions of the failure load and delamination damage during dynamic loading during SHPB tests upon glass-epoxy 3D woven composite material.

The rate sensitivity of end-clamped carbon fibre monolithic and sandwich beams undergoing soft impact were modelled using the finite element method by Russell, Liu [156]. The study demonstrated that, without the inclusion of the material rate-dependency, the quasi-static material properties grossly over-predicted the deflection and damage of the composite beams. The authors used a simplistic methodology for the incorporation of rate dependency by the use of a viscosity coefficient η. The viscosity time-coefficient is used to continuously update the fibre and matrix tensile and compressive damage variables, governing the time at which they reach their corresponding steady-state values. Numerically, the viscosity coefficient, during explicit numerical calculations, works to increase the material fracture energy with increasing loading rates. Via a calibration study, this methodology allowed for accurate predictions of damage modes and deflections of composite beams under impact.

2.8 Numerical modelling of 3D woven composites under impact loading

Due to the severely non-linear response of woven structures undergoing dynamic impact, often the most effective method for the prediction of material response is the use of numerical modelling. An overview of some the predominant methodologies employed for the numerical simulation of 3D woven composites undergoing impact loading will now be presented.

Ji, Sun [247] utilised eight node brick elements within ABAQUS/Explicit to model 3D orthogonal woven composite plates under a modified split Hopkinson

bar (SHPB) apparatus indenter impact experiments. User-defined subroutines (VUMAT) were developed to incorporate the failure criteria and constitutive behaviour for the material. The sizes of elements within the model were kept equal to the size of the unit cell of the 3D woven material. The load-displacement curves and energy absorption within the plate showed reasonable fidelity to experimental testing, demonstrating that even with modelling with effective unit-cell properties, reasonable fidelity can be achieved. However, due to the nature of not explicitly modelling the through-thickness reinforcement, it is impossible to classify the damage within it, and to determine the influence of which it has. Also, the localised damage mechanisms of 3D woven composite materials cannot be model utilising such a simplified methodology. For example, the asymmetric fracture of through-thickness reinforcement causing modifications to the global response of the plate.

Ji and Kim [248] present a modelling strategy based on micromechanics, using the Direct Numerical Simulations (DNS) approach via LS-DYNA commercial code to investigate the low velocity impact response 3D woven interlock composites. The DNS analysis methodology works on the concept that composites can be directly modelled by taking into account their microstructures, with each microstructure having its own independent material definitions. The method allows for the modelling of the response of the material in high levels of detail. The DNS method was shown to have good agreement with homogenised methods. However, modelling at such high levels of detail allows for only small samples to be simulated, and numerical calculations are computationally expensive. The authors also employed isotropic material properties for tows, which is not the case, as material properties differ in the longitudinal and transverse directions.

Sun, Liu [249] conducted FE simulations of an orthogonal woven composite, investigating the damage modes induced under ballistic impact. The actual geometry of a bullet was modelled, impacting upon rectangular plates at velocities up to those expected of assault rifle muzzle velocity (approximately 850 ms^{-1}). Eight-node brick elements of size equal to that of the unit cell of the material were

used to model half of the composite plate within ABAQUS/Explicit. The model was validated by experimental testing, showing reasonable fidelity in regards to residual projectile velocity and damage modes. The modelling strategy also appears to show excellent stability, modelling full penetration events of high velocity sharp-tipped projectile, however, the symmetrical modelling methodology required components to be symmetrical and assumes symmetrical damage distribution which is not necessarily true. Also, the transverse displacement degrees of freedom of the projectile were constrained, potentially reducing fidelity of projectile travel path.

Li, Sun [250] performed numerical calculations to simulate damage of a 3D woven angle interlock composite using ABAQUS/Explicit. The model consisted of a rectangular composite plate, and standard geometry for military bullet. A coefficient of friction of 0.2 was utilised for contact between bullet and target plate. The constitutive model of the unit cell was determined by using the X-model, Y-model and Z-model and employed with a VUMAT material model. Four different mesh schemes were employed, demonstrating that element size has little effect on the impact behaviour. The model was validated via experimental testing, however, no rate dependency was included within the model.

The majority of the numerical modelling strategies within the literature either rely on reduced geometrical detailing at a unit-cell level, incorporating the effects of the through-thickness reinforcement within the unit cell, or micromechanical models, which are too computationally expensive for the simulation of full-scale samples. This thesis attempts to provide a reasonable middle ground, with meso-scale modelling of in-plane fibre architecture (of which the damage modes are linked to micro-mechanical damage modes) and explicit modelling of through-thickness reinforcement. This allows for a compromise between detail and practicality which can be utilised to investigate the influence of the through-thickness reinforcement on the global response of composite structures under a variety of load cases. It is not presented as a perfect solution to the numerical modelling of 3D woven composites, however, the scale and complexity of the modelling is optimised for the sample sizes and load cases within this

investigation. The extraction of material properties from quasi-static material tests presents an attractive and convenient alternative to previously established methods.

There are currently no published experimental or numerical studies on the multi-hit ballistic impact characterisation of 3D woven composite materials. This thesis attempts to begin the discussion on this matter via the use of a meso-scale modelling strategy, validated by ballistic impact experiments on 3D woven beam samples. The level of detailing within the model allows for full-scale simulation of entire plates, for simulation times long enough for two consecutive projectile strikes.

CHAPTER 3

QUASI-STATIC COLLAPSE OF 3D WOVEN CARBON FIBRE COMPOSITES

Summary

An experimental and numerical investigation was undertaken to characterise the collapse mechanisms of 3D orthogonal woven carbon fibre composites during the load cases of in-plane uni-axial tension and compression and out-of-plane bending. Two different fibre architectures, varying only by the density of through-thickness reinforcement, were tested. In addition, a qualitative comparison was made with a similar UD-laminate material. Cantilever beam tests were carried out to isolate two distinct collapse mechanisms, i.e. bending governed deformation and shear governed deformation. 3D woven composites exhibited significantly reduced delamination in comparison to a similar UD-laminate material. An investigation into the efficacy of an embedded element modelling strategy for both in-plane tension and compression and out-of-plane bending experiments was undertaken. The predictions were generally in good agreement with experimental measurements. A comparison between the experimental and numerically obtained results indicated that a more detailed constitutive model of cohesive contact would achieve higher fidelity during simulation of short cantilever beam tests. Numerical modelling of pre-delaminated beams demonstrated significant structural enhancement in 3D woven composites due to the presence of the through-thickness reinforcement.

3.1 Introduction

Three-dimensional woven composites have distinct advantages over two-dimensional fibre reinforced composite due to their considerably enhanced through-the-thickness properties. The in-plane characteristics of 3D woven composites have been comprehensively studied in the literature. i.e. the tensile properties [90, 91, 95, 97, 251-254], and the compressive properties investigated by Cox, Dadkhah [130], Cox, Dadkhah [95], and Budiansky and Fleck [255]. It was noted that geometric flaws in the preform such as tow crimp, and tow damage due to preform and composite manufacturing caused localised failure of tows. Also, highly localised strain and damage initiation was discovered within resin rich areas, commonly surrounding binder-tow surfaces. In compression, it was suggested that behaviour is dominated by kink band formation, i.e. a localised discontinuity of fibre direction. The formation of these kink bands was also proposed to be influenced by local geometrical defects, such as fibre misalignment.

Simply reporting the in-plane characteristics of woven composite materials is not sufficient to fully characterise the material, as the principle reasoning behind the addition of the through-thickness tow is to improve the inter-laminar properties of the composite. Therefore, it is these properties which are of great importance to design engineers. The literature review within this thesis provides a more comprehensive overview of the tensile and compressive properties of 3D woven composites with respect to the addition of the through-the-thickness (TTT) reinforcement.

This work makes two distinct contributions to the literature on the characterisation of orthogonal 3D woven composites. First, the response of orthogonal 3D woven composites under in-plane loading and out-of-plane bending is investigated. This is done with a combination of a cantilever beam test set-up inclusive of DIC-analysis. Second, a meso-scale modelling strategy is introduced, utilising effective tow properties extracted from uni-axial tension and compression tests. The finite element modelling is used to provide further insights into the experimental data,

and to demonstrate its efficacy and limitations. Finally, numerical calculations are undertaken for pre-delaminated composite beams in order to demonstrate the structural enhancement provided by the TTT reinforcement.

3.2 3D woven composite material description and manufacturing process

This study used 3D orthogonal woven carbon fibre reinforcements with two through-the-thickness (TTT) binder densities[1]. The two different fibre architectures are shown in Figure 3.1(a). The first material has a binder-to-warp-stack ratio of 1:1 (i.e. each binder tow being separated by one vertical stack of warp tows), being referred to as full TTT reinforcement in this paper, while the other reinforcement has a binder-to-warp-stack ratio of 1:2 (i.e. each binder tow being separated by two vertical stacks of warp tows), referred to as the half TTT. Throughout this thesis, the warp tow longitudinal direction is referred to as x-direction, the weft tow longitudinal direction is referred to as y-direction and the through-the-thickness direction is referred to as z-direction. Microscopic images of the composites cross-sections, shown in Figure 3.1(b), were used to measure the average values for the fibre architecture dimensions within the cured composites. Shown graphically in Figure 3.1(a), average width and thickness of warp tows were 1.70 mm and 0.177 mm respectively. Average width and thickness of weft tows were 1.40 mm and 0.230 mm respectively. Average width of TTT reinforcement was 0.5 mm with spacing of 1.74 mm in the full TTT and 3.48 mm in the half TTT material. Average thickness of TTT reinforcement was 0.1 mm. Both materials contained an alternating stack of 9 weft layers and 8 warp layers giving a total thickness of 3.5 mm for the cured composites panels. The top and bottom tows were orientated along the weft direction, and were the only tows with an induced crimp caused by binder influence, shown in Figure 3.1(b). The induced crimp angle in the top and bottom weft yarns was 7º from horizontal. The total composite fibre volume fraction was 0.56 for the full TTT composites, and 0.55 for the half TTT composites. As discussed later in this chapter, in order to

[1] Carbon fibre preforms kindly provided by Sigmatex, UK

derive the effective tow properties for FE modelling of 3D woven composite materials, it is necessary to calculate the tow volume fraction within each orientation. The tow volume fraction in warp and weft direction was measured by calculating the total tow cross-sectional area in each direction, taken from microscopic images, and dividing into the total area of the cross section. For the Full TTT cured composites, the tow volume fraction was measured as 0.285 along the warp direction and 0.531 along the weft direction. The carbon fibre tows were AKSACA A-38 with 6K filaments for warp and weft tows, and 3K filaments for binder tows. The diameter of carbon fibre within each tow was 7 μm. The fibre volume fraction within each tow for the warp, weft, and TTT-reinforcement was 0.785, 0.692, and 0.795, respectively. These volume fractions are the averages of a stack of tows, and not the total volume fraction. Figure 3.1 presents a magnified view of a singular tow, demonstrating the high volume fraction.

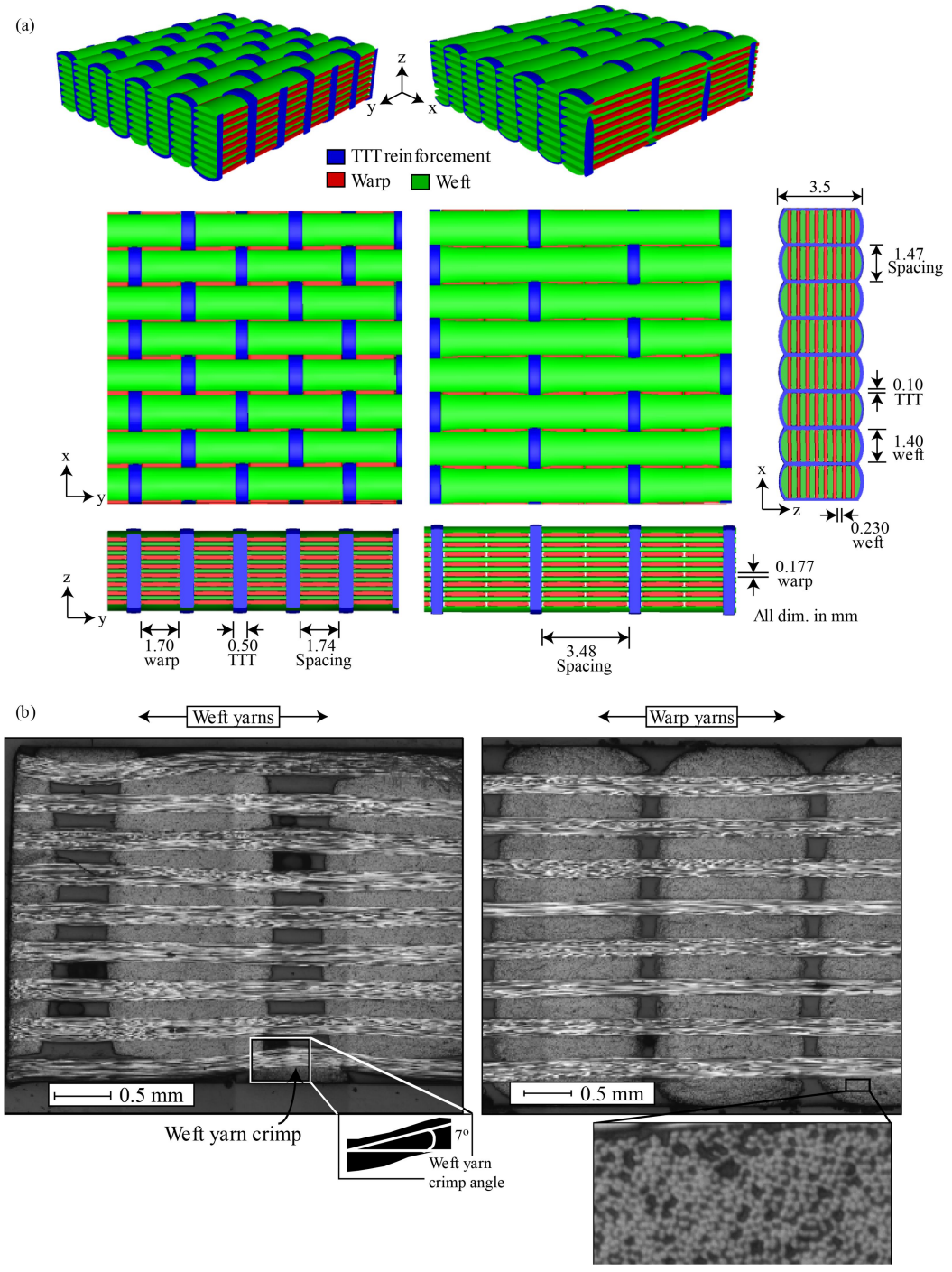


Figure 3.1(a) 3D orthogonal woven carbon composites showing Full through-the-thickness (TTT) reinforcement on the left and Half TTT reinforcement on the right. Dimensions are the average measurements of the cured composites. (b) Microscopic images of the Full TTT composites cross-sections along the weft and warp directions.

3.2.1 Composite manufacturing

The Epoxy resin used for composite material was Gurit Prime 20LV, with the ratio of slow hardener to resin by weight of 26:100. Standard vacuum infusion technique was utilised for the resin injection within a steel mould tool. Four inlet ports were located at each corner of the panel and one outlet port was located at the centre of the panel. The dry fabric was compacted by the tool due to 8 bolts tightened around the edge of the tool. A pressure pot was filled with compressed air; with the pressure being increased gradually in steps of 1 bar throughout infusion up to a maximum of 6 bars. At the same time, a vacuum was drawn through the outlet port at the centre of the tool to pull resin through the system. The panel size was 250 mm x 250 mm with a thickness of 3.5 mm. The filled mould was left in an oven for 7 hours at 65ºC. Approximately 10 mm of material was cut from each edge of the panel in order to remove any potential edge effects caused by cutting and handling of the dry fabric. The final cured areal density of the composite was 5210 gm^{-2} for the Half TTT material and 5300 gm^{-2} for the Full TTT material.

3.3 In-plane tension and compression coupon tests[2]

Quasi-static (2mm/min) uniaxial material coupon tests were conducted on the Full TTT 3D woven composites, in order to determine its in-plane mechanical properties under tension and compression. The experiments adopted EN ISO 527-4 method for tensile testing using dog bone shaped samples, and ASTM D3410/B for compression testing. The tests were conducted on a screw-driven Instron© 5581 test machine with a static 50kN loadcell. The axial nominal strain was measured using an Instron© 2630 series clip-on extensometer, and confirmed with single Stingray© F-146B Firewire Camera video gauge employing Imetrum© post processing Video Gauge© software. The nominal stress was determined from

[2] 0/90° tension and compression testing on 3D woven composite and subsequent SEM images undertaken by Araf Miran. MSc Dissertation submitted to the University of Nottingham, Aref Miran (2012).

the load cell of the test rig. At least 5 repeat measurements were taken for tension and compression tests in warp and weft directions.

The tensile and compressive tests in the ±45º orientation were performed in a way that the warp and weft tows were positioned at ±45º to the loading axis. Both samples orientated with longitudinal warp or longitudinal weft yarns had a width of 12 mm and a length of 60 mm. In order to prevent global buckling during compressive testing, the gauge length for the compressive tests was set as 12 mm. However, as the video gauge only took measurements along one face of the sample, it is not possible to confirm the complete negation of any bending within the sample.

Characteristic tensile and compressive stress-strain curves of the 3D woven carbon composite are presented in Figure 3.2. Young's Modulus in the tensile tests were 44.3 and 74.6 GPa for warp and weft directions, respectively. Young's modulus in the compressive tests were 54.0 GPa and 77.4 GPa in the warp and weft directions, respectively. The weft direction has a higher volume fraction, and thus has increased stiffness. The tension and compression tests showed elastic-brittle fracture both in the warp and weft direction. This was governed mainly by fibre reinforcement fracture, as being observed from the scanning electron microscope (SEM) images of the fracture surfaces. Fracture occurred at the location of the TTT-reinforcement for both compression and tension testing of samples orientated along the y-direction (weft). Fracture location was attributed to stress concentrations due to crimping of longitudinal tows at the TTT-reinforcement location. For tensile and compressive testing along the x-direction (warp), fracture occurred in longitudinal tows revealing resin rich channels and TTT-reinforcement at the fracture surface. Further analysis regarding the nature of the fracture events is assisted by finite element (FE) predictions and presented, along with microscopic images of failed samples, later on in this chapter. It should be noted that there is no significant delamination, and no buckling of plies during these tests. This is different to the failure mechanisms under the cantilever bending test in the following section. Material tests conducted with fibres

orientated at ±45º show a weaker, but more ductile response as they are largely governed by the relatively soft matrix material. This is consistent with the ductile, matrix dominated behaviour observed by Gerlach, Siviour [72] for orthogonal 3D woven carbon composite material tested with fibres orientated ±45º to loading direction.

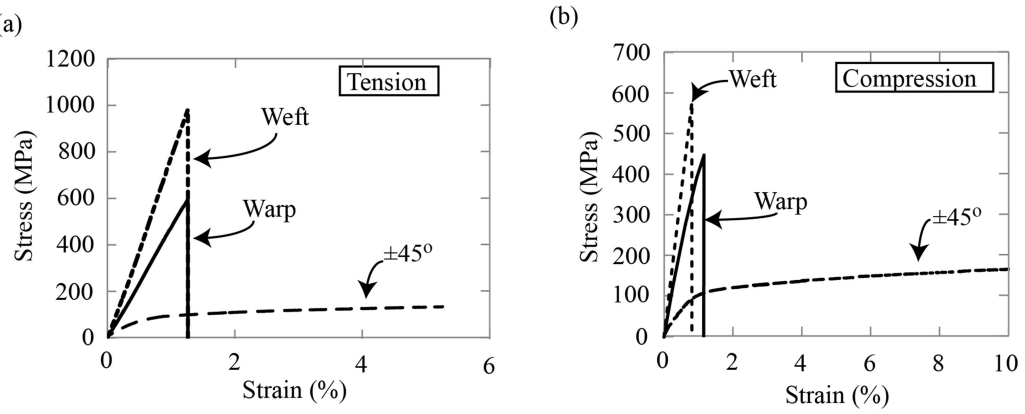


Figure 3.2. Typical stress-strain curves during quasi-static uni-axial material coupon tests of the full TTT 3D woven composites with longitudinal fibres orientated along the warp, weft and ±45° directions under (a) Tension; (b) Compression.

3.4 Cantilever beam bending tests - 3D woven composite

Figure 3.3(a) presents a sketch of the cantilever beam bending test. Beam specimens of width w = 20 mm were cut along both directions (longitudinal warp or weft yarns), from the two different 3D woven composites panels. One end of the beams was clamped into a custom-designed fixture in stainless steel with M6 bolts. This fixture was subsequently bolted onto a steel I-Beam attached to an Instron 5581 test machine with a static 50 kN load cell. The Instron test machine provided a constant displacement rate at 4mm/min for a 10 mm diameter roller in constant contact with the free end of the beams. The diameter of roller was chosen to be similar to that of previous investigations into the bending response of fibre reinforced composites, for example Cui, Wisnom [256]. The larger size was selected as an attempt to reduce local surface fibre damage caused by the roller.

Initial testing indicated that the length of the cantilever beam that extended past the roller position had no influence on the response of the beams. Figure 3.3(b) presents a sketch of the cantilever beam test showing the fibre orientation with respect to the cantilever beam.

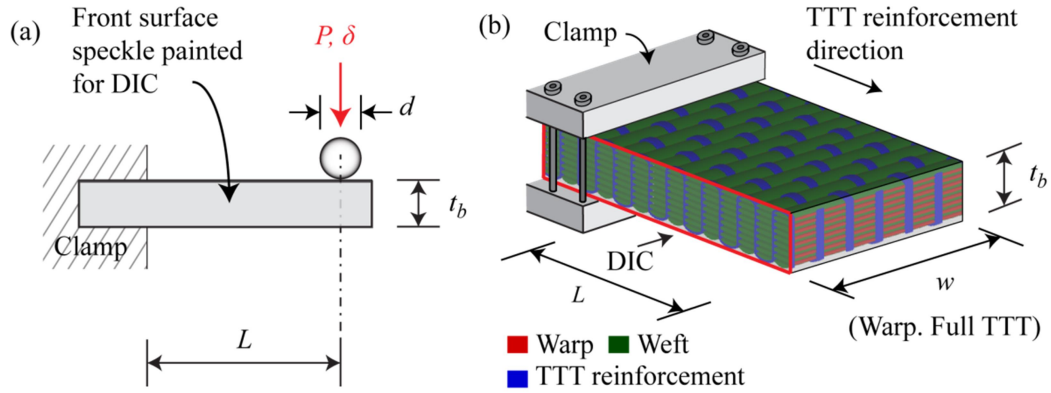


Figure 3.3. (a) Sketch of cantilever beam test, showing front surface painted for DIC analysis. (b) Sketch of composite beam orientated along the x-direction (warp).

In order to classify the collapse response of the beams, a set of experiments were conducted with cantilever beams of varying length loaded to failure. Through this, it was possible to identify two distinct collapse mechanisms, and the transition between them. Figure 3.4(a) presents the normalised force applied by the roller against normalised roller deflection $\overline{\delta} = \delta / L$ along the z-direction for a range of beam lengths. The roller displacement is normalised against the cantilever beam length. Beam collapse is defined as the initial drop-off in resisted load for the shear dominated mechanism, and the drop-off of load resisted after initial linear behaviour for bending dominated mechanisms. These locations are marked as P_c on Figure 3.4(a). For brevity, only the set of experiments of beams of Full TTT material, with beams orientated along the x-direction (warp) are presented. However, beams orientated along the weft direction, and beams of Half TTT material exhibited the same characteristics. The results demonstrate two distinct collapse responses. The short beams, i.e. 7 mm, 8mm, and 10 mm beam lengths, have a linear elastic response up until collapse, and then demonstrate a secondary

rise in load resisted before ultimate beam failure. Long beams, i.e. 15 mm, 40 mm and 110 mm, exhibit a softening regime and then an incremental reduction in load resisted until failure. The moment of beam collapse is highlighted on each of the load-deflection curves presented in Figure 3.4(a). Figure 3.4(b) presents the collapse load P_c of the beams as a function of beam length L. The two distinct regimes are visible from the data. Simple beam theory was used to curve fit the effective stress within the beam at collapse. It is presented as an approximation in order to demonstrate the transition between the two regimes, i.e. $P_c^b = \sigma_x w t_b^{\,2} / 6L$ for bending dominated long beams and $P_c^s = \tau_{xy} w t_b$ for shear dominated short beams, with L, w and t_b as the beam length, width, and thickness, respectively. The initial drop-off of load resisted during short beam tests corresponds to initial matrix cracking within the beam, and will be demonstrated later using DIC and FE analysis. Using Figure 3.4(b), the transition beam length between shear and bending dominated collapse regimes is estimated at approximately $L \approx 12.5$ mm. It was determined that beam lengths of 8 mm and 40 mm, for short and long beams respectively, would be suitable lengths for more detailed study.

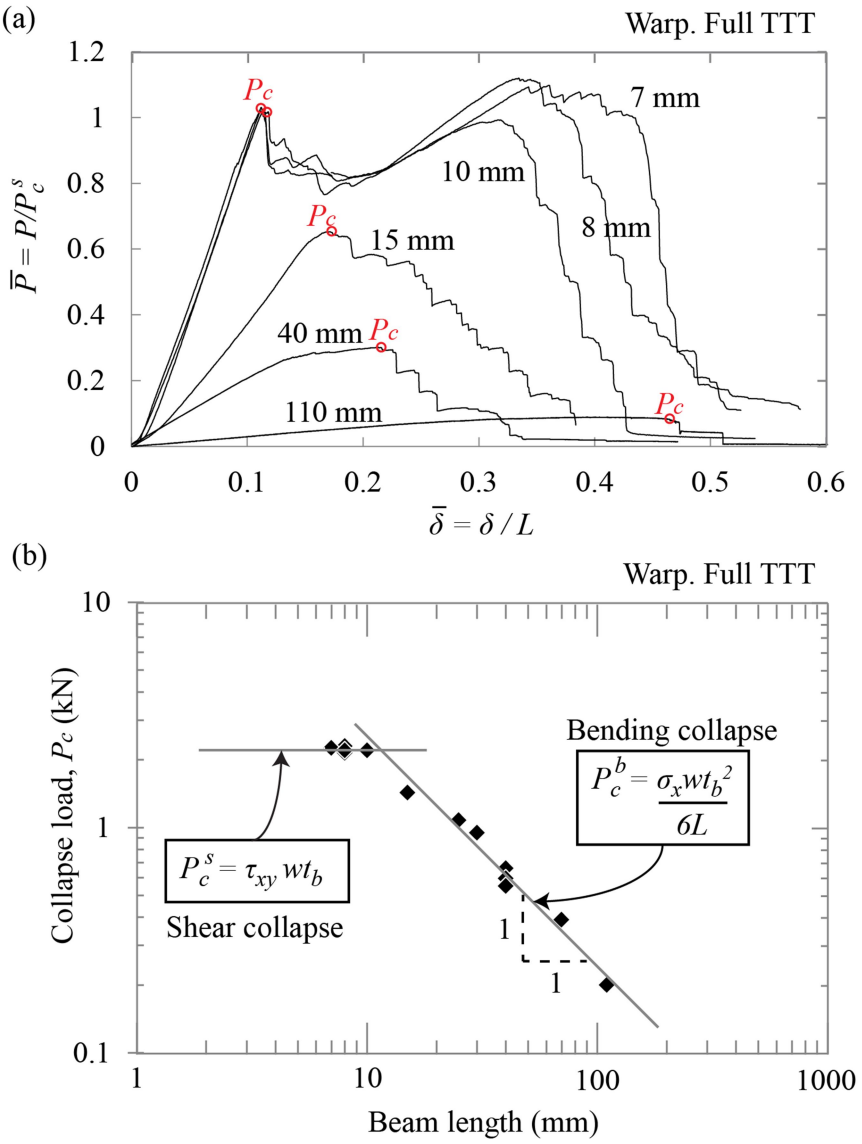


Figure 3.4(a) Force applied by the roller against normalised roller deflection along the z-direction for a range of beam lengths. Beams orientated along the warp direction (Full TTT material). (b) The collapse load for a range of beam lengths orientated along the warp direction Full TTT. Also plotted are curve fitted collapse load values showing short beam shear dominated collapse and long beam bending dominated collapse regime.

3.4.1 Long cantilever bending tests

The behaviour of the long cantilever beams is governed by bending deformation rather than by shear deformation. Figure 3.5(a) and (b) show the force imposed by the roller as a function of roller displacement along z-direction for long (40 mm) cantilever beams for Full TTT and Half TTT material orientated along the x-direction (warp) and y-direction (weft), respectively. For both orientations, there is no significant difference between the behaviour of the two materials tested. To understand the failure mechanism of the long beams, Figure 3.5(c) shows the full field strain measurement ε_{xx} for normal strain along x-direction (warp) on the front surface of the beam, acquired by the Digital Image Correlation (DIC) technique, for the composite beam with Full TTT reinforcement orientated along the x-direction (warp). The normal strain ε_{xx} was chosen to be displayed as the long beam cantilever test exhibits a bending deformation mechanism. The images can be related to the corresponding load – displacement relation shown in Figure 3.5(a). In the elastic region, up to point A, there are local increases of tensile strain at the top of the beam. These locations correspond to the resin rich regions at the positions of TTT reinforcement in the specimen. The load-displacement response became non-linear from Point A to Point B, which corresponds to a rapid increase in local compressive strain at the bottom of the beam. Optical microscopic images of the beam post-test, presented in Figure 4(c), show the failure mechanism at the bottom of the beam to be microbuckling of longitudinal tows and crushing of a transverse tow at the clamped edge. The failure mechanism at the top of the beam was a tensile crack, propagating downwards as the test progressed. No delamination was observed during either the Full TTT or the Half TTT long beam cantilever tests.

The failure mode is identical for both warp and weft direction for both binder densities of long beam test. An X-ray μCT scan taken post-test of a 40 mm Full TTT beam orientated along the x-direction (warp) is shown in Figure 5(a). The image can be used to understand how the tensile crack interacts with the TTT-

reinforcement within the internal structure of the beam. The CT image presented in Figure 3.6(a) shows a slice at the TTT-reinforcement location, and demonstrates two tensile cracks located at the inside edges of the TTT-reinforcement. It is worth noting that the location of the CT image is between the primary longitudinal load-bearing warp tows, therefore they are not visible in the image. Figure 3.6(b) shows the location of the CT image in relation to the cantilever beam.

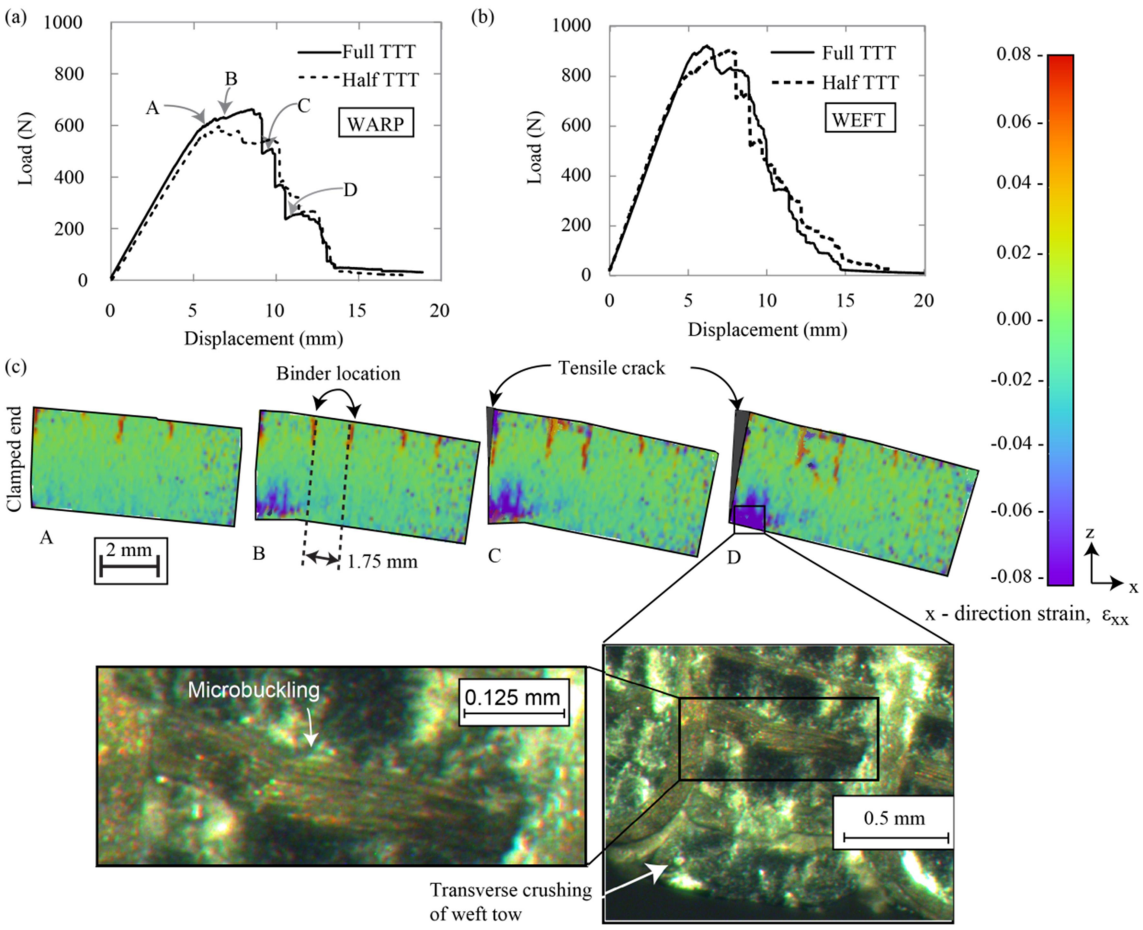


Figure 3.5. Long (40 mm) cantilever beam tests results showing the force applied by the roller against vertical roller displacement relationship for beams orientated along (a) x-direction (warp); (b) y-direction (weft); (c) the progressive strain field ε_{xx} with A, B, C and D corresponding to the respective points in (a) (obtained via DIC analysis), and the post-test optical microscopic images showing localised

damage of an edge weft tow and microbuckling of a warp tow constrained between the TTT reinforcement.

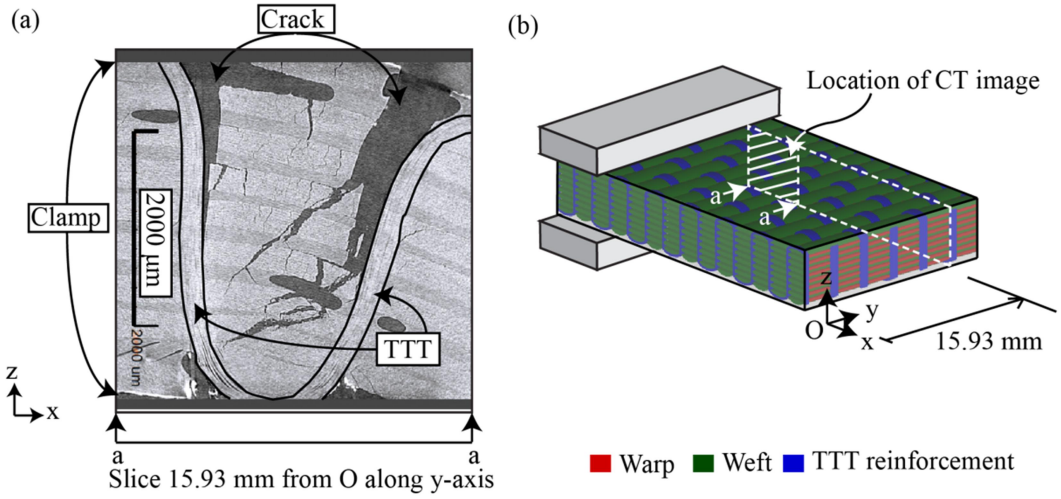


Figure 3.6. μCT image of long (40 mm) cantilever beam test along the x-direction (warp) showing tensile cracks forming at the clamp location; (b) the location of the μCT image segment in relation to the cantilever beam.

3.4.2 Short cantilever bending tests

The behaviour of the short cantilever beams is governed by a shear dominated mechanism. Figure 3.7(a) and (b) shows the force imposed by the roller as a function of roller displacement along the z-direction for the Full TTT and Half TTT short cantilever beams, with beams orientated along x-direction (warp) and y-direction (weft), respectively. For both beam orientations, the density of the TTT reinforcement has small effect on the load-displacement relationship of the short cantilever beams. The DIC images showing shear strain, γ_{xz}, at selected roller displacements, are presented in Figure 3.7(c) for the Full TTT reinforcement beams orientated along the x-direction (warp). As shown in Figure 3.7(a) and (c), up to point A the load-displacement response is linear elastic, with local increases in inter-ply shear strain, shown as the yellow and blue colouring in Figure 3.7(c). After the peak load at point B, delamination occurs around the neutral axis of the beam and TTT reinforcement, where shear strain is higher than

at other locations. This delamination continues to point C, where the tows on the top of the beam begin to fracture under tensile stress.

At point D, the beam has begun to fail by fibre fracture on the top of the beam, with significant development of inter-laminar shear strains (see the peak shear strain locations in D of Figure 3.7(c)). The large tensile crack propagates after the point of peak load, widening until ultimate failure of the beam. Shown by a comparison between Figure 3.7(a) and (b), beams orientated along the x-direction (warp) have a more rapid drop off in load resisted, compared to the more gradual load-bearing reduction of beams orientated along the y-direction (weft). Thus, it can be deduced, that beams orientated along the same direction as the TTT-reinforcement, i.e. x-direction (warp), are provided with greater confinement than those orientated transversely to it.

In order to investigate the damage mechanisms throughout the beam thickness, X-Ray μCT scans were undertaken post cantilever bending tests. In Figure 3.8, cross sections a-a and c-c are located in between the positions of TTT-reinforcement within the beam. It is at these locations that load bearing longitudinal warp tows are visible. Although both of these cross sectional images are located in between the TTT-reinforcement, it is evident that the damage mechanisms demonstrated are different. In cross section a-a there is seen to be delamination and ply buckling, with the length of delamination clearly resisted by the presence of the TTT-reinforcement. In cross-section c-c, the only major damage mechanism present is that of the large tensile crack at the clamp. This evidence demonstrates that during FE modelling of 3D woven composite materials, any assumptions of periodicity (for example the unit cell methodology) become invalid during the development of damage within the material. It was seen that in cross-sectional images at the location of TTT-reinforcement, no delamination was recorded (see Figure 3.8 section b-b). The supressed delamination seen with the 3D woven composite is different to that presented with short cantilever beam test of a UD-laminate material in Section 3.5.2. The suppression of delamination propagation

within the material is the primary benefit from the inclusion of the TTT reinforcement.

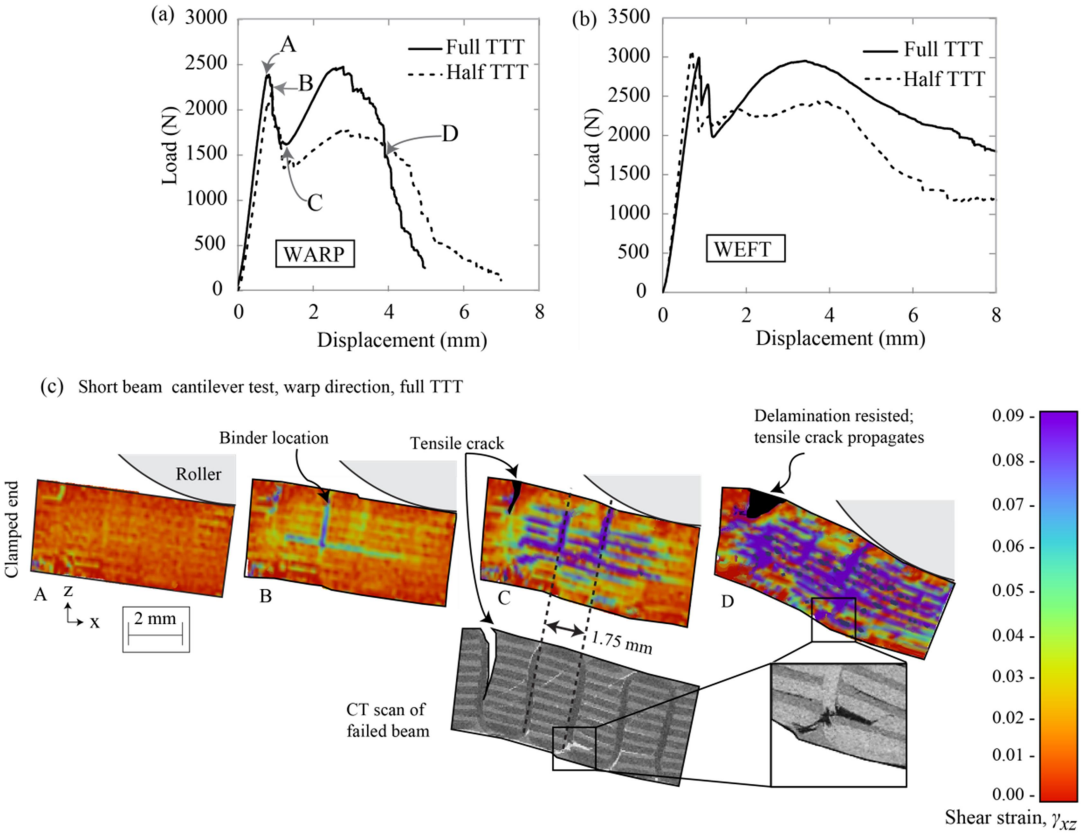


Figure 3.7. Short (8 mm) cantilever beam test results. The force applied by the roller against vertical roller displacement relationship for beams orientated along (a) x-direction (warp); (b) y-direction (weft); (c) Progressive shear strain fields γ_{xz} with A, B, C and D corresponding to the load-displacement curve for the full TTT along the x-direction (warp) in (a) (obtained via DIC analysis), together with μCT images demonstrating location of fracture.

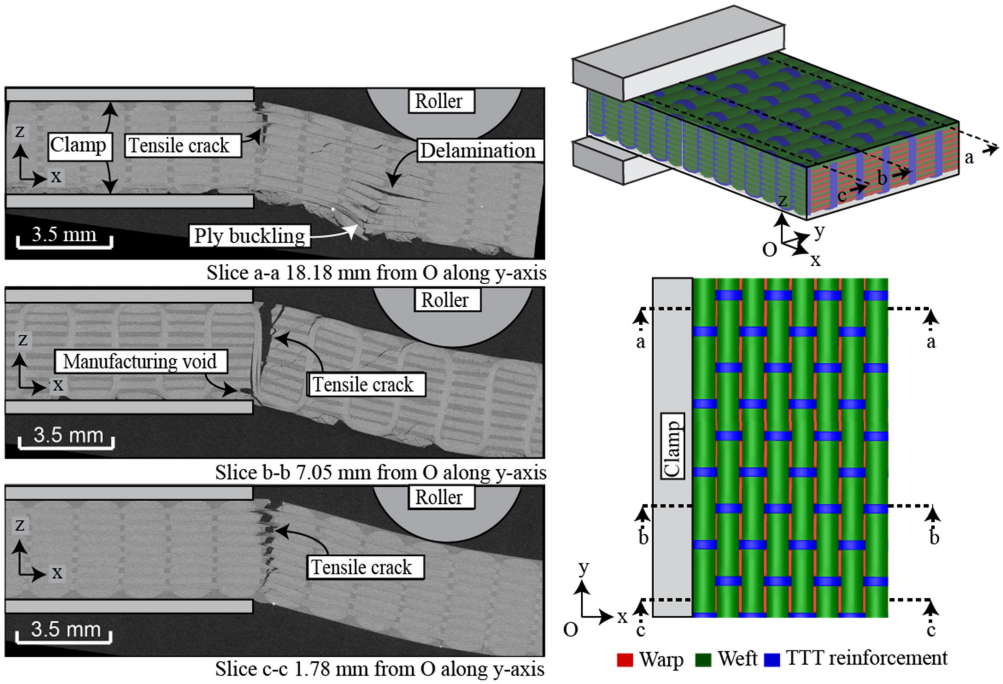


Figure 3.8. µCT images of short beam failure modes of the Full TTT 3D woven composites orientated along the x-direction (warp).

3.5 UD Laminate Cantilever Beam Bending

UD-laminate long (40mm) and short (8mm) cantilever beam bending results are presented. The purpose of this testing is to provide an experimental comparison of the overall response with that of the 3D woven composite material. The material used is aerospace grade cross-ply carbon fibre with symmetrical 0/90° plies of 8 layers. T700 (24k) fibres with a diameter of 7 µm were used. As matrix, MTM57 epoxy was used. The cured composite thickness was 5.16 mm. The resulting fibre volume fraction was 0.55. It is worth noting that due to differing material geometry and differing fibres and matrix type, a quantitative comparison cannot be made to the 3D woven material, only of the general collapse response demonstrated during the test.

3.5.1 UD laminate long beam

Figure 3.9(a) presents the force applied by the roller against vertical roller displacement for the UD-laminate long beam test. Linear deformation was

recorded in the first phase up to point B. Past this, microbuckling of the bottom ply due to compression occurs, causing a reduction of stiffness. The resisted load increases until a peak load, at which wide-spread delamination occurs. This is different to the 3D woven material which retains full beam section and ultimate failure is a tensile crack forming on the top surface and propagating into the material (see Figure 3.5). It should be noted that, unlike the results of the 3D woven material in warp direction, no tensile cracks are formed at the top surface. The failure mechanism becomes that of wide-spread delamination, and differs from the 3D woven material because there is no TTT reinforcement to resist crack growth.

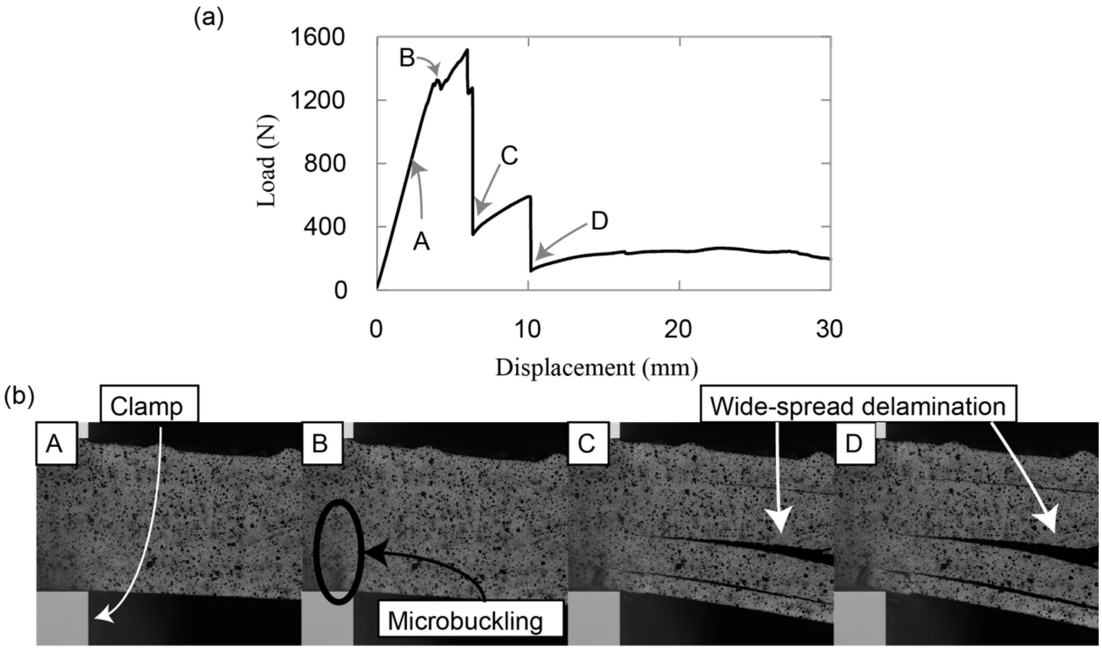


Figure 3.9. Long (40mm) cantilever beam test of a UD laminate material. (a)force applied by the roller against vertical roller displacement relationship (b) photographic montage during the test.

3.5.2 UD laminate short beam

As with the long beam UD laminate test, the short beam UD laminate cantilever beams experienced wide-spread delamination. Figure 3.10(a) presents the force

applied by the roller against vertical deflection of the roller for the test, (b) presents a montage of deformation of the beam, and (c) presents optical microscopic images showing kink band formation on the bottom 0º ply. The first portion of the test, with point A in the middle, is in the linear elastic loading phase. Post peak-load, at point B, significant delamination has already occurred. From point B to point C there is seen to be a slight increase in the load resisted; this is because the delaminated plies are still resisting load. 45º intra-laminar shear matrix cracking within the transversely orientated plies is also demonstrated from B onwards. Delamination and intra-laminar shear matrix cracking continue from point D onwards until ultimate loss of load bearing capability of the beam. Kinking bands are present in 0º plies below the neutral axis of the beam, and one is shown magnified in Figure 3.10(b).

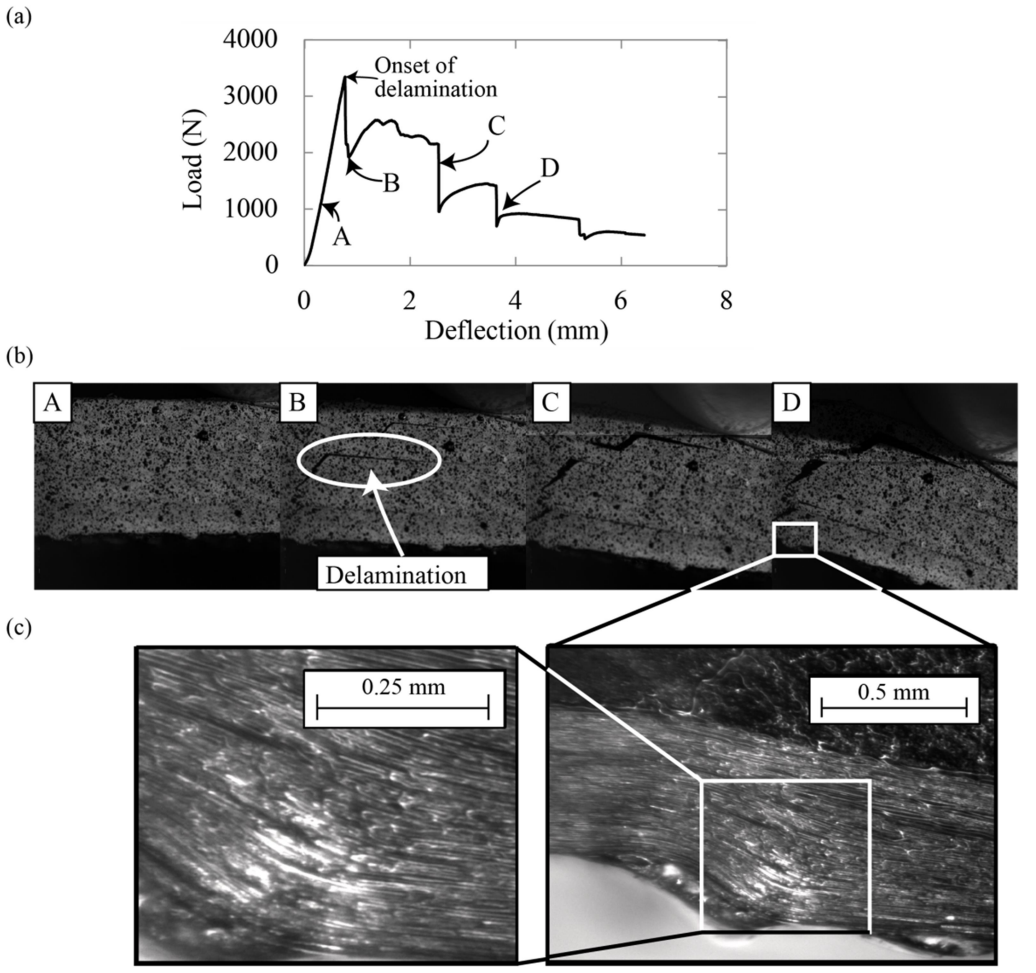


Figure 3.10. Short (8mm) beam cantilever beam test of UD laminate material. (a) force applied by the roller against vertical roller displacement relationship (b) montage of deformation throughout the test showing delamination and intra-laminar matrix cracking (c) optical microscopic images of the bottom ply.

3.6 Finite element analysis

The primary aims of the numerical calculations presented in the following sections are:

- To examine the validity of the proposed FE modelling strategy in the prediction of both the elastic response and collapse measured or observed during in-plane tension and compression tests and out-of-plane cantilever bending test. The modelling strategy utilises the constitutive models of Matzenmiller, Lubliner [178] and Hashin [165] for fibre composites.
- To provide an in-depth understanding of the experimental results.

3.6.1 FE model of orthogonal 3D woven composites

A three dimensional (3D) finite element analysis was conducted by using the explicit solver in ABAQUS (Version 6.12). Each individual tow in weft, warp and TTT-directions was modelled with 4-noded double curved shell element (S4 in ABAQUS notation), with 5 integration points through the thickness. The length of side of each element was 0.25 mm; see Figure 3.11(a) for a sketch of the finite element model. The orientation option in ABAQUS was used to assign the local fibre orientations in individual tows. The geometric data for defining the locations and cross sectional areas of the tows or TTT-reinforcement were taken from microscopic images. See Figure 3.1(b) for an example of such an image utilised for FE modelling. The fibre architecture varies throughout the structure due to the presence of the binder and randomly orientated flaws. Therefore, an average of the tow cross-sectional sizes and positions was taken in order to recreate the geometry of the specimen in the FE model. The matrix was modelled using quadratic solid elements (C3D8 in ABAQUS notation) of second-order accuracy.

The total number of shell and solid elements was 91,000 elements for the short beam model, and 474,000 elements for the long beam model; a numerical study demonstrated that this mesh density achieved a converged result. Shell elements, representing the reinforcement tows, were embedded in solid elements, which represented the resin matrix. Seen in Figure 3.11(a), the embedded element constraint within ABAQUS, i.e., the translational Degrees of Freedom (DoF) of the nodes in the shell elements are constrained to the interpolated values of the corresponding DoF in the solid elements (host elements). The rotational degrees of freedom of the embedded shell elements are not constrained and are retained throughout the calculation. To minimise the errors induced by interpolation, the length of each side of the shell elements and the solid elements were the same. Effectively, this means that the mass and stiffness of the tows are added into the model without the difficulties introduced via compatibility of meshing and misshapen elements often associated with continuous mesh models. This methodology allows for efficient meshing of both matrix and tow components, however, care must be taken to ensure that mesh density is sufficient in order to resolve local stress gradients and to transfer displacement from the host elements to the embedded elements. Shell elements were chosen to model the tows due to the inherent high aspect ratio of individual tows. Shell elements allow for efficient meshing of the tows, however, disallow capturing of any through-thickness effects within the tows themselves.

To simulate delamination through thickness, the solid "block" of matrix was split into 17 layers which correspond to the 9 weft and 8 warp tow layers. These layers were joined together using the "cohesive contact" option within ABAQUS.

Elements were deleted from the calculation as the damage criteria (as defined later) reach a value of unity. These elements are thus removed from the remainder of the calculation.

For cantilever beam simulation, the loading roller was simulated as a rigid body (a cylinder with diameter 10 mm and length 20 mm, see Figure 3.11(b), using discrete rigid body elements (R3D4 in ABAQUS notation). This corresponded to

the cantilever beam bending experimental set up. The roller was moved downward along the z–direction with a constant displacement. The general contact option within ABAQUS was used to model the interaction between the roller and the cantilever beam with an assumed tangential friction coefficient of 0.3. The translational degrees of freedom of the matrix, and the translation and rotational degrees of freedom of the tows were constrained at the clamped end of the beam simulations. This gave a free length of 8 mm for short beam calculations and 40 mm for long beam calculations. Simulations were conducted on 40 mm length long beams, as opposed to the longest beam length tested, in order to lower calculation time. For the simulation of the in-plane tensile/compressive tests, the translational degrees of freedom of the matrix, and the translation and rotational degrees of freedom of the tows were constrained at one end of the sample, and the other subjected to a constant displacement along either the x or y-direction. Global mass scaling was employed in order to increase the elements with the smallest time-step and speed up calculations. Total quantity of mass scaling was below 5% additional mass per part. To ensure the events under simulation were quasi-static, the loading speed of the roller or tensile/compressive deformation was controlled so that the kinetic energy in the whole system was less than 5% of the total energy. The simulations were conducted in parallel mode (8 CPUs) using the High Performance Computing (HPC) facility at the University of Nottingham.

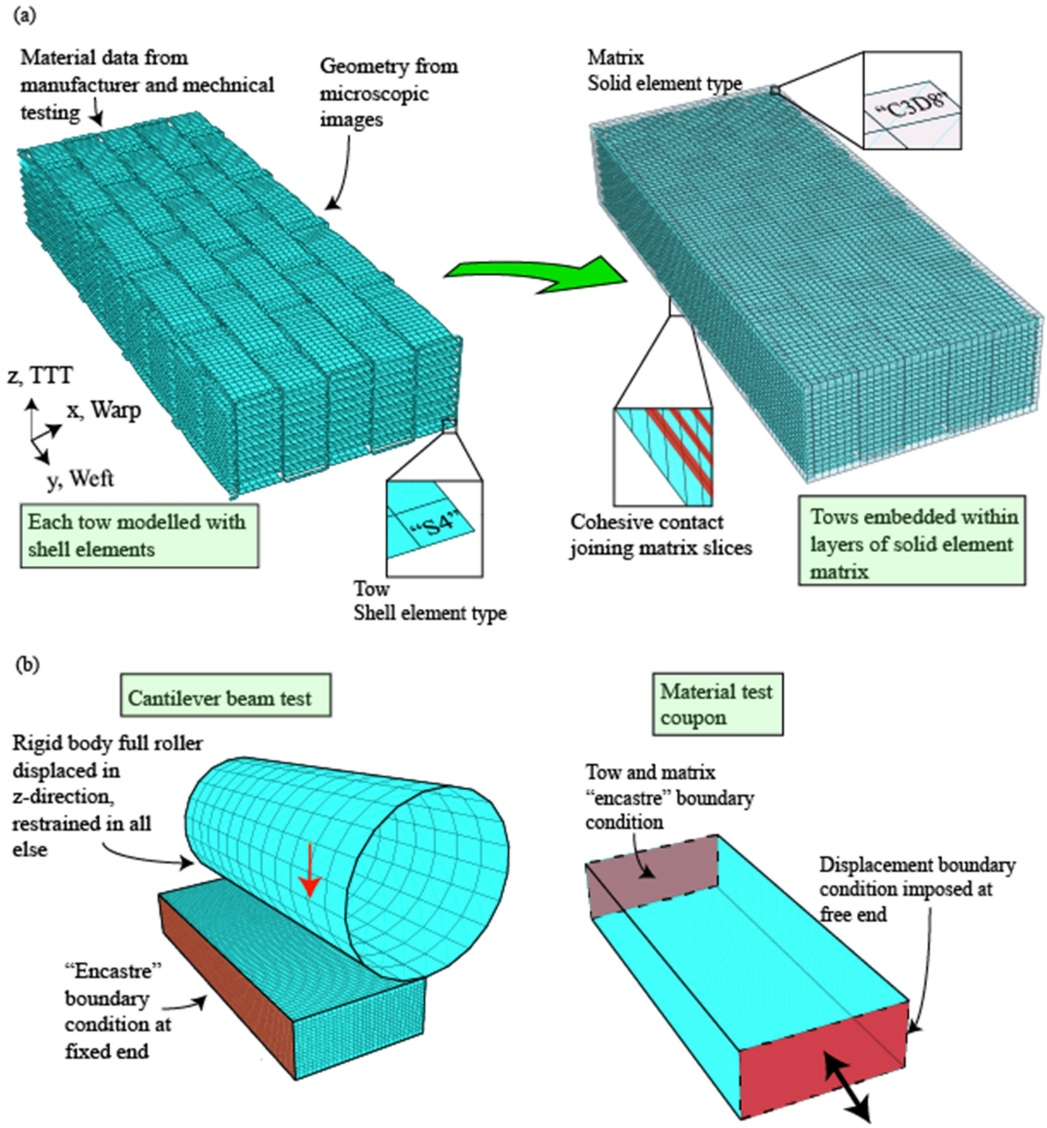


Figure 3.11(a) Finite element modelling strategy employed within this study (b) the two different types of simulations which were undertaken; cantilever structural tests and uni-axial tension and compression material tests.

3.6.2 Description of the constitutive laws employed for FE simulation

The constitutive model of Matzenmiller et al., (1995) and Hashin (1980) for fibre composites were employed to capture the observed collapse modes of tows and TTT-reinforcement. The matrix material was modelled as a linear elastic isotropic

solid with a J2-flow theory elastic-ideally plastic solid with a failure criterion set at a critical von Mises effective strain.

Both the weft and warp tows as well as TTT-reinforcement were modelled as shell elements embedded in matrix host elements. Note the local coordinate system for a tow is denoted by numbers, with $_{11}$ and $_{22}$ being longitudinal and transverse to the in-plane fibre direction, respectively. Each tow and TTT-reinforcement were treated as an orthotropic material under plane stress condition, i.e., $\sigma_{33} = \sigma_{13} = \sigma_{23} = 0$. The in-plane stress-strain relation for the materials without damage is given as;

$$\begin{Bmatrix} \varepsilon_{11} \\ \varepsilon_{22} \\ \gamma_{12} \end{Bmatrix} = \begin{bmatrix} 1/\overline{E}_{11} & -\overline{\nu}_{12}/\overline{E}_{11} & 0 \\ -\overline{\nu}_{21}/\overline{E}_{22} & 1/\overline{E}_{22} & 0 \\ 0 & 0 & 1/\overline{G}_{12} \end{bmatrix} \begin{Bmatrix} \sigma_{11} \\ \sigma_{22} \\ \sigma_{12} \end{Bmatrix} \tag{3.1}$$

Where $\sigma_{ij}\,(i, j = 1,2)$ are in-plane stress components ; ε_{11} and ε_{22} are the direct strains in the x1 and x2 directions, respectively; γ_{12} is the engineering shear strain; $\overline{E}_{11}$, $\overline{E}_{22}$, $\overline{G}_{12}$, $\overline{\nu}_{12}$ and $\overline{\nu}_{21}$ are Young's modulus along the two directions , shear modulus and the two Poisson's ratios with $\overline{\nu}_{21} = \left(\overline{E}_{22} / \overline{E}_{11}\right) \overline{\nu}_{12}$. The undamaged matrix material was treated as a linear elastic solid. The constitutive model is given as;

$$\begin{Bmatrix} \hat{\varepsilon}_{11} \\ \hat{\varepsilon}_{22} \\ \hat{\varepsilon}_{33} \\ \hat{\gamma}_{12} \\ \hat{\gamma}_{13} \\ \hat{\gamma}_{23} \end{Bmatrix} = \begin{Bmatrix} 1/E_m & -\nu_m/E_m & -\nu_m/E_m & 0 & 0 & 0 \\ -\nu_m/E_m & 1/E_m & -\nu_m/E_m & 0 & 0 & 0 \\ -\nu/E_m & -\nu_m/E_m & 1/E_m & 0 & 0 & 0 \\ 0 & 0 & 0 & 1/G_m & 0 & 0 \\ 0 & 0 & 0 & 0 & 1/G_m & 0 \\ 0 & 0 & 0 & 0 & 0 & 1/G_m \end{Bmatrix} \begin{Bmatrix} \\ \\ \\ \\ \\ \end{Bmatrix} \tag{3.2}$$

where $\hat{\sigma}_{ij}\,(i, j = 1,2,3)$ are stress components in the matrix; $\hat{\varepsilon}_{ii}\,(i = 1,2,3)$ are the direct strain components and $\gamma_{ij}\,(i, j = 1,2,3, i \neq j)$ the shear strain components;

E_m, G_m and ν_m are Young's modulus , shear modulus and Poisson's ratio, respectively, of the matrix material.

3.6.3 The damage model for warp and weft tows and TTT-reinforcement

For the tows and or TTT-reinforcement, the anisotropic damage model developed by Matzenmiller et al., (1995) as well as the damage initiation model for fibre reinforced composites developed by Hashin (1980) were employed in the simulation, which accounts for the four damage modes, i.e. fibre rupture under tension, fibre buckling and kinking under compression, matrix cracking under transverse tension and shear and matrix crushing under transverse compression or shearing. Similar to the concept of yield surface in plasticity theory, the damage locus could be defined in the space of stress according to the Hashin damage initiation criteria. For a stress state within the damage locus, the material is in undamaged state and the stress-strain relation is described by Equation (3.1). Damage initiates when the critical stress state in the damage locus is attained or exceeded. Four scalar damage variables, corresponding to the four damage modes, are introduced to represent the effects of the damage modes. Post initiation of damage, the response of the material is governed by

$$\begin{Bmatrix} \varepsilon_{11} \\ \varepsilon_{22} \\ \gamma_{12} \end{Bmatrix} = \begin{bmatrix} 1/\left[\overline{E}_{11}(1-d_f)\right] & -\overline{\nu}_{21}/\left[\overline{E}_{11}(1-d_f)\right] & 0 \\ -\overline{\nu}_{12}/\left[\overline{E}_{22}(1-d_m)\right] & 1/\left[\overline{E}_{22}(1-d_m)\right] & 0 \\ 0 & 0 & 1/\left[\overline{G}_{12}(1-d_s)\right] \end{bmatrix} \begin{Bmatrix} \sigma_{11} \\ \sigma_{22} \\ \sigma_{12} \end{Bmatrix} \quad (3.3)$$

where $$d_f = \begin{cases} d_f^t & \text{if } \sigma_{11} \geq 0 \\ d_f^c & \text{otherwise} \end{cases} \quad \text{and} \quad d_m = \begin{cases} d_m^t & \text{if } \sigma_{22} \geq 0 \\ d_m^c & \text{otherwise} \end{cases} \quad (3.4)$$

Here, d_f^t, d_f^c, d_m^t and d_m^c are the damage variables for fibre damage under tension and compression, matrix damage under tension and compression , respectively . d_s is the shear damage variable, defined as

$$d_s \equiv 1-(1-d_f^t)(1-d_f^c)(1-d_m^t)(1-d_m^c) \quad (3.5)$$

The shear damage variable is used later in this section in order to visualise the location of damage during finite element simulations of in-plane uni-axial coupon tests. It is useful as a resultant damage variable, combining tension and compression for both longitudinal and transverse directions.

In the undamaged state, the damage variables are set to zeros. During the stage of damage initiation and evolution, damage variables evolve from zeros to a maximum value of unity controlled by the strain in the material. The damage evolution law follows that proposed by Matzenmiller, Lubliner [178]. The damage will only develop when the stress state exceeds the critical stress surface given by;

$$\frac{\langle \sigma_{11} \rangle}{(1-d_f^t)\overline{X}^T} \leq 1 \quad \text{when } d_f^t > 0 \tag{3.6}$$

$$\frac{-\langle \sigma_{11} \rangle}{(1-d_f^c)\overline{X}^C} \leq 1 \quad \text{when } d_f^c > 0 \tag{3.7}$$

$$\left(\frac{\langle \sigma_{11} \rangle}{(1-d_m^t)\overline{Y}}\right)^2 + \left(\frac{2\sigma_{12}}{(1-d_s)\overline{Y}}\right)^2 \leq 1 \quad \text{when } d_m^t, d_s > 0 \tag{3.8}$$

or

$$\left(\frac{\langle -\sigma_{22} \rangle}{(1-d_m^c)\overline{Y}}\right)^2 + \left(\frac{2\sigma_{12}}{(1-d_s)\overline{Y}}\right)^2 \leq 1 \quad \text{when } d_m^c, d_s > 0 \tag{3.9}$$

where $\langle\ \rangle$ represents the Macaulay bracket of value zero when its augment is negative. $\overline{X}^T$ and $\overline{X}^C$ denote the tensile and compressive strength at damage initiation during loading along the fibre direction. $\overline{Y}$ denotes the tensile and compressive strength along the transverse direction.

The four independent damage variables, d_f^t, d_f^c, d_m^t and d_m^c, increase if the stress state lies beyond the critical space defined in Eqs. (3.6) to (3.9).

The damage variables are assumed to evolve in a way that the stress decreases linearly with increasing strain once damage initiates. The following relations are

used to update the damage variables, following the conditions within eqn. (3.6) to eqn. (3.9);

$$d_f^t = \frac{\frac{2J_f^t}{l_e\overline{X}^T}\left(\langle\varepsilon_{11}\rangle - \overline{X}^T/\overline{E}_{11}\right)}{\langle\varepsilon_{11}\rangle\left(\frac{2J_f^t}{l_e\overline{X}^T} - \overline{X}^T/\overline{E}_{11}\right)} \leq 1 \tag{3.10}$$

$$d_f^c = \frac{\frac{2J_f^c}{l_e\overline{X}^c}\left(\langle\varepsilon_{11}\rangle - \overline{X}^c/\overline{E}_{11}\right)}{\langle\varepsilon_{11}\rangle\left(\frac{2J_f^c}{l_e\overline{X}^c} - \overline{X}^c/\overline{E}_{11}\right)} \leq 1 \tag{3.11}$$

$$d_m^t = \frac{\frac{2J_m}{l_e\overline{Y}}\left(\sqrt{\langle\varepsilon_{22}\rangle^2 + \varepsilon_{12}^2} - \overline{Y}/\overline{E}_{22}\right)}{\sqrt{\langle\varepsilon_{22}\rangle^2 + \varepsilon_{12}^2}\left(\frac{2J_m}{l_e\overline{Y}} - \overline{Y}/\overline{E}_{22}\right)} \leq 1 \tag{3.12}$$

$$d_m^c = \frac{\frac{2J_m}{l_e\overline{Y}}\left(\sqrt{\langle-\varepsilon_{22}\rangle^2 + \varepsilon_{12}^2} - \overline{Y}/\overline{E}_{22}\right)}{\sqrt{\langle-\varepsilon_{22}\rangle^2 + \varepsilon_{12}^2}\left(\frac{2J_m}{l_e\overline{Y}} - \overline{Y}/\overline{E}_{22}\right)} \leq 1 \tag{3.13}$$

where l_e is a characteristic length scale which is the same as the length across a finite element; J_f^t, J_f^c and J_m are the tensile fibre fracture energy, compressive fibre fracture energy and the matrix fracture energy, respectively.

3.6.4 Matrix material damage model

The matrix material was treated as a J2-flow theory based elastic-ideally plastic solid with the undamaged elastic response dictated by Equation (3.2) and uniaxial tensile strength $\overline{\sigma}_Y^o$. In order to model the damage in the matrix, the damage initiation criteria was defined as $\overline{\varepsilon}_{pl} = \overline{\varepsilon}_c$, where $\overline{\varepsilon}_{pl}$ and $\overline{\varepsilon}_c$ denote the von Mises effective plastic strain and a critical strain, respectively. After damage initiation, a

damage variable, D $(0 \le D \le 1)$, is employed for degradation of the elasticity, i.e. $(1-D)E_m$, and softening of the yield stress, i.e. $(1-D)\hat{\sigma}_Y^0$, which is dictated by the following equation;

$$\frac{dD}{dt} = \frac{L_e \hat{\sigma}_Y^o}{2J_m} \frac{d\bar{\varepsilon}_{pl}}{dt} \tag{3.14}$$

where L_e denotes a characteristic length scale, J_m the fracture energy and t time. The damage variable is set to zero before damage initiation.

3.6.5 Cohesive law for interface between layers through the thickness

The matrix material was split into 17 layers through the thickness, corresponding to the 9 weft and 8 warp tow layers. A cohesive contact law was used to model the interface between layers, which simulates the traction-separation behaviour between them and allows the FE model to simulate delamination at these locations. It is noted that it was at these locations that delamination occurred during experimental testing. For an undamaged cohesive contact, the behaviour across the interface is dictated by the following elastic response

$$\begin{Bmatrix} t_n \\ t_s \\ t_t \end{Bmatrix} = \begin{Bmatrix} k_n & 0 & 0 \\ 0 & k_s & 0 \\ 0 & 0 & k_t \end{Bmatrix} \begin{Bmatrix} \delta_n \\ \delta_s \\ \delta_t \end{Bmatrix} \tag{3.15}$$

where t_n, δ_n and k_n denote the normal traction, separations and stiffness, respectively; $\{t_s, t_t\}, \{\delta_s, \delta_t\}$ and $\{k_s, k_t\}$ the two shear tractions, separations and coefficients of stiffness, respectively. The behaviour is uncoupled, i.e. pure normal separation in isolation does not cause any cohesive forces in any of the shear directions and pure shear displacement does not cause any normal cohesive forces.

The failure mechanism of the cohesive contact consists of both a damage initiation criterion and a damage evolution law. Damage develops when the traction stresses lie outside the following surface;

$$\left[\frac{\langle t_n \rangle}{(1-\hbar)T_n}\right]^2 + \left[\frac{\langle t_s \rangle}{(1-\hbar)T_s}\right]^2 + \left[\frac{\langle t_t \rangle}{(1-\hbar)T_s}\right]^2 \leq 1 \tag{3.16}$$

where T_n and T_s denote the maximum allowable uncoupled traction forces along normal and shear directions, respectively; $\hbar\ (0 \leq \hbar \leq 1)$ denotes the damage variable for cohesive contact with $\hbar = 0$ for undamaged state and $\hbar = 1$ for fully damaged state. The damage variable is defined in terms of the fracture energy, J_G, given as

$$\hbar = \frac{\dfrac{2J_G}{t_e^0}\left(\delta_e^{\max} - \delta_e^0\right)}{\delta_e^{\max}\left(\dfrac{2J_G}{t_e^0} - \delta_e^0\right)} \leq 1 \tag{3.17}$$

where $\delta_e^{\max}$ is the maximum value of the effective separation that occurs during loading; t_e^0 and δ_e^0 are the effective traction and separation at the damage initiation point. The effective separation, δ_e, and effective traction, t_e, is given by the following relationship from Camanho and Dávila [258];

$$\delta_e \equiv \sqrt{\langle \delta_n \rangle^2 + \delta_s^2 + \delta_t^2} \tag{3.18}$$

$$t_e \equiv \sqrt{\langle t_n \rangle^2 + t_s^2 + t_t^2} \tag{3.19}$$

The damage evolution is defined as linear softening and, at any given moment, has the form

$$t_n = \begin{cases} (1-\hbar)k_n\delta_n & \text{when } \delta_n > 0 \\ k_n\delta_n & \text{otherwise} \end{cases} \tag{3.20}$$

$$t_s = (1-\hbar)k_s\delta_s \tag{3.21}$$

$$t_t = (1-\hbar)k_t\delta_t \tag{3.22}$$

Note that in compression, i.e. when $\delta_n \leq 0$, the interaction between the two matrix layers is reduced to a penalty contact algorithm. In order to simulate the interaction behaviour of fully damaged cohesive contacts the "general contact" option within ABAQUS was used with a tangential friction coefficient of 0.3.

The normal and shear stiffness, k_n and k_s respectively, were estimated from manufacturer's data assuming an initial interface size of 0.1 mm. The normal and shear traction, t_n and t_s respectively, were estimated from onset of non-linearity during the matrix dominated ±45º material tensile test results. The fracture energy, J_G, was not directly measured and estimated from ±45º material tensile test results. The values of these parameters are given in Table 3.1.

Table 3.1. Material parameters for the cohesive contact between matrix slices

Property	Value
k_n	35 GPa mm^{-1}
k_s, k_t	20 GPa mm^{-1}
t_n	80 MPa
t_s	40 MPa
J_G	650 J m^{-2}

3.7 Calibration of material properties employed in FE simulations

3.7.1 Weft tows, warp tows and TTT-reinforcement as shell elements

As shown in Section 3.6.2, ten parameters are required in order to define the elastic property, damage initiation and damage evolution of tows and TTT-reinforcement, i.e. $\overline{E}_1, \overline{E}_2, \overline{\nu}_{12}, \overline{G}_{12}, \overline{X}^T, \overline{X}^C$, $\overline{Y}$, $\overline{J}_1^T$, $\overline{J}_1^C$ and J_m. These parameters could be estimated using the rule of mixtures based on either manufacturer's data or material coupon tests. We first consider application of manufacturer's data. Consider a tow with fibre volume fraction V_t, we have;

$$\overline{E}_1 = V_t E_f + (1 - V_t) E_m \tag{3.23}$$

$$\overline{G}_{12} = \frac{G_{12f} G_m}{V_t G_m + (1 - V_t) G_{12f}} \tag{3.24}$$

$$\overline{\nu}_{12} = V_t \nu_f + (1 - V_t) \nu_m \tag{3.25}$$

$$\overline{X}^T = V_t X_f + (1 - V_t) \overline{\sigma}_Y^o \tag{3.26}$$

$$\overline{X}^C = V_t X_f + (1 - V_t) \overline{\sigma}_Y^o \tag{3.27}$$

where the A-38 carbon fibres of diameter 7 μm within the fibre reinforcement were assumed to be isotropic and using ISO 10618 test methods have a tensile modulus E_f of 240 GPa, and a longitudinal tensile strength X_f of 3800 MPa. Fibre Poisson's ratio ν_f was assumed to be 0.25 giving an in-plane shear modulus G_{12f} of 96 GPa. The transverse longitudinal modulus, $\overline{E}_2$, is matrix dominated and can simply be estimated as the Young's modulus of cured epoxy matrix 3.5 GPa. Researchers wishing to following a similar methodology for estimating material properties are suggested to avoid such a gross simplification, however, for the

load cases explored within this thesis this methodology was deemed acceptable. Warp and weft tows contained 6000 fibres, and TTT reinforcement tows contained 3000 fibres. The fibre volume fractions of warp, weft and TTT reinforcement tows were measured using microscopic cross sectional images as 0.785, 0.692, and 0.795, respectively.

Alternatively, these parameters could be estimated based on experimental measurement as follows. Let V_{tow}^{weft} and V_{tow}^{warp} denote the volume fractions of weft tows and warp tows within a composite test sample, respectively, which can be calculated as,

$$V_{tow}^{weft} = \frac{n_{weft} A_{tow}^{weft}}{A_y}, \quad V_{tow}^{warp} = \frac{n_{warp} A_{tow}^{warp}}{A_x} \tag{3.28}$$

where A_{tow}^{weft} and A_{tow}^{warp} denote the average transverse cross section areas for a weft tow and a warp tow, respectively, n_{weft} and n_{warp} the number of the weft tows and warp tows in the composite sample and A_y and A_x are the areas of cross sections of the composite along the y(weft) and x(warp) axis, respectively. Based on the rule of mixtures we have

$$\overline{E}_1 = \frac{E_x^T - (1 - V_{tow}^{warp}) E_m}{V_{tow}^{warp}}, \overline{G}_{12} = \frac{G_{xy} G_m V_{tow}^{warp}}{V_{tow}^{arp} G_m + \left(1 - V_{tow}^{warp}\right) G_{xy}}, \tag{3.29}$$

$$\overline{v}_{12} = \frac{v_{xy} - (1 - V_{tow}^{warp}) v_m}{V_{tow}^{warp}}$$

$$\overline{X}^T = \left(\frac{E_x^T - (1 - V_{tow}^{warp}) E_m}{V_{tow}^{warp}} \right) \frac{X_x^T}{E_x^T}, \overline{X}^C = \left(\frac{E_x^C - (1 - V_{tow}^{warp}) E_m}{V_{tow}^{warp}} \right) \frac{X_x^C}{E_x^C} \tag{3.30}$$

for warp tows, and

$$\overline{E}_1^T = \frac{E_y^T - (1 - V_{tow}^{warp})E_m}{V_{tow}^{warp}}, \overline{G}_{12} = \frac{G_{xy}G_m V_{tow}^{weft}}{V_{tow}^{weft}G_m + \left(1 - V_{tow}^{weft}\right)G_{xy}}, \overline{v}_{12} = \frac{v_{xy} - (1 - V_{tow}^{weft})v_m}{V_{tow}^{weft}}$$

(3.31)

$$\overline{X}^T = \left(\frac{E_y^T - (1 - V_{tow}^{weft})E_m}{V_{tow}^{weft}}\right)\frac{X_y^T}{E_y^T}, \overline{X}^C = \left(\frac{E_y^T - (1 - V_{tow}^{weft})E_m}{V_{tow}^{weft}}\right)\frac{X_y^C}{E_y^C} \quad (3.32)$$

for weft tows. Here, $\left\{E_x^T, X_x^T, X_x^C\right\}$ and $\left\{E_y^T, X_y^T, X_y^C\right\}$ are the measured material tensile Young's modulus, tensile strength and compressive strength along x (warp) direction and y (weft) direction, respectively, υ_{xy} is the measured in-plane Poisson's ratio. These parameters are obtained by the 0/90° coupon tests, as the failure of the 0/90º test coupons was governed by the failure of the warp/weft tows. It is assumed in Eqns. (3.30) and (3.32), that the strain to failure of the tows along the loading direction within a test sample is identical to that of the composite itself. G_{xy} is the measured shear modulus obtained by the ±45º coupon tests.

The material parameters estimated based on manufacturer's data and material coupon tests are compared in Table 3.2. These material data were employed in FE simulation of 0/90º coupon tests in comparison with experimental measurement. It was demonstrated that the approach described in Eqns. (3.23) through (3.27) overestimated $\overline{E}_1$, $\overline{X}^T$ and $\overline{X}^C$. This is commonly attributed to (i) inherent fibre waviness within the composite, which reduces the stiffness, (ii) fibre misalignment and micromechanical flaws within the composite, which reduces tensile strength, and (iii) kink band formation and microbuckling of fibres, which reduces the compressive strength of tows [130]. However, the values for tow shear modulus, $\overline{G}_{12}$, obtained in Eqns. (29) and (31) are lower than that of pure matrix material, which are unrealistic. Thus, Eqn. (24) using manufacturer's data was used to calculate tow shear modulus.

Table 3.2. Tow material properties calculated from manufacturer's data and material testing. The values underlined give the best fit between FE simulation results and experimental measurement in regards to the stress strain response of the material.

Property	Calculations from Manufacturer's data Equations (3.23)-(3.27)	Calculations from Material tests Equations (3.29-(3.32)
Warp tow		
$\overline{E}_1$ (GPa)	189.2	<u>146.8</u>
$\overline{E}_2$ (GPa)	<u>3.5</u>	N/A
$\overline{v}_{12}$	0.26	<u>0.35</u>
$\overline{G}_{12}$ (GPa)	<u>14.37</u>	0.46
$\overline{X}^T$ (GPa)	3.15	<u>2.02</u>
$\overline{X}^C$ (GPa)	3.15	<u>1.61</u>
$\overline{Y}$ (MPa)	83	<u>80</u>
Weft tow		
$\overline{E}_1$ (GPa)	167.3	<u>137.4</u>
$\overline{E}_2$ (GPa)	<u>3.5</u>	N/A
$\overline{v}_{12}$	0.27	<u>0.35</u>
$\overline{G}_{12}$ (GPa)	<u>7.16</u>	1.06
$\overline{X}^T$ (GPa)	2.86	<u>1.72</u>
$\overline{X}^C$ (GPa)	2.86	<u>1.10</u>
$\overline{Y}$ (MPa)	83	<u>80</u>

The tow transverse modulus, $\overline{E}_2$, is dominated by matrix. Again, this value was taken from manufacturer's data. There is a doubling up of the elastic properties in the transverse direction as the same volume is occupied by both the matrix and the tow. A parametric study was conducted for both in-plane and cantilever beam bending simulations and revealed that even if the transverse stiffness of the tows were reduced by ten times, in order to avoid superposition, there was no effect on the results. It can be concluded that the model is insensitive to matrix superposition effects.

The transverse strength of tows, $\overline{Y}$, is matrix dominated. The material parameter for the strength of the matrix was estimated from the on-set of non-linearity of the

matrix dominated uni-axial tensile coupon tests on the 3D woven composite with fibres aligned at ±45° to the loading axis, i.e. $\overline{Y} = 80$ MPa.

The longitudinal tensile and compressive tow fracture energies, $\overline{J}_1^t$ and $\overline{J}_1^c$ were calculated using the following equations;

$$\overline{J}_1^t = 0.5 \times \frac{l_e \left(\overline{X}_1^T\right)^2}{\overline{E}_1} \times 1.2 \tag{3.33}$$

and

$$\overline{J}_1^c = 0.5 \times \frac{l_e \left(\overline{X}_1^C\right)^2}{\overline{E}_1} \times 1.2 \tag{3.34}$$

The transverse fracture energy of the tow is assumed to be the same as the matrix material, again taken from ±45º coupon tests. The fibre volume fraction of the TTT reinforcement was calculated as being 0.795, almost identical to that of the warp tows. To avoid any material testing along the TTT reinforcement direction, the warp and TTT reinforcement material properties were assumed to be the same within the model. Table 3.3 summarises all of the material properties used for the matrix and tows within the finite element model.

Table 3.3 Material properties of matrix and tows for the composite material used in the constitutive model in the FE calculations.

Material	Property	Value
Matrix	E_m (GPa)	3.5
	ν_m	0.3
	Density (g mm^{-3})	0.001144
	Yield Stress σ_y (MPa)	80
	Fracture strain $\hat{\varepsilon}_c$	0.25
	J_m (Jm^{-2})	650
Warp Yarn	$\overline{E}_1$ (GPa)	146.8
	$\overline{E}_2$ (GPa)	3.5
	$\overline{\nu}_{12}$	0.25

	$\overline{G}_{12}$, $\overline{G}_{13}$, $\overline{G}_{23}$ (GPa)	14.37
	Density (g mm^{-3})	0.001628
	$\overline{X}^T$ (MPa)	2020
	$\overline{X}^C$ (MPa)	1610
	$\overline{Y}$ (MPa)	80
	$\overline{X}^s$, $\overline{Y}^s$ (MPa)	40
	$\overline{J}_1^t / l_e$ (MPa)	16.68
	$\overline{J}_1^c / l_e$ (MPa)	10.6
	J_m / l_e (MPa)	7.90
Weft Yarn	$\overline{E}_1$ (GPa)	135.7
	$\overline{E}_2$ (GPa)	3.5
	$\overline{\nu}_{12}$	0.25
	$\overline{G}_{12}$, $\overline{G}_{13}$, $\overline{G}_{23}$ (GPa)	7.16
	Density (g mm^{-3})	0.00157
	$\overline{X}^T$ (MPa)	1720
	$\overline{X}^C$ (MPa)	1110
	$\overline{Y}$ (MPa)	80
	$\overline{X}^s$, $\overline{Y}^s$ (MPa)	40
	$\overline{J}_1^t / l_e$ (MPa)	13.08
	$\overline{J}_1^c / l_e$ (MPa)	5.45
	J_m / l_e (MPa)	7.90

3.7.2 Matrix material as solid elements

The Young's modulus, E_m, and density, ρ_m, employed in the FE simulation for the pure matrix material, i.e. Prime© 20LV epoxy matrix, were taken from data provided by the manufacturer, i.e. $E_m = 3.5\,\text{GPa}$ and $\hat{\rho} = 1.144\,\text{g/cm}^3$. The yield strength, $\hat{\sigma}_Y^o$, fracture strain , $\hat{\varepsilon}_c$, and fracture energy, J_m, were estimated from ±45º tensile coupon tests , in which the failure of test samples is dominated by the strength of the matrix material, i.e. $\hat{\sigma}_Y^o = 80\,\text{MPa}$, $\hat{\varepsilon}_c = 0.25$ and $J_m = 650 Jm^{-2}$. The Poisson's ratio ν_m was estimated as 0.3.

3.8 FE simulation results for in-plane coupon tests

In order to validate the modelling approach, the finite element calculations of in-plane tension and compression test coupons were conducted in comparison with experimental measurements as shown in Figure 3.12(a) for tests conducted along the warp direction and (b) for tests conducted along the weft direction. The finite element simulation captures the stiffness and peak stress of uniaxial compression/tension tests. The location and nature of damage is also predicted by the FE model, and will be investigated now in more detail.

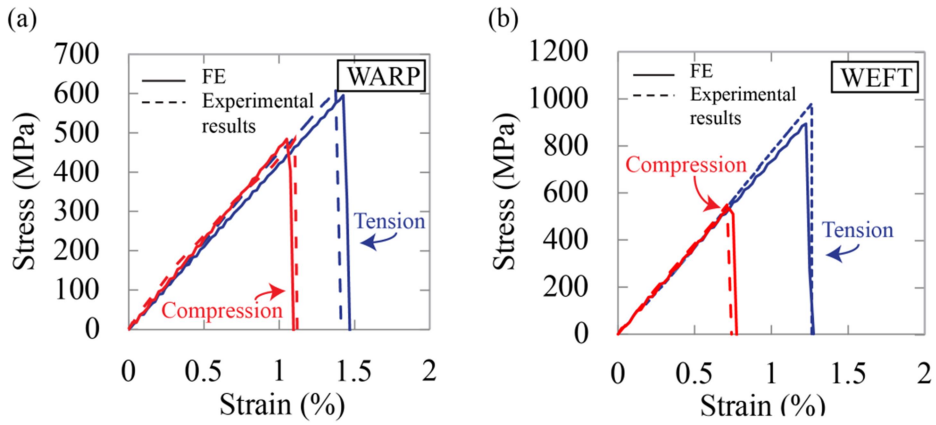


Figure 3.12. Comparison between the finite element predictions and the experimental data of uni-axial quasi-static compressive and tensile stress-strain responses (a) Warp direction and (b) Weft direction.

The finite element model predicts that the material response under uniaxial tension and compression is dominated by the in-plane tows. Figure 3.13(a) presents the contour of in-plane stress along y-direction (weft), σ_{yy}, within the top surface layer tows, based on the coordinate system defined in Figure 3.8, under y- direction (weft) uniaxial compression testing immediately prior to failure of the sample, obtained by the finite element simulations. At the positions of the TTT-reinforcement, there is a clear increase in magnitude of σ_{yy}. This is attributed to crimping within the surface weft tows induced by the TTT-reinforcement. The predicted ratio of maximum to minimum stress σ_{yy} in the

surface weft tows is approximately 4.0, with the peak stress immediately prior to fracture being identical to that of the longitudinal compressive strength of weft tows, $\overline{X}^C$ = 1.1 GPa. This notably high ratio is analogous to the stress concentration factor of 5.5 recorded in notched CFRP samples under compression fatigue loading in Soutis, Fleck [259], which is defined as the ratio of local stress to remote stress. To understand stress distribution through the thickness of the sample, Figure 3.13(b) shows the contours of σ_{yy}, immediately prior to failure, within selected weft yarns that share the same x-y locations. Again, both surface tows have significant stress concentrations owing to the crimping induced by the TTT-reinforcement. However, as the crimping has less influence on the geometries of internal weft tows than those of the surface tows, the stress concentrations in internal tows are less significant. The staggered binder location at the top and bottom surfaces of the material causes an alternating pattern of relatively high and low local stresses throughout the thickness of the material. It is this stress variance through the thickness of the material which leads to the "step" shape fracture phenomena. The location of the fracture surface corresponds exactly to the position of maximum longitudinal stress σ_{yy} shown in Figure 3.13(a) and follows the stress distribution through the thickness as shown in Figure 3.13(b). Figure 3.13(c) and (d) show the fractured sample obtained by FE simulation and experiment, respectively. The contour shown in Figure 3.13(c) shows the damage variable, d_s, within the tows. The finite element simulation captures the shape of the fracture surface.

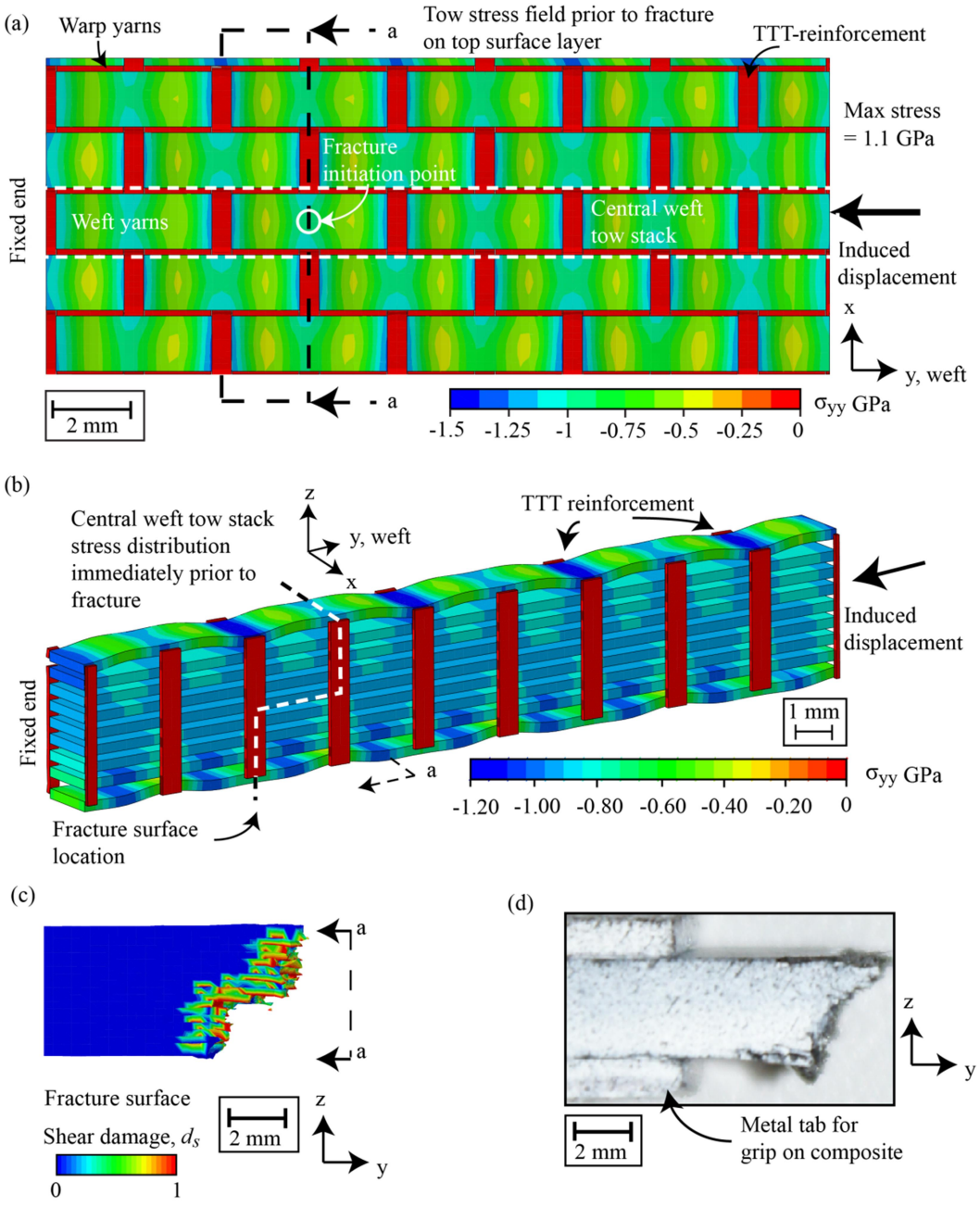


Figure 3.13. Finite element simulation of uni-axial compression test along weft direction : (a) In-plane stress field σ_{yy} on the top surface layer immediately prior to sample failure (b) In-plane stress field σ_{yy} throughout the central weft tow stack immediately prior to fracture. The location of the central weft tow stack is shown in (a). (c) FE prediction of fracture surface with contour showing tow shear

damage criterion, d_s, and (d) Photographic image of fracture surface from the compression experiment.

For the same sample under tensile testing along y-direction (weft), Figure 3.14(a) shows the contours of in-plane stress along y-direction (weft), σ_{yy}, within the top surface layer tows, while (b) shows the shear damage variable, d_s, at the fracture surface of the fibre reinforcement immediately after sample fracture. Although the response was governed by the tensile response of the in-plane tows, the shear damage variable was chosen as it allows a convenient visualisation of a combination of the four damage modes (see Section 3.6.3). Once fracture initiates within a longitudinal weft tow, it rapidly propagates throughout the material, including through the centre of the TTT-reinforcement. Again, longitudinal stress, σ_{yy}, increases at the TTT-reinforcement position, which gives rise to final fracture location, as shown in Figure 3.14(b).

In Figure 3.14(a), the ratio of maximum to minimum stress σ_{yy} in the weft tow is approximately 1.8, with the maximum stress prior to the onset of fracture being 1.72 GPa which is equal to the longitudinal tensile strength of the weft tows, $\overline{X}^T$. The maximum to minimum stress ratio during tensile testing is lower than that of the compressive testing. This is because during the tensile test, the reinforcement deformation effectively "straightens out", reducing the crimp angle and, thus, its effect. This also serves to supress the "step" shape fracture surface. The FE predication is consistent with experimental observation, i.e. the fracture occurred at a TTT-reinforcement position, see Figure 3.14(c) for the microscopic image of the fracture surface.

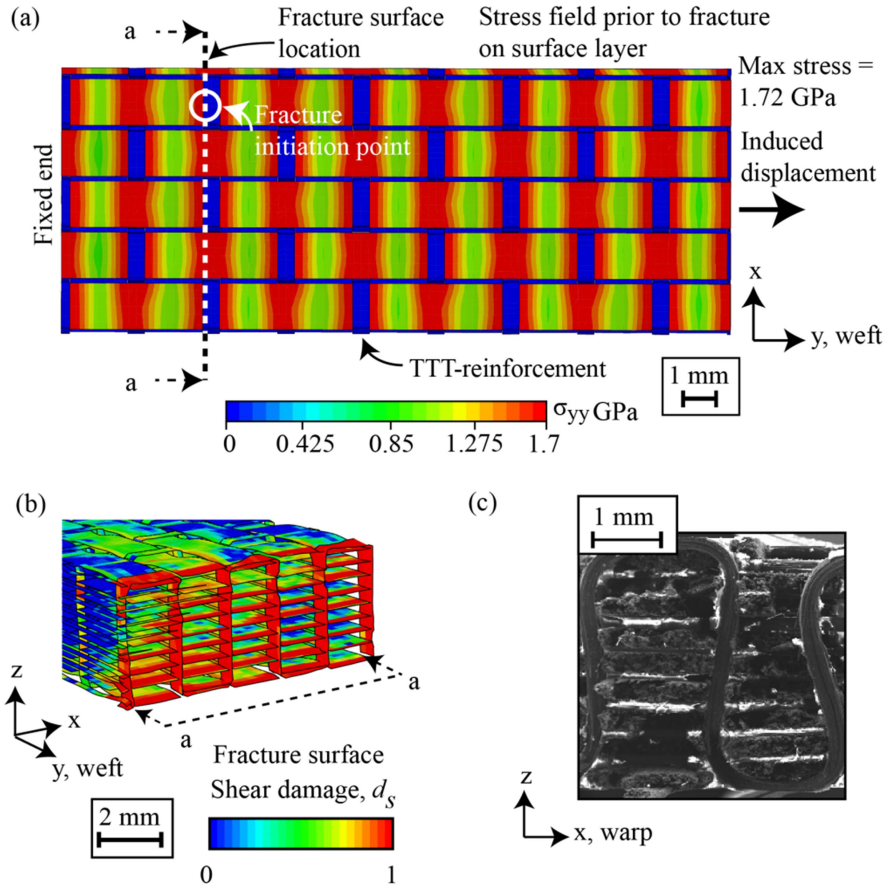


Figure 3.14. Finite element simulation of uni-axial tension test along weft direction. (a) In-plane stress field σ_{yy} on the top surface corresponding to peak load (b) FE prediction of fracture surface with contour showing tow shear damage d_s and (c) SEM image of fracture surface from the tension experiment.

The response immediately prior to fracture of a test coupon under uniaxial compression test along the x–direction (warp) obtained by FE simulation is shown in Figure 3.15(a) for the contours of in-plane stress in the fibre reinforcement, σ_{xx} . The response is governed by in-plane warp yarns. There are no significant stress concentrations owing to crimping induced by the TTT-reinforcement. The stress distribution within the longitudinal warp yarns is relatively homogenous, with maximum stress immediately prior to fracture being identical to that of the longitudinal compressive strength of warp tows $\overline{X}^C = 1.6$ GPa. Hence, the TTT-reinforcement has negligible influence on the failure of the test coupons. The top

layer of transverse (weft) yarns and the top surface of the TTT reinforcement have been visually removed for clarity.

Figure 3.15(b) presents the shear damage variable, d_s, at the fracture surface immediately after the fracture event. A comparison is made with SEM images of the fracture surface of the compression experiment, presented in Figure 3.15(c). The FE predication is consistent with the experimental observation, i.e. brittle fraction of in-plane warp yarns and resin rich channels which reveal binder locations. For brevity, the detailed simulation results of the tensile coupon tests along x–direction (warp) are not shown here as the failure mechanism is similar to that of the compressive test along x-direction (warp), as described above. Again, the TTT-reinforcement has negligible influence on failure of the test coupons.

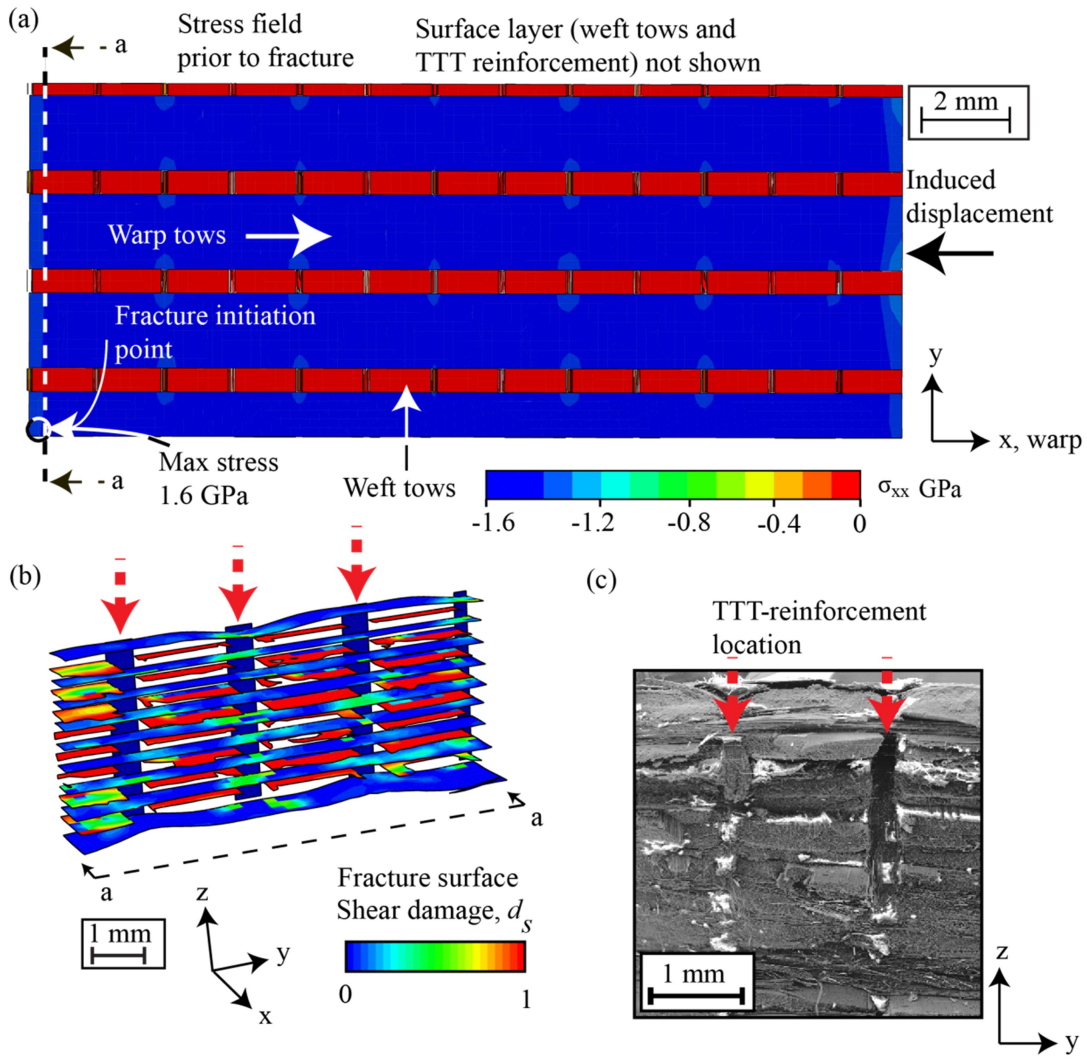


Figure 3.15. Finite element simulation of uni-axial compression test along warp direction. (a) In-plane stress field corresponding to the peak load with top weft and TTT reinforcement layer not shown in order to reveal the longitudinal warp tows (b) Finite element prediction of fracture surface with contour showing shear damage d_s in tows and (c) SEM image of fracture surface from the compression experiment.

3.9 FE simulations of cantilever beam tests

3.9.1 Long beam

For long cantilever beams, Figure 3.16(a) shows a comparison between the experimental measurement and FE predictions of the force imposed by the roller as a function of roller displacement along z-direction with length of the beam, L = 40 mm, and thickness , t_b = 3.5 mm. Only the results for the beam oriented along warp direction is presented. The agreement between experimental measurements and FE predictions is reasonably good. Figure 3.16(b) shows the montage obtained by FE calculations with contour representing strain along x–direction, ε_{xx} . As expected, the long beam failed under bending mechanism, i.e. tensile failure within top tows and compressive failure within bottom tows.

At Point A, immediately prior to peak load, there is seen to be an increase of local compressive longitudinal strain at the bottom of the beam at the clamp position. Between Point A and Point B there is a rapid drop-off in load resisted by the beam, this is caused by an increase of tensile fibre damage of longitudinal warp tows at the top of the beam. This corresponds well to the tensile crack seen during experimental testing, presented in Figure 4. Tensile fibre damage is the cause of the local increase in tensile longitudinal strain at the top of the beam, seen at Point B. In between Point C and D, the FE prediction captures progressive, sudden reductions in load resisted by the beam. This was also demonstrated via the experimental testing. The FE model allows for further elucidation of the exact nature of this phenomenon, and is traced to successive compressive damage of individual tows located at the clamp. This serves to further amplify the buckling of the plies at the clamp. The numerically predicted buckling length of warp tows at the bottom of the beam was approximately 1.5 mm, this coincides to the gap in between TTT-reinforcement positions, and corresponds well to microscopic images of the experimental test presented in Figure 3.5(c)

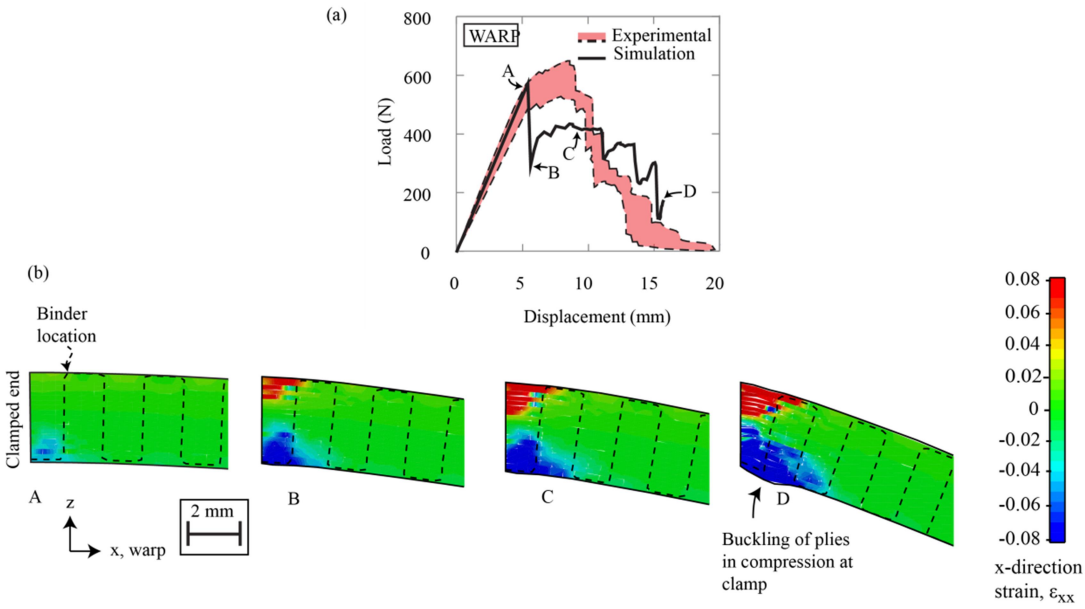


Figure 3.16. Experimental data and FE prediction of force applied by the roller against vertical roller displacement relationship during long cantilever beam bending test (40 mm) along x-direction (warp). Results presented here are only for the Full TTT; (b) Predicted beam deformation corresponding to the points A, B, C and D on the load-displacement curve by FE simulation in (a).

3.9.2 Short beam

Figure 3.17(a) and (b) show a comparison between experimental measurements and FE predictions of the force imposed by the roller as a function of roller displacement along z-direction throughout short cantilever beam tests with length of the beam, L = 8 mm , and thickness , t_b = 3.5 mm along the warp and weft directions, respectively. Due to material variability, the experimental results are presented as an area bound by the minimum and maximum loads obtained through multiple tests. The numerical calculations show effects of the three different binder densities, Full, Half, and No TTT reinforcement. The beams are orientated along both warp and weft directions, as shown in Figure 3.17(a) and (b), respectively. For both cases, the predictions are accurate during the elastic phase of the deformation (e.g. up to Point A in Figure 3.17(a)) and exhibit an accurate prediction of the initial peak load. Figure 3.17(c) shows a montage of FE

predictions along the warp direction with Full TTT reinforcement at three selected deflections in comparison with experimental measurement shown in Figure 3.7(c). The three selected deflections are A, at the initial peak load, where the beam is deforming elastically; B, immediately after the peak load, at the onset of collapse of the beam and C, at the trough, the local minimum of load resisted after the initial peak load.

The contours shown in Figure 3.17(c) represent shear strain, γ_{xz}, of the specimen as the deformation of the beam is governed by shear deflection. Up until point A, the beam deforms elastically, which agrees well with experimental results. At Point B, a hinge forms in the FE predictions at the clamped end of the beam due to damage of the top warp tows. The shear strain field is shown to be almost identical to the shear strain field measured by DIC during experimental testing, i.e. Point B in Figure 3.7(c). At locations of TTT reinforcement, shear strain is much higher than other places. At point C, it can be seen that delamination has propagated longitudinally along the beam. However, the development of delamination is different from that observed in the experiment, see Point C of Figure 3.7(c). During the experiment, the delamination propagates throughout the entire length of the beam, and this is not captured within the FE model. It is suggested that the discrepancy between the FE prediction and experimental results is due to the use of an oversimplified constitutive model for the cohesive interaction.

Finite element calculations in Figure 3.17(a) and (b) also reveal the effect of TTT reinforcement on load versus vertical roller deflection relation is small. The montages of FE predictions along the warp direction with full TTT reinforcement and without TTT reinforcement are compared in Figure 3.17(c) and (d). It demonstrates that delamination is arrested by the presence of the TTT reinforcement, see point C in Figure 3.17(c), while an uninhibited progression of delamination occurs with the absence of TTT reinforcement, see point C in Figure 3.17(d). The numerically predicted delamination length for the Full TTT case was 3.0 mm; this corresponds well to the experimentally measured delamination

length of 2.8 mm. The numerical prediction of the delamination length of the No TTT material was 5.5 mm.

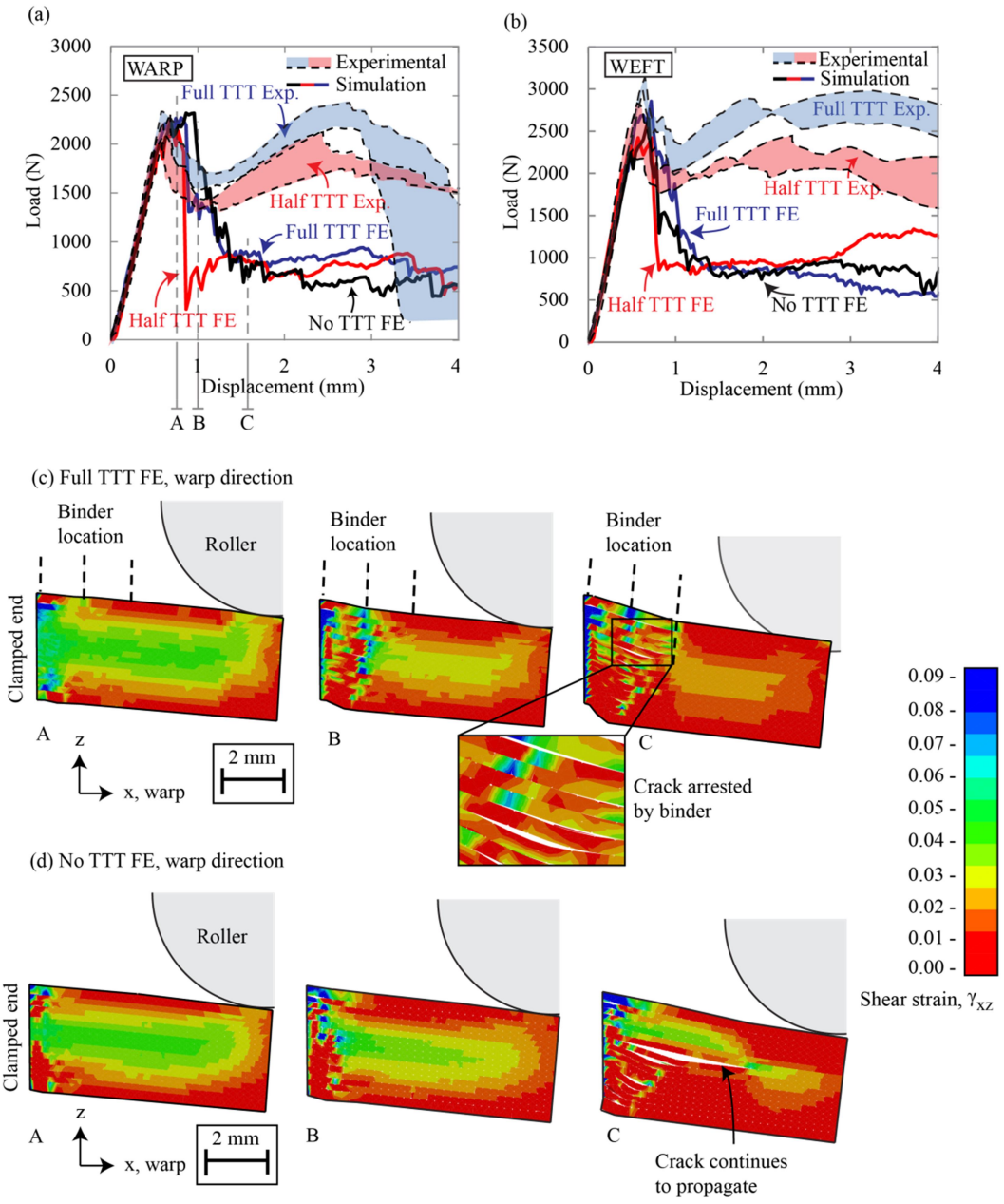


Figure 3.17(a) and (b) Experimental data and FE predictions of the force applied by the roller against vertical roller displacement relationship during short cantilever beam bending tests (8 mm) along for x-direction (warp) and y-direction (weft), respectively. Predictions for three different binder densities are shown; as Full TTT, Half TTT, and TTT reinforcement removed; (c) and (d) predicted beam

deformations corresponding to the points A, B and C on the load-displacement curve by FE simulation in (a), plotted with a logarithmic shear strain field γ_{xz}, for Full TTT and TTT reinforcement removed material, respectively.

3.10 Pre-delaminated composite cantilever beams

To further investigate the ability of the TTT reinforcement to provide structural enhancements to composite cantilever beams, finite element simulations were undertaken with the cohesive contacts deactivated from the FE model. This allows for large relative deformations between the matrix "slices" with each slice bound only be the TTT reinforcement. This effectively represents a composite structure that has been fully delaminated, with no other damage within the structure. Simulations of all three binder densities were undertaken for both short and long beams in the warp direction (Full, Half and TTT removed). The results presented in Figure 3.17 and Figure 3.18 are for the long and short beam simulations, respectively.

Even in this fully delaminated case, with the presence of the TTT reinforcement, the long cantilever beams resist approximately half the maximum loads as measured in the experimental testing for the original beams, see Figure 4(a). The FE simulation results indicate only a minor difference in the load resistance between the Full and Half TTT binder density, this agrees well with experimental results shown in Figure 4. The pre-delaminated long beam without TTT reinforcement has almost no load bearing capacity. The deformed configurations of long beams without cohesive contact with and without TTT reinforcement are compared in Figure 3.18(b) and (c). The TTT reinforcement is seen to provide structural rigidity to the beam. When the TTT reinforcement is removed, the response is purely governed by frictional forces.

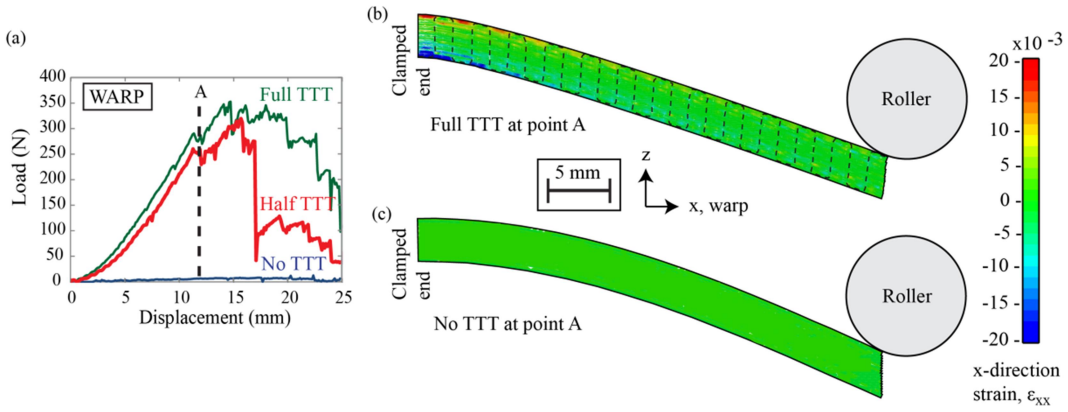


Figure 3.18(a) Finite element prediction of the load resisted against vertical roller displacement of long beam cantilever tests (40 mm) along the x-direction (warp) with cohesive contact removed ; (b) Longitudinal strain field ε_{xx} of Full TTT material beam corresponding to point A in Figure (a); (c) Longitudinal strain field ε_{xx} of No TTT material beam at point A in Figure (a).

As shown in Figure 3.19(a), for the short beams with cohesive contact removed, the TTT reinforcement is shown to allow an increase in the load resisted by the beam throughout the simulation. There is seen to be a difference between the response of the Full and Half TTT material, with the Full TTT material providing higher load resistance than the Half TTT material. The influence of the density of the TTT reinforcement on the load carried by the short cantilever beam becomes increasingly more significant when deflections become larger, i.e. deflections greater than approximately 60% of the beam thickness. The deformed configurations of short beams with cohesive contact removed with and without the presence of the binder are compared in Figure 3.19(b) and (c).

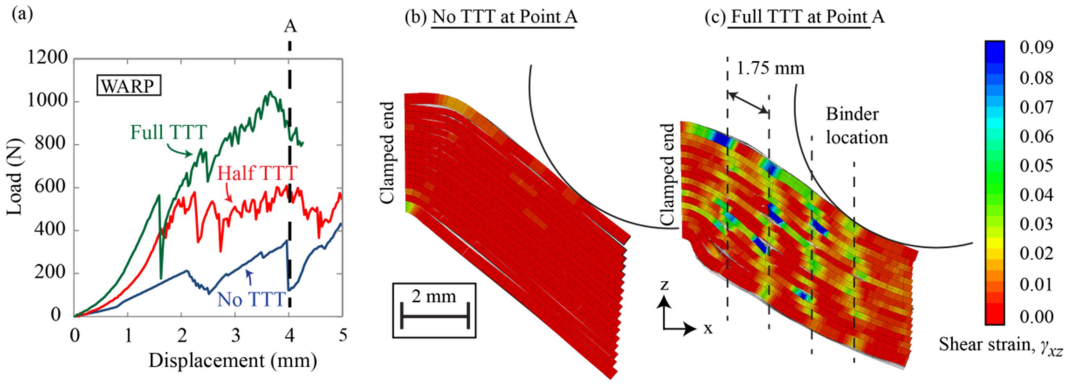


Figure 3.19(a) Finite element prediction of load resisted against vertical roller displacement of short beam cantilever tests (8 mm) orientated along the x-direction (warp) with cohesive contact removed; (b) Shear strain field γ_{xz} of No TTT beam at point A in figure (a); (c) Shear strain field γ_{xz} of Full TTT beam at point A in Figure (a).

3.11 Concluding remarks

The in-plane and out-of-plane properties of orthogonal 3D woven composites have been investigated in detail through this study. The cantilever beam test has been shown to be effective in isolating the two collapse mechanisms of orthogonal 3D woven composite materials; bending deformation dominated long beam tests, and shear deformation dominated short beam tests.

The TTT reinforcement of 3D woven composites prevents delamination with long cantilever bending tests, while it provides containment and limited changes to post-peak load response with short beam tests. Delamination is shown in short cantilever beam tests, however, in long beam tests the failure mechanism is a large tensile crack and compressive buckling of longitudinal fibres at the clamped end. DIC analysis indicates increased local strain at TTT reinforcement positions for both long beam and short beam tests due to the presence of matrix pockets.

A finite element modelling strategy was presented and validated with experimental results of in-plane tension and compression test and cantilever bending tests. In regards to the in-plane tension and compression tests, the FE

model does not provide a truly predictive tool as the material properties were extracted from the mechanical tests themselves. However, the simulations can be used to provide further insight into the behaviour of the material, as shown for compressive testing along the weft direction. High levels of fidelity are shown for stiffness and peak load of long and short cantilever beam tests. However, the model is unable to capture the post initial peak load response of the short cantilever beam tests. It is suggested that improving the constitutive model of the cohesive contact would enhance the accuracy of the finite element model. Also, it is suggested that the modelling strategy does not capture the confinement pressure provided by the TTT reinforcement.

Capturing the secondary rise in resisted load presented by short 3D woven composite beams proved difficult, even with major modifications to the material properties. A parameter study was conducted on the cohesive interaction within the model, increasing the stiffness, strength, and fracture energy of the interface. It was determined that these values could not be modified in a way which would provide a secondary rise in resisted load. It is suggested that a simple linear softening relationship for a cohesive interaction is insufficient for capturing mechanisms such as crack bridging, transverse matrix cracking, and fibre pullout. The rising R-curve exhibited within 3D woven composites for Mode I and Mode II crack propagation [104] requires a more complex constitutive law for the interface, such as the super-imposed bilinear law as discussed by Dávila, Rose [211]. It was also shown via a parameter study that the model is insensitive to superposition effects, i.e. the doubling up of the elastic properties between embedded shell elements and host solid elements, for the in-plane tension and compression and cantilever beam bending simulations. A parameter study on the transverse stiffness of the tows revealed that this material property was not critical to the load cases investigated within this study.

The use of element deletion within the simulations can help to prevent excessively distorted elements during the progression of damage within the beam. However, the deletion of elements may well lead to a diversion from reality during the

progression of damage with large deformations of the cantilever beam. In reality, damaged material, such as crushed matrix, would still be present and provide additional resistance during progressive loading of the beam. A more comprehensive investigation into the role of element deletion within numerical simulations, combined with refinement of the post-damage constitutive laws used, is suggested for improving the simulation of the post-damage onset behaviour of the cantilever beams.

A further word of caution is to be added. The thesis presents a fast increase in complexity to model the 3D woven composite material. Researchers wishing to pursue similar lines of investigation are recommended to build confidence in the modelling strategy by initially undertaking calculations of reduced complexity. From this, a more comprehensive review of the modelling strategy can be presented.

CHAPTER 4

SOFT IMPACT OF ORTHOGONAL 3D WOVEN COMPOSITES

Summary

The previous chapter investigated the quasi-static collapse mechanisms of 3D woven composite materials, highlighting the importance of the through-thickness weave. This chapter moves on to examine the dynamic response of the same orthogonal through-the-thickness woven composites under blast loading. Emphasis is given to the role of the through-thickness reinforcement throughout the event.

This study presents an experimental and numerical investigation into the dynamic response of 3D orthogonal woven carbon composites during soft impact. Composite beams of two different fibre architectures, varying only by the density of through-thickness reinforcement, were centrally impacted by metallic foam projectiles. Using high speed photography, the centre-point back-face deflection was measured as a function of projectile impulse. Qualitative comparisons are made with a similar uni-directional laminate material. No visible delamination occurred in orthogonal 3D woven samples, and failure was caused by tensile fibre fracture at the gripped ends. This contrasts with uni-direction carbon fibre laminates, which exhibit a combination of wide-spread delamination and tensile fracture. Post-impact clamped-clamped beam bending tests were undertaken across the range of impact velocities tested in order to investigate any internal damage within the material. Increasing impact velocity caused a reduction of beam stiffness: this phenomenon was more pronounced in composites with higher density of through-thickness reinforcement. A three-dimensional finite element modelling strategy is presented and validated, showing excellent agreement with the experiment in terms of back-face deflection and damage mechanisms. The

numerical analyses confirm negligible influence from though-thickness reinforcement in regards to back-face deflection, but significant reductions in delamination damage propagation. Finite element modelling was used to demonstrate the significant structural enhancements provided by the through-the-thickness weave. The contributions to the field made by this research include the characterisation of 3D woven composite materials under high-speed soft impact, and the demonstration of how established finite-element modelling methodologies can be applied to the simulation of orthogonal woven textile composite materials undergoing soft impact.

4.1 Introduction

Lightweight composite materials are an increasingly popular choice for the design of highly mobile vehicles such as troop transporters. The current design methodology for the enhancement of the blast protective systems for such vehicles in the addition of metallic, composite or ceramic armour panels, or combinations thereof, to the exterior. Often these materials provide no primary structural role to the vehicle, serving to increase vehicle weight. Therefore, the search for materials which can provide sufficient stiffness for primary structures, with inherent resistance to impact damage, is of great importance. The high specific stiffness and strength of fibre reinforced composite materials, combined with the damage reduction provided by through-the-thickness reinforcement, makes 3D woven composites an obvious choice for further investigation.

There have been numerous studies conducted into the ballistic impact performance of 3D woven composite materials, in particular, in the development and validation of numerical modelling strategies [250, 260-262]. They indicate the enhanced structural performance of the 3D weave in the reduction of damage within the composite. However, in regards to blast loading of composite structures, in particular the load case of shallow-buried land mine detonation, research in the literature is sparse, and primarily limited to laminate composite materials [156, 157]. The objective of this research is to provide a comprehensive

investigation into the potential of 3D woven composites to resist soft impact loading without inducing widespread delamination damage within the material. Particular attention is given to the role of the through-thickness reinforcement during soft impact events.

The outline of the study is as follows. First, the dynamic test protocol is described. Next, a description of the finite element modelling strategy, which is a modified version to that presented in Chapter 3, is presented. Then, a discussion of the soft impact experiment results is presented, aided with finite element predictions. After this, post impact clamped-clamped beam tests, conducted in order to investigate any internal damage within the composite beams, are reported. The chapter concludes with a summary of the main contributions of the research.

4.2 Materials and properties

The same two 3D woven composite materials as investigated under quasi-static loading in Chapter 3 are utilised again in this study for dynamic soft impact testing. For brevity, the material geometry, manufacturing methodology, and material properties will not be presented again here, and the reader is referred back to Chapter 3 of this thesis for these details.

Quasi-static (2mm/min) compression tests were undertaken on the Alporas aluminium foam material that used for the projectiles in the soft impact experiment. A screw-driven Instron© 5581 test machine with a static 50 kN load cell was used for testing, with the displacement and axial stress read directly from the load cell of the test rig. The compressive stress-strain response of the aluminium foam material is presented in Figure 4.1. The foam material exhibits a plateau at a stress of approximately 2.2 MPa, corresponding to the plastic buckling of cell walls. The foam exhibits densification behaviour at higher strains.

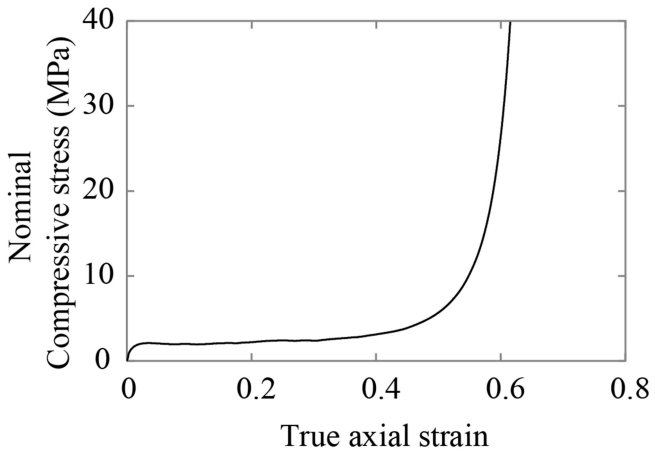


Figure 4.1. Quasi-static uniaxial compression stress-strain curve for the Alporas aluminium foam projectile.

4.3 Soft impact testing

4.3.1 Dynamic soft impact response

The use of metallic foam projectiles as a method of providing well-characterised shock pulses was introduced by Radford, Deshpande [147] and subsequently utilised within multiple studies for sandwich plates of various designs [153-155]. It was shown that the impact of the metallic foam projectile imparts upon structures a remarkably similar momentum transferal as to that of structures impacted by columns of sand particles. Therefore, this methodology is a practical technique for investigating the response of materials undergoing a real-world load case of a shallow buried landmine explosion. Due to the well-characterised pressure pulse, varying with velocity and length of projectile, and convenience of not utilising actual sand columns, this methodology was chosen to be employed in the current study.

4.3.2 Test protocol

Figure 4.2 presents a sketch of the experimental set up for soft impact tests. Samples of width w = 40 mm and length L = 250 mm were cut from the fully

cured composite panels. The beams were fixed into a steel sample fixture, which in turn was bolted into an aluminium alloy frame by a total of 8 M6 bolts. Clamped beams had a gauge length of l_0 = 170 mm. The distance from the gas gun muzzle to the front edge of composite samples was s = 200 mm. A three litre diving cylinder with a custom designed fitting was pressurised either up to 6.5 bars of pressurised air for lower velocity tests, or up to 45 bars of pressurised nitrogen (oxygen free) for higher velocity tests. Pressure was released via a fast-acting solenoid valve, accelerating projectiles down a 3.5 m long barrel. Barrel material was hardened steel, with an outer diameter of 40 mm and a bore diameter of 28 mm. A more detailed description of the design of the pressurised gas gun system is presented in the Appendix to this thesis.

Projectiles were circular cylindrical of length $l_p = 50$ mm and diameter $d_p = 27.5$ mm . Projectiles were electro-discharge machined from a block of Alporas© aluminium foam material of density $\rho_p = 310\ \text{kg m}^{-3}$. The exit velocity of projectile v_0 was measured in two ways; by two laser gates at the muzzle end of the barrel and high speed photography. Exit velocity of projectile in the tests fell within the range $160\ \text{ms}^{-1} \le v_0 \le 270\ \text{ms}^{-1}$. This corresponded to a projectile momentum per unit area $I_0 = \rho_0 l_p v_0$ in the range of $2.48 \le I_0 \le 4.19$ kPa s . The variation of speed between that measured from the lasers gates and using the high speed camera was recorded to be no more than 5%. High speed photography was employed in order to measure the back face deflection of the beams. The high speed camera model Phantom Mercury HS v12.1 with a global electronic shutter was used. Typical recordings had a frame rate of 22,000 fps and an exposure time of 35 μs. At a recorded resolution of 304 x 400, the pixel size on the front surface of the beam samples was approximately 0.23 mm.

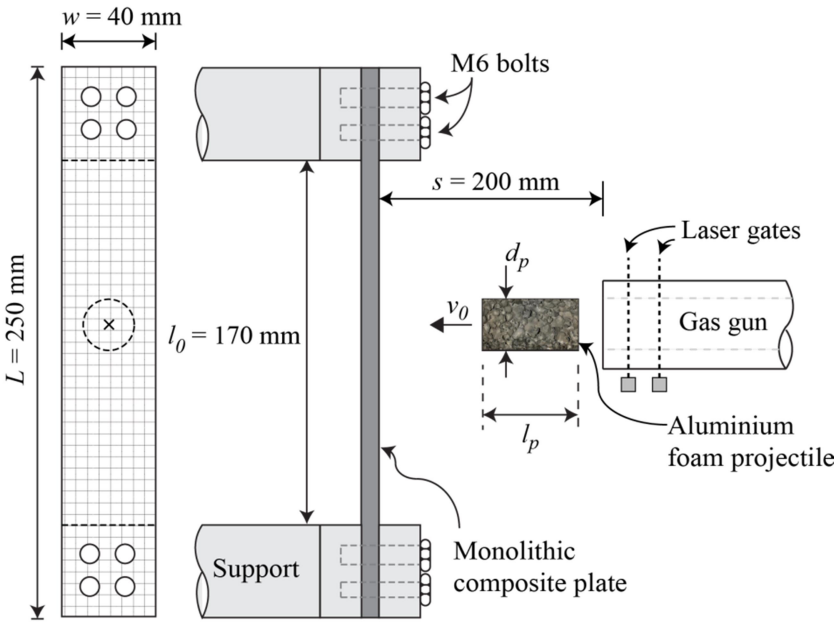


Figure 4.2. Sketch of experimental set up of dynamic soft impact tests on orthogonal 3D woven composite panels.

4.4 Soft Impact Finite Element Analysis

Finite element (FE) modelling can aid interpretation of the experimental tests and provide further insight into the results. As with the modelling strategy presented in Chapter 3, the constitutive model of Matzenmiller, Lubliner [178] and Hashin [165] for fibre composites is utilised, implemented within the commercial finite element code ABAQUS. The primary aims of the modelling technique are:

- To develop a full scale FE modelling strategy to predict the response of 3D woven composite materials undergoing soft impact.
- To further investigate the role of TTT-reinforcement during the soft impact event of orthogonal 3D woven composites.

4.4.1 FE analysis of orthogonal 3D woven composites

Three-dimensional (3D) finite element modelling was conducted using the explicit solver within ABAQUS (Version 6.12). Each of the 17 layers of the

composite material was modelled individually, with each layer alternating between either warp or weft tow, and matrix material. In-plane tows, through-thickness reinforcement, and matrix material were all modelled using 4-noded doubly curved reduced integration shell elements (S4R in ABAQUS notation), with 5 integration points through the thickness. Element size of in-plane architecture was approximately 1.25 mm. See Figure 4.3 for a sketch of the modelling strategy. ABAQUS orientation assignment control was used to assign local fibre orientations for individual tows. Cross sectional microscopic images, e.g. Figure 3.1(b), were used in order to acquire the geometrical data such as tow sizes and locations. Each composite layer (consisting of tows and matrix) was joined together via the "cohesive contact" option in ABAQUS. This was done in order to allow the model to simulate delamination. It was at these locations that delamination was recorded during soft impact of a UD-laminate composite material by Kandan, Russell [157]. The constitutive law of the cohesive contact is presented in Chapter 3.

The through-thickness reinforcement was explicitly modelled independently to the in-plane fibre architecture. The geometric detailing was again taken from cross-sectional microscopic images. The translational and rotational nodal Degrees of Freedom (DoF) of the through-thickness reinforcement were tied to the translational and rotational DoF of the in-plane fibre architecture via the tie constraint option within ABAQUS. Element size of through-thickness reinforcement was approximately 0.7 mm.

Eight-node general purpose linear reduced integration brick elements (C3D8R in ABAQUS notation) were used to model the aluminium foam projectile. The projectile consisted of an isotropic crushable foam using a crushable foam hardening law and rate dependency introduced via a power law.

Fixed boundary conditions were employed at the two edges of the composite sample, giving a gauge length of 170 mm. During experimental testing, clamped samples may experience minor oscillations within the grip during impact.

However, it was observed that the peak deflection during the impact events occurred before any oscillations within the grip. Therefore, the oscillations had no effect on the results of back-face deflection obtained. A total of 210,000 shell elements were used for the composite material, and 14,100 solid elements for the projectile. A numerical study determined that this mesh density provided converged results. All material properties, except the in-plane shear stiffness of tow reinforcement, were estimated from uni-axial mechanical tests performed on the composite. The constitutive models for the fibre tows, and cohesive contact between the layers of the composite material are identical to that of the model presented in Chapter 3 and will not be repeated here. The matrix elements were assigned the material properties as the same stiffness and strength as that in the previous model design. However, the matrix is no longer modelled with solid elements, and instead is modelled as plane-stress shell elements with identical transverse and longitudinal properties. The constitutive model of the metallic foam projectile is presented in Section 4.4.4. For the calculations, 8 CPU parallel processing was provided by the High Performance Computing (HPC) system at the University of Nottingham.

The numerical study utilised models based on two different material geometries used within the experimental investigation i.e. Full TTT and Half TTT. In order to study the effect of the TTT reinforcement, simulations were undertaken with the binder removed. The in-plane geometry for this model was based upon that of the either the Full TTT or Half TTT material. This model is referred to as No TTT throughout this chapter, and is identical to non-crimp composite materials. To investigate the influence of the in-plane fibre architecture, an equivalent UD-laminate material was utilised. The Equivalent UD-laminate does not explicitly model the geometry of each individual tow; the tows and matrix channels are homogenised into one effective laminate, and the TTT reinforcement is removed. For clarification, Figure 4.3(a), (b), and (c) presents sketches of the top layer of the Full TTT, No TTT, and Equivalent UD-laminate material FE models, respectively.

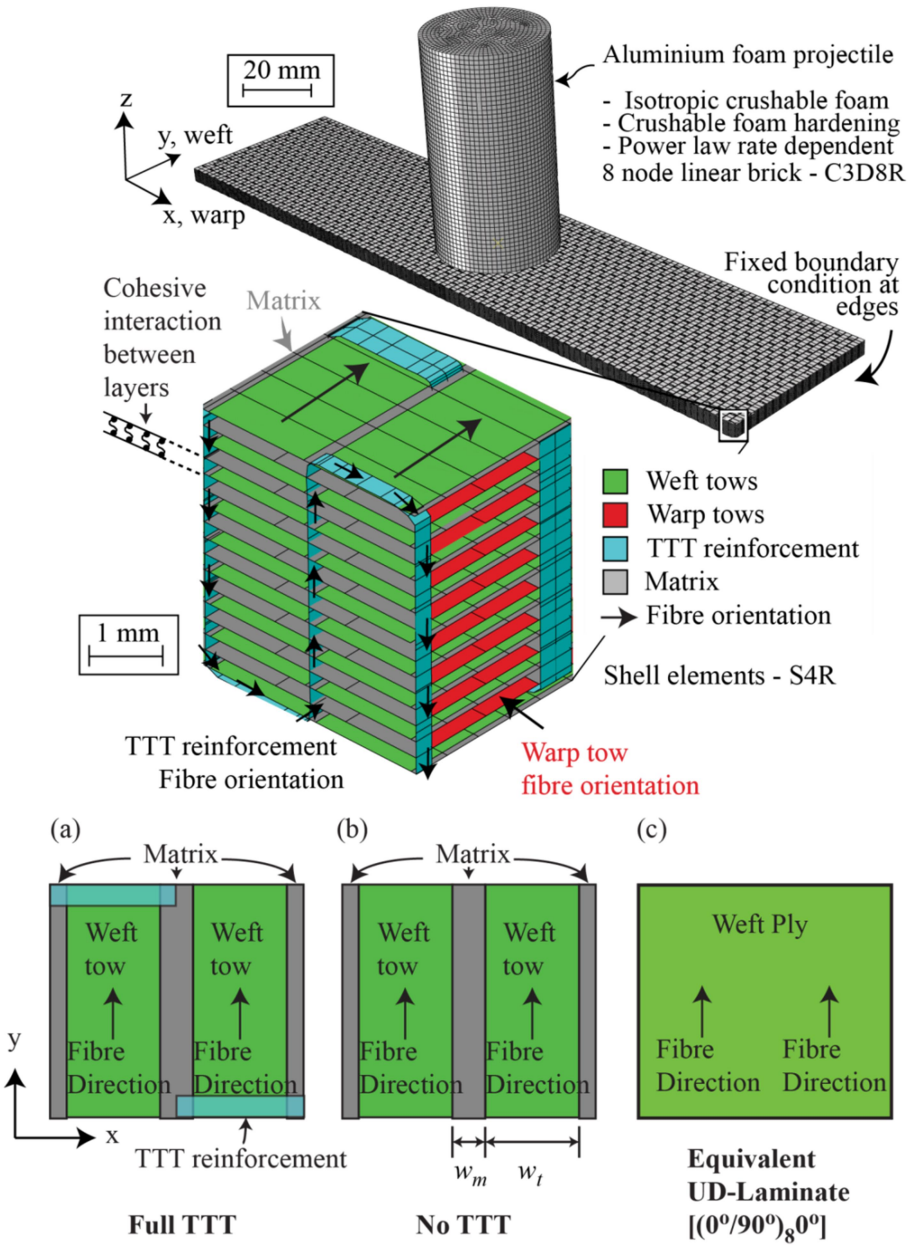


Figure 4.3. Finite element model for the simulation of orthogonal 3D woven carbon composites undergoing soft impact. Arrows indicate direction of fibre orientation. Sketches of top layers for (a) Full TTT (b) No TTT and (c) Equivalent UD-Laminate models are also shown.

4.4.2 Soft impact FE constitutive model

In order to simulate the response of composite material under soft impact, the constitutive model of Hashin [165] and Matzenmiller, Lubliner [178] were employed to model the behaviours of in-plane tows, the TTT reinforcement, and the inter-tow matrix elements. Exclusive of rate-dependency, the constitutive models employed for the composite material and cohesive interaction were identical to that of the quasi-static FE model presented in Chapter 3 and will not be repeated here.

4.4.3 Rate dependency of tow and matrix material

Numerous studies have demonstrated the role of the strain-rate dependent behaviour of 3D woven carbon fibre reinforced composites [72, 235]. Preliminary simulations of soft impact events indicated that without the inclusion of rate dependency within the composite material, the predictions of the onset and propagation of damage were inaccurate. In order to simulate rate dependency within the materials, a viscous regularisation scheme is employed for in-plane tows, TTT reinforcement, and matrix material. A viscosity coefficient η, following Duvaunt and Lions [263], is introduced to further update each of the four previously-defined damage variables (d_f^t, d_f^c, d_m^t and d_m^c). The viscous damage variables are defined as;

$$\dot{d}_i^v = \frac{1}{\eta_t}\left(d_i - d_i^v\right) \tag{4.1}$$

where η_t represents the relaxation time of the system, with d_i is the previously defined inviscid damage variable, with i denoting one of the four damage modes (I through IV for d_f^t, d_f^c, d_m^t and d_m^c, respectively). The term d_i^v is used to compute the damaged stiffness matrix and is updated by;

$$d_i^v\Big|_{t_0+\Delta t} = \frac{\Delta t}{\eta + \Delta t} d_i\Big|_{t_0+\Delta t} + \frac{\eta}{\eta + \Delta t} d_i^v\Big|_{t_0} \tag{4.2}$$

This effectively slows down the rate of damage evolution, with an increasing rate of deformation leading to increasing fracture energies. A numerical calibration study led to the value $\eta = 5$ μs . It was assumed to be identical for tension and compression for both longitudinal and transverse damage modes. The calibrated value corresponds well with previously calibrated values of η for carbon fibre reinforced epoxy materials, as presented in Russell, Liu [156].

4.4.4 Constitutive model for the metal foam projectile

The compressive continuum constitutive model for metal foams developed by Deshpande and Fleck [264] was used to model the Alporas aluminium foam projectiles. The von Mises effective stress, defined as

$$\sigma_e \equiv \sqrt{3 s_{ij} s_{ij} / 2} \tag{4.3}$$

with s_{ij} as the usual deviatoric stress. The yield surface for the metal foam is isotropic and follows the yield function ϕ by

$$\phi \equiv \hat{\sigma} - Y \leq 0 \tag{4.4}$$

where the equivalent stress $\hat{\sigma}$ is given by

$$\hat{\sigma}^2 \equiv \frac{1}{[1+(\alpha/3)^2]} \left[\sigma_e^2 + \alpha^2 \sigma_m^2\right] \tag{4.5}$$

where the mean stress, $\sigma_m \equiv \sigma_{kk}/3$, and the ratio of deviatoric strength to hydrostatic strength, α, define the shape of the yield surface. The right hand side of the equation is chosen so that $\hat{\sigma}$ denotes the stress experienced in a uniaxial tension or compression test. The shape factor, α, can be computed using the relation

$$\alpha = \frac{3k}{\sqrt{9-k^2}} \text{ with } k = \frac{\sigma_c^0}{\sigma_{kk,c}^0} \tag{4.6}$$

where σ_c^0 is the initial yield stress in uniaxial compression, and $\sigma_{kk,c}^0$ is the initial yield stress in hydrostatic compression.

Equations (4.3) and (4.4) describe an elliptical yield surface in (σ_m, σ_e) space. Y is equal to the uniaxial strength in tension and compression, and the hydrostatic yield strength equal to

$$\sigma_{kk} = \frac{\sqrt{1+(\alpha/3)^2}}{\alpha} Y \tag{4.7}$$

The plastic Poisson's ratio υ_p in a uniaxial compression test has the predicted dependence upon α

$$\upsilon_p = -\frac{\dot{\varepsilon}_{11}^p}{\dot{\varepsilon}_{33}^p} = \frac{(1/2)-(\alpha/3)^2}{1+(\alpha/3)^2} \tag{4.8}$$

Consistent with the quasi-static behaviour of the Alporas aluminium foam, the plastic Poisson's ratio $\upsilon_p = 0$, which sets the shape factor, $\alpha = 3/\sqrt{2}$. Following results from uniaxial compressive tests on the aluminium foam material, presented in Figure 4.1, the uniaxial yield stress, σ_c, versus the true uniaxial plastic strain relationship is approximated by

$$\sigma_c = \begin{Bmatrix} \sigma_{pl} & \hat{\varepsilon}^P \le \varepsilon_D \\ \infty & \text{otherwise} \end{Bmatrix} \tag{4.9}$$

with the plateau strength of the foam σ_{pl} = 2.2 MPa and the true densification strain ε_D = 1.6. Characterisation of shock wave propagation through a metallic foam is presented by Radford, Deshpande [147]. A large stress jump is seen across the shock front during progressive densification of the foam, with the width of the shock front being of the order of the cell size of the material, $w_s \approx 5$ mm.

Typical length of element during finite element calculations for the metallic foam was 1.5 mm; sufficiently small enough to resolve the stress gradient.

Bulk viscosity is a critical term when modelling the propagation of shock waves within compressible materials, such as the aluminium foam. By default, ABAQUS includes a small amount of bulk viscosity in order to improve the modelling of high-speed dynamic events by damping out oscillations within a shockwave. A default linear damping coefficient of 0.06 and quadratic damping coefficient of 1.2 were included within the simulations. The quadratic term is included in order to smear a shock wave over several elements. The width of the shock front of the aluminium foam material can be approximated by the cell size of the material, i.e. 5 mm, and comparing that with the element size of 1.5 mm, a small amount of shockwave smearing is considered reasonable.

4.4.5 Matrix material

The isotropic matrix material is characterised by six parameters i.e. Young's modulus E_m, shear modulus $\hat{G}_{12}$, Poisson's ratio $\hat{\nu}_{12}$, normal strength σ_m, shear strength τ_m, and fracture energy J_m. The Young's modulus was obtained from manufacturer's data of cured epoxy matrix $E_m = 3.5$ GPa. The matrix Poisson's ratio, $\hat{\nu}_{12}$, and shear modulus $\hat{G}_{12}$,were also taken from the manufacturer's data of cured epoxy matrix, as 0.3 and 2 GPa, respectively. Longitudinal and transverse strengths were identical and estimated from matrix dominated ±45º tension coupon tests as $\sigma_m = 80$ MPa. The shear strength was estimated to be half that of the normal strength $\tau_m = 40$ MPa. The transverse and longitudinal tensile and compressive fracture energies were identical to each other and estimated from matrix dominated ±45º tension coupon tests as $J_m = 650$ J m^{-2}. The density of matrix was taken from manufacturer's data for cured epoxy resin, i.e. $\rho_m = 1.144$ g/cm^3.

4.4.6 Equivalent UD-laminate material

It is difficult to find a UD-laminate that is equivalent to a 3D woven material for experimental testing due to variations in material properties or geometry [99]. By employing the rule of mixtures to the tow and matrix properties of a 3D woven composite within an FE model, it is possible to create an equivalent UD-laminate material. The following material properties for the warp and weft tows within the 3D woven material model are mapped into their corresponding values of an equivalent UD-laminate model, i.e. longitudinal Young's modulus $\widetilde{E}_1$, in-plane shear modulus $\widetilde{G}_{12}$, longitudinal tensile strength $\widetilde{X}^T$, longitudinal compressive strength $\widetilde{X}^C$, longitudinal tensile fracture energy, $\widetilde{J}_1^t$, longitudinal compressive fracture energy $\widetilde{J}_1^c$, and density ρ^{UD}. Let the volume fraction of a tow within a warp or weft layer follow;

$$V_t^{UD} = w_t /(w_t + w_m) \tag{4.10}$$

where w_t denotes width of tow and w_m denotes width of inter-tow matrix channel, as shown in Figure 4.3. Using the previously calculated values of tow Young's modulus and strength, the effective laminate properties are estimated as

$$\widetilde{E}_1 = V_t^{UD}\overline{E}_1 + (1-V_t^{UD})E_m \tag{4.11}$$

$$\widetilde{G}_{12} = \frac{\overline{G}_{12}G_m}{V_t^{UD}G_m + \left(1-V_t^{UD}\right)\overline{G}_{12}} \tag{4.12}$$

$$\widetilde{X}^T = V_t^{UD}\overline{X}^T + \left(1-V_t^{UD}\right)X_m \tag{4.13}$$

$$\widetilde{X}^C = V_t^{UD}\overline{X}^C + \left(1-V_t^{UD}\right)X_m \tag{4.14}$$

$$\widetilde{J}_1^t = 0.5 \times \frac{l_e(\widetilde{X}^T)^2}{\widetilde{E}_1} \times 1.2 \tag{4.15}$$

$$\widetilde{J}_1^c = 0.5 \times \frac{l_e(\widetilde{X}^C)^2}{\widetilde{E}_1} \times 1.2 \tag{4.16}$$

$$\rho^{UD} = V_t^{UD}\rho^{tow} + (1 - V_t^{UD})\rho_m \tag{4.17}$$

with E_m as the Young's modulus of cured epoxy resin. The modified Equivalent UD-laminate properties are presented in

Table 4.1. A sketch of the top surface of the Equivalent UD-laminate material is presented in Figure 4.3(c).

Table 4.1. Equivalent UD-laminate properties (modified values)

Orientation	**Warp**	**Weft**
Density (kg m^{-3})	1525	1530
$\widetilde{E}_1$ (GPa)	122.2	126.4
$\widetilde{G}_{12}$ (GPa)	5.78	4.93
$\widetilde{X}^T$ (MPa)	1590	1590
$\widetilde{X}^C$ (MPa)	1280	1040
$\widetilde{J}_1^t$ (MPa)	12.41	12.00
$\widetilde{J}_1^c$ (MPa)	8.04	5.13

4.5 Results and discussion

A summary of the results from the experimental testing, supplemented with finite element analysis will now be presented. Focus is given to the transient back-face deflection of beams during impact events, the damage mechanisms exhibited, and the role of the through-the-thickness reinforcement. The back-face deflection is a key component of analysis of the response of materials, as protective systems undergoing too great a deflection during impact can result in serious physical harm to vehicle occupants. The back-face deflection of a beam undergoing soft impact is likely to be a combination of the beams elastic stretching response and a function of the damage sustained by the beam.

4.5.1 Transient deflection of beams

Soft impact experiments and FE modelling were conducted on the Full and Half TTT 3D woven composite panels orientated along the x-direction (warp) and y-direction (weft). Due to the lower fibre volume fraction in the warp direction, in comparison to the weft, the warp direction is shown to be unfavourable for resisting the loading. Figure 4.4 presents the measured and FE predicted normalised back-face deflections $\hat{\delta}$ of Full TTT composite beams orientated along the y-direction (weft) as a function of normalised time after moment of impact $\hat{t}$ for impulsive loading of (a) $I_0 = 2.48$ kPa s, (b) $I_0 = 2.64$ kPa s, (c) $I_0 = 3.33$ kPa s, and (d) $I_0 = 4.03$ kPa s. Also presented are FE predictions of the response of Full TTT material, No TTT material and Equivalent UD-laminate material. In order to characterise the response of the composite beams during impact, the time parameter normalised against the crush time of the projectile is used, i.e. $\hat{t} \equiv t\, v_0 / l_p$ with t as time after contact between projectile and beam, v_0 as projectile velocity, and l_p as length of projectile. In order to remain dimensionless, a normalised deflection term $\hat{\delta} \equiv \delta / l_0$ is also used with δ as the back-face deflection of the beam at centre-span and l_0 as the free length of the beam sample. The peak back-face deflection experienced by the beam during the impact event occurs at a normalised time of approximately between $\hat{t} = 1 - 1.5$. $\hat{t} = 1$ corresponds to the time at which projectile densification has completed.

FE predictions over the entire range of experimentally tested impulses show reasonable fidelity in regards to the peak back-face deflection exhibited by the beam during the test. The FE model also predicts the time at which the peak deflection occurs during the test. The restitution of the beam occurs later than the prediction, due to oscillations within the clamp during the experiment increasing the time taken for reflection of the bending wave. However, the peak deflection of the beams occurred before the oscillations within the clamp, and therefore had no influence from them. Figure 4.5(a) and (b) present recorded and predicted

montages of the deformation of a Full TTT 3D woven beam orientated along the y-direction (weft) undergoing an impact event of $I_0 = 2.64$ kPa s, respectively. The corresponding locations A-E match with the positions highlighted in Figure 4.4(b). The FE prediction is shown to model accurately the deformed configuration of the beam, and the crushing of the metal foam material. For a projectile impact of impulse $I_0 = 4.03$ kPa s upon Full TTT beams orientated along the weft direction, the FE model predicts the in-plane weft yarns to be experiencing strain rates in the order $100s^{-1}$ during the initial propagation of the tensile stress wave. It is suggested, with reference to Section 4.4.4, that a more detailed study with regards to the linear and quadratic bulk viscosity coefficients employed within the numerical calculations could lead to great fidelity of model. In regards to the experimental methodology, material variability and imperfect sample clamping conditions may well also influence the fidelity of simulations. No studies regarding the boundary conditions of the FE model are presented here, but suggested as potential regions of interest for future researchers.

The FE predicted back-face deflection against time response during a soft impact event for beams orientated along the y-direction (weft) of the 3D woven composite material is compared to an equivalent UD-laminate material in Figure 4.4. The Equivalent UD-laminate material exhibits the same predicted back-face deflection during the soft impact event as the Full TTT material and the No TTT-reinforcement material. This result indicates that neither the TTT reinforcement nor the beam in-plane fibre architecture have influence on the back-face deflection of composite beams undergoing soft-impact within the range of impulses tested in this study. The small-scale local increases in the back-face deflection demonstrated by the UD-laminate, shown in Figure 4.4, is attributed to delamination damage allowing relative displacement of the bottom layer due to the transferral of momentum. The Equivalent UD-laminate material was also predicted to exhibit a similar amount of delamination damage as the No TTT reinforcement material.

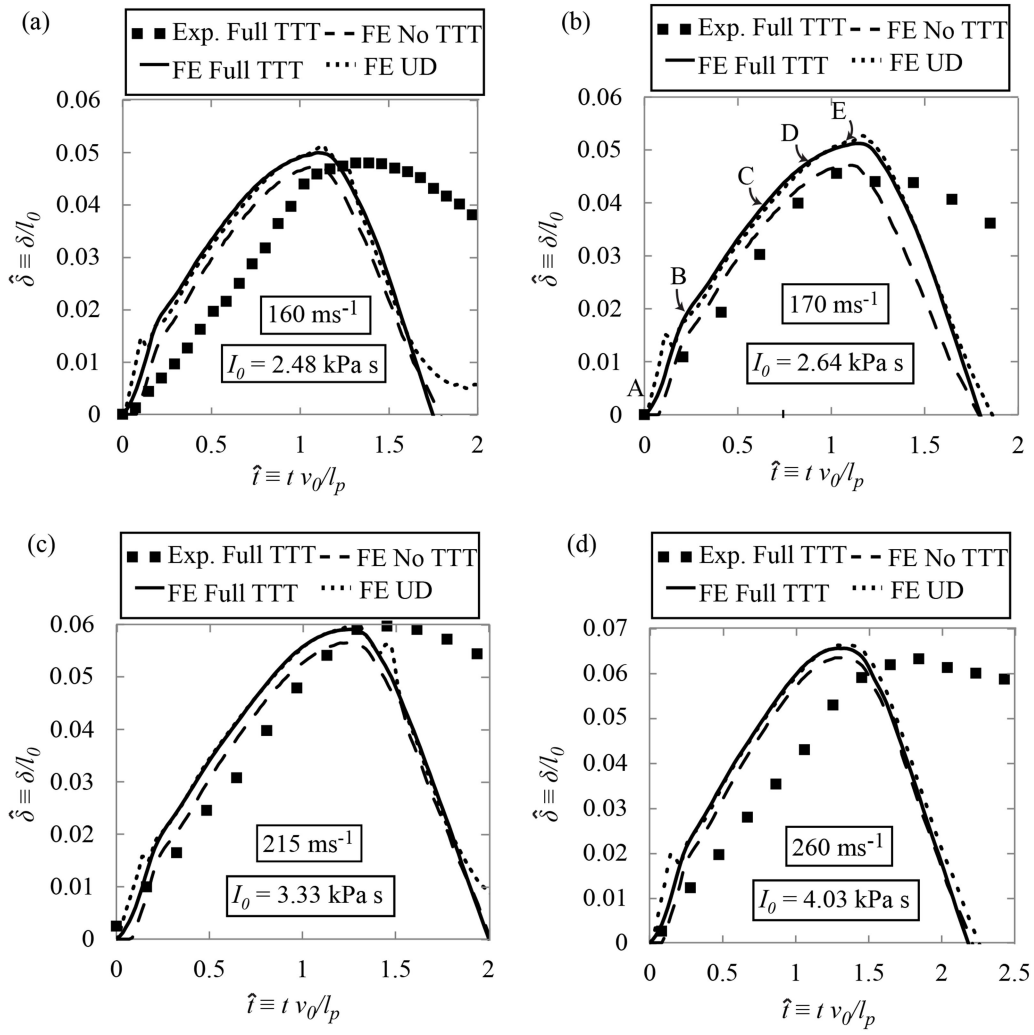


Figure 4.4. Comparison of experimental results for Full TTT material and FE prediction for normalised back-face deflection $\hat{\delta} \equiv \delta / l_0$ as a function of normalised time $\hat{t} \equiv t\, v_0 / l_p$. Full TTT beams orientated along the y-direction (weft). Three different case studies for numerical modelling results are presented; Full TTT reinforcement, No TTT, and an Equivalent UD-laminate material. Projectile impulses I_0 were (a) 2.5 kPa s, (b) 2.6 kPa s, (c) 3.3 kPa s, and (d) 4.0 kPa s. Points A-E corresponds to the montage images presented in Figure 4.5.

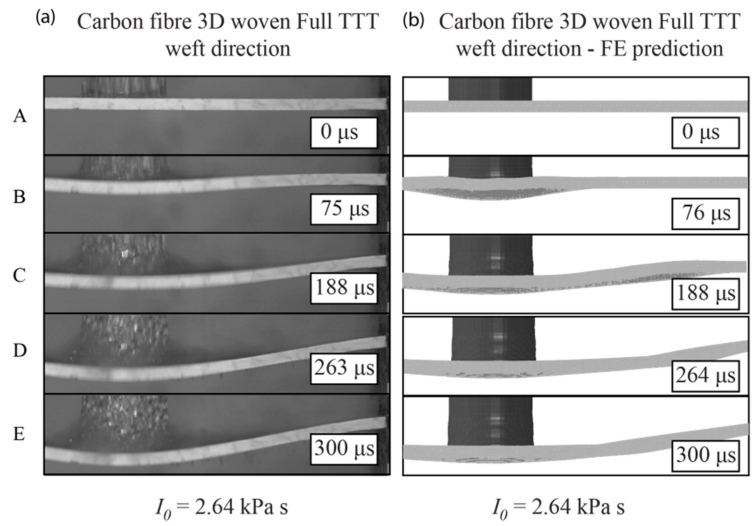


Figure 4.5. Deformation montage of 3D orthogonal woven carbon-fibre composites under soft impact of impulse $I_0 = 2.64$ kPa s beams orientated along the y-direction (weft) (a) Experiment (b) Finite element prediction. Points A-E refer to the corresponding positions on Figure 4.4(b).

4.5.2 Effect of Through-the-thickness reinforcement density on back-face deflection

The Full TTT and Half TTT materials have a small variation in material areal density; 5.30 kg m^{-2} and 5.21 kg m^{-2}, respectively. Therefore, to make a comparison of the response of the samples during a soft impact event, a non-dimensional group is used. A non-dimensional group suggested by Xue and Hutchinson [265] is defined as;

$$\bar{I}_0 = \frac{I_0}{cM} \tag{4.18}$$

Where c is a characteristic wave speed, here taken to be the longitudinal wave speed of the composite material c = 7060 ms^{-1}, and M is the areal mass of the sample. A non-dimensional peak deflection, $\bar{\delta}_{\max}$, is also used, and is defined as;

$$\bar{\delta}_{\max} = \frac{\delta_{\max}}{l_0} \tag{4.19}$$

Where $\delta_{\max}$ is the maximum back-face deflection of the sample experienced during the experiment. Normalised maximum back-face deflection captured by high speed photography during experimental tests of Full and Half TTT material as a function of imposed normalised impulse are plotted in Figure 4.6. It can be seen that in this case there is no significant difference in the maximum back-face deflection between the two materials tested. Also plotted is the normalised impulse at which small scale fibre fracture damage was recorded on the top surface of the beams.

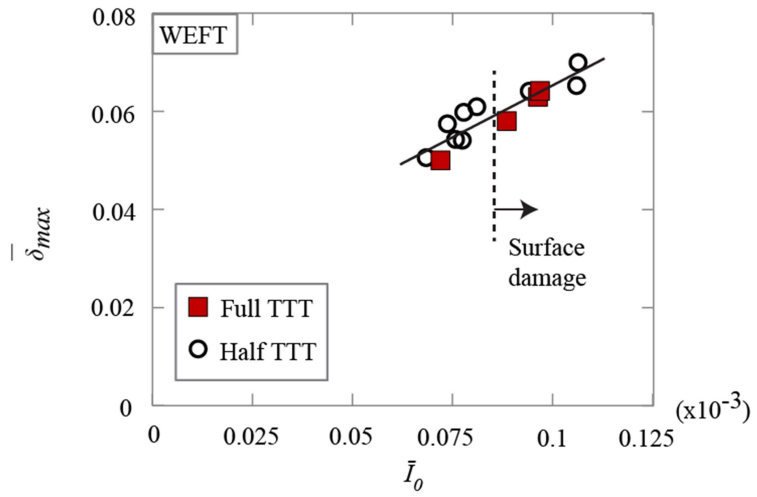


Figure 4.6. Comparison of the normalised maximum back face deflection $\bar{\delta}_{\max}$ during soft impact as a function of normalised impact impulse $\bar{I}_0$ upon 3D woven carbon composites of two different TTT reinforcement densities.

4.5.3 Damage during soft impact

Experimental tests of Half TTT orthogonal 3D woven composite material beams orientated along the x-direction (warp), demonstrated the primary damage mechanism of beams undergoing a soft impact event to be longitudinal fibre fracture occurring at the clamped ends. Beams orientated along the x-direction

(warp) had a lower volume fraction than those orientated along the y-direction (weft), and therefore, were shown to have a reduced ability of resisting soft impact loading. FE simulations of beams orientated along the x-direction (warp) were also undertaken for two impulses; 2.95 kPa s, in which no catastrophic damage occurred, and 4.19 kPa s, in which the beam failed. The normalised experimentally recorded and predicted back-face deflection $\hat{\delta}$ against normalised time $\hat{t}$ after impact of two velocities of projectile for beams orientated along the x-direction (warp) are presented in Figure 4.7. Excellent fidelity is shown for the higher velocity, with an accurate prediction of both the back-face deflection against time and moment of catastrophic fibre fracture within the sample.

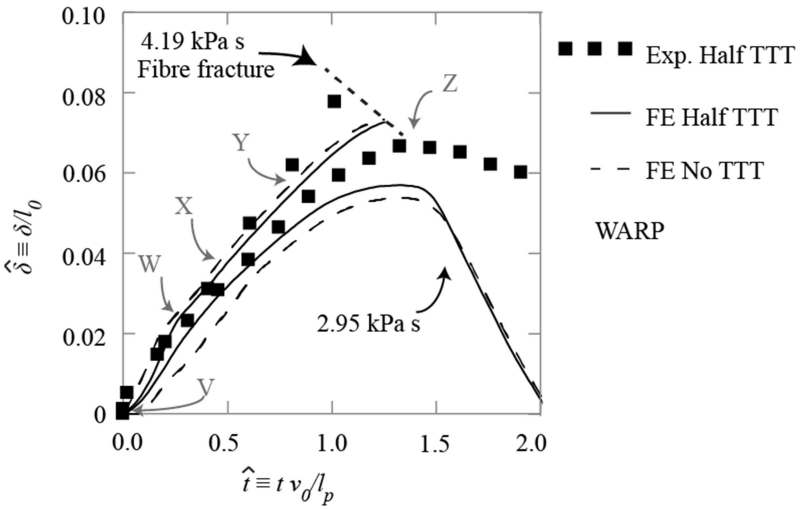


Figure 4.7. Maximum normalised back-face deflection $\hat{\delta} \equiv \delta / 2l_0$ against normalised time after impact $\hat{t} \equiv tv_0 / l_p$. FE simulation and experimental results for beams orientated along the x-direction (warp). The instants V-Z correspond to the montage images presented in Figure 4.8.

To understand the failure mechanism of beams under soft impact, Figure 4.8(a) and (b) presents the experimental montage and numerical prediction of a Half TTT 3D woven material orientated along the x-direction (warp) loaded with impulse $I_0 = 4.19$ kPa s, respectively. The instants V-Z correspond with the

positions highlighted in Figure 4.7. As shown in Figure 4.8(b), the onset of element damage at the gripped ends corresponds to the beginning of the reflection of the bending wave (t = 264 μs). Figure 4.8(c) presents the montage of a similar UD-laminate beam undergoing an impulse $I_0 = 2.90$ kPa s . It allows a comparison of the damage modes between a 3D woven carbon composite of density 5.21 kgm^{-3} and a similar UD laminate [(0º/90º)$_7$ 0º] material of density 5.86 kg m^{-3} presented by Kandan, Russell [157]. The UD laminate beams had a thickness t_b = 3.75 mm, width w = 35 mm, and gauge length l_0 = 200 mm. The UD-laminate had properties of in-plane tensile Young's modulus $E_l = 85$ GPa , tensile strength $\sigma_l^t = 980$ MPa , and compressive strength $\sigma_l^c = 630$ MPa , these are similar values to that of the 3D woven composite material. The UD laminate material exhibited both delamination across the entire length of the beam, and catastrophic longitudinal fibre fracture.

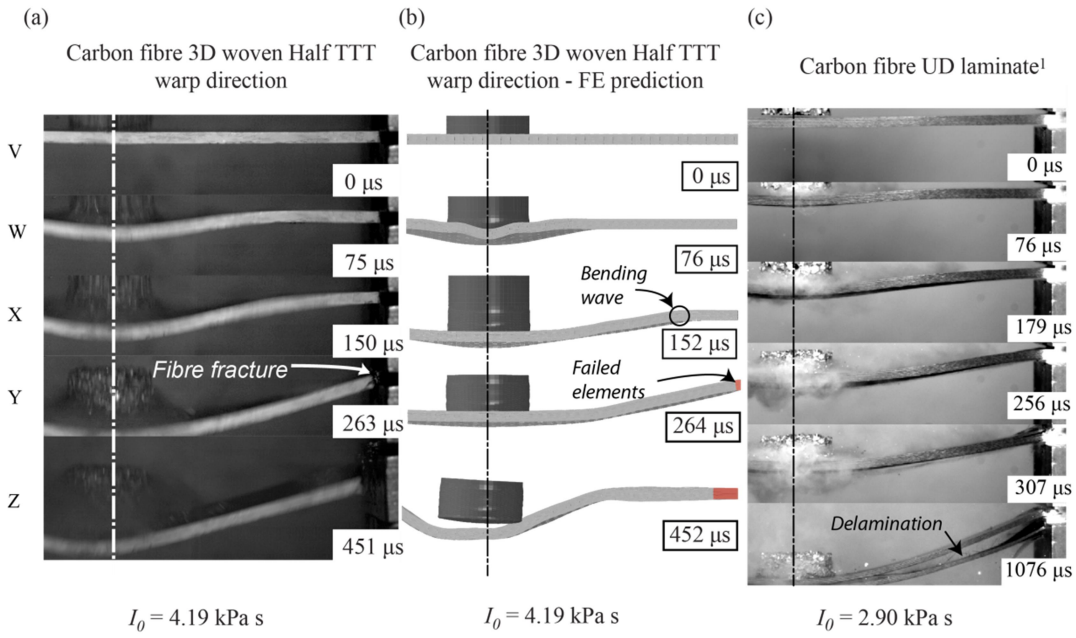


Figure 4.8. Deformation montage of carbon-fibre composites under soft impact testing showing (a) Half TTT 3D orthogonal woven composite beam orientated along the x-direction (warp) $I_0 = 4.19$ kPa s , (b) Finite element prediction of Half TTT 3D orthogonal woven composite beam orientated along the x-direction

(warp) $I_0 = 4.19$ kPa s, and (c) UD-laminate material presented in Kandan, Russell [157]1 $I_0 = 2.90$ kPa s. Points V-Z correspond to the locations noted in Figure 4.7.

Photographic images of 3D woven composite beams orientated along the x-direction (warp) post impact test of impulse $I_0 = 4.19$ kPa s are shown in Figure 4.9. At higher impulses, i.e. $I_0 \approx 4.19$ kPa s, the 3D woven composite material exhibited a catastrophic failure mechanism of longitudinal fibre fracture, occurring at the TTT reinforcement location, at the clamp. Also presented in Figure 4.9 is the numerical prediction of fracture surfaces. The predicted fracture surfaces compare favourably to the experimental results i.e. fracture of in-plane tows at the clamp location, exposing though-the-thickness reinforcement. Examination of both the experimental and predicted fracture surfaces reveals no visible delamination. In contrast, UD-laminate composites has been reported experience delamination at impulses lower than catastrophic beam failure [156]. In contrast, at impulses lower than those which caused catastrophic fibre fracture, the 3D woven material exhibited no delamination, and only minor surface fibre fracture. The difference between the 3D woven material and an equivalent UD-laminate material will be investigated later via numerical modelling in Section 4.7.

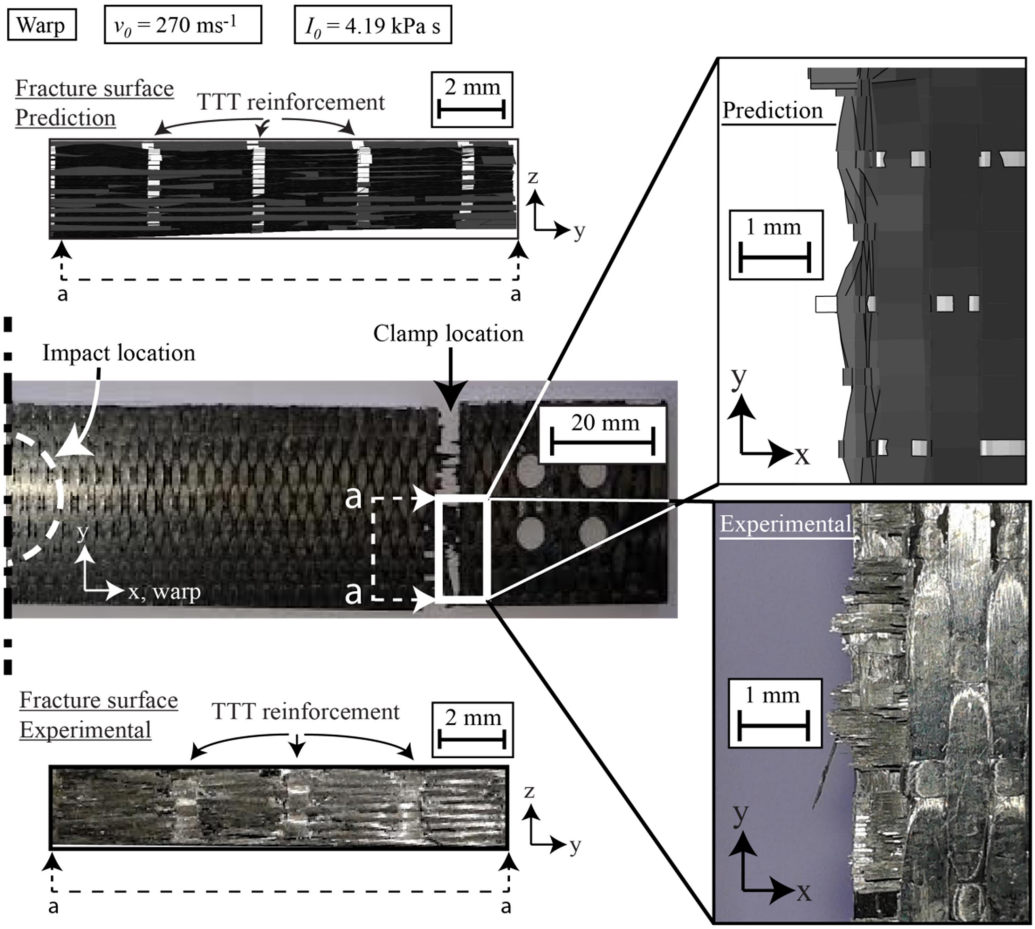


Figure 4.9. Photographic images and FE predictions of damage modes exhibited by Half TTT 3D woven carbon composite undergoing soft impact , tested at $I_0 = 4.19$ kPa s . Beam orientated along the x-direction (warp).

Beams orientated along the y-direction (weft) had a higher volume fraction that those orientated along the x-direction (warp). Even at the highest impulses tested within this study were not high enough to cause fibre fracture of beams orientated along the y-direction (weft). After soft impact of impulse greater than $I_0 \geq 3$ kPa s , damage was observed on the front surface of the sample. This damage consisted of small-scale fibre fractures within longitudinal surface tows. This damage was almost entirely restricted to underneath the projectile impact location. Microscopic images showing the surface damage of a Half TTT beam

orientated along the y-direction (weft) undergoing an impact event $I_0 = 3.33$ kPa s are presented in Figure 4.10(c).

To investigate the difference in damage mechanisms between the Full and Half TTT materials, numerical predictions of Full and Half TTT material beams orientated along the y-direction (weft) impacted at an impulse of $I_0 = 3.33$ kPa s were conducted. Both beams resisted delamination equally well, and there was no significant difference in the tensile damage of fibres. However, there were differences in extent of the compressive damage of surface weft tows between the two materials. Figure 4.10(a) and (b) present the predicted compressive fibre damage initiation on the top surface of beams 800 μs after projectile impact $I_0 = 3.33$ kPa s. A value of 1 indicates the onset of damage. The localised in-plane compressive fibre damage at the centre of the beam corresponds well to the surface damage observed experimentally, and shown in Figure 4.10(c). This damage is more pronounced in the Full TTT material in comparison with the Half TTT material. The damage was observed to be concentrated at the top surface of the beam, and reduced significantly towards the centre of the beam. Any damage of surface weft tows at this location could contribute to the reduction of stiffness during post-impact clamped-clamped beam experiments. It is this location which fracture occurred during post-impact clamp-clamped beam bending tests, presented in the proceeding section.

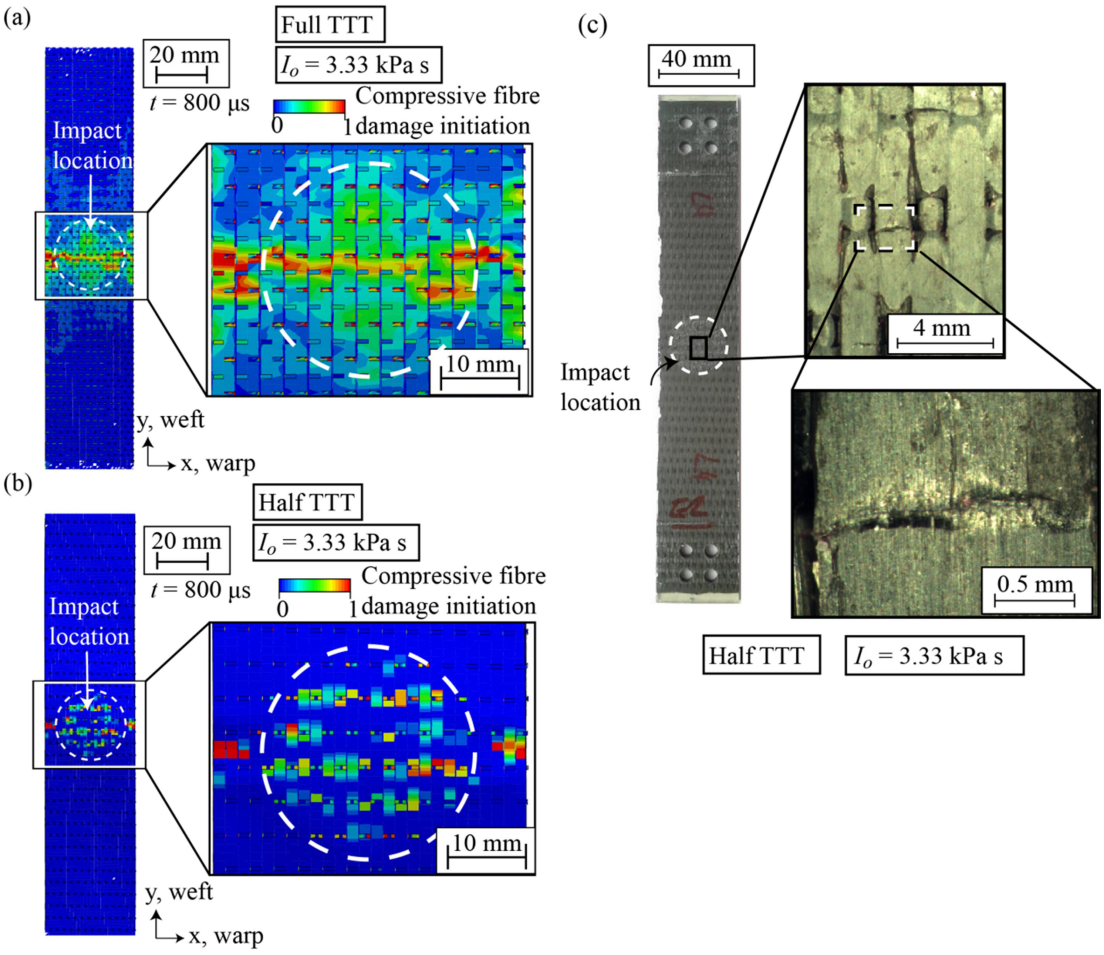


Figure 4.10(a) and (b) Finite element simulations of the predicted compressive damage initiation on the front surface of orthogonal 3D woven composite beams undergoing a soft impact event $I_0 = 3.33$ kPa s for Full TTT and Half TTT material , respectively. Time t is the time after moment of projectile impact upon beam. A value of 1 corresponds to the onset of compressive fibre damage. (c) Optical microscopic images of fibre breakage on the front surface of impact tests of a Half TTT orthogonal 3D woven material after experimental impact of impulse $I_0 = 3.33$ KPa s . Beams orientated along the y-direction (weft).

4.6 Post impact quasi-static bending response

Beams orientated along the y-direction (weft) exhibited only minor visible damage during the soft impact event, even up to the highest impulses tested. However, there still could be internal damage that could reduce the structural capacity of the beam. In order to investigate this, post impact, samples of both TTT reinforcement densities were tested in a quasi-static clamped-clamped beam bending test. Figure 4.11 presents a sketch of the experimental setup for the quasi-static beam bending test. Results of the experiment are compared to that of a virgin sample. The beams were aligned along the y-direction (weft), as co-ordinate system defined in Chapter 2. The beams were fixed at both ends in a custom-designed clamp of stainless steel, with the clamp subsequently fixed onto an I-beam. The spans of the beams between the clamped ends was L_b = 180 mm. This free span length was purposefully chosen to be longer than the original impact test beam length in order to capture damage sustained within the clamp position during soft impact testing. The beams were centrally loaded by a roller across their entire width, w. Width of clamped beam tested in this investigation was w = 40 mm, identical to the width of impact samples. A screw-driven Instron© 5581 test machine with a static 50 kN load cell provided a constant quasi-static displacement of the roller along the vertical axis (z-direction) of 5 mm/min. Roller displacement along the vertical axis, δ_b , and load imposed by the roller , P, was measured directly from the load cell of the testing rig. The stiffness was calculated from between a vertical roller displacement of between 2.5 mm and 7.5 mm, in order to avoid any contributions from initial movement within the clamp.

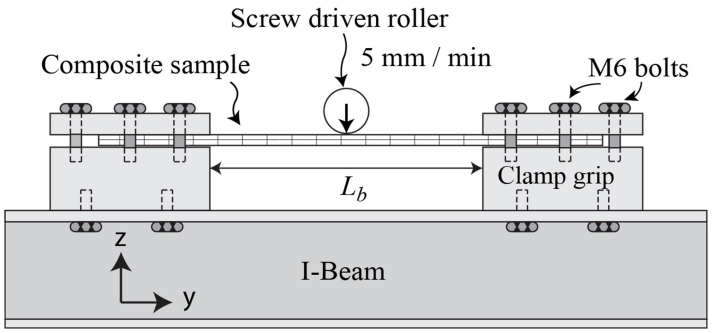


Figure 4.11. Sketch showing the experimental setup of the clamped beam quasi-static bending test.

Figure 4.12 shows the load imposed by the roller, *P*, against vertical roller displacement δp for the clamped beam test for the Full TTT material. Beams are shown to retain structural integrity even after undergoing relatively high-impulse impacts $(I_0 \geq 3.0 \text{ kPa s})$. Beam response was linear elastic up until a displacement $\delta_b \approx 12 \text{ mm}$, when brittle fracture of in-plane reinforcement tows occurred. Beam failure was attributed to fibre fracture at the centre of the samples, directly under the roller position. This position is also the projectile impact location, and location of small-scale fibre damage, presented in the previous section. The location of fibre fracture was the same for impacted and un-impacted beams, indicating that the surface damage at this location was not the root cause for failure at this position. This fracture location differs to that of the UD-laminate material presented in Kandan, Russell [157], which exhibits fibre fracture at the clamp location. Although, due to differing beam geometries in the test, it is not possible to say if the change if fracture position is due to material differences or beam geometry.

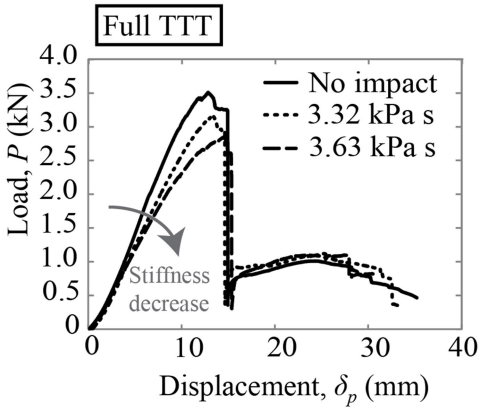


Figure 4.12. Load imposed by the roller P against roller vertical displacement δ_p for post-impact clamped-clamped beam tests for Full TTT material. Beams orientated along y-direction (weft).

The peak load recorded during clamped beam test as a function of impact velocity is presented in Figure 4.13(a). It can be seen that there is no significant reduction in strength of beam for either the Full TTT or Half TTT material even after the highest velocity of impact. The variation shown here is typical as to what is expected due to stochastic flaws within the material. Figure 4.13(b) presents the stiffness of post-impact clamped-clamped beam experiment as a function of impact velocity. There is a slight reduction in stiffness during post-impact testing, with stiffness reducing linearly with increasing impact velocity. The reduction in stiffness is seen to be greater with the Full TTT binder material relative to the Half TTT binder material. It is suggested that this is due to more highly constrained in-plane fibres in the Full TTT material undergoing more damage during impact testing. FE simulations presented in Section 4.5.3 confirm that higher TTT reinforcement density can lead to increased damage in the material.

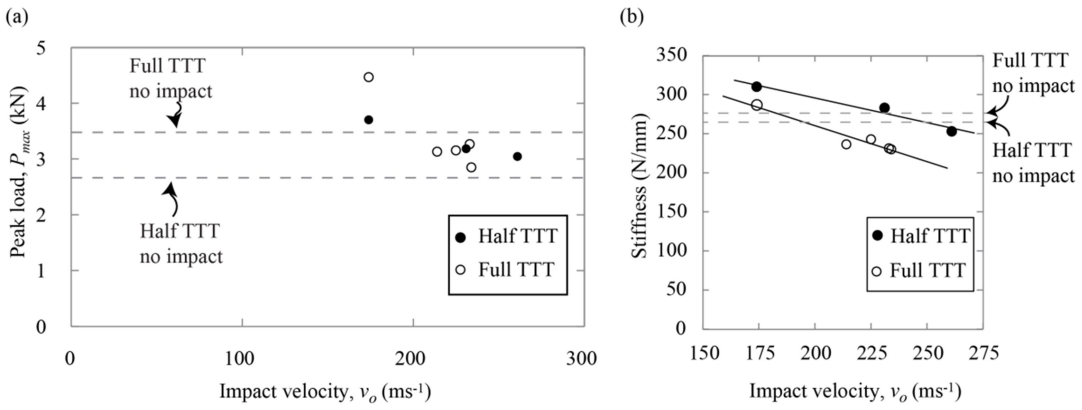


Figure 4.13 (a) Summary of the peak load during post-impact clamped beam testing verses the velocity of impact v_0. (b) Stiffness of post-impact clamped beam testing versus the velocity of impact, v_0.

4.7 The role of the TTT reinforcement

As demonstrated in Figure 4.4, the presence of the binder has no contribution to the back-face deflection of the beams. However, the following section will show that there is a remarkable difference in the delamination damage sustained within the composite material. To investigate this, numerical modelling of Full and No TTT material beam along the y-direction (weft), was undertaken. Predicted cohesive interaction damage contours within the beam at time t = 700 μs after the moment of impact show that the TTT reinforcement is extremely effective at reducing delamination damage sustained. This is shown in Figure 4.14(a) and (b), where a comparison is made with and without the presence of the binder, respectively. The contour shown in Figure 4.14 presents the cohesive interaction damage variable, $\hbar$, which at a value of 1 represents fully damaged interaction between layers. Without the presence of the TTT reinforcement, the delamination damage propagates along the entire length of the beam. However, with the presence of the TTT reinforcement, damage is notably reduced, being almost entirely restricted in location to directly under the projectile. This compares favourably with the experimental results, where no visible delamination was noted, even up to impulses which induce catastrophic longitudinal fibre fracture.

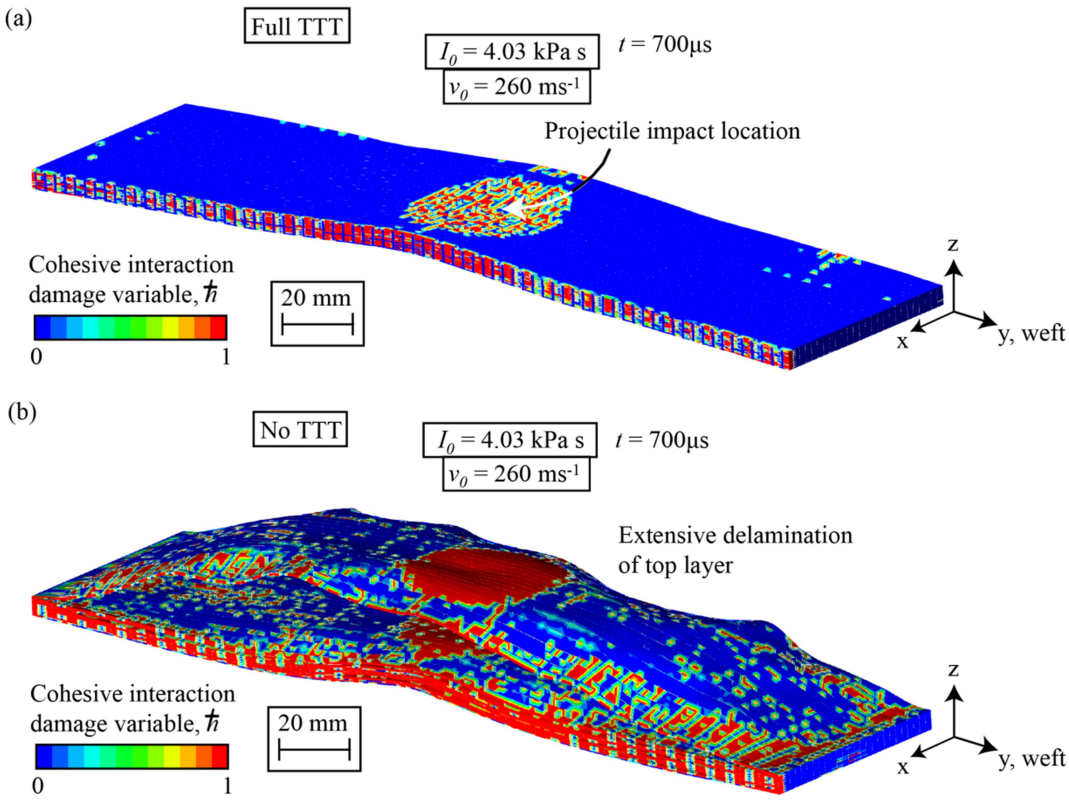


Figure 4.14. Finite element predicted deformation of an orthogonal 3D woven carbon composite undergoing a soft impact event $I_0 = 4.03$ kPa s showing (a) Full TTT and (b) No TTT model. Contour plot shows damage variable of cohesive interaction, $\hbar$, demonstrating locations of delamination within the beam. A value of $\hbar = 1$ indicates fully delaminated regions. $t = 0$ corresponds to the moment of projectile impact on the sample. Beams orientated along the y-direction (weft).

In order to further investigate the role of the through-the-thickness, simulations of soft impact events were undertaken with the cohesive interaction between layers removed. This removal of the cohesive interaction effectively simulates a fully pre-delaminated case. Inter-penetration between layers was now prevented via a penalty contact algorithm. Through this method, it is possible to simulate the material under severe conditions. It can be seen from Figure 4.15 that even with the cohesive interaction removed, the TTT reinforcement provides structural

integrity to the beam, retaining its cross section throughout the test. This is juxtaposed by the predictions with both the TTT-reinforcement and cohesive interaction removed, where extensive delaminations are shown throughout the entire length of the beam. A transferal of momentum through the beam causes a large relative displacement of the top and bottom layers of the composite. Also presented are simulations for the case of Half TTT material and the equivalent UD-laminate material. The Half TTT material exhibits a response identical to that of the Full TTT material, indicating that, in regards to the material in this study, halving the TTT reinforcement density provides no reduction in structural integrity. The Equivalent UD-laminate material behaves identically to that of the No TTT material; indicating again that in-plane reinforcement topology provides negligible influence on beam structural integrity during impulsive loading. The results presented in Figure 4.15 gives indications of the superior performance of the 3D woven beams undergoing multi-hit soft impact. For example, a UD-laminate beam which had previously been undergone a soft impact event would perform far less favourably compared to a 3D woven composite.

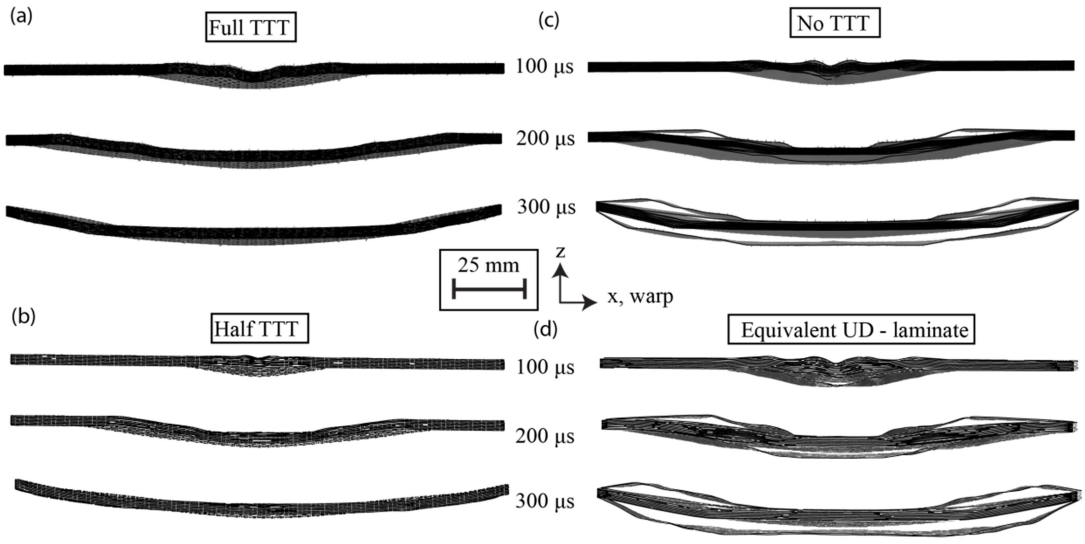


Figure 4.15. Montage of finite element simulations of a soft impact event of impulse $I_0 = 2.96$ kPa s with cohesive contact removed on (a) Full TTT orthogonal 3D woven composite (b) Half TTT orthogonal 3D woven composite

(c) 3D woven composite with TTT-reinforcement removed, and (d) Equivalent UD-laminate material. $t = 0$ corresponds to the moment of projectile impact upon the beam. Beams orientated along the x-direction (warp).

4.8 Concluding Remarks

An experimental and numerical investigation was undertaken on the dynamic soft impact response of two orthogonal 3D woven composite materials varying only by density of though-the-thickness (TTT) reinforcement. 3D woven composites demonstrated remarkably reduced delamination damage during soft impact events in comparison with UD-laminate material. The failure mechanism of 3D woven composite beams was longitudinal fibre fracture at the clamped ends. At impulses lower than those which caused catastrophic fibre fracture, only minor, localised fibre fracture on the surface of beams was recorded. The two different densities of through-thickness reinforcement experimentally tested within the study had no difference in the back-face deflection experienced during soft impact. This was confirmed with the use of a finite element modelling strategy which explicitly models the geometry of the through-the-thickness reinforcement. FE modelling also showed that an equivalent UD laminate material will have the same maximum back-face deflection as a 3D woven material during a soft impact event, indicating that the in-plane architecture has no influence on the transient deflection of beams. However, modelling of an equivalent UD-laminate material did reveal greatly increased delamination damage sustained than that of the 3D woven material.

The 3D woven composite beams were shown to retain structural integrity even during high-impulse soft impact tests, with no delamination up to final fibre fracture. In order to investigate potential internal damage within the beam, clamped beam bending tests were conducted post-impact. These tests reveal negligible variations in strength and only minor reductions in beam stiffness after soft impact for 3D woven material. This indicates the potential for 3D woven composites to perform well during resistance of multiple soft impacts. The

stiffness reduction post-impact was seen to be greater with the composite containing a higher density of though-thickness reinforcement. Finite element simulations of soft impact on 3D woven composites of two different reinforcement densities indicated varying compressive fibre damage on the front surface of the beams; demonstrating the potential for increased damage with higher densities of TTT-reinforcement. Finite element predictions of pre-delaminated beams undergoing soft impact demonstrated significant structural enhancement provided by the TTT-reinforcement.

CHAPTER 5

BALLISTIC IMPACT OF 3D WOVEN COMPOSITES: BEAMS AND CIRCULAR PLATES

Summary

The preceding chapter explored the damage mitigation properties of 3D woven composites under soft impact loading. This chapter utilises the "homogenised" finite element modelling strategy developed and validated for soft impact events in Chapter 4 to characterise the singular and multi-hit ballistic impact response of fibre reinforced composite materials. An experimental and numerical investigation is first undertaken into the ballistic impact response of 3D woven composite clamped rectangular beam samples. The numerical modelling strategy is validated against experimental results, and applied to an investigation into the singular and multi-hit ballistic impact response of clamped circular plates with and without TTT reinforcement. Plate deformed configurations, stress distributions, and damage mechanisms are discussed. The study is supplemented with a numerical parameter study on the influence of the inter-laminar shear strength of laminate composites on the ballistic limit of circular clamped plates.

Ballistic impact experimental tests on clamped rectangular beam samples were undertaken in order to determine the damage mechanisms within the 3D woven composite material and for validation of the FE modelling technique. Clamped rectangular beam samples were chosen in order to record to the back-face deflection of samples throughout the impact event. The experimental study revealed three distinct categories of beam response: (i) low velocity impacts ($v_0 \leq 105\,\mathrm{ms}^{-1}$) which demonstrated projectile rebound, with increasing matrix cracking and localised fibre fracture, (ii) medium velocity impact ($110\,\mathrm{ms}^{-1} \leq v_0 \leq 140\,\mathrm{ms}^{-1}$) which exhibited a stretch-deformation dominated

failure mechanism, i.e. “ripping” through the width of the beam at the centre of the sample due to longitudinal fibre fracture, and (iii) higher velocity impacts ($v_0 \geq 145\,\mathrm{ms}^{-1}$) which demonstrated projectile penetration, combined with longitudinal fibre fracture at the centre of the sample. Here, the term “beam failure” is described as either fibre fracture across the entire width of the beam sample, or projectile penetration. The finite element model was shown to have sufficient fidelity in order to capture the characteristic damage modes of the three response types. For multi-hit numerical simulations of laminate composites, the finite element model was further validated by a comparison of the multi-hit ballistic limit surface and of the damage modes exhibited during clamped circular plate ballistic impact experiments as presented by Kandan, Russell [162] and Kandan, Russell [266].

The 3D woven material was predicted to have a higher concentration of damage under the projectile strike position during ballistic impact loading of clamped circular plates. This is in keeping with the general consensus within the literature for a reduction in the size of damage area due to impact loading with the presence of TTT reinforcement [267]. The enhanced structural integrity of the plate due to the TTT reinforcement was predicted to supress the development of damage remote from the projectile strike location, and to reduce bending deformation within the plate. This led to an 8% increase in the predicted ballistic limit inclusive of TTT reinforcement for a singular impact event. The TTT reinforcement was predicted to improve the multi-hit impact performance of composite plates for multi-hit impacts of relatively high primary impact velocity, i.e. the initial impact being above 60% of the ballistic limit of the plate. Here, the ballistic limit is defined as the velocity at which the predicted plate response changes from projectile rebound to projectile penetration.

A parameter study was conducted to investigate the influence of the inter-laminar shear strength of 0/90° laminate composites on the predicted ballistic limit of circular clamped plates. An increase of the inter-laminar shear strength led to a

reduction in area of the delamination damage within the plate, and a reduction in the predicted ballistic limit of plates. The numerical calculations were used to trace this reduction in ballistic limit to a modification of the deformation configuration of the plate, and ultimately, leading to less favourable damage modes. The response of higher inter-laminar shear strength plates were predicted to be dominated by that of bending deformation, with stress concentrations at the top and bottom of the plate through the thickness causing an increase in the total damage sustained. This subsequently acted to reduce the predicted ballistic limit of the plates. Laminates with lower inter-laminar shear strength, or no interaction between layers, was predicted to be primarily governed by stretch deformation, causing a rise in ballistic limit by approximately 45% for plates simulated with no inter-laminar interaction. This study improves the understanding of the influence of inter-laminar properties on the ballistic response of fibre reinforced composite materials, providing mechanistic interpretations of the phenomena demonstrated.

5.1 Introduction

The high specific stiffness and strength of fibre reinforced composite materials, combined with their low coefficient of thermal expansion, are excellent incentives for their use within protective systems for highly mobile vehicles. The dynamic impact of debris upon aircraft systems is of great concern and is often a critical load case for design engineers to consider. Common sources of impact events for aeronautical structures include hail stones, bird strikes, and runway debris. The first two of these impact systems are classified as soft body impact, the third is that of solid projectiles. During take-off and landing, aircrafts can receive impact events from runway debris at velocities up to approximately 250 ms^{-1} [268-271]. These impacts can cause damage to the fibre reinforcement, the matrix material and can introduce delamination damage within laminate composites.

A numerical study undertaken by Ghosh and De [261] identified how orthogonal through-thickness reinforcement can influence the ballistic response of a composite plate. They gave a detailed account of how the TTT-reinforcement can

modify the local response of the composite material, demonstrating numerical predictions of the propagation of damage within the fibre and the matrix. They demonstrate increased propagation of damage along the direction of TTT reinforcement. However, the damage and stress wave propagation within the material was only studied in detail for the initial stages of the impact event and only at the location within the immediate vicinity of the projectile strike position. The work presented here attempts to build upon studies such as this to characterise the global structural response of the plates, focusing on projectile velocities close to the ballistic limit of the composite plates. By explicitly modelling the geometry of the TTT reinforcement, and by modelling the entire sample during the impact event, it is possible to investigate the contribution in which it plays during ballistic impact loading.

Rarely is the design of protective systems adequate for a singular impact event. For example, upon inspection of the reinforced carbon-carbon composite plates for a single flight mission of the spaceship Discovery, a total of 176 different impact damage sites were recorded [272]. Even though the ability for structures to protect against multiple impacts is integral in the design of protective systems, the current literature generally shies away from such investigations. One difficulty in conducting multi-hit impact studies is the method of characterisation. A commonly performed method of characterisation is the recording of damage within the plate. This can be either through visual inspection [273], c-scan, energy absorption within the material [274], or compression after impact (CAI) testing [274].

This chapter begins with a description the experimental testing and numerical modelling strategy for the ballistic impact events upon 3D woven clamped beam samples. The numerical model is validated against the back-face deflection and damage mechanisms exhibit during experimental testing. A numerical investigation into the response of clamped circular composite plates with and without TTT reinforcement undergoing a singular hard-impact event is then presented. Attention is given to the distribution of stress throughout the material,

material damage characterisation, and plate penetration mechanisms. A secondary validation for multi-hit impact is then presented with reference to a published multi-hit experimental study on a UD-laminate composite. Afterwards, the predicted multi-hit ballistic limit surfaces of 3D woven composite and equivalent UD-laminate plates are presented. Damage distribution and penetration mechanisms are discussed, with reference to the singular hit numerical predictions. A parameter study is then conducted to ascertain the influence of inter-laminar shear strength on the ballistic limit of UD-laminate composite plates. Finally, conclusions are drawn from the work and recommendations for future studies are given.

5.2 Finite element modelling

The three-dimensional (3D) finite model was created within the ABAQUS (Version 6.12) explicit solver. The modelling strategy employed the constitutive models for fibre reinforced composites of Hashin [165] and Matzenmiller, Lubliner [178]. Each of the layers within the laminate were modelled separately using 4-noded doubly curved reduced integration shell elements (S4R in ABAQUS notation), with 5 integration points throughout the thickness. The translation and rotational degrees of freedom were constrained around the periphery of all the plies. The plies were joined together through the thickness with a cohesive interaction, the constitutive law identical to that as given in Chapter 4 of this thesis. The stainless steel projectile consisted of a stainless steel sphere of diameter d_p = 12.7 mm and mass m_p = 8.3 g. This mass was assigned by the inertial assignment command within ABAQUS, at the centre of the projectile. The projectile was assumed to incur negligible deformation throughout the penetration event, and was modelled a discrete rigid body. Justification of the shell element choice is primarily due to the high in-plane to thickness length ratio of each ply, relatively low impact velocities, and a rounded projectile geometry. The spherical projectile is not expected to induce significant through-thickness shear damage underneath the projectile, with comparison to a sharp-tipped projectile such a bullet. Further justification of the shell element choice being that

at impact velocities in the vicinity of the ballistic limit of CFRP composite plates, the dominant failure mechanism of the in-plane fibre architecture is expected to be that of tensile fracture [275]. A review of the efficacy of the use of shell elements in the transient analysis of a dynamic impact event is presented by Lahtinen and Pramila [276]. The element size for the laminate was approximately 800 μm. Three different finite element models were created:

1. 17 layer orthogonal 3D woven composite **beam** model, for validation of the modelling strategy for ballistic impact upon 3D woven composites,
2. 15 layer UD-laminate circular **plate** – used for further validation of the multi-hit simulation methodology, and for the inter-laminar strength parameter study.
3. 17 layer orthogonal 3D woven composite circular **plate**, for prediction of the singular and multi-hit ballistic impact response. The TTT reinforcement can be supressed in order to investigate its effects.

5.3 Ballistic impact upon 3D woven composite beams

Figure 5.1(a) presents a sketch of the experimental set up for ballistic impact upon orthogonal 3D woven composite beam samples. Experiments were undertaken in order to determine the damage modes presented during ballistic impact of beam samples, and for ballistic impact numerical modelling validation. Samples of width w = 40 mm, and length L = 250 mm were cut from fully cured composite panels. Beam samples were chosen for validation to allow for the recording of the transient back-face deflection of samples through-out the test. Four holes for M6 bolts were drilled into the top and bottom of the samples, and the beams were fixed into a steel sample fixture. The steel sample fixture was bolted onto an aluminium alloy frame, housed within a protective polycarbonate shield. Clamped beams had a free length l_0 = 170 mm. The stand-off between the front edge of the sample and the gas gun was s = 200 mm. Stainless steel spherical projectiles of diameter d_p = 12.7 mm and mass m_p = 8.3 g were accelerated via a pressurised gas gun. The gas gun utilised pressurised air up to a pressure of 6.5 bar, and

pressurised nitrogen (oxygen free) for pressures up to 45 bar. The pressurised gas filled a 3-litre diving cylinder. Pressure was released via a fast-acting solenoid valve. The gas gun had a stainless-steel barrel of length 3.5 m, bore diameter 13 mm and thickness 1.5 mm. A series of holes were drilled into the muzzle end of the barrel in order to allow for gas release. Two laser gates were set up at the muzzle end of the barrel in order to measure the exit velocity of projectile. The velocity measured by the laser gates was confirmed with high speed photography. Further details of the design of the gas gun system are presented in the Appendix to this thesis. Projectiles in the experiments were accelerated to a velocity range $60\ \text{ms}^{-1} \le v_0 \le 190\ \text{ms}^{-1}$ giving a projectile kinetic energy range of $15\ \text{J} \le J_k \le 149\ \text{J}$. This velocity range corresponds to characteristic impact events from debris striking the underside of an aircraft during take-off and landing [268-271]. High speed photography was used to record the transient deformation and damage mechanisms of beams during impact. The back-face is defined at the surface of the sample distal to the projectile impact. The high speed camera model Phantom Mercury HS v12.1 with a global electronic shutter, a frame rate of approximately 57,000 fps and an exposure time of 10 μs was used. At a resolution of 304 x 400, this gave an approximate pixel size on the front surface of beam samples of 0.35 mm. Beam samples were chosen for FE model validation in order to compare the back-face deflection as well as the damage modes exhibited. Figure 5.1(b) presents a sketch of the FE meshed geometry of the ballistic impact simulation on 3D woven beam samples. The methodology followed that of the homogenised geometry presented in Chapter 4, i.e. the individual tows and the matrix channels are homogenised into one effective laminate using the rule of mixtures. The projectile was simulated by a spherical rigid body. Full TTT and Half TTT material beams were simulated, with beams orientated along the x-direction (warp). The in-plane fibre architecture of the two material types was assumed to be identical. The material properties assigned to the homogenised layers and TTT reinforcement were identical to that as presented in Chapter 4.

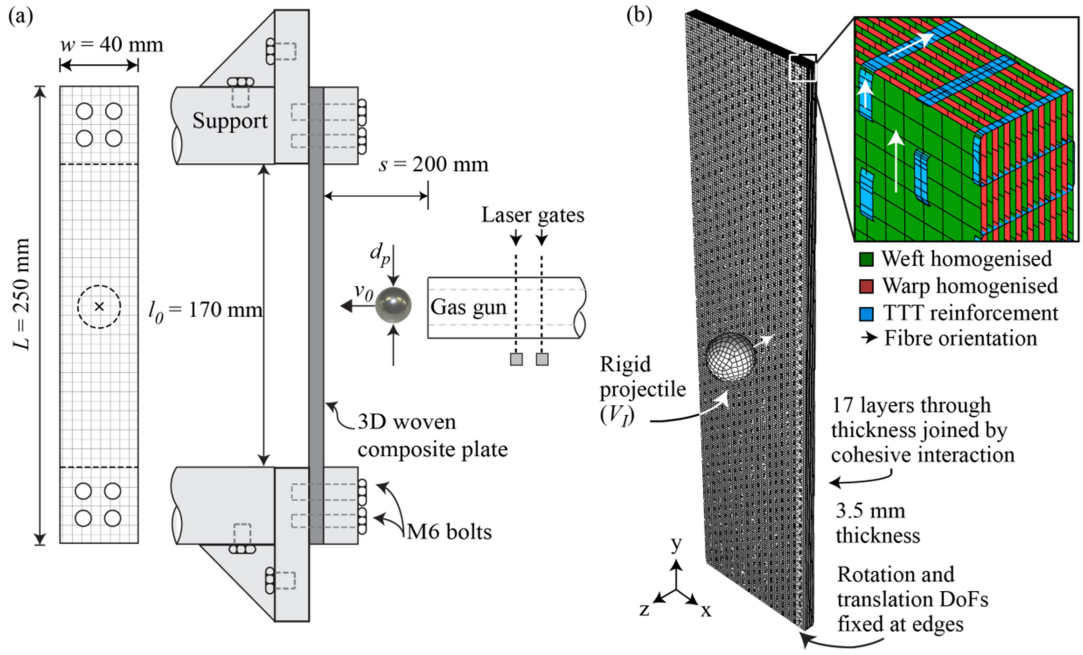


Figure 5.1. (a) Sketch of experimental set up for ballistic impact of 3D woven composite beams (b) Meshed geometry of homogenised 3D woven ballistic beam impact simulation.

5.3.1 Deformation and damage mechanisms during clamped-beam ballistic impact loading

The response of the 3D woven composite beams during ballistic impact tests exhibited three distinct mechanisms dependent on the velocity of the projectile:

Low velocity ($v_0 \leq 110\,\mathrm{ms}^{-1}$) - The beam deflects and the projectile is rebounded. Damage incurred within the beam ranges from relatively superficial surface fibre fracture and localised matrix cracking under projectile location to extensive longitudinal fibre fracture and matrix cracking along the centre of the beam.

Medium velocity ($110 \leq v_0 \leq 140\,\mathrm{ms}^{-1}$) - Kinetic energy of the projectile is high enough to cause failure of beam samples. The failure mechanism is stretch dominated; the beam deflects significantly further than the thickness of the beam and longitudinal fibre fracture occurs at the centre line of the beam. This fracture

position occurs at the location of through-thickness reinforcement, as this is clearly the location of stress concentrations within the material (as demonstrated within the quasi-static finite element analysis within Chapter 3 of this thesis). The through-thickness reinforcement is revealed upon viewing of the fracture surface.

High velocity ($v_0 \geq 140\,\mathrm{ms}^{-1}$) - Kinetic energy of the projectile is high enough to penetrate through the sample. Projectile penetration occurs before the beam can reach significant out-of-plane deflection. Damage mechanisms are extensive fibre fracture and matrix cracking. Damage of the TTT reinforcement occurred up to 20 mm away from projectile impact site. Specifically, the crowns of the through-thickness reinforcement were removed. Penetration was also coupled with longitudinal fibre fracture across the centre-line of the sample, similar to that as the medium velocity stretch-dominated damage mode.

The back-face deflection of Full TTT beams orientated along the x-direction (warp) as a function of time after projectile impact on the sample for three impact velocities; $v_0 = 70\,\mathrm{ms}^{-1}$, $v_0 = 110\,\mathrm{ms}^{-1}$ and $v_0 = 148\,\mathrm{ms}^{-1}$ is presented in Figure 5.2(a). Figure 5.2(b) presents the results for Half TTT beams of impact velocities $v_0 = 76\,\mathrm{ms}^{-1}$, $v_0 = 105\,\mathrm{ms}^{-1}$ and $v_0 = 190\,\mathrm{ms}^{-1}$. Comparisons between experimental results and numerical predictions are favourable in regards to the maximum back-face deflection and time at which it occurs. The accuracy of the prediction decreases as time progresses due to complications arising from imperfect clamped boundary conditions within the experimental test, as discussed during soft impact in Chapter 4 of this thesis. Fidelity of the impact velocity $v_0 = 148\,\mathrm{ms}^{-1}$ was seen to be reduced due to an over-prediction of deflection by the FE model. Figure 5.2(a) and (b) also show the time at which catastrophic longitudinal beam fracture or projectile penetration occurs. Points labelled ‘P’ on the graph represent projectile penetration, and points labelled ‘F’ represent stretch-dominated beam fracture.

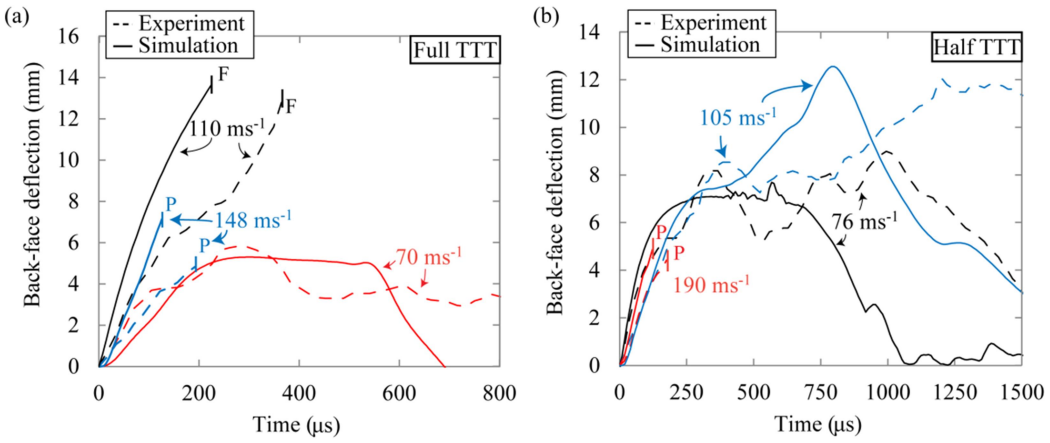


Figure 5.2. Validation of the numerical modelling strategies via the simulation of rigid impact upon orthogonal 3D woven composite beams (a) back-face deflection against time after impact for Full TTT composite samples orientated along the x-direction (warp) impacted with velocity $v_0 = 70\,\mathrm{ms}^{-1}$, $v_0 = 110\,\mathrm{ms}^{-1}$ and $v_0 = 148\,\mathrm{ms}^{-1}$ (b) back-face deflection against time after impact for Half TTT composite samples orientated along the x-direction (warp) impacted with velocity $v_0 = 76\,\mathrm{ms}^{-1}$, $v_0 = 105\,\mathrm{ms}^{-1}$ and $v_0 = 190\,\mathrm{ms}^{-1}$

The experimental and numerically predicted montage of a Half TTT beam deformation during an impact of velocity $v_0 = 76\ \mathrm{ms}^{-1}$ is presented in Figure 5.3(a). The simulation predicts the propagation of a bending wave originating from the impact location to the beam clamped edges, travelling at a velocity of approximately 130 ms^{-1}. The transient location of the bending wave throughout the experiment and simulation is marked on the montage. The FE model shows reasonable fidelity to experimental results in regards to back-face deflection of beams. Figure 5.3(b) and (c) present a comparison between the experimentally recorded and FE predicted deformation for a Full TTT beam impacted at $v_0 = 110\,\mathrm{ms}^{-1}$ and for a Half TTT beam impacted at $v_0 = 190\,\mathrm{ms}^{-1}$.The FE model predicts the three distinct beam response regimes, of which will be compared in detail through optical microscopic images of beams post-test.

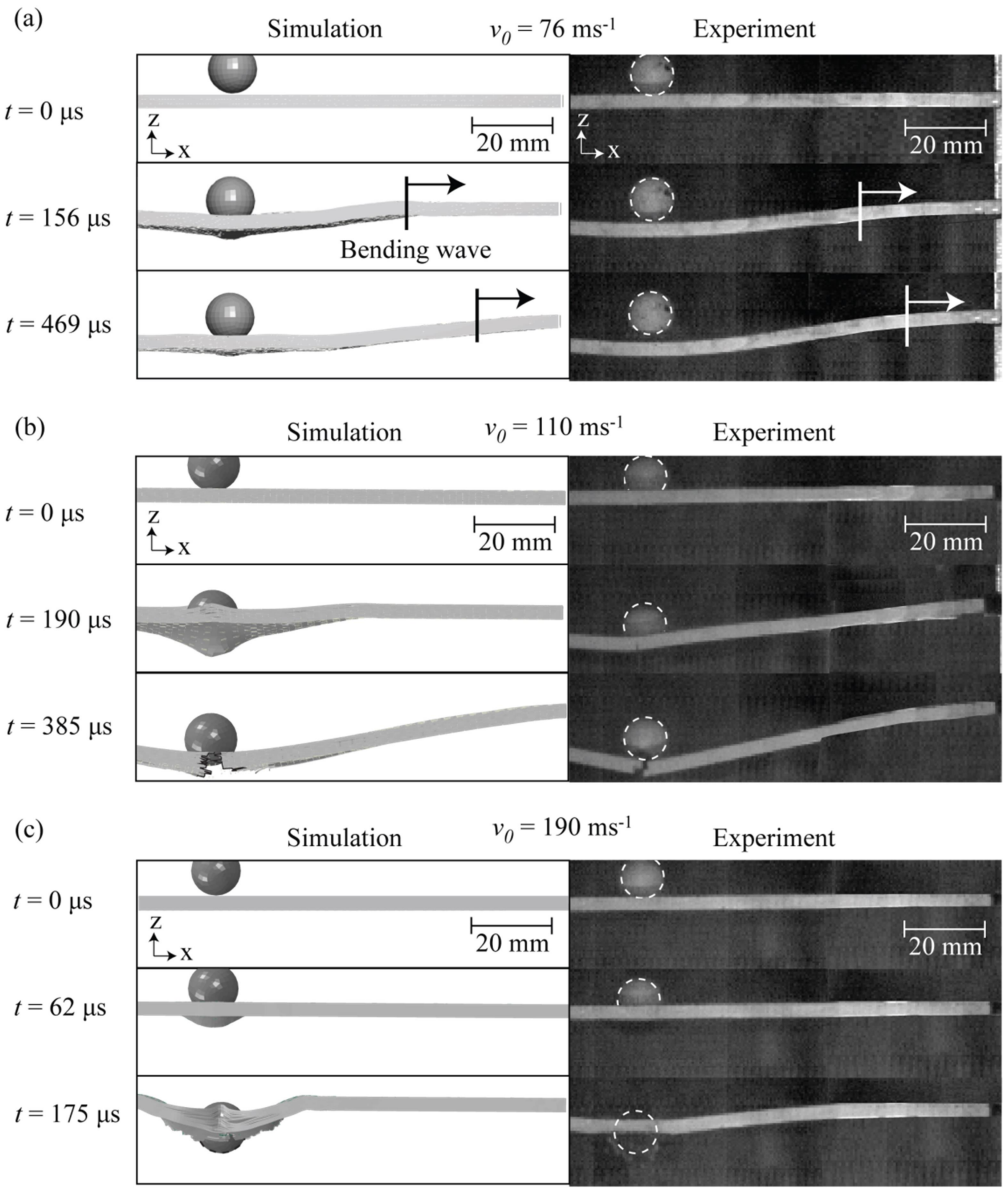


Figure 5.3 FE predicted and experimentally recorded transient deformation of (a) Half TTT beam during impact $v_0 = 76\,\mathrm{ms}^{-1}$, (b) Full TTT beam during impact $v_0 = 110\mathrm{ms}^{-1}$ and (c) Half TTT beam during impact $v_0 = 190\mathrm{ms}^{-1}$.

Figure 5.4(a) and (b) present a comparison between surface optical microscopic images taken post-test and the numerically predicted response of an impact velocity $v_0 = 76\,\mathrm{ms}^{-1}$ on Half TTT material for the front surface and back surface

of sample, respectively. For the front surface, localised matrix cracking and fibre fracture of surface (weft) tows were both recorded and predicted by the numerical model. Small-scale fibre fracture was observed and predicted underneath the projectile strike locations. The back surface demonstrated significant matrix cracking across the entire width of the beam. This damage to the matrix was significant enough to cause removal of transverse (weft) tows from the sample. As demonstrated by Figure 5.4(b), the numerical model predicts significant tensile matrix damage incurred within the beam along the centre line of the back-surface of the sample.

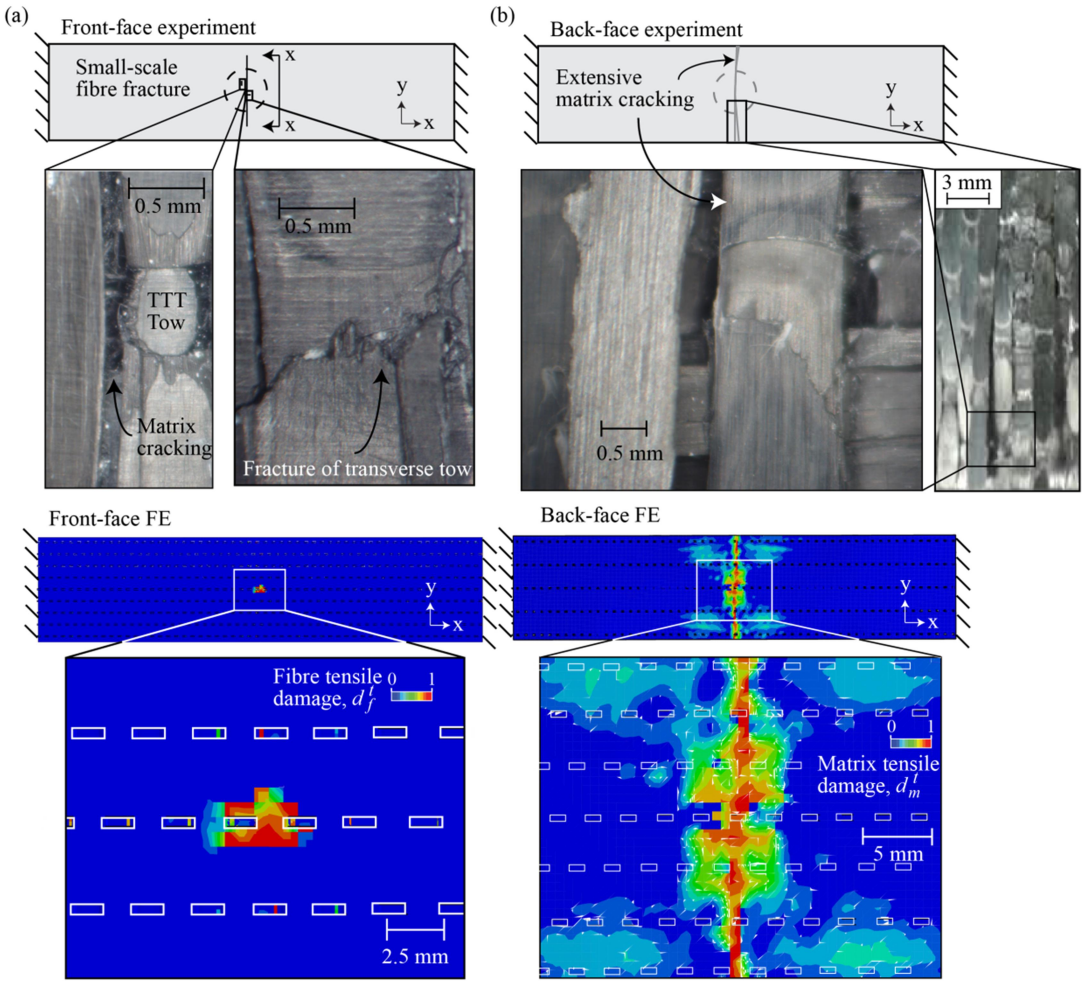


Figure 5.4. Comparison between experimentally observed and predicted damage mechanisms for a lower velocity projectile $v_0 = 76\ \mathrm{ms}^{-1}$ impacting upon Half TTT

material beam orientated along the x-direction (warp). (a) front-face sample, contour shows tensile fibre damage d_t^f. (b) back-face of sample contour shows predicted matrix tensile damage d_t^m.

Figure 5.5 presents optical microscopic images of the same sample cross-sectioned across the centre line of the beam. The location of the cross-section is that as denoted by x-x in Figure 5.4(a). It shows the localised, sub-surface damage underneath the projectile location. The damage includes transverse and inter-laminar matrix cracking and damage to the through-thickness reinforcement under the projectile strike location. As with the short cantilever beam testing presented in Chapter 3, inter-laminar matrix crack propagation is arrested by the presence of nearby through-thickness reinforcement. Damage to the TTT-reinforcement is observed and predicted underneath the projectile strike location.

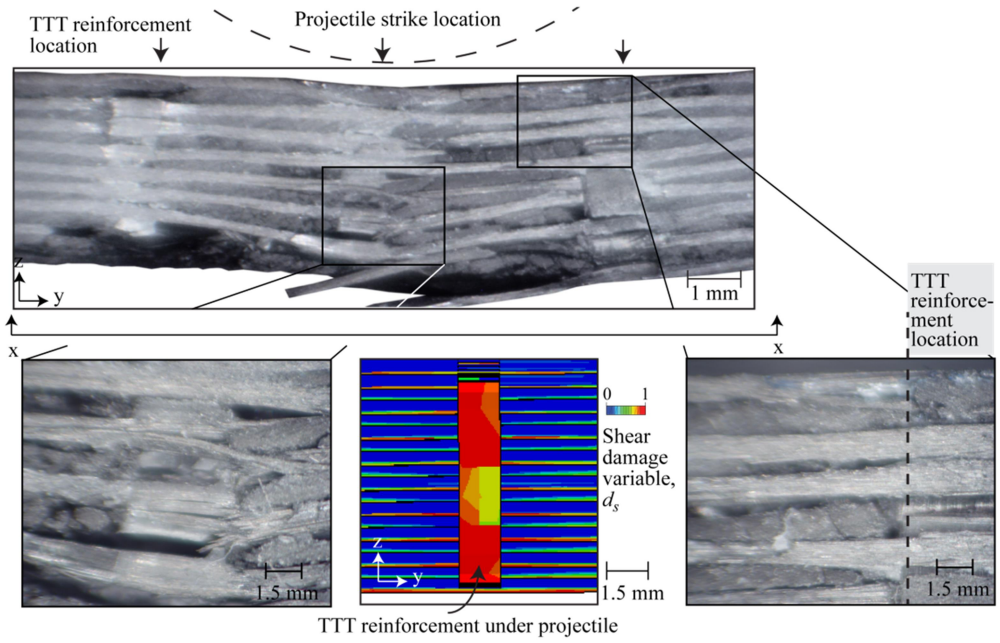


Figure 5.5 Optical microscopic images of cross-sectioned sample of lower velocity projectile $v_0 = 76\ \text{ms}^{-1}$ impacting upon Half TTT material beam orientated along the x-direction (warp). Cross section corresponds to location in Figure 5.4. The predicted and experimentally observed stretch-dominated failure mechanism, characterised by in-plane fibre fracture across the length of the beam

at the centre of the sample, is presented in Figure 5.6. Brittle fracture reveals through-thickness reinforcement at the fracture surface. The FE predicted contour shows shear damage, d_s, with fully damaged elements removed from the visualisation. The dominant stretch in-plane tensile fibre fracture mechanism is coupled with localised matrix under the projectile location due to high contact stresses. The matrix cracking is demonstrated on both post-experiment optical microscopic images, and the FE prediction.

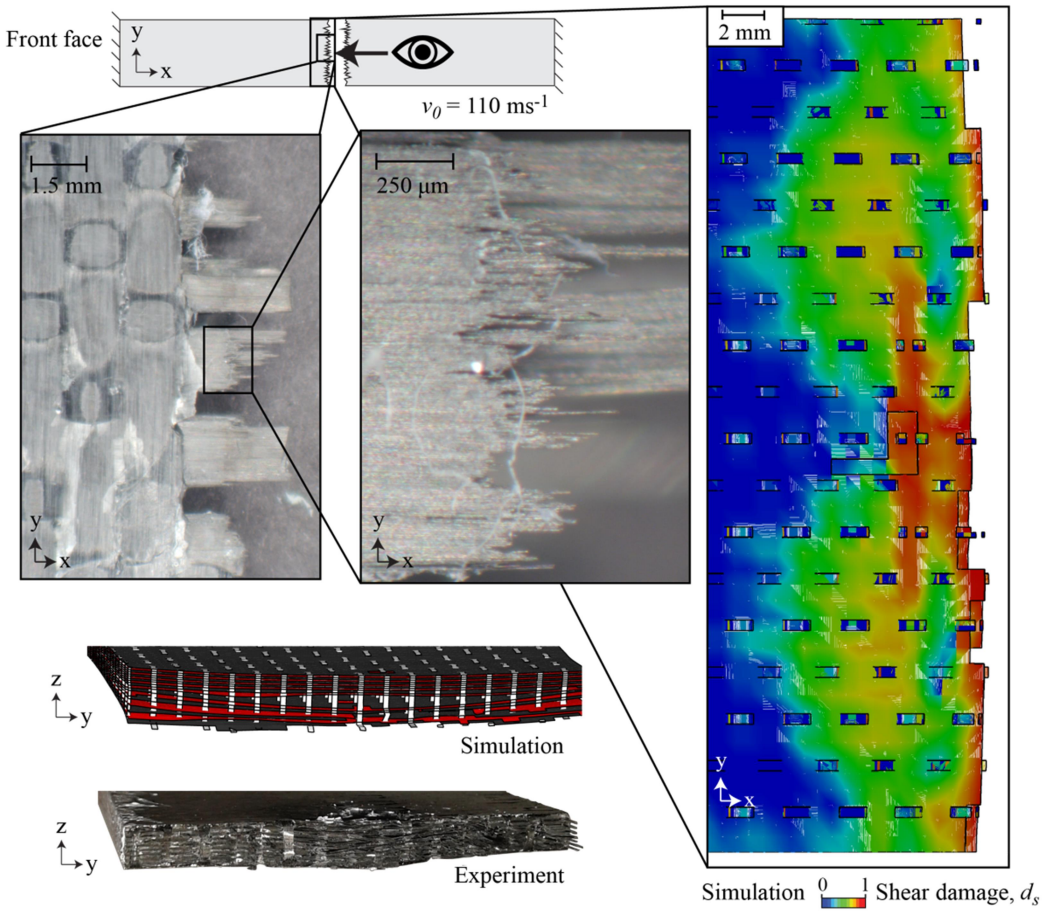


Figure 5.6. Comparison between experimentally observed and predicted damage mechanisms for a medium velocity projectile $v_0 = 110\ \text{ms}^{-1}$ impacting upon Full TTT material. Contour shows shear damage, d_s, with fully damaged elements removed from the visualisation.

The predicted and experimentally observed penetration damage mechanisms for a high velocity impact $v_0 = 190\,\text{ms}^{-1}$, characterised by significant localised damage and projectile penetration, is presented in Figure 5.7. Tensile fracture of the TTT reinforcement at areas remote from the projectile impact location caused removal of TTT reinforcement crowns. This is shown by a comparison between the post-test optical microscopic images and the FE predicted longitudinal tensile fibre damage of the TTT reinforcement presented in Figure 5.7.

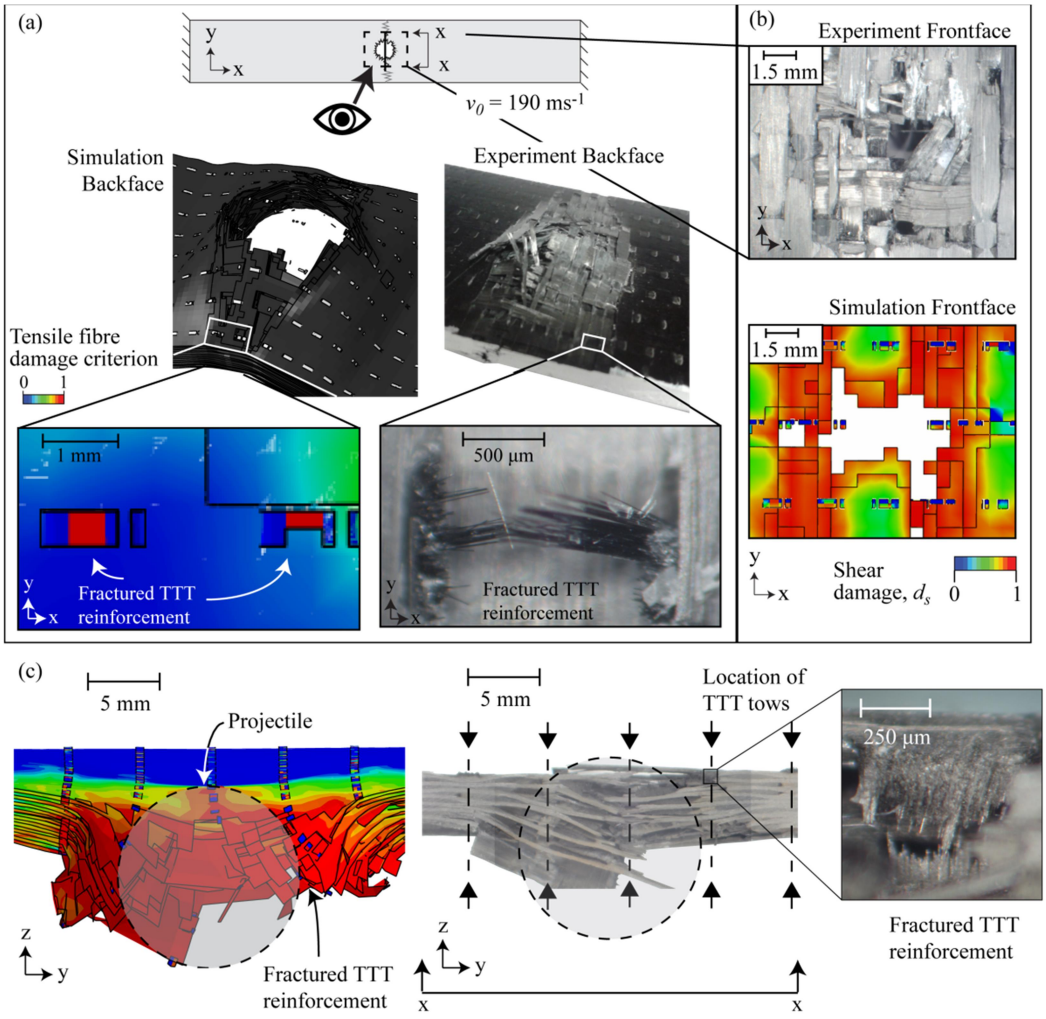


Figure 5.7. Comparison between experimentally observed and predicted damage mechanisms for a high velocity projectile $v_0 = 190\ \text{ms}^{-1}$ impacting upon a Half TTT composite beam. Contour for the back-face at the location of TTT reinforcement

shows tensile fibre damage with fully damage elements removed from the visualisation. (c) Numerically predicted and experimentally recorded cross-sectional images of sample post impact. Location of cross-section is demonstrated in (a). Contour for the front face and section-view shows shear damage, d_s, with fully damaged elements removed from the visualisation.

5.4 3D woven singular-hit impact simulations

Numerical predictions of singular impact events upon 3D woven composite circular plates are now presented. Global stress distributions and damage mechanisms are investigated and will be later used to provide a mechanistic interpretation of the predicted multi-hit ballistic impact response. Figure 5.8 presents a sketch of the meshed geometry of the singular-hit ballistic impact simulation upon 3D woven composite circular plates. To investigate the response of the composite material under ballistic impact, singular impact simulations with and without the presence of the TTT reinforcement were undertaken. Through this, the role of the through-the-thickness reinforcement during ballistic impact testing can be elucidated.

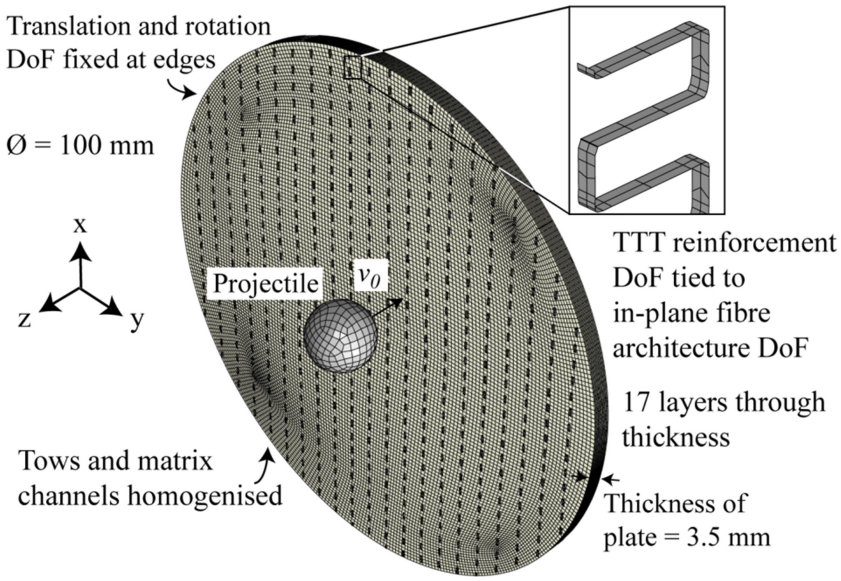


Figure 5.8. Meshed geometry for singular-hit ballistic impact simulations upon 3D woven composite circular plates.

5.4.1 Deformed configuration and stress distribution

The two material types demonstrate different damage and deformation mechanisms during penetration. In short, the presence of the TTT-reinforcement caused an 8% increase in the predicted ballistic limit of the composite plate, i.e. an increase from V_L = 152.5 ms^{-1} without TTT reinforcement to V_L = 165.0 ms^{-1} inclusive of TTT reinforcement. There is a distinct shortage of studies within the literature regarding the comparison of the ballistic limit between 3D woven and equivalent UD-laminate materials. Comparisons between 3D and 2D woven plates provide a range of conclusions. An experimental study on the ballistic impact response of clamped fibre reinforced composite plates recorded approximately a 14% increase in 3D woven carbon compared to 2D woven carbon material [277], although no mechanistic reasoning was provided at the time. A different study impacting clamped samples with a .30 calibre fragment simulating projectile [267] recorded a 5% reduction in ballistic limit for a 6% orthogonally woven composite in comparison with a 2D plain weave carbon composite. Plates with and without TTT reinforcement were predicted to experience longitudinal fibre fracture throughout the thickness of the plate under the projectile strike location at a velocity of approximately $v_0 = 0.6\, V_L$. This agrees well with ballistic impact testing of CFRP plates presented by Kandan, Russell [266]. The predicted mechanisms demonstrated during the test will now be described.

During the initial stages of ballistic impact, the FE model reveals the propagation of a high velocity tensile stress wave from the projectile impact location, travelling towards the clamp. This tensile stress wave primarily follows the in-plane fibre orientation, and travels at the longitudinal speed of sound within the material. This is shown clearly in the first montage image for the prediction of longitudinal tensile stress during a rigid spherical impact upon both 3D woven composite and UD-laminate composite in Figure 5.9. As described by analytical

models [278, 279], the inward flow of material towards the centre point allows the initial bulging of the plate underneath the projectile. This tensile stress wave was predicted to have the same velocity and magnitude with and without the presence of the binder. This is demonstrated with the first image of the montages presented in Figure 5.9(a) and (b). The stress within the back-face of the plates is presented here as it gives an indication of the transferal of stress throughout the thickness of the plate.

A lower velocity bending wave then propagates radially out from the impact location, travelling towards the clamped edges. The velocity of the bending wave is increased along the fibre direction, resulting in a characteristic 'diamond' shape pattern of stresses and deflections. This coincides well with the experimentally measured back-face deflection of composite plates under spherical projectile impact reported by Kandan, Russell [266], and for numerical simulations of anisotropic stress wave propagation of a 3D woven composite material presented by Ghosh and De [261]. Figure 5.9(c) presents the longitudinal stress within the through-thickness reinforcement at time t = 125 μs after the moment of projectile impact. Stress concentrations were predicted within the though-thickness reinforcement, coinciding with the transient position of the propagating bending wave. Extensive compressive fibre damage within the through-thickness reinforcement is predicted under the projectile location, in particular for the TTT reinforcement crowns. In the 3D woven composite, stress transferal from the in-plane fibre architecture to the through-thickness reinforcement was demonstrated. This causes a significant reduction in in-plane longitudinal tensile stress throughout the plate, and also local reductions in stress at the positions of the TTT reinforcement. This is demonstrated by a comparison of the predicted longitudinal stress distribution with and without the through-thickness reinforcement in Figure 5.9(a) and (b). The predicted longitudinal stress within the TTT reinforcement is shown in Figure 5.9(c). Transient stress transferal to the TTT reinforcement is demonstrated, following the location of the bending wave.

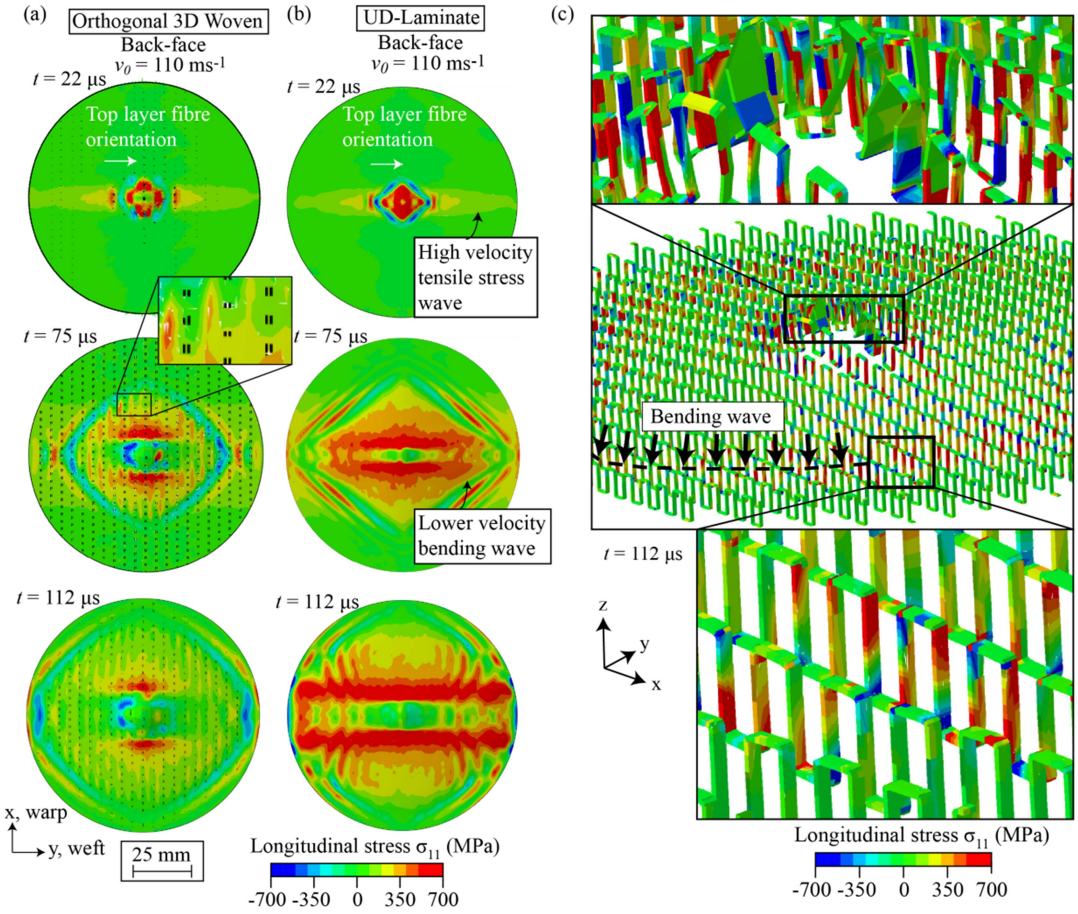


Figure 5.9. Predicted transient longitudinal tensile stress field on back-face of plate impacted by a singular rigid spherical projectile of velocity $v_0 = 110\ \text{ms}^{-1}$ for (a) Half TTT Orthogonal 3D woven composite (b) Equivalent UD-laminate composite. Time *t* is the moment of projectile impact upon plate. (c) Predicted longitudinal stress in the through-thickness reinforcement at time after impact *t* = 112 µs of impact velocity $v_0 = 110\ \text{ms}^{-1}$.

5.4.2 UD-laminate clamped plate deformation and penetration mechanisms

The sequence of penetration mechanisms predicted by the numerical calculations for the equivalent UD-laminate material is illustrated in Figure 5.10, and outlined below:

i. as the projectile makes contact with the plate, a tensile stress wave develops within the material, travelling along the fibre direction out towards the clamped edges. This allows for the initial deformation of the plate.
ii. a travelling bending hinge propagates out from the impact location, travelling with a greater velocity along the principal fibre directions. This causes a growing cone of out-of-plane deformation underneath the projectile location.
iii. delamination damage then becomes significant. Due to the transferal of momentum, it is seen to be more prominent in the bottom ply of the composite. Simultaneous to this, cross shaped fibre fractures develop, propagating away from the impact location and brittle cone fibre fracture occurs underneath the projectile location.
iv. as the impact event continues, cross-shaped fractures increase in size, and combined with the bending deformation of delaminated plies, allows for the pass-through of the projectile.

The separate events of the penetration; the formation of the initial brittle fracture cone underneath the projectile, the propagation of cross-splits, and the bending deformation of delaminated plies, naturally leads to a case in which the projectile has enough kinetic energy to active one or two modes, but not to penetrate. The finite element model captures a specific velocity, i.e. v_0= 150 ms^{-1}, in which the projectile becomes trapped within the material. This transition point between projectile rebound and penetration, occurs at kinetic energies high enough to cause fibre fracture, yet not high enough for plate deformation allowing for complete projectile pass-through. The damage modes, and the transition point between rebound and penetration phenomenon, corresponds well to that recorded by experimental testing of CFRP plates by Kandan, Russell [280] and Hazell and Appleby-Thomas [281]. Figure 5.10 presents a sketch of a cross section of the plate showing the penetration mechanisms described here, along with a montage of the penetration event predicted by the FE method. The contour of Figure

5.10(b) shows the onset of longitudinal fibre tensile damage. The finite element prediction clearly demonstrates the cross-shaped damage distribution, along with bending of plies to allow for projectile pass-through. Fully damaged elements have been removed from the visualisation to improve clarity. Figure 5.10(c) presents a side-by-side comparison of cross-sectional x-ray image of an impact of velocity v_0 = 206 ms^{-1} upon a [0°/90°$_7$/0°] UD-laminate composite as presented by Karthikeyen Kandan PhD thesis (2012) [282] and numerically predicted response of the equivalent UD-laminate material undergoing an impact velocity of v_0 = 155 ms^{-1}. The UD-laminate material demonstrates spring back of proximal laminae, and extensive delamination remote from the projectile strike position. This response is different in the case inclusive of the TTT reinforcement, as presented later in Figure 5.11.

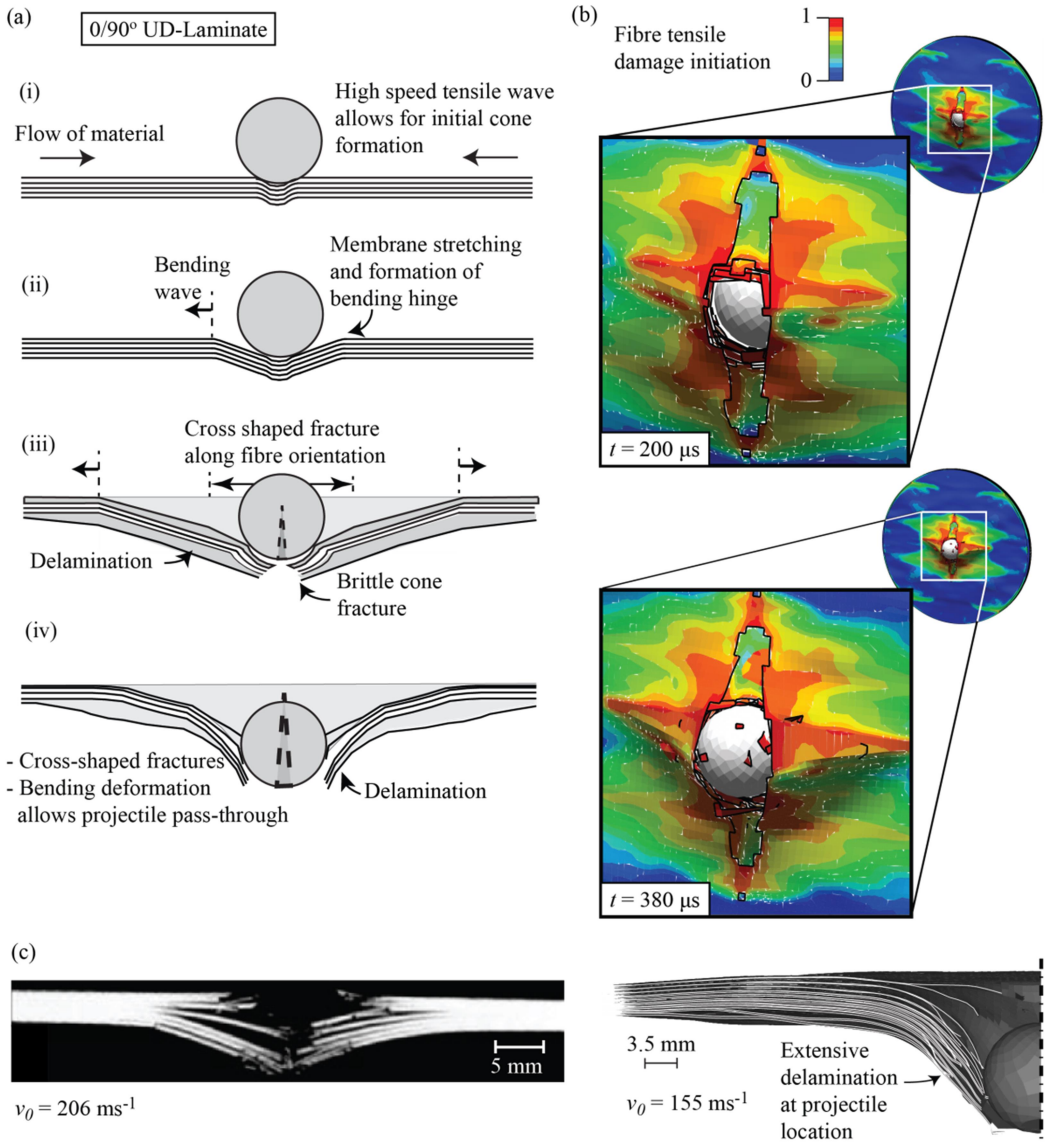


Figure 5.10(a) Sketch of penetration mechanisms demonstrated by FE predictions of ballistic penetration event v_0 = 155 ms^{-1}: (i) inward flow of material allowing for initial bulging of plate, (ii) membrane stretching and formation of travelling bending hinge, (iii) brittle cone fracture and formation of cross shaped fracture of fibre reinforcement following principal fibre direction (iv) development of cross-shaped fibre fracture and wide-spread bending deformation of plate allowing for projectile pass-through. (b) montage of penetration event with contour showing longitudinal fibre damage initiation. A value of 1 indicates the onset of damage. (c) comparison of cross section of penetrated UD-laminate sample. Left:

[0°/90°$_7$/0°] layup composite impacted at 206 ms^{-1} presented in Karthikeyan Kandan PhD Thesis (2013) [282]. Right: This study, FE simulation of equivalent UD-laminate clamped plate as shown in (b).

5.4.3 3D woven composite plates deformation and penetration mechanisms

FE simulations of a penetration event of a 3D woven composite material impacted by a projectile velocity of $v_0 = 170\,\mathrm{ms}^{-1}$ were undertaken in order to ascertain the deformed configuration and damage mechanisms during penetration. Comparisons are made without the presence of the TTT reinforcement. Figure 5.11(a) and (b) presents a sketch of the mechanisms and the numerically predicted longitudinal fibre damage contours during penetration, respectively. The main stages of the event are outlined below:

i. The propagation of a longitudinal tensile stress wave along the principal fibre direction allows for the initial cone formation. This is identical to the UD-laminate material.
ii. Membrane stretching occurs and a bending wave emanates from the impact location and travels towards the clamped edges. This is identical to the UD-laminate material.
iii. A combination of compressive fracture of through-thickness reinforcement and tensile fracture of longitudinal fibre reinforcement occurs under the projectile location. The in-plane tensile fibre fracture begins on the surface distal to projectile strike and propagates upwards towards the strike face.
iv. Localised deformation and damage of in-plane plies and through-thickness reinforcement around the projectile location allows for projectile penetration. Delamination within the material is restricted from under the projectile strike location up until the nearest un-damaged TTT reinforcement tow.

The final image shows the predicted asymmetric damage as the TTT reinforcement tow is fractured on the right hand side, causing a change in the local deformation. Capturing asymmetrical damage such as this is one of the key advantages of explicitly modelling the binder. Images of the FE prediction of an impact of velocity $v_0 = 170\,\mathrm{ms}^{-1}$, presented in Figure 5.11(b), clearly demonstrate damage concentrated under the projectile. This is different to the cross-shaped fracture and bending deformation predicted with the UD-laminate material. In regards to the back surface of the plates, the damage was predicted to propagate more favourably along the direction of the TTT reinforcement, as opposed to the fibre orientation. Figure 5.11(c) presents a cross-sectional view of the numerically predicted response of the 3D woven composite plate undergoing an impact of velocity 170 ms^{-1}. Delamination was shown to be supressed by the presence of the TTT reinforcement. No delamination was noted at locations away from the immediate location of penetration, corresponding well to the damage shown via cross-sectional microscopic images of projectile penetration of Half TTT beam samples presented in Figure 5.7(c).

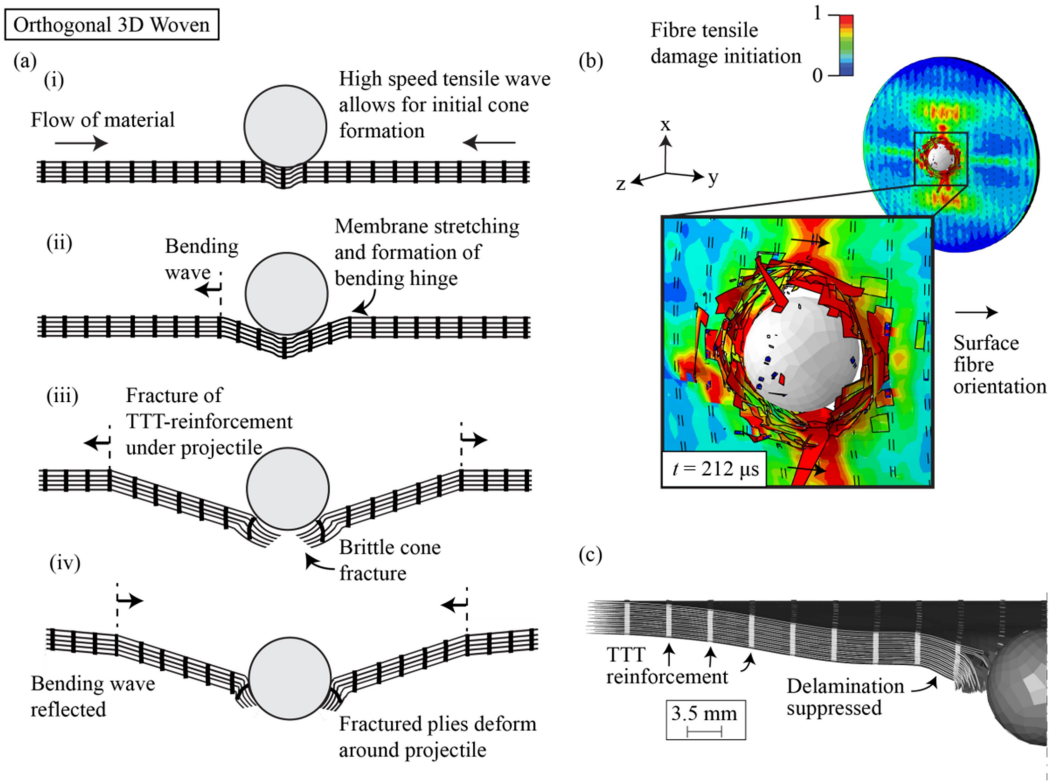


Figure 5.11(a) Predicted mechanisms of deformation and penetration of orthogonal 3D woven composite material undergoing impact v_0 = 170 ms^{-1} : (i) inward flow of material allowing for initial bulging of plate, (ii) membrane stretching and formation of travelling bending hinge, (iii) fracture of TTT-reinforcement under projectile and brittle cone shaped fracture of in-plane fibre architecture, (iv) localised deformation and damage of in-plane fibre architecture allowing for projectile penetration, (b) Predicted deformed configuration and locations of initiation of tensile fibre damage of 3D woven composite material. A value of 1 indicates the onset of longitudinal tensile damage. (c) Cross-sectional image of the numerically predicted response of Half TTT 3D woven composite plate sample subjected to impact velocity v_0 = 170 ms^{-1}.

5.4.4 Fibre damage distribution

Figure 5.12(a) and (b) presents the predicted tensile fibre damage initiation on the front-face of composite laminate plates undergoing ballistic impact of v_0 = 110

ms^{-1} at time after impact $t = 225$ µs with and without the presence of TTT reinforcement, respectively. A damage initiation value of 1 indicates the onset of damage of elements. The time chosen corresponds to the time at which the damage within the plates has fully developed for both cases. The top surface ply fibres are orientated along the y-direction (weft). The stress transferal from the in-plane fibre architecture to the through-thickness reinforcement (as shown in Figure 5.9) effectively acts to reduce the fibre damage in the plate remote from the impact location; concentrating damage to the impact location. This has the effect of resisting the cross-shaped damage mode, reducing plate bending deformation. The tensile fibre damage was predicted to propagate more significantly in the direction of the TTT reinforcement for the 3D woven sample, and along the in-plane fibre orientation for the UD-laminate.

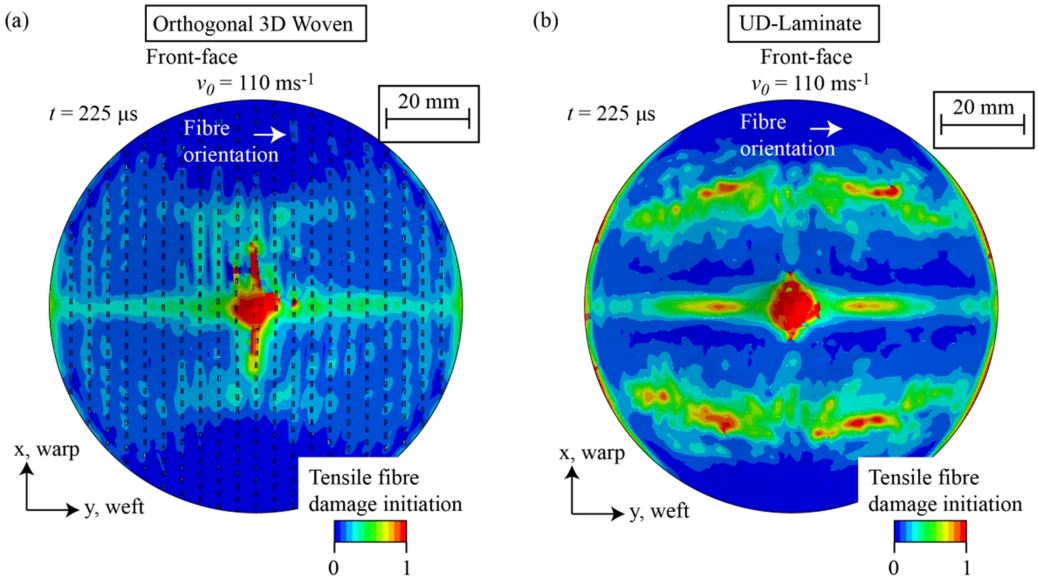


Figure 5.12(a) and (b) Predicted tensile fibre damage initiation on the front-face of composite laminate beams undergoing ballistic impact of $v_0 = 110$ ms^{-1} at time after impact $t = 225$ µs for material with and without through-thickness reinforcement, respectively. Time $t = 0$ corresponds to the moment of projectile impact on plate. A damage initiation value of 1 indicates the onset of damage of elements. Top ply fibres orientated along the y-direction (weft).

5.5 Multi-hit ballistic impact modelling validation (UD-laminate)

In order to validate the multi-hit finite element modelling strategy, and provide confirmation of the efficacy of the in-plane constitutive and contact laws within the model, simulations of a previously conducted experimental study [162] on the multi-hit ballistic properties of a carbon fibre reinforced epoxy laminate composite material were undertaken. Simulations were undertaken with projectile velocities ranging from $0\ \mathrm{ms}^{-1} < v_0 \leq 100\ \mathrm{ms}^{-1}$. Figure 5.13(a) presents a sketch of the meshed geometry of the validation simulations conducted on the UD-laminate composite material.

The multi-hit finite element simulations presented in this study followed the same methodology as the numerical study on 304 stainless steel clamped plates by Russell [163]. Whilst the first projectile was imparted with a velocity V_I at the beginning of the simulation, the second projectile was set further away from the plate, and imparted with velocity V_{II}. The second projectile followed the same trajectory as the first. Contact between the two projectiles was removed using the "exclude surface pair" option within ABAQUS, allowing the second projectile to pass through the first in order to impact upon the plate. In order to limit the influence from the reflecting stress waves within the plate due to the first impact, the second projectile was set far enough back in order for the calculations to remain a reasonable length. Although it should be noted, due to computational time constraints, the plate was experiencing stress wave reflections at the moment of secondary impact. This would potentially modify the response of the plate, and the influence of the projectile off-set is investigated in more detail later in this chapter.

The two velocities, V_I and V_{II} can be used to define a point in 2D space of a binary event that is either projectile rebound or projectile penetration. Successive simulations were conducted of increasing projectile velocities, until the ballistic limit surface was predicted to within an accuracy of 2.5 ms^{-1}. The material

properties utilised for the UD-laminate multi-hit validation simulations followed those presented by [156] and are presented in

Table 5.1. The 15 layer 0/90 carbon fibre reinforced epoxy laminate material is identical to the material used within the multi-hit ballistic impact study presented by Kandan et al. [162]. The only modification was that of the viscosity coefficient, which was varied in order to provide a more accurate prediction of damage propagation during ballistic impact loading throughout the plate. The material parameters for the cohesive interface between the surfaces of each ply of the UD-laminate multi-hit validation model are shown in Table 5.2. The cohesive interface was assumed to be rate insensitive.

Table 5.1. The material properties of each uni-directional ply of laminate composite material employed within the constitutive model of the multi-hit validation FE model.

Laminate Property	Value
Density (g mm^{-3})	0.00157
E_1 (GPa)	170
E_2 (GPa)	5.1
G_{12}, G_{13}, G_{23} (GPa)	4.7
$v_{12} = v_{21}$	0.15
X_T (MPa)	1960
X_C (MPa)	1260
Y (MPa)	160
J_{1t} / l_e (MPa)	13.6
J_{1c} / l_e (MPa)	5.6
J_m / l_e (MPa)	9.6
Ply thickness (mm)	0.25
Total thickness (mm)	3.75
η (us)	3

Table 5.2. The material parameters for the cohesive interface between the surfaces of each ply of laminate model within the multi-hit validation FE calculations.

Inter-laminar property	Value
k_n (GPa mm^{-1})	5.12
k_s (GPa mm^{-1})	4.72
t_n (MPa)	160
t_s (MPa)	80
J_G (J m^{-2})	5150

For validation, comparisons between the predicted ballistic limit and multi-hit ballistic limit surface are made between the numerical calculations and

experimental results. The experimental study conducted by Kandan, Russell [162] recorded a ballistic limit of 95 ms^{-1}, whilst the numerical calculations in this study predict a ballistic limit of 100 ms^{-1} ± 2.5 ms^{-1}. A comparison between the experimental results and numerically predicted ballistic limit surface is presented in Figure 5.13(b). The characteristic shape of the limit surface is that of a limited reduction in secondary ballistic limit for lower velocity primary impacts, then a sharp decrease in secondary ballistic limit as fibre plies become fractured from the initial impact event. This occurs at initial velocities of approximately 60-65% of the ballistic limit of the plate.

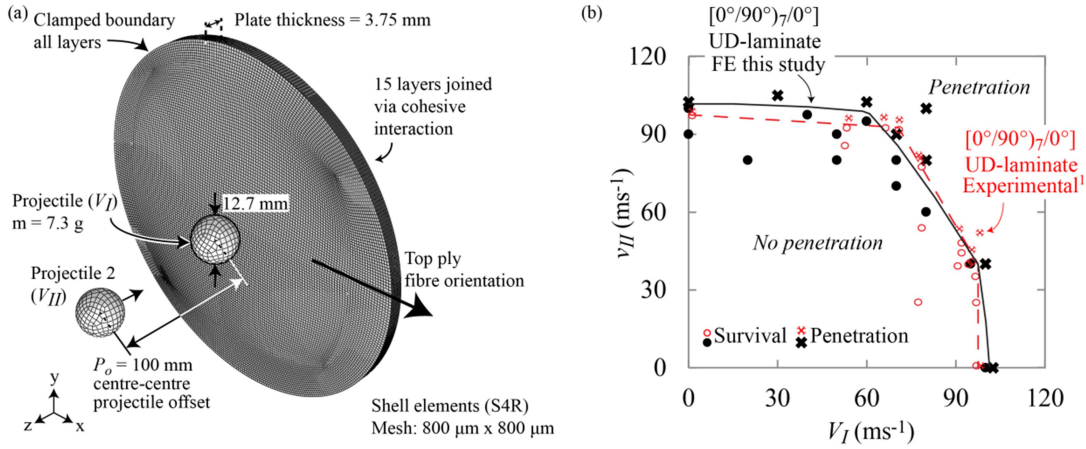


Figure 5.13(a) Meshed geometry of impact simulations on UD-laminate carbon fibre composite material. (b) validation of multi-hit modelling strategy via a comparison of FE predicted ballistic limit surface and experimentally recorded ballistic limit surface presented in Kandan, Russell [162][1] for a carbon fibre reinforced epoxy matrix 15-ply UD-laminate composite of ply layup [0°/90°)$_7$/0°].

5.6 Clamped circular plate multi-hit ballistic impact predictions

The validated FE modelling strategy was employed for the multi-hit simulation of 3D woven composite circular plates. A sketch of the meshed geometry of the multi-hit simulation methodology is presented in Figure 5.14. Contact between the

two projectiles is again removed and an off-set of 100 mm between the centre points is set between them along the z-direction.

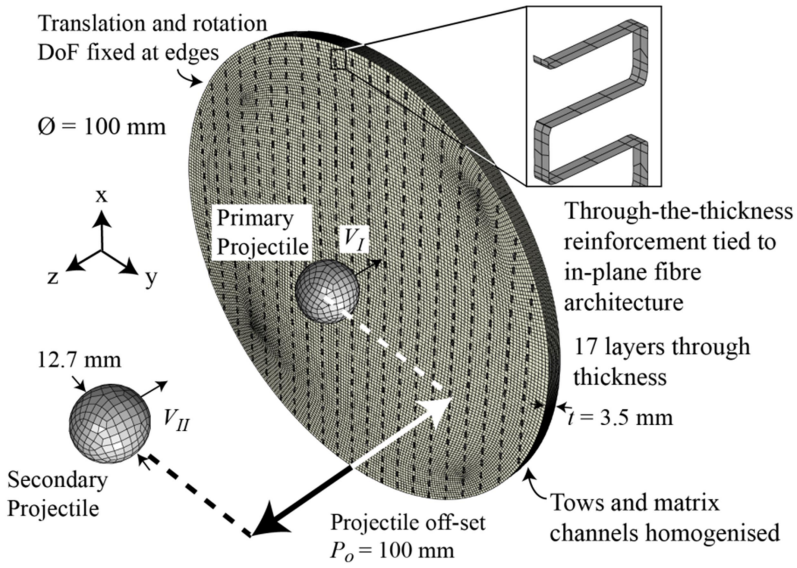


Figure 5.14 Meshed geometry for multi-hit ballistic impact simulations upon 3D woven composite circular plates.

The geometry of the fibre reinforcement was again based upon that of the "Half TTT" 3D woven composite material as described in detail within Chapter 3 of this thesis. Firstly, the predicted multi-hit ballistic limit surface of 3D woven composite material will be presented. Then a detailed examination of role of the TTT-reinforcement in the modification of the damage modes and plate deformation during a multi-hit ballistic event will be given. Finally, an investigation will be undertaken regarding the off-set distance between the primary and secondary projectiles during the FE simulation of multi-hit impact events.

5.6.1 Multi-hit ballistic limit surface

Figure 5.15(a) presents the predicted ballistic limit surface of a 3D woven composite plate in $V_I - V_{II}$ space. Each individual double-hit impact event is

recorded within the space as either a circle for plate survival or a cross for projectile penetration. Dashed lines are included representing a linear interaction and no interaction between the first and second impacts. Due to the elastic-brittle nature of the 3D woven composite material, the general characteristic of the limit surface is expected to similar to of other fibre reinforced composites, such as the UD-laminate material presented by Kandan, Russell [162]. Figure 5.15(b) presents the ballistic limit surfaces for the two materials, normalised against the predicted ballistic limit of each material. It is useful for demonstrating the difference between the predicted behaviours of the materials, independent of absolute ballistic limit.

Up to a primary impact velocity of approximately $V_I = 0.75\,V_L$, the reduction in ballistic limit for the secondary impact is linearly reduced to 85% of that of un-impacted plates. Primary impacts of velocities $V_I \geq 0.75\,V_L$ demonstrate a sharp decrease in the predicted secondary ballistic limit of the plate, i.e. the ballistic limit of the secondary projectile impact. This transition point corresponds to the predicted projectile velocity at which causes fracture of the longitudinal fibres throughout the entire thickness of the plate under the projectile location.

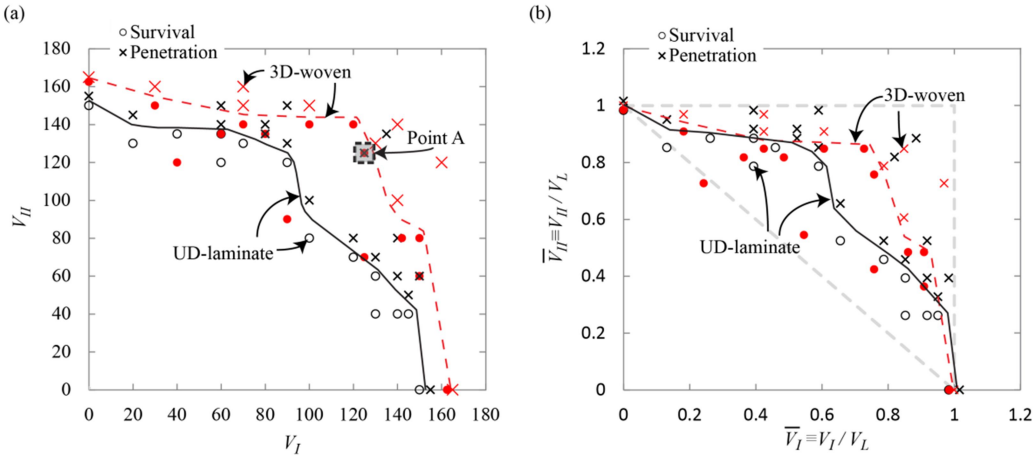


Figure 5.15(a) FE prediction of the multi-hit ballistic limit surface of Half TTT 3D woven composite material and equivalent UD-laminate. Point A corresponds to the multi-hit impact event presented in Figure 5.16. (b) Predicted normalised

multi-hit ballistic limit surface of Half TTT 3D woven composite material and equivalent UD-laminate. Values are normalised against the predicted ballistic limit of each material V_L. Point A corresponds to the response shown in Figure 5.16.

5.6.2 Multi-hit damage mechanisms

Figure 5.16(a) and (b) presents a comparison of the damage of composite plates with and without the presence of the TTT reinforcement for an equi-velocity impact $V_I = V_{II} = 125\,\mathrm{ms}^{-1}$, respectively. This event is marked as Point A in Figure 5.15(a). It is at this velocity that the UD-laminate plate was predicted to have been penetrated, and the 3D woven material predicted to have caused projectile rebound. The primary impact upon the 3D woven material induces concentrated damage underneath the projectile strike location, extending more significantly along the TTT reinforcement orientation. This damage is present throughout the thickness of the plate. The predominant damage mode was predicted to be tensile fracture of in-plane fibre architecture. This is combined with compressive damage of the TTT reinforcement crowns directly under the projectile strike position, and tensile damage of the through-thickness component of the TTT reinforcement in the immediate surrounding area. The secondary impact then causes a propagation of the same damage, following the principal fibre directions, creating a characteristic "cross-shaped" damage distribution. During this stage, the TTT reinforcement is shown to prevent excessive deformation of the plate, resisting projectile penetration. In spite of in-plane fibre fracture occurring throughout the thickness of the plate, the projectile is rebounded.

The equivalent UD-laminate presents a differing damage distribution and penetration mechanism for multi-hit impacts. The primary impact induces fibre fracture throughout the thickness of the plate. The secondary impact causes the damage to propagate and the characteristic cross-shaped damage mode becomes exaggerated. The cross-shaped damage effectively splits the composite plate into

four quadrants. Without the presence of the TTT reinforcement, bending of these quadrants is unimpeded, allowing for projectile pass-through. After projectile pass-through the spring-back effect is demonstrated, with the four quadrants returning to their original configuration. This spring-back effect is demonstrative of the bending deformation of the plate. The bending of the plate, and subsequent pass through of the projectile, causes a reduction of damage underneath the projectile for the equivalent UD-laminate case, this is demonstrated in the final images in Figure 5.16.

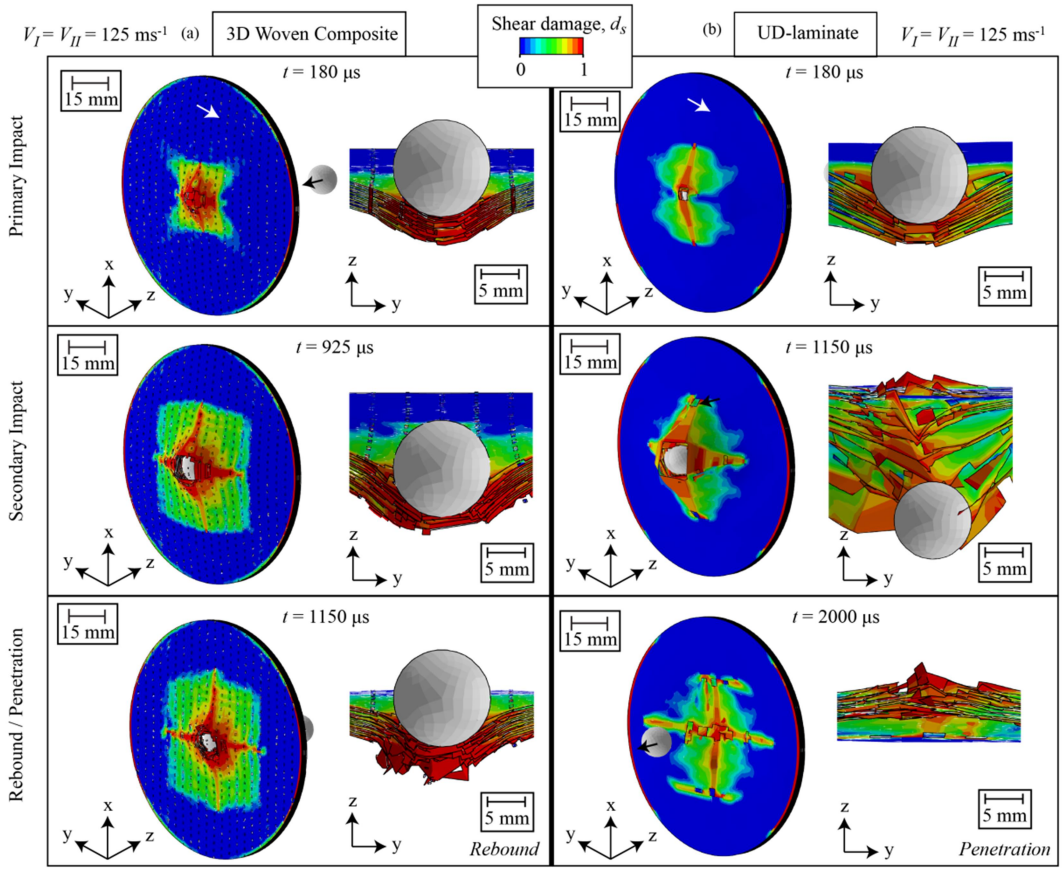


Figure 5.16. Isometric and cross-sectional views of predicted damage and deformed configuration of composite plates for an equi-velocity multi-hit event $V_I = V_{II} = 125$ ms^{-1} (a) 3D woven composite, (b) Equivalent UD-laminate material. Contour shows predicted shear damage variable d_s with a value of 1

indicating fully damaged regions. The arrow on the surface of the plate is indicative of the surface ply fibre orientation.

5.6.3 Projectile off-set

During multi-hit impact simulation there is a transitionary period that occurs between the primary and secondary impact events. Due to the reflection of stress waves within the plate during this time, there exists a degree of uncertainty as to exactly what configuration the plate will be in as the secondary impact takes place. In order to investigate as to what effect this transitionary period may have on the response of the plate, simulations of three different projectile off-sets were conducted.

Figure 5.17 presents a comparison between the deformed configuration of plate at the moment of secondary impact, and the deformed configurations and damage distribution immediately prior to penetration of the secondary projectile for projectile off-set of (a) 50 mm, (b) 100 mm, and (c) 150 mm. Projectile velocities were $V_I = V_{II} = 145\,\mathrm{ms}^{-1}$. The projectile off-set P_o is defined as the linear distance between the centre-points of the two projectiles along the z-axis, as visually depicted in Figure 5.14(a). In the case of an off-set of 50 mm, the secondary projectile impacts upon the plate before plate restitution occurs. Off-sets of 100 mm and 150 mm allow for complete plate restitution, however, small residual oscillations and reflected stress waves within the plate result in a different response during secondary impact. This is demonstrated with the cross sectional images of the deformed configuration of the plates immediately prior to penetration presented in Figure 5.17(a), (b) and (c) for off-sets of 50, 100, and 150 mm, respectively. The off-set of 100 mm presents greater bending of the plate, whilst the 150 mm off-set case presents significantly reduced bending, with more localised damage under the projectile location. Figure 5.17 also presents a comparison of the distribution of predicted damage on the front surface of the plate immediately prior to penetration. In regards to the predicted damage distribution on the front surface of the plate, there is no significant difference. In

all cases, the damage on the surface develops more significantly along the binder direction than the surface fibre orientation.

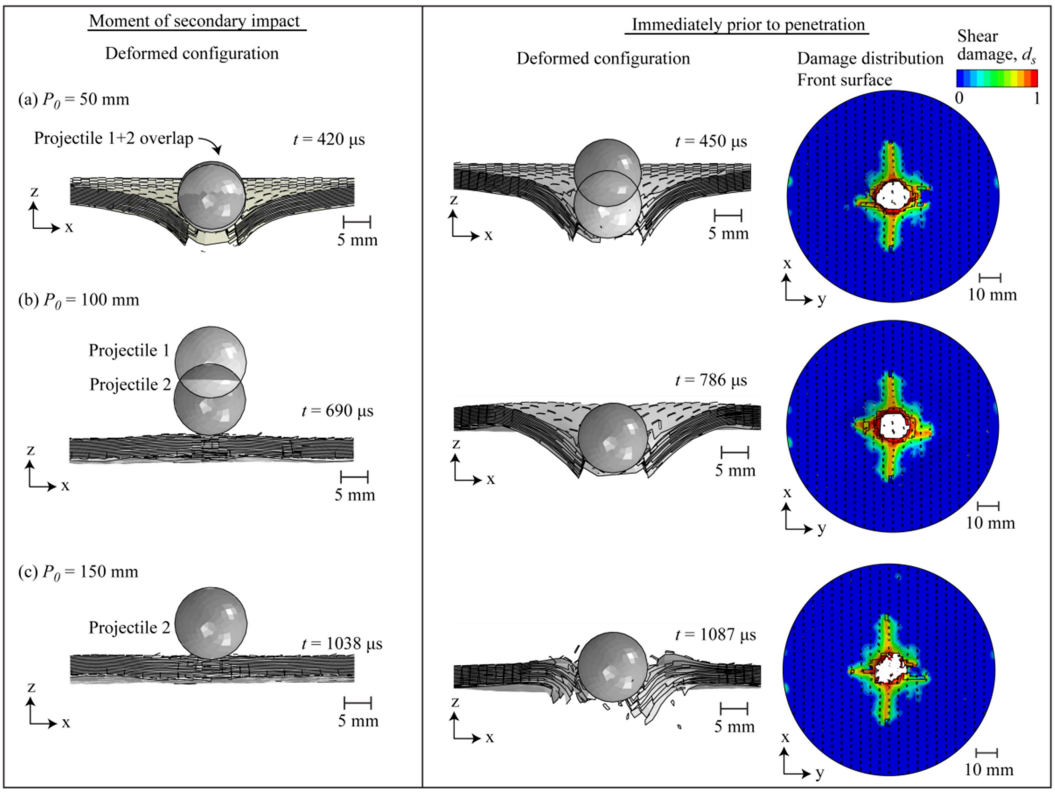


Figure 5.17. Numerically predicted deformed configuration of plate at the moment of secondary impact and deformed configuration and damage distribution within the front surface of the plate immediately prior to penetration for projectile off-set of (a) 50 mm, (b) 100 mm, (c) 150 mm. Half TTT material. Impact velocity $V_I = V_{II} = 145 \text{ms}^{-1}$. Damage distribution displays shear damage, d_s, with fully damaged elements deleted and removed from the visualisation.

5.7 Inter-laminar shear strength on the ballistic limit of UD-laminate composite plates

The study within this chapter has focused exclusively thus far on the influence of the through-the-thickness weave on the ballistic impact response of composite materials. However, as indicated by recent experimental studies, matrix shear strength can cause large modifications to the ballistic limit of composite laminate

plates [266]. They found that, for identical fibre properties and volume fraction, composites of lower matrix shear strength exhibited a significantly increased ballistic limit. No mechanistic mechanisms were given at the time for the reasoning behind this variation. A numerical parameter study is presented here in order to investigate the influence of inter-laminar shear strength on the ballistic limit of UD-laminate composite plates. The material investigated is the 15 layer 0/90° UD-laminate composite as presented earlier in this chapter, using the material data as presented in

Table 5.1 and Table 5.2. Simulations of increasing projectile velocities were undertaken at a range of inter-laminar shear strengths $(8\ \text{MPa} \le t_s \le 4000\ \text{MPa})$ in order to ascertain the predicted ballistic limit of each case to within 2.5 ms^{-1}. The normal strength remained constant as given in Table 5.2. A simulation was also undertaken with the cohesive interaction removed. This is referred to as the "Free Plies" case. In this case, the cohesive interaction between layers was removed, and the contact between them was reduced to that of the general contact algorithm within ABAQUS.

5.7.1 Numerically predicted ballistic limit

The predicted ballistic limit as a function of inter-laminar shear strength is presented in Figure 5.18. Increase of the inter-laminar shear strength gave a logarithmic decrease in the predicted ballistic limit V_L of the plate. Also presented in Figure 5.18 is the ballistic limit of the free plies case. The ballistic limit of the free plies case was estimated to be approximately 1.45 times higher than that of the regular composite material $(t_s = 80\ \text{MPa})$.

It is proposed that the primary mechanism which leads to the modification of the ballistic limit with varying inter-laminar shear strength is the modification of the area of delamination. This in turn changes the deformation mode and distribution of damage throughout the plate. This will be investigated in more detail in the remaining sections of this chapter.

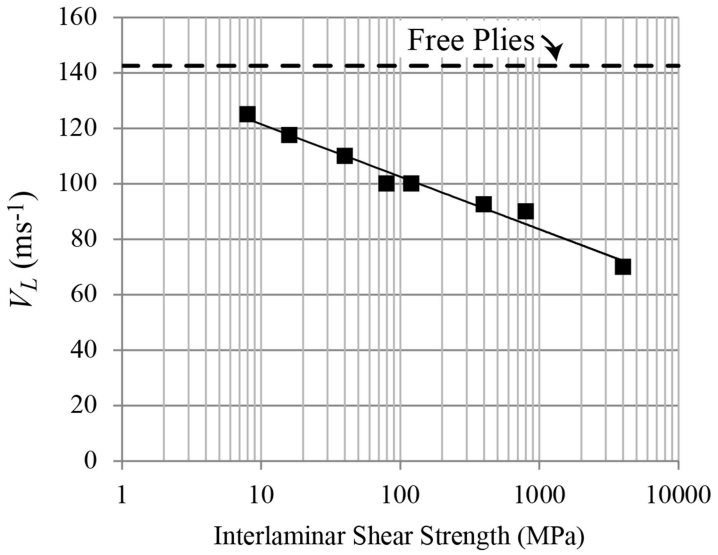


Figure 5.18. Predicted ballistic limit as a function of inter-laminar shear strength for a uni-directional laminate plate.

5.8 Concluding remarks

The impact properties of 3D woven composite and UD-laminate materials were investigated and compared via the use of a 3D numerical modelling strategy employed within the explicit version of the commercial software ABAQUS, simulating rigid-body projectiles within the velocity range $60\ \text{ms}^{-1} \leq v_0 \leq 150\ \text{ms}^{-1}$. The 3D woven ballistic impact numerical modelling strategy was validated via the deformed configurations and damage modes exhibited during experimental testing of spherical stainless steel projectiles impacting upon clamped 3D woven composite beam samples. Ballistic impact experiments upon 3D woven composite beam samples revealed two distinct damage modes; medium velocity stretch dominated fracture of in-plane fibre reinforcement, and higher velocity projectile penetration. The multi-hit impact simulation methodology for composite materials was validated by the comparison of a numerically predicted multi-hit ballistic limit surface of a UD-laminate material of layup $[(0°/90°)_7/0°]$ to that obtained experimentally by Kandan, Russell [162].

For the simulations of ballistic impact upon 3D woven composites, the transferal of stress from the in-plane fibre architecture to the through-thickness reinforcement was shown to reduce longitudinal stress within the in-plane fibres. This stress reduction was shown to be significant throughout the entire plate. The transferal of stress modifies the distribution of damage within the plate. The 3D woven composite exhibited more localised damage under the projectile strike location, whereas the equivalent UD-laminate material exhibited damage remote to the projectile strike location, with a characteristic "cross-shape" distribution.

The through-the-thickness reinforcement was shown to modify the penetration mechanisms of the material. For UD-laminate composites, a combination of the cross-shaped damage distribution and localised in-plane fibre fracture throughout the thickness of the material at the strike location allowed for large bending deformations of delaminated plates, leading to the pass-through of the projectile. The more highly concentrated damage mechanisms demonstrated by the 3D woven composite material led to a modification of the predicted penetration mechanism to that of extensive fracturing of in-plane and through-thickness reinforcement at the strike location. The fractured plies deformed locally, allowing for projectile pass-through. Delamination was restricted in location from under the projectile strike position, up until the closest TTT reinforcement tow. The 3D woven material exhibited asymmetrical damage distribution due to localised damage within the through-thickness reinforcement, and reduced propagation of delamination in comparison with the UD-laminate material. Finite element simulations predict an 8% increase in ballistic limit during singular impact events exclusively due to the presence of the through-the-thickness reinforcement.

Multi-hit impact FE simulations were undertaken to define the predicted ballistic limit surface in $v_I - v_{II}$ space of the 3D woven composite material, following the methodology introduced by Kandan, Russell [162]. 3D woven composite material and equivalent UD-laminate composite exhibited similar multi-hit ballistic limit

surfaces. However, the through-the-thickness reinforcement was shown to supress the bending deformation demonstrated within the UD-laminate. In regards to ballistic limit of the plate, this gave rise to enhanced performance of 3D woven composite compared to an equivalent UD-laminate material for higher velocity primary impacts, i.e. over 65% of the ballistic limit of the plate for the initial strike.

A numerical parameter study was undertaken for the projectile off-set for the simulation of multi-hit events. Varying the off-set from 50 mm to 150 mm for two successive impacts of $V_I = V_{II} = 145\ \text{ms}^{-1}$ gave rise to different plate configurations at the moment of secondary impact; 50 mm offset the projectile strikes whilst the plate is still deformed from the initial impact, and 150 mm off-set was shown to exhibit a different deformation mechanism around the projectile strike location during penetration of the second projectile. The predicted damage on the front surface of the beams was shown to be similar for the three off-set values.

Finite element analysis was employed to investigate the influence of inter-laminar shear strength of a fibre reinforced laminate composite under ballistic impact loading. In particular, the predicted ballistic limits of the plates were compared as a function of the inter-laminar shear strength. The resulting modification of the predicted ballistic limit was then traced back to changes in the damage distribution, damage modes, and the global deformed configuration of the plates during impact. For composite laminate plates of regular inter-laminar shear strength t_s = 80 MPa, a cross-shaped fibre tensile fracture damage mode was predicted, showing good agreement with experimental testing presented in the literature.

Composite laminate plates of inter-laminar shear strengths within the range simulated within this study ($8\,\text{MPa} \le t_s \le 3000\,\text{MPa}$) all exhibit delamination damage under the projectile strike location. However, increasing the inter-laminar

shear strength led to an increase in the distribution of damage remote from the projectile strike location.

5.9 Discussion and recommendations for future work

The numerical modelling of ballistic penetration of composite material with inherently complex geometries is plagued with difficulties. Some of these issues will now be discussed. One such example of these difficulties is the maintenance of numerical stability throughout the impact event. Due to the extensive reduction of element stiffness due to damage within the material, and large-scale deflections associated with projectile penetration, the finite element method often does not maintain numerical stability long enough to finish calculations. This issue is exacerbated during multi-hit simulations as it is combined with the interaction of reflected stress waves returning from the edge of the plates. It was determined that the impact methodology used for soft impact loading (as presented in Chapter 4) was unsuitable for the multi-hit simulation due to the high aspect ratio of the matrix elements between tows. This led to numerical instabilities due to excessive rotation of nodes, or distortion of slender elements. To combat this, the "Equivalent UD-laminate" modelling strategy, as presented in Chapter 4, was utilised for multi-hit simulations – this strategy allowed for more regular, stable elements within the in-plane architecture. Even with this, certain combinations of velocities were still presented instabilities at later stages of the impact events. Most commonly, the unstable calculations were when the primary impact was more than 95% of the ballistic limit of the material. An alternate modelling strategy for future work may include the conversion of fully damaged, or near fully-damaged, elements to particles in order to prevent excessive distortions of the mesh. The modelling strategy relies on calibration in the form of rate dependency and is therefore not a true predictive tool. The use of the numerical model here is for analysis purposes as opposed to the increased level of fidelity of prediction achieved by numerical models of higher detail.

The current work is limited to only one orthogonal through-the-thickness weave type. Alternate weave patterns such as angle-interlock or changes to the through-thickness reinforcement densities may exhibit significantly different multi-hit performance and are therefore suggested for future research.

The inter-laminar shear strength parameter study is related to interleafed composites, i.e. the addition of a high toughness resin to a laminate system, as first introduced by American Cyanamid [283]. The ability of interleafed laminates to increase the impact resistance of composite material systems by as much as 80% [284] means that the development and optimisation of such techniques could prove beneficial for the design of protective systems. However, despite its potential, the open literature has a relatively sparse covering of this topic.

Although the parameter study is limited to the inter-laminar shear strength, it begins to address the theoretical possibilities of designing new interleafed composite laminate systems that can be optimised for structural stiffness and impact damage resistance. Numerical modelling could be used in order to determine the optimum material interface properties and interleaf layup for structural stiffness and impact protection. Such studies would be able to expand upon experimental investigations such as the one undertaken on the interleafing sequence of a graphite/epoxy laminate [285], comparing the quantity of impact damage and CAI response.

The 3D woven multi-hit ballistic impact study and the inter-laminar shear strength parameter study presented in this chapter are related to each other by the damage modes inherent to fibre reinforced composites under ballistic impact loading. The distribution of damage and subsequent deformation of plates is the key driver in their performance. A reduction of the inter-laminar shear strength was shown to supress the development of the cross-shaped damage mode for UD-laminate composites, whilst the presence of through-the-thickness reinforcement was shown to reduce the propagation of this damage and subsequent bending within the plate, providing an increase to the ballistic limit.

CHAPTER 6

CONCLUSIONS AND RECOMMENDATIONS FOR FUTURE STUDY

6.1 Conclusions

As defined in Chapter 1, the objectives of the thesis were: (i) to develop the understanding of the collapse mechanisms of orthogonal 3D woven composites under quasi-static in-plane tension and compression and out-of-plane bending, (ii) to characterise the response of orthogonal 3D woven carbon fibre composites during dynamic soft impact loading, (iii) to understand the influence of fibre architecture and inter-laminar shear strength on the response of fibre reinforced composites undergoing singular and multi-hit ballistic impact loading. The conclusions drawn from the work presented in Chapter 3 through to Chapter 5 in this thesis are summarised below, with regards to the fulfilment of these objectives. Afterwards, recommendations are made for future works.

6.1.1 Quasi-static collapse of 3D woven carbon fibre composites

The quasi-static in-plane and out-of-plane properties of orthogonal 3D woven composites were investigated in detail via a combined experimental and numerical study. Qualitative comparisons were made with a similar UD-laminate material.

The cantilever beam test was shown to be effective in isolating two distinct collapse mechanisms of orthogonal 3D woven composite materials: bending deformation dominated long beam tests, and shear deformation dominated short beam tests. DIC analysis and post-fracture μ-CT scans were used to classify to the response of the material.

The through-the-thickness reinforcement within orthogonal 3D woven composites prevents delamination with long cantilever beam tests, and provides containment and limited change to the post-peak load response of short beam tests. Failure modes for long beam tests was the propagation of a tensile bending crack and a combination of delamination and in-plane fibre fracture for short beam tests.

A full scale embedded-element numerical modelling strategy was shown to be effective at predicting quasi-static in-plane tension and compression material coupon tests. The numerical model showed good fidelity for long cantilever beam tests, and for the prediction of the stiffness and initial peak load of short cantilever beam tests. It is suggested that the lack of fidelity for the post-peak load response of the short cantilever beam tests is due to the simplified constitutive model of the cohesive interaction, and simplification of the contribution of the through-thickness reinforcement by the element-tie methodology.

Numerical calculations indicate the potential of the through-thickness reinforcement to provide structural containment to pre-delaminated beams.

A parameter study indicated that the numerical model is insensitive to superposition effects, i.e. the doubling up of the elastic properties between the embedded shell and host solid elements for both in-plane and bending simulations.

The isolation and classification of the two distinct failure mechanisms exhibited by 3D woven composites under bending loading is a novel contribution to the literature.

6.1.2 Soft impact of orthogonal 3D woven composites

A combined experimental and numerical modelling study was undertaken in order to investigate the response of orthogonal 3D woven composite undergoing dynamic soft impact loading. High speed camera images were used to record the back-face deflection, and qualitative comparisons of damage modes made with a similar UD-laminate material.

The presence or density of the through-the-thickness reinforcement was shown to provide no significant influence to the back-face deflection of beams.

3D woven composite beams demonstrated no visible delamination, even when impacted at impulses high enough to cause catastrophic fibre fracture. Failure

mode was that of longitudinal fibre fracture at clamped ends due to stress concentrations and reflection of the bending wave. This is different to the extensive delamination exhibited by UD-laminate beams.

Post-impact clamped-clamped beam tests revealed negligible reductions of strength and small reductions in stiffness of orthogonal 3D woven composite beam post impact. The composite with a higher density of TTT reinforcement was seen to undergo a greater reduction of stiffness in comparison with the material with a lower density of TTT reinforcement.

FE simulations indicated the potential for TTT reinforcement to provide structural integrity even for pre-delaminated beams.

The soft impact response of orthogonal 3D woven composite materials has not previously been classified. The experimental and numerical study presented within Chapter 4 of this thesis provides a comprehensive investigation into the material's performance. A modified version of the numerical modelling strategy presented in Chapter 3 was shown to be suitable for predicting the back-face deflection and damage modes presented by the beams during soft impact.

6.1.3 Multi-hit ballistic impact characterisation of 3D woven composites

A study on the multi-hit ballistic impact response of carbon fibre reinforced composite materials was undertaken via the use of numerical modelling of singular and multi-hit single-site impact events with and without the presence of through-the-thickness reinforcement. The finite element modelling strategy was validated via ballistic impact simulations on orthogonal 3D woven composite beam samples.

Ballistic impact upon 3D woven composite beams gave rise to three distinct response types: (i) low velocity projectile reflection, with a combination of matrix cracking and damage to surface yarns, (ii) intermediate velocity stretch dominated

tensile fracture of beams at beam centre span, (iii) high velocity projectile penetration of beams combined with longitudinal fibre fracture at the beam centre-span position.

A significant reduction of stress within the in-plane fibre architecture remote from the projectile impact location was predicted due to the presence of the TTT reinforcement.

TTT reinforcement was predicted to provide an 8% increase to the ballistic limit of clamped circular plates. This was traced to a variation in predicted penetration mechanisms; UD-laminate composite plates exhibited bending of delaminated plies allowing early-onset projectile pass-through, lowering the ballistic limit.

In regards to the predicted multi-hit ballistic limit surface, the 3D woven composite material was predicted to have enhanced protection for relatively high velocity multi-hit impact events ($V_I \geq 0.75\, V_L$).

The single site multi-hit performance of 3D woven composites have has not yet previously been reported within the open literature. The numerical study presented in Chapter 5 of this thesis is the first attempt at describing the mechanisms in which through-the-thickness reinforcement can modify global damage and penetration mechanisms, ultimately leading to increased performance during multi-hit impact loading. The modelling strategy presented is ideal for use for multi-hit impacts due to the length of calculation time required for both impacts necessitating an efficient strategy.

Inter-laminar shear strength on the ballistic response of carbon fibre reinforced polymers (CFRPs)

A numerical modelling parameter study was undertaken on the ballistic impact response of laminate composite circular plates. The matrix properties of the material were investigated by varying the inter-laminar shear strength of the

cohesive interaction of the finite element model and examining the influence on the predicted damage modes and ballistic limit of plates.

All plates were predicted to undergo delaminated damage directly under the projectile strike location. Decreasing the inter-laminar shear strength of the composite plates caused an increase in the delamination damage remote from the impact location.

Increasing the inter-laminar shear strength led to a decrease in the predicted ballistic limit of plate; up to approximately 1.45 times increase for a 40 times increase in inter-laminar shear strength.

Fully delaminated regions within the plate after impact strike cause a modification in the deformed configuration of samples. Fully delaminated plates, i.e. simulations with no cohesive surface between layers, exhibit a deformation cone with one singular angle of which can be predicted by simple 1D analytical formula. Increased the inter-laminar shear strength caused plates to exhibit bending dominated deformation behaviour.

The increase of inter-laminar shear strength led to a modification of damage distribution throughout the thickness of the laminate plates; higher shear strengths led to a greater concentration of damage at the top and bottom surfaces of the samples, indicative of a bending dominated damage mode.

The work is related to a manufacturing technique referred to as “inter-leafing”. This is the inclusion of inter-laminar layers between plies of a laminate with differing properties to the surrounding matrix in order to improve performance under impact loading. The results presented within Chapter 5 are directly relevant to the development of this technology. Again, the analysis of the global deformed configurations of laminate plates is only possible with a full-scale modelling strategy. The question of the exact mechanistic reasoning behind an increased ballistic limit with decreasing matrix shear strength has been raised within the literature, and this work has begun to answer that.

6.2 Limitation of current study and future works

The following recommendations are suggested for future works:

6.2.1 Quasi-static collapse of 3D woven carbon fibre composites

Out-of-plane bending of other woven architectures

The study presented in Chapter 3 within this thesis is limited to only an orthogonal through-the-thickness weave architecture. It is suggested for further development of the characterisation of the out-of-plane collapse properties of 3D woven composite, and to further demonstrate the efficacy of the numerical modelling methodology, that alternative weave patterns be studied. This could prove useful for carbon fibre textile manufacturers for the optimisation of the future weave designs.

It is suggested that for improvement of the fidelity of simulation of the post peak-load response of short, shear deformation dominated cantilever beam bending experiments, the constitutive model of the cohesive contact be modified. An example of such mixed mode traction-separation constitutive model which may increase modelling fidelity is the Benzeggagh-Kenane (BK) fracture energy based criterion [258].

6.2.2 Soft impact of orthogonal 3D woven composites

The numerical modelling strategy employed within this study simplifies the interaction between the through-the-thickness reinforcement and the in-plane fibre architecture via the use of the element tie methodology. In reality, it has been reported that the deterrence of delamination may be due to limited frictional contact between the through-thickness reinforcement and the in-plane fibre architecture. It is therefore suggested that future studies be conducted in order to ascertain precisely the suitability of this simplification for the purpose of the simulation 3D woven composites undergoing soft impact and other load cases.

The soft impact experimental study was limited only to orthogonal through-the-thickness woven composite materials, it is yet to be seen if, for example, an angle-interlock architecture can provide equally effective damage mitigation. Therefore, this is also suggested as further research to lead on from this study.

Due to the exceptional damage mitigation properties of the woven composite demonstrated in Chapter 4, it is suggested that another load case be studied. Soft body impact, representing that of bird strikes, for example upon turbo fan engine fan blades and cases, is a critical load case which is integral to engineers for the design and development of the next generation of fan blades. For future work, it is suggested that the finite element modelling strategy developed within Chapter 4 be coupled with smooth-particle hydrodynamics to allow for the simulation of gelatine projectile strike upon the material. This, in conjunction with experimental testing, would provide comprehensive classification of orthogonal 3D woven composites under soft impact loading.

6.2.3 Multi-hit ballistic impact characterisation of 3D woven composites

Again, the limitation of one woven fibre architecture is inherent within the multi-hit ballistic impact numerical study presented in Chapter 5. Also, in reality, actual dynamic loading of structures may not include a double rigid impact event at exactly the same position. It is suggested that further characterisation of the 3D woven composites under impact load cases may be undertaken by a multi-hit study where the secondary impact is remote to the first. A study such as this could provide information regarding the progression of damage within the material and its influence upon ballistic penetration resistance.

Also, in reference to loading which maybe more representative to that which would be found in actual systems, the multi-hit investigation could be extended to include more than one load-case. For example, the combined hard and soft impact loading experienced by structures resisting buried landmine explosions may well

be the critical load case for the material selection of mobile vehicle protective systems. This combined load case was eluded to in the introduction to this thesis, and is suggested as future work for development of complete characterisation of 3D woven composites materials and the advantages they yield over traditional UD-laminates.

As computer systems become more powerful, and numerical calculations quicker, the modelling strategy presented within Chapter 5 could be adapted to yield greater detail. The use of shell elements for the ballistic impact simulation of 3D woven composites limits the impact velocities to relatively low, and the projectile to be spherical in shape. Jagged projectiles, which may well be produced during FOD on structures, would require a modified modelling strategy to capture the shear damage modes.

6.3 Published Work

Chapter 4 has been published within ASME: Journal of Applied Mechanics
Paul Turner, Tao Liu, and Xuesen Zeng. "Dynamic Response of Orthogonal Three-Dimensional Woven Carbon Composite Beams Under Soft Impact." Journal of Applied Mechanics 82.12 (2015): 121008. DOI: 10.1115/1.4031455

The work within Chapters 3 and 4 has been published at an international conference on composite materials (ECCM 16):
Paul Turner, Tao Liu and Xuesen Zeng (2014) Bending Characteristics of 3D woven carbon composites In: 16TH EUROPEAN CONFERENCE ON COMPOSITE MATERIALS.

Chapter 3 has been published within in Composite Structures journal. “Collapse of 3D Orthogonal Woven Carbon Fibre Composites Under In-plane Tension/Compression and Out-of-plane Bending Composite Structures”. Composite Structures Volume 142 (2016) DOI:10.1016/j.compstruct.2016.01.100

BIBLIOGRAPHY

1. Smith, C.S., *Design of marine structures in composite materials*. 1990: Elsevier London.

2. Haresceugh, R., *Aircraft and aerospace applications of composites.* Pergamon Press plc, Concise Encyclopedia of Composite Materials, 1989: p. 1-7.

3. Niu, M.C.-Y., *Composite airframe structures: practical design information and data*. 1992: Adaso Adastra Engineering Center.

4. Beardmore, P., *Automotive components: fabrication.* Pergamon Press plc, Concise Encyclopedia of Composite Materials, 1989: p. 24-31.

5. Marks, P., *Warning signs*, in *New Scientist*. 2005. p. 38-42.

6. Lee, L., et al., *Effect of weaving damage on the tensile properties of three-dimensional woven composites.* Composite Structures, 2002. **57**(1): p. 405-413.

7. Rudov-Clark, S., et al. *Weaving Damage to Three-Dimensional Glass-Polymer Composites*. in *44 th AIAA/ASME/ASCE/AHS/ASC Structures, Structural Dynamics, and Materials Conference*. 2003.

8. Mouritz, A., et al., *Review of applications for advanced three-dimensional fibre textile composites.* Composites Part A: applied science and manufacturing, 1999. **30**(12): p. 1445-1461.

9. Bannister, M., et al., *The manufacture of glass/epoxy composites with multilayer woven architectures.* Composites Part A: applied science and manufacturing, 1998. **29**(3): p. 293-300.

10. Tamuzs, V., S. Tarasovs, and U. Vilks, *Delamination properties of translaminar-reinforced composites.* Composites Science and Technology, 2003. **63**(10): p. 1423-1431.

11. Mouritz, A., C. Baini, and I. Herszberg, *Mode I interlaminar fracture toughness properties of advanced textile fibreglass composites.* Composites Part A: applied science and manufacturing, 1999. **30**(7): p. 859-870.

12. Ding, Y., W. Wenger, and R. McIlhagger, *Structural characterization and mechanical properties of 3-D woven composites.* Broadening horizons with advanced materials and processes, 1993: p. 1-9.

13. Shyr, T.-W. and Y.-H. Pan, *Impact resistance and damage characteristics of composite laminates.* Composite Structures, 2003. **62**(2): p. 193-203.

14. Wisnom, M., *The role of delamination in failure of fibre-reinforced composites.* Philosophical Transactions of the Royal Society of London A:

Mathematical, Physical and Engineering Sciences, 2012. **370**(1965): p. 1850-1870.

15. Li, X., S.R. Hallett, and M.R. Wisnom, *Predicting the effect of through-thickness compressive stress on delamination using interface elements.* Composites Part A: applied science and manufacturing, 2008. **39**(2): p. 218-230.

16. Ogi, K., et al., *Impact damage and residual tensile strength of a CF-SMC composite.* Advanced Composite Materials, 2013. **22**(1): p. 29-47.

17. Balasubramani, V. and S.R. Boopathy, *Prediction of residual tensile strength of lamianted composites after low velocity impact.* 2006.

18. Guedra-Degeorges, D., *Recent advances to assess mono-and multi-delaminations behaviour of aerospace composites.* Composites Science and Technology, 2006. **66**(6): p. 796-806.

19. Soutis, C. and P. Curtis, *Prediction of the post-impact compressive strength of CFRP laminated composites.* Composites Science and Technology, 1996. **56**(6): p. 677-684.

20. Pavier, M. and M. Clarke, *Finite element prediction of the post-impact compressive strength of fibre composites.* Composite Structures, 1996. **36**(1): p. 141-153.

21. Kedward, K., R. Wilson, and S. McLean, *Flexure of simply curved composite shapes.* composites, 1989. **20**(6): p. 527-536.

22. Martin, R., *Delamination failure in a unidirectional curved composite laminate.* Composite materials: Testing and design., 1992. **10**: p. 365-383.

23. Favre, J.-P., *Residual thermal stresses in fibre reinforced composite materials- A review.* Journal of the Mechanical Behavior of Materials, 1988. **1**(1): p. 37-53.

24. Zimmermann, K., D. Zenkert, and M. Siemetzki, *Testing and analysis of ultra thick composites.* Composites Part B: Engineering, 2010. **41**(4): p. 326-336.

25. Sjoblom, P.O., J.T. Hartness, and T.M. Cordell, *On low-velocity impact testing of composite materials.* Journal of composite materials, 1988. **22**(1): p. 30-52.

26. Geubelle, P.H. and J.S. Baylor, *Impact-induced delamination of composites: a 2D simulation.* Composites Part B: Engineering, 1998. **29**(5): p. 589-602.

27. Salpekar, S. and T. O'Brien, *Analysis of matrix cracking and local delamination in (0/θ/− θ) s graphite epoxy laminates under tensile load.* Journal of composites technology & research, 1993. **15**(2): p. 95-100.

28. Wisnom, M.R., M. Jones, and W. Cui, *Failure of tapered composites under static and fatigue tension loading.* AIAA journal, 1995. **33**(5): p. 911-918.

29. Thomas, D. and J. Webber, *A design study into the delamination behaviour of tapered composites.* Composite Structures, 1994. **27**(4): p. 379-388.

30. Fish, J.C. and S.W. Lee, *Delamination of tapered composite structures.* Engineering Fracture Mechanics, 1989. **34**(1): p. 43-54.

31. Lorriot, T., et al., *Onset of free-edge delamination in composite laminates under tensile loading.* Composites Part B: Engineering, 2003. **34**(5): p. 459-471.

32. Cui, W., M.R. Wisnom, and M. Jones, *An experimental and analytical study of delamination of unidirectional specimens with cut central plies.* Journal of reinforced plastics and composites, 1994. **13**(8): p. 722-739.

33. O'brien, T., *Characterization of delamination onset and growth in a composite laminate.* Damage in composite materials, ASTM STP, 1982. **775**(2): p. 140-167.

34. Sun, C. and S. Zhou, *Failure of quasi-isotropic composite laminates with free edges.* Journal of reinforced plastics and composites, 1988. **7**(6): p. 515-557.

35. Wisnom, M., B. Khan, and S. Hallett, *Size effects in unnotched tensile strength of unidirectional and quasi-isotropic carbon/epoxy composites.* Composite Structures, 2008. **84**(1): p. 21-28.

36. Kortschot, M.T. and P.W. Beaumont, *Damage mechanics of composite materials: I—Measurements of damage and strength.* Composites Science and Technology, 1990. **39**(4): p. 289-301.

37. Lagace, P.A., *Notch sensitivity of graphite/epoxy fabric laminates.* Composites Science and Technology, 1986. **26**(2): p. 95-117.

38. Wang, J., P. Callus, and M. Bannister, *Experimental and numerical investigation of the tension and compression strength of un-notched and notched quasi-isotropic laminates.* Composite Structures, 2004. **64**(3): p. 297-306.

39. O'higgins, R., M. McCarthy, and C. McCarthy, *Comparison of open hole tension characteristics of high strength glass and carbon fibre-reinforced composite materials.* Composites Science and Technology, 2008. **68**(13): p. 2770-2778.

40. Carlsson, L.A., C.-G. Aronsson, and J. Bäcklund, *Notch sensitivity of thermoset and thermoplastic laminates loaded in tension.* Journal of Materials Science, 1989. **24**(5): p. 1670-1682.

41. Xu, X., et al., *An experimental investigation into size effects in quasi-isotropic carbon/epoxy laminates with sharp and blunt notches.* Composites Science and Technology, 2014. **100**: p. 220-227.

42. Wisnom, M.R. and S.R. Hallett, *The role of delamination in strength, failure mechanism and hole size effect in open hole tensile tests on quasi-isotropic laminates.* Composites Part A: applied science and manufacturing, 2009. **40**(4): p. 335-342.

43. Hallett, S., et al., *An experimental and numerical investigation into the damage mechanisms in notched composites.* Composites Part A: applied science and manufacturing, 2009. **40**(5): p. 613-624.

44. Tan, J., V. Deshpande, and N. Fleck, *Failure mechanisms of a notched CFRP laminate under multi-axial loading.* Composites Part A: applied science and manufacturing, 2015. **77**: p. 56-66.

45. Budiansky, B. and N.A. Fleck, *Compressive failure of fibre composites.* Journal of the Mechanics and Physics of Solids, 1993. **41**(1): p. 183-211.

46. Soutis, C., P. Curtis, and N. Fleck, *Compressive failure of notched carbon fibre composites.* Proceedings of the Royal Society of London. Series A: Mathematical and Physical Sciences, 1993. **440**(1909): p. 241-256.

47. Lee, J. and C. Soutis, *Measuring the notched compressive strength of composite laminates: specimen size effects.* Composites Science and Technology, 2008. **68**(12): p. 2359-2366.

48. Soutis, C., N. Fleck, and P. Curtis, *Hole-hole interaction in carbon fibre/epoxy laminates under uniaxial compression.* composites, 1991. **22**(1): p. 31-38.

49. Garg, A.C., *Delamination—a damage mode in composite structures.* Engineering Fracture Mechanics, 1988. **29**(5): p. 557-584.

50. Glossop, N., et al., *Optical fibre damage detection for an aircraft composite leading edge.* composites, 1990. **21**(1): p. 71-80.

51. Waite, S., *Use of embedded optical fibre for early fatigue damage detection in composite materials.* composites, 1990. **21**(2): p. 148-154.

52. Waite, S., R. Tatam, and A. Jackson, *Use of optical fibre for damage and strain detection in composite materials.* composites, 1988. **19**(6): p. 435-442.

53. Kitade, S., T. Fukuda, and K. Osaka, *Fiber optic method for detection of impact induced damage in composite laminates.* Journal of the Society of Materials Science, Japan(Japan), 1995. **44**(504): p. 1196-1200.

54. Measures, R., *Advances toward fiber optic based smart structures.* Optical engineering(Bellingham. Print), 1992. **31**(1): p. 34-47.

55. Bhatia, V., et al., *Optical fiber sensing technique for edge-induced and internal delamination detection in composites.* Smart Materials and Structures, 1995. **4**(3): p. 164.

56. Chang, C.-C. and J. Sirkis, *Impact-induced damage of laminated graphite/epoxy composites monitored using embedded in-line fiber etalon optic sensors.* Journal of Intelligent Material Systems and Structures, 1997. **8**(10): p. 829-841.

57. Elvin, N., et al., *A novel fiber optic delamination detection scheme: theoretical and experimental feasibility studies.* Journal of Intelligent Material Systems and Structures, 1999. **10**(4): p. 314-321.

58. LeBlanc, M. and R.M. Measures, *Impact damage assessment in composite materials with embedded fibre-optic sensors.* Composites Engineering, 1992. **2**(5): p. 573-596.

59. Akira, T., K. Hideo, and K. Matsuura. *Application of electric potential method to smart composite structures for detecting delamination*. in *Proceedings of the Tenth International Conference on Composite Materials: Structures*. 1995. Woodhead Publishing.

60. Todoroki, A., M. Tanaka, and Y. Shimamura, *Measurement of orthotropic electric conductance of CFRP laminates and analysis of the effect on delamination monitoring with an electric resistance change method.* Composites Science and Technology, 2002. **62**(5): p. 619-628.

61. Todoroki, A., Y. Tanaka, and Y. Shimamura, *Response surface for delamination monitoring of graphite/epoxy composite using electric resistance change.* Structural Health Monitoring, 2000: p. 308-316.

62. Todoroki, A., Y. Tanaka, and Y. Shimamura, *Electric resistance change method for identification of embedded delamination of CFRP plates.*

Journal of the Society of Materials Science, Japan(Japan), 2001. **50**(5): p. 495-501.

63. Orłowska, A., P. Kołakowski, and J. Holnicki-Szulc, *Detecting delamination zones in composites by embedded electrical grid and thermographic methods.* Smart Materials and Structures, 2011. **20**(10): p. 105009.

64. Chang, F.-K. and M. Lin, *Diagnostic layer and methods for detecting structural integrity of composite and metallic materials*. 2002, Google Patents.

65. Qing, X.P., et al., *Built-in sensor network for structural health monitoring of composite structure.* Journal of Intelligent Material Systems and Structures, 2007. **18**(1): p. 39-49.

66. Zou, Y., L. Tong, and G. Steven, *Vibration-based model-dependent damage (delamination) identification and health monitoring for composite structures—a review.* Journal of Sound and vibration, 2000. **230**(2): p. 357-378.

67. Heida, J., P. Konijnenberg, and W. tHart, *Characterization of impact damage in carbon-epoxy composites.* Professional Engineering Publishing Limited, Impact and Dynamic Fracture of Polymers and Composites(UK), 1995: p. 359-370.

68. Cawley, P., *The rapid non-destructive inspection of large composite structures.* composites, 1994. **25**(5): p. 351-357.

69. Aymerich, F. and S. Meili, *Ultrasonic evaluation of matrix damage in impacted composite laminates.* Composites Part B: Engineering, 2000. **31**(1): p. 1-6.

70. Scarponi, C. and G. Briotti, *Ultrasonic technique for the evaluation of delaminations on CFRP, GFRP, KFRP composite materials.* Composites Part B: Engineering, 2000. **31**(3): p. 237-243.

71. Kažys, R. and L. Svilainis, *Ultrasonic detection and characterization of delaminations in thin composite plates using signal processing techniques.* Ultrasonics, 1997. **35**(5): p. 367-383.

72. Gerlach, R., et al., *In-plane and through-thickness properties, failure modes, damage and delamination in 3D woven carbon fibre composites subjected to impact loading.* Composites Science and Technology, 2012. **72**(3): p. 397-411.

73. Růžek, R., R. Lohonka, and J. Jironč, *Ultrasonic C-Scan and shearography NDI techniques evaluation of impact defects identification.* NDT & E International, 2006. **39**(2): p. 132-142.

74. Liu, D., et al., *The evaluation of delamination - an edge replication study.* Experimental Techniques, 1987. **11**(5): p. 20-25.

75. McDonald, S., et al., *X-ray tomographic imaging of Ti/SiC composites.* Journal of microscopy, 2003. **209**(2): p. 102-112.

76. Symons, D.D., *Characterisation of indentation damage in 0/90 lay-up T300/914 CFRP.* Composites Science and Technology, 2000. **60**(3): p. 391-401.

77. Schilling, P.J., et al., *X-ray computed microtomography of internal damage in fiber reinforced polymer matrix composites.* Composites Science and Technology, 2005. **65**(14): p. 2071-2078.

78. Maire, E., et al., *Recent results on 3D characterisation of microstructure and damage of metal matrix composites and a metallic foam using X-ray tomography.* Materials Science and Engineering: A, 2001. **319**: p. 216-219.

79. Geandier, G., et al., *Microstructural analysis of alumina chromium composites by X-ray tomography and 3-D finite element simulation of thermal stresses.* Scripta materialia, 2003. **48**(8): p. 1219-1224.

80. Lavoie, J.A. and E. Adolfsson, *Stitch cracks in constraint plies adjacent to a cracked ply.* Journal of composite materials, 2001. **35**(23): p. 2077-2097.

81. Zumpano, G., et al. *Structural damage analysis on a typical aeronautical structure using piezoelectric devices*. in *42 nd AIAA/ASME/ASCE/AHS/ASC Structures, Structural Dynamics, and Materials Conference and Exhibit*. 2001.

82. Doebling, S.W., et al., *Damage identification and health monitoring of structural and mechanical systems from changes in their vibration characteristics: a literature review*. 1996, Los Alamos National Lab., NM (United States).

83. Ratcliffe, C.P., *Damage detection using a modified Laplacian operator on mode shape data.* Journal of Sound and vibration, 1997. **204**(3): p. 505-517.

84. Kamiya, R., et al., *Some recent advances in the fabrication and design of three-dimensional textile preforms: a review.* Composites Science and Technology, 2000. **60**(1): p. 33-47.

85. Tong, L., A.P. Mouritz, and M. Bannister, *3D fibre reinforced polymer composites*. 2002: Elsevier.

86. Bogdanovich, A.E., *Multi-scale modeling, stress and failure analyses of 3-D woven composites.* Journal of Materials Science, 2006. **41**(20): p. 6547-6590.

87. Naik, N., S.N. Azad, and P.D. Prasad, *Stress and failure analysis of 3D angle interlock woven composites.* Journal of composite materials, 2002. **36**(1): p. 93-123.

88. Naik, N., et al., *Stress and failure analysis of 3D orthogonal interlock woven composites.* Journal of reinforced plastics and composites, 2001. **20**(17): p. 1485-1523.

89. Xiao, X., et al., *Through-thickness permeability study of orthogonal and angle-interlock woven fabrics.* Journal of Materials Science, 2015. **50**(3): p. 1257-1266.

90. Leong, K., et al., *The effect of binder path on the tensile properties and failure of multilayer woven CFRP composites.* Composites Science and Technology, 2000. **60**(1): p. 149-156.

91. Cox, B.N., M.S. Dadkhah, and W. Morris, *On the tensile failure of 3D woven composites.* Composites Part A: applied science and manufacturing, 1996. **27**(6): p. 447-458.

92. Dickinson, L., G. Farley, and M. Hinders, *Translaminar reinforced composites: a review.* Journal of composites technology & research, 1999. **21**(1): p. 3-15.

93. Cox, B.N. and G. Flanagan, *Handbook of analytical methods for textile composites*. Vol. 4750. 1997: National Aeronautics and Space Administration.

94. D'Amato, E., *Nonlinearities in mechanical behavior of textile composites.* Composite Structures, 2005. **71**(1): p. 61-67.

95. Cox, B., et al., *Failure mechanisms of 3D woven composites in tension, compression, and bending.* Acta Metallurgica et Materialia, 1994. **42**(12): p. 3967-3984.

96. Cox, B., et al., *Micromechanics of fatigue in woven and stitched composites*. Vol. 4626. 1994: National Aeronautics and Space Administration, Langley Research Center.

97. Callus, P., et al., *Tensile properties and failure mechanisms of 3D woven GRP composites.* Composites Part A: applied science and manufacturing, 1999. **30**(11): p. 1277-1287.

98. Kuo, W.-S., T.-H. Ko, and Y.-C. Shiah, *Compressive damage in three-axis woven thermoplastic composites.* Journal of Thermoplastic Composite Materials, 2006. **19**(4): p. 357-373.

99. Mouritz, A. and B. Cox, *A mechanistic interpretation of the comparative in-plane mechanical properties of 3D woven, stitched and pinned composites.* Composites Part A: applied science and manufacturing, 2010. **41**(6): p. 709-728.

100. Spearing, S. and A.G. Evans, *The role of fiber bridging in the delamination resistance of fiber-reinforced composites.* Acta Metallurgica et Materialia, 1992. **40**(9): p. 2191-2199.

101. De Morais, A., et al., *Mode-I interlaminar fracture of carbon/epoxy cross-ply composites.* Composites Science and Technology, 2002. **62**(5): p. 679-686.

102. La Saponara, V. and G.A. Kardomateas, *Crack branching in cross-ply composites: an experimental study.* Composite Structures, 2001. **53**(3): p. 333-344.

103. Sørensen, B.F. and T.K. Jacobsen, *Large-scale bridging in composites: R-curves and bridging laws.* Composites Part A: applied science and manufacturing, 1998. **29**(11): p. 1443-1451.

104. Fishpool, D., et al., *Interlaminar toughness characterisation of 3D woven carbon fibre composites.* Plastics, Rubber and Composites, 2013. **42**(3): p. 108-114.

105. Rudov-Clark, S., *Experimental investigation of the tensile properties and failure mechanisms of three-dimensional woven composites.* 2007.

106. Wang, Y. and D. Zhao, *Characterization of interlaminar fracture behaviour of woven fabric reinforced polymeric composites.* composites, 1995. **26**(2): p. 115-124.

107. Byun, J.-H., J.W. Gillespie, and T.-W. Chou, *Mode I delamination of a three-dimensional fabric composite.* Journal of composite materials, 1990. **24**(5): p. 497-518.

108. Blackman, B. and J. Williams. *On the mode II testing of carbon-fibre polymer composites*. in *ECF12, Sheffield 1998*. 1998.

109. Vanderkley, P.S., *Mode I-mode II delamination fractrue toughness of a unidirectional graphite/epoxy composite*. 1981, Texas A&M University.

110. Russell, A.J. and K.N. Street, *The effect of matrix toughness on delamination: static and fatigue fracture under mode II shear loading of graphite fiber composites.* Toughened Composites, ASTM STP, 1987. **937**: p. 275-294.

111. Martin, R., T. Elms, and S. Bowron. *Characterisation of mode II delamination using the 4 ENF*. in *4 th European Conference on Composites: Testing and Standardisation*. 1998.

112. Martin, R. and B. Davidson, *Mode II fracture toughness evaluation using four point bend, end notched flexure test.* Plastics, Rubber and Composites, 1999. **28**(8): p. 401-406.

113. ASTM, *D790-03*, in *Standard Test Methods for Flexural Properties of Unreinforced and Reinforced Plastics and Electrical Insulating Materials*. 2003. p. 1-11.

114. Blackman, B., A. Brunner, and J. Williams, *Mode II fracture testing of composites: a new look at an old problem.* Engineering Fracture Mechanics, 2006. **73**(16): p. 2443-2455.

115. Schuecker, C. and B.D. Davidson, *Effect of friction on the perceived mode II delamination toughness from three-and four-point bend end-notched flexure tests.* ASTM SPECIAL TECHNICAL PUBLICATION, 2001. **1383**: p. 334-344.

116. Robinson, P., *A concept for experimentally evaluating the effect of friction in the 4-ENF interlaminar toughness test.* International Journal of Fracture, 2001. **110**(3): p. 37-42.

117. Reedy, E. and T. Guess, *Comparison of interlocked fabric and laminated fabric Kevlar 49/epoxy composites.* Journal of Composites Technology and Research, 1985. **7**: p. 136.

118. Ding, Y., et al., *Comparison of the fatigue behaviour of 2-D and 3-D woven fabric reinforced composites.* Journal of materials processing technology, 1995. **55**(3): p. 171-177.

119. Wang, Y. and D. Zhao, *Effect of fabric structures on the mechanical properties of 3-D textile composites.* Journal of industrial textiles, 2006. **35**(3): p. 239-256.

120. Arendts, F., K. Drechsler, and J. Brandt. *Manufacturing and mechanical performance of composites with 3D woven fiber reinforcement*. in *Proceedings of the 38th International SAMPE Symposium*. 1989.

121. Lee, B., K. Leong, and I. Herszberg, *Effect of weaving on the tensile properties of carbon fibre tows and woven composites.* Journal of reinforced plastics and composites, 2001. **20**(8): p. 652-670.

122. Yan, Y. and Y.Q. DING, *Comparison of static properties of 2-D and 3-D woven fabric reinforced composites.* Journal of composites technology & research, 1999. **21**(1): p. 33-36.

123. Brandt, J., et al., *Manufacture and performance of carbon/epoxy 3-D woven composites.* 1992.

124. Rudov-Clark, S. and A. Mouritz, *Tensile fatigue properties of a 3D orthogonal woven composite.* Composites Part A: applied science and manufacturing, 2008. **39**(6): p. 1018-1024.

125. Rudov-Clark, S., et al., *Fibre damage in the manufacture of advanced three-dimensional woven composites.* Composites Part A: applied science and manufacturing, 2003. **34**(10): p. 963-970.

126. Marissen, R. and H. Brouwer, *The significance of fibre microbuckling for the flexural strength of a composite.* Composites Science and Technology, 1999. **59**(3): p. 327-330.

127. Hahn, H.T. and J.G. Williams, *Compression failure mechanisms in unidirectional composites.* Composite Materials: Testing and Design, 1986: p. 115-139.

128. Yang, B., et al., *Bending, compression, and shear behavior of woven glass fiber–epoxy composites.* Composites Part B: Engineering, 2000. **31**(8): p. 715-721.

129. Farley, G.L. and L.C. Dickinson. *Mechanical response of composite materials with through-the-thickness reinforcement*. in *NASA conference publication*. 1991.

130. Cox, B., et al., *Mechanisms of compressive failure in 3D composites.* Acta Metallurgica et Materialia, 1992. **40**(12): p. 3285-3298.

131. Cox, B., W. Carter, and N. Fleck, *A binary model of textile composites—I. Formulation.* Acta Metallurgica et Materialia, 1994. **42**(10): p. 3463-3479.

132. Hirokawa, T., et al. *The characteristics of 3-D orthogonal woven fabric reinforced composites*. in *Proceedings of the 36th international SAMPE symposium, Covina, CA*. 1991.

133. Gerlach, R., et al., *Experimental characterisation and constitutive modelling of RTM-6 resin under impact loading.* Polymer, 2008. **49**(11): p. 2728-2737.

134. Daniel, I., R. LaBedz, and T. Liber, *New method for testing composites at very high strain rates.* Experimental Mechanics, 1981. **21**(2): p. 71-77.

135. Zhou, Y., D. Jiang, and Y. Xia, *Tensile mechanical behavior of T300 and M40J fiber bundles at different strain rate.* Journal of Materials Science, 2001. **36**(4): p. 919-922.

136. Greenhalgh, E. and M. Hiley, *The assessment of novel materials and processes for the impact tolerant design of stiffened composite aerospace structures.* Composites Part A: applied science and manufacturing, 2003. **34**(2): p. 151-161.

137. Zhou, G. and G. Davies, *Characterization of thick glass woven roving/polyester laminates: 1. Tension, compression and shear.* composites, 1995. **26**(8): p. 579-586.

138. Luo, Y., et al., *Transverse impact behavior and energy absorption of three-dimensional orthogonal hybrid woven composites.* Composite Structures, 2007. **81**(2): p. 202-209.

139. Walter, T., et al., *Monotonic and cyclic short beam shear response of 3D woven composites.* Composites Science and Technology, 2010. **70**(15): p. 2190-2197.

140. Mallick, P.K., *Fiber-reinforced composites: materials, manufacturing, and design*. 1993: CRC press.

141. Gras, R., et al., *Identification of the out-of-plane shear modulus of a 3D woven composite.* Experimental Mechanics, 2013. **53**(5): p. 719-730.

142. Zhang, D., et al., *Flexural Behavior of a Layer-to-Layer Orthogonal Interlocked Three-Dimensional Textile Composite.* Journal of Engineering Materials and Technology, 2012. **134**(3): p. 031009.

143. Fukuda, H., *A new bending test method of advanced composites.* Experimental Mechanics, 1989. **29**(3): p. 330-335.

144. Liu, G., et al., *Collapse of a composite beam made from ultra high molecular-weight polyethylene fibres.* Journal of the Mechanics and Physics of Solids, 2014. **63**: p. 320-335.

145. LeBlanc, J., et al., *Shock loading of three-dimensional woven composite materials.* Composite Structures, 2007. **79**(3): p. 344-355.

146. Tekalur, S.A., A.E. Bogdanovich, and A. Shukla, *Shock loading response of sandwich panels with 3-D woven E-glass composite skins and stitched foam core.* Composites Science and Technology, 2009. **69**(6): p. 736-753.

147. Radford, D., V. Deshpande, and N. Fleck, *The use of metal foam projectiles to simulate shock loading on a structure.* International Journal of Impact Engineering, 2005. **31**(9): p. 1152-1171.

148. Abrate, S., B. Castanie, and Y.D. Rajapakse, *Dynamic Failure of Composite and Sandwich Structures*. Vol. 192. 2012: Springer Science & Business Media.

149. Swisdak Jr, M.M., *Explosion Effects and Properties. Part II. Explosion Effects in Water*. 1978, DTIC Document.

150. Cole, R., *Underwater explosions.* Princeton UP, 1948.

151. Smith, P.D. and J.G. Hetherington, *Blast and ballistic loading of structures*. 1994: Digital Press.

152. Liu, T., et al., *The impact of sand slugs against beams and plates: Coupled discrete particle/finite element simulations.* Journal of the Mechanics and Physics of Solids, 2013. **61**(8): p. 1798-1821.

153. Radford, D., N. Fleck, and V. Deshpande, *The response of clamped sandwich beams subjected to shock loading.* International Journal of Impact Engineering, 2006. **32**(6): p. 968-987.

154. Radford, D., et al., *The response of clamped sandwich plates with metallic foam cores to simulated blast loading.* International Journal of solids and structures, 2006. **43**(7): p. 2243-2259.

155. McShane, G., et al., *The response of clamped sandwich plates with lattice cores subjected to shock loading.* European Journal of Mechanics-A/Solids, 2006. **25**(2): p. 215-229.

156. Russell, B., et al., *The soft impact of composite sandwich beams with a square-honeycomb core.* International Journal of Impact Engineering, 2012. **48**: p. 65-81.

157. Kandan, K., et al., *The soft impact response of composite laminate beams.* International Journal of Impact Engineering, 2013. **60**(0): p. 24-36.

158. Parga-Landa, B., et al., *Analytical simulation of stress wave propagation in composite materials.* Composite Structures, 1999. **45**(2): p. 125-129.

159. Qian, L., M. Qu, and G. Feng, *Study on terminal effects of dense fragment cluster impact on armor plate. Part I: analytical model.* International Journal of Impact Engineering, 2005. **31**(6): p. 755-767.

160. Qian, L. and M. Qu, *Study on terminal effects of dense fragment cluster impact on armor plate. Part II: numerical simulations.* International Journal of Impact Engineering, 2005. **31**(6): p. 769-780.

161. Deka, L., S. Bartus, and U. Vaidya, *Multi-site impact response of S2-glass/epoxy composite laminates.* Composites Science and Technology, 2009. **69**(6): p. 725-735.

162. Kandan, K., et al., *Multi-hit armour characterisation of metal-composite bi-layers.* Journal of mechanics of materials and structures, 2013. **7**(7): p. 721-734.

163. Russell, B., *Multi-hit ballistic damage characterisation of 304 stainless steel plates with finite elements.* Materials & Design, 2014. **58**: p. 252-264.

164. Tsai, S.W. and E.M. Wu, *A general theory of strength for anisotropic materials.* Journal of composite materials, 1971. **5**(1): p. 58-80.

165. Hashin, Z., *Failure criteria for unidirectional fiber composites.* Journal of applied mechanics, 1980. **47**(2): p. 329-334.

166. Chang, F.-K. and K.-Y. Chang, *A progressive damage model for laminated composites containing stress concentrations.* Journal of composite materials, 1987. **21**(9): p. 834-855.

167. Kachanov, L.M., *On the creep fracture time.* Izv Akad, Nauk USSR Otd Tech, 1958. **8**: p. 26-31.

168. Talreja, R., *Damage characterization by internal variables.* Composite materials series, 1994: p. 53-53.

169. Frantziskonis, G., *Distributed damage in composites, theory and verification.* Composite Structures, 1988. **10**(2): p. 165-184.

170. Frantziskonis, G. and S. Joshi, *Damage evolution and constitutive behavior of advanced composites.* Composite Structures, 1990. **16**(4): p. 341-357.

171. Ladeveze, P. and E. LeDantec, *Damage modelling of the elementary ply for laminated composites.* Composites Science and Technology, 1992. **43**(3): p. 257-267.

172. Ladevèze, P. and G. Lubineau, *On a damage mesomodel for laminates: micro–meso relationships, possibilities and limits.* Composites Science and Technology, 2001. **61**(15): p. 2149-2158.

173. Ladeveze, P. and G. Lubineau, *An enhanced mesomodel for laminates based on micromechanics.* Composites Science and Technology, 2002. **62**(4): p. 533-541.

174. Allix, O. and P. Ladevèze, *Interlaminar interface modelling for the prediction of delamination.* Composite Structures, 1992. **22**(4): p. 235-242.

175. Ladeveze, P. and G. Lubineau, *On a damage mesomodel for laminates: micromechanics basis and improvement.* Mechanics of materials, 2003. **35**(8): p. 763-775.

176. Coutellier, D. and P. Rozycki, *Multi-layered multi-material finite element for crashworthiness studies.* Composites Part A: applied science and manufacturing, 2000. **31**(8): p. 841-851.

177. Johnson, A., A. Pickett, and P. Rozycki, *Computational methods for predicting impact damage in composite structures.* Composites Science and Technology, 2001. **61**(15): p. 2183-2192.

178. Matzenmiller, A., J. Lubliner, and R. Taylor, *A constitutive model for anisotropic damage in fiber-composites.* Mechanics of materials, 1995. **20**(2): p. 125-152.

179. Ortiz, M., *A constitutive theory for the inelastic behavior of concrete.* Mechanics of materials, 1985. **4**(1): p. 67-93.

180. Yazdani, S. and H. Schreyer, *An anisotropic damage model with dilatation for concrete.* Mechanics of materials, 1988. **7**(3): p. 231-244.

181. Ju, J., *On energy-based coupled elastoplastic damage theories: constitutive modeling and computational aspects.* International Journal of solids and structures, 1989. **25**(7): p. 803-833.

182. Williams, K.V. and R. Vaziri, *Application of a damage mechanics model for predicting the impact response of composite materials.* Computers & structures, 2001. **79**(10): p. 997-1011.

183. Hou, J., et al., *Prediction of impact damage in composite plates.* Composites Science and Technology, 2000. **60**(2): p. 273-281.

184. Luo, R., E. Green, and C. Morrison, *An approach to evaluate the impact damage initiation and propagation in composite plates.* Composites Part B: Engineering, 2001. **32**(6): p. 513-520.

185. Guan, Z. and C. Yang, *Low-velocity impact and damage process of composite laminates.* Journal of composite materials, 2002. **36**(7): p. 851-871.

186. Iannucci, L., *Progressive failure modelling of woven carbon composite under impact.* International Journal of Impact Engineering, 2006. **32**(6): p. 1013-1043.

187. Batra, R., G. Gopinath, and J. Zheng, *Damage and failure in low energy impact of fiber-reinforced polymeric composite laminates.* Composite Structures, 2012. **94**(2): p. 540-547.

188. Sheikh, A.H., P.H. Bull, and J.A. Kepler, *Behaviour of multiple composite plates subjected to ballistic impact.* Composites Science and Technology, 2009. **69**(6): p. 704-710.

189. Grujicic, M., et al., *A computational analysis of the ballistic performance of light-weight hybrid composite armors.* Applied Surface Science, 2006. **253**(2): p. 730-745.

190. Silva, M.A., C. Cismaşiu, and C. Chiorean, *Numerical simulation of ballistic impact on composite laminates.* International Journal of Impact Engineering, 2005. **31**(3): p. 289-306.

191. Chang, K.-Y., S. Llu, and F.-K. Chang, *Damage tolerance of laminated composites containing an open hole and subjected to tensile loadings.* Journal of composite materials, 1991. **25**(3): p. 274-301.

192. Shokrieh, M.M. and L.B. Lessard, *Progressive fatigue damage modeling of composite materials, Part I: Modeling.* Journal of composite materials, 2000. **34**(13): p. 1056-1080.

193. Yang, Q. and B. Cox, *Cohesive models for damage evolution in laminated composites.* International Journal of Fracture, 2005. **133**(2): p. 107-137.

194. Rybicki, E.F. and M. Kanninen, *A finite element calculation of stress intensity factors by a modified crack closure integral.* Engineering Fracture Mechanics, 1977. **9**(4): p. 931-938.

195. Shivakumar, K., P. Tan, and J. Newman, *A virtual crack-closure technique for calculating stress intensity factors for cracked three dimensional bodies.* International Journal of Fracture, 1988. **36**(3): p. R43-R50.

196. Raju, I., K. Hivakumar, and J. Rews, *Three-dimensional elastic analysis of a composite double cantilever beam specimen.* AIAA journal, 1988. **26**(12): p. 1493-1498.

197. Dattaguru, B., et al., *Finite element estimates of strain energy release rate components at the tip of an interface crack under mode I loading.* Engineering Fracture Mechanics, 1994. **49**(3): p. 451-463.

198. Borg, R., L. Nilsson, and K. Simonsson, *Simulation of low velocity impact on fiber laminates using a cohesive zone based delamination model.* Composites Science and Technology, 2004. **64**(2): p. 279-288.

199. Zou, Z., et al. *General expressions for energy–release rates for delamination in composite laminates*. in *Proceedings of the Royal Society of London A: Mathematical, Physical and Engineering Sciences*. 2002. The Royal Society.

200. Tay, T., *Characterization and analysis of delamination fracture in composites: an overview of developments from 1990 to 2001.* Applied Mechanics Reviews, 2003. **56**(1): p. 1-32.

201. Dolbow, J. and T. Belytschko, *A finite element method for crack growth without remeshing.* Int. J. Numer. Meth. Eng, 1999. **46**(1): p. 131-150.

202. Gifford, L.N. and P.D. Hilton, *Stress intensity factors by enriched finite elements.* Engineering Fracture Mechanics, 1978. **10**(3): p. 485-496.

203. Huynh, D. and T. Belytschko, *The extended finite element method for fracture in composite materials.* International Journal for Numerical Methods in Engineering, 2009. **77**(2): p. 214-239.

204. Kästner, M., G. Haasemann, and V. Ulbricht, *Multiscale XFEM-modelling and simulation of the inelastic material behaviour of textile-reinforced polymers.* International Journal for Numerical Methods in Engineering, 2011. **86**(4-5): p. 477-498.

205. Motamedi, D. and S. Mohammadi, *Fracture analysis of composites by time independent moving-crack orthotropic XFEM.* International Journal of Mechanical Sciences, 2012. **54**(1): p. 20-37.

206. Wang, Z., et al., *Numerical simulation of crack growth in brittle matrix of particle reinforced composites using the xfem technique.* Acta Mechanica Solida Sinica, 2012. **25**(1): p. 9-21.

207. Fries, T.P., *A corrected XFEM approximation without problems in blending elements.* International Journal for Numerical Methods in Engineering, 2008. **75**(5): p. 503-532.

208. Zou, Z., S. Reid, and S. Li, *A continuum damage model for delaminations in laminated composites.* Journal of the Mechanics and Physics of Solids, 2003. **51**(2): p. 333-356.

209. Li, S., S.R. Reid, and Z. Zou, *Modelling damage of multiple delaminations and transverse matrix cracking in laminated composites due to low velocity lateral impact.* Composites Science and Technology, 2006. **66**(6): p. 827-836.

210. Espinosa, H., S. Dwivedi, and H.-C. Lu, *Modeling impact induced delamination of woven fiber reinforced composites with contact/cohesive laws.* Computer Methods in Applied Mechanics and Engineering, 2000. **183**(3): p. 259-290.

211. Dávila, C.G., C.A. Rose, and P.P. Camanho, *A procedure for superposing linear cohesive laws to represent multiple damage mechanisms in the fracture of composites.* International Journal of Fracture, 2009. **158**(2): p. 211-223.

212. Cox, B. and M. Dadkhah, *The macroscopic elasticity of 3D woven composites.* Journal of composite materials, 1995. **29**(6): p. 785-819.

213. Ishikawa, T. and T.-W. Chou, *Stiffness and strength behaviour of woven fabric composites.* Journal of Materials Science, 1982. **17**(11): p. 3211-3220.

214. Tarnopol'skii, Y.M., V. Polyakov, and I. Zhigun, *Composite materials reinforced with a system of three straight, mutually orthogonal fibers.* Polymer Mechanics, 1973. **9**(5): p. 754-759.

215. Kregers, A. and Y.G. Melbardis, *Determination of the deformability of three-dimensionally reinforced composites by the stiffness averaging method.* Mechanics of Composite Materials, 1978. **14**(1): p. 1-5.

216. Kregers, A. and Y.G. Melbardis, *Calculation of the deformability of a three-dimensionally reinforced composite with an elastoplastic matrix.* Mechanics of Composite Materials, 1983. **18**(4): p. 408-413.

217. Yang, J.-M., C.-L. Ma, and T.-W. Chou, *Fiber inclination model of three-dimensional textile structural composites.* Journal of composite materials, 1986. **20**(5): p. 472-484.

218. Li, S., *Boundary conditions for unit cells from periodic microstructures and their implications.* Composites Science and Technology, 2008. **68**(9): p. 1962-1974.

219. Zeng, X., et al., *Geometrical modelling of 3D woven reinforcements for polymer composites: Prediction of fabric permeability and composite mechanical properties.* Composites Part A: applied science and manufacturing, 2014. **56**: p. 150-160.

220. Green, S., et al., *Mechanical modelling of 3D woven composites considering realistic unit cell geometry.* Composite Structures, 2014. **118**: p. 284-293.

221. Wang, X., et al., *Multi-scale analyses of 3D woven composite based on periodicity boundary conditions.* Journal of composite materials, 2007. **41**(14): p. 1773-1788.

222. Xia, Z., et al., *On selection of repeated unit cell model and application of unified periodic boundary conditions in micro-mechanical analysis of composites.* International Journal of solids and structures, 2006. **43**(2): p. 266-278.

223. Nagai, K., et al., *Strength analysis for three-dimensional fibre reinforced composites.* Adv Preform Mater, 1995(2): p. 161-176.

224. Huang, H. and A.M. Waas, *Compressive response of Z-pinned woven glass fiber textile composite laminates: Modeling and computations.* Composites Science and Technology, 2009. **69**(14): p. 2338-2344.

225. Huang, H.J. and A.M. Waas, *Modeling and predicting the compression strength limiting mechanisms in Z-pinned textile composites.* Composites Part B: Engineering, 2009. **40**(6): p. 530-539.

226. Thuruthimattam, B. and N. Naik, *Mechanical characterization of hybrid 3D orthogonally woven composites.* AIAA journal, 1998. **98**(1809).

227. Tan, P., L. Tong, and G. Steven, *Behavior of 3D orthogonal woven CFRP composites. Part II. FEA and analytical modeling approaches.* Composites Part A: applied science and manufacturing, 2000. **31**(3): p. 273-281.

228. Bogdanovich, A.E. *Progressive failure modeling and strength predictions of 3-D woven composites*. in *Proceedings of the 50th AIAA/ASME/ASCE/AHS/ASC Structures, Structural Dynamics, and Materials Conference, Palm Springs, CA, USA*. 2009.

229. Xu, J., et al., *A binary model of textile composites—II. The elastic regime.* Acta Metallurgica et Materialia, 1995. **43**(9): p. 3511-3524.

230. McGlockton, M., B. Cox, and R. McMeeking, *A binary model of textile composites: III high failure strain and work of fracture in 3D weaves.* Journal of the Mechanics and Physics of Solids, 2003. **51**(8): p. 1573-1600.

231. Hsiao, H. and I. Daniel, *Strain rate behavior of composite materials.* Composites Part B: Engineering, 1998. **29**(5): p. 521-533.

232. Gilat, A., R.K. Goldberg, and G.D. Roberts, *Experimental study of strain-rate-dependent behavior of carbon/epoxy composite.* Composites Science and Technology, 2002. **62**(10): p. 1469-1476.

233. Barre, S., T. Chotard, and M. Benzeggagh, *Comparative study of strain rate effects on mechanical properties of glass fibre-reinforced thermoset matrix composite.* Composites Part A: applied science and manufacturing, 1996. **27**(12): p. 1169-1181.

234. Welsh, L. and J. Harding, *Effect of strain rate on the tensile failure of woven reinforced polyester resin composites.* Le Journal de Physique Colloques, 1985. **46**(C5): p. C5-405-C5-414.

235. Pankow, M., et al., *Split Hopkinson pressure bar testing of 3D woven composites.* Composites Science and Technology, 2011. **71**(9): p. 1196-1208.

236. Tay, T., H. Ang, and V. Shim, *An empirical strain rate-dependent constitutive relationship for glass-fibre reinforced epoxy and pure epoxy.* Composite Structures, 1995. **33**(4): p. 201-210.

237. Li, Z. and J. Lambros, *Strain rate effects on the thermomechanical behavior of polymers.* International Journal of solids and structures, 2001. **38**(20): p. 3549-3562.

238. Gilat, A., R.K. Goldberg, and G.D. Roberts, *Strain rate sensitivity of epoxy resin in tensile and shear loading.* Journal of Aerospace Engineering, 2007.

239. Ochola, R., et al., *Mechanical behaviour of glass and carbon fibre reinforced composites at varying strain rates.* Composite Structures, 2004. **63**(3): p. 455-467.

240. Groves, S.E., et al., *High strain rate effects for composite materials.* ASTM SPECIAL TECHNICAL PUBLICATION, 1993. **1206**: p. 162-162.

241. Melin, L. and L. Asp, *Effects of strain rate on transverse tension properties of a carbon/epoxy composite: studied by moire photography.* Composites Part A: applied science and manufacturing, 1999. **30**(3): p. 305-316.

242. Jacob, G.C., et al., *Strain rate effects on the mechanical properties of polymer composite materials.* Journal of Applied Polymer Science, 2004. **94**(1): p. 296-301.

243. Wei, X., et al., *A new rate-dependent unidirectional composite model–Application to panels subjected to underwater blast.* Journal of the Mechanics and Physics of Solids, 2013. **61**(6): p. 1305-1318.

244. Daniel, I.M., et al., *Engineering mechanics of composite materials*. Vol. 3. 1994: Oxford university press New York.

245. Daniel, I.M., et al., *Interfiber/interlaminar failure of composites under multi-axial states of stress.* Composites Science and Technology, 2009. **69**(6): p. 764-771.

246. Pankow, M., et al., *Modeling the response, strength and degradation of 3D woven composites subjected to high rate loading.* Composite Structures, 2012. **94**(5): p. 1590-1604.

247. Ji, C., et al., *Impact damage of 3D orthogonal woven composite circular plates.* Applied Composite Materials, 2007. **14**(5-6): p. 343-362.

248. Ji, K.H. and S.J. Kim, *Dynamic direct numerical simulation of woven composites for low-velocity impact.* Journal of composite materials, 2007. **41**(2): p. 175-200.

249. Sun, B., Y. Liu, and B. Gu, *A unit cell approach of finite element calculation of ballistic impact damage of 3-D orthogonal woven composite.* Composites Part B: Engineering, 2009. **40**(6): p. 552-560.

250. Li, Z., B. Sun, and B. Gu, *FEM simulation of 3D angle-interlock woven composite under ballistic impact from unit cell approach.* Computational Materials Science, 2010. **49**(1): p. 171-183.

251. Cristian, I., et al., *A study of strength transfer from tow to textile composite using different reinforcement architectures.* Applied Composite Materials, 2012. **19**(3-4): p. 427-442.

252. Stig, F. and S. Hallström, *Assessment of the mechanical properties of a new 3D woven fibre composite material.* Composites Science and Technology, 2009. **69**(11): p. 1686-1692.

253. Quinn, J., A. McIlhagger, and R. McIlhagger, *Examination of the failure of 3D woven composites.* Composites Part A: applied science and manufacturing, 2008. **39**(2): p. 273-283.

254. Bogdanovich, A.E. *Advancements in manufacturing and applications of 3D woven preforms and composites*. in *Proceeding of the 16th international conference on composites materials (ICCM-16)*. 2007.

255. Budiansky, B. and N.A. Fleck, *Compressive kinking of fiber composites: a topical review.* Applied Mechanics Reviews, 1994. **47**(6S): p. S246-S250.

256. Cui, W., M. Wisnom, and M. Jones, *Failure mechanisms in three and four point short beam bending tests of unidirectional glass/epoxy.* The Journal of Strain Analysis for Engineering Design, 1992. **27**(4): p. 235-243.

257. Cui, W.C. and M.R. Wisnom, *Contact finite element analysis of three-and four-point short-beam bending of unidirectional composites.* Composites Science and Technology, 1992. **45**(4): p. 323-334.

258. Camanho, P.P. and C.G. Dávila, *Mixed-mode decohesion finite elements for the simulation of delamination in composite materials.* NASA-Technical paper, 2002. **211737**(1): p. 33.

259. Soutis, C., N. Fleck, and P. Smith, *Compression fatigue behaviour of notched carbon fibre-epoxy laminates.* International journal of fatigue, 1991. **13**(4): p. 303-312.

260. Yu, Y., X. Wang, and C. Lim, *Ballistic impact of 3D orthogonal woven composite by a spherical bullet: experimental study and numerical simulation.* International Journal of Engineering and Applied Sciences, 2009. **1**: p. 11-18.

261. Ghosh, R. and S. De, *Z-fiber influence on high speed penetration of 3D orthogonal woven fiber composites.* Mechanics of materials, 2014. **68**: p. 147-163.

262. Jia, X., B. Sun, and B. Gu, *A numerical simulation on ballistic penetration damage of 3D orthogonal woven fabric at microstructure level.* International Journal of Damage Mechanics, 2011: p. 1056789510397078.

263. Duvaunt, G. and J. Lions, *Inequalities in Mechanics and Physics*. 1976: Springer.

264. Deshpande, V. and N. Fleck, *High strain rate compressive behaviour of aluminium alloy foams.* International Journal of Impact Engineering, 2000. **24**(3): p. 277-298.

265. Xue, Z. and J.W. Hutchinson, *A comparative study of impulse-resistant metal sandwich plates.* International Journal of Impact Engineering, 2004. **30**(10): p. 1283-1305.

266. Kandan, K., et al., *The effect of shear strength on the ballistic response of laminated composite plates.* European Journal of Mechanics-A/Solids, 2013. **42**: p. 35-53.

267. Yen, C.-F., et al. *Dynamic Characterization and Modeling of 3D Woven Composite Ballistic Behavior*. in *American Society of Composites, 26th Annual Technical Conference*. 2011.

268. Mines, R., S. McKown, and R. Birch, *Impact of aircraft rubber tyre fragments on aluminium alloy plates: I—Experimental.* International Journal of Impact Engineering, 2007. **34**(4): p. 627-646.

269. Karagiozova, D. and R. Mines, *Impact of aircraft rubber tyre fragments on aluminium alloy plates: II—Numerical simulation using LS-DYNA.* International Journal of Impact Engineering, 2007. **34**(4): p. 647-667.

270. Peters, J. and R. Ritchie, *Foreign-object damage and high-cycle fatigue: role of microstructure in Ti–6Al–4V.* International journal of fatigue, 2001. **23**: p. 413-421.

271. Martinez, C.M., et al., *Effects of ballistic impact damage on fatigue crack initiation in Ti–6Al–4V simulated engine blades.* Materials Science and Engineering: A, 2002. **325**(1): p. 465-477.

272. Walker, J.D., *From Columbia to Discovery: Understanding the impact threat to the space shuttle.* International Journal of Impact Engineering, 2009. **36**(2): p. 303-317.

273. Appleby-Thomas, G.J., P.J. Hazell, and G. Dahini, *On the response of two commercially-important CFRP structures to multiple ice impacts.* Composite Structures, 2011. **93**(10): p. 2619-2627.

274. Icten, B.M., *Repeated impact behavior of glass/epoxy laminates.* Polymer Composites, 2009. **30**(11): p. 1562-1569.

275. Hazell, P., et al., *Normal and oblique penetration of woven CFRP laminates by a high velocity steel sphere.* Composites Part A: applied science and manufacturing, 2008. **39**(5): p. 866-874.

276. Lahtinen, H. and A. Pramila, *Accuracy of composite shell elements in transient analysis involving multiple impacts.* Computers & structures, 1996. **59**(4): p. 593-600.

277. Zhou, F., et al., *An experimental comparison of different carbon and glass laminates for ballistic protection.* 18TH INTERNATIONAL CONFERENCE ON COMPOSITE MATERIALS 2011.

278. Phoenix, S.L. and P.K. Porwal, *A new membrane model for the ballistic impact response and V 50 performance of multi-ply fibrous systems.* International Journal of solids and structures, 2003. **40**(24): p. 6723-6765.

279. Mamivand, M. and G. Liaghat, *A model for ballistic impact on multi-layer fabric targets.* International Journal of Impact Engineering, 2010. **37**(7): p. 806-812.

280. Kandan, K., et al. *Novel characterisation technique for assessment of damage to plates by ballistic impact*. in *ICCM International Conferences on Composite Materials*. 2011.

281. Hazell, P. and G. Appleby-Thomas, *A study on the energy dissipation of several different CFRP-based targets completely penetrated by a high velocity projectile.* Composite Structures, 2009. **91**(1): p. 103-109.

282. Kandan, K., *Dynamic Response of Polyethelene Composites*. 2013, University of Cambridge.

283. Evans, R.E. and J.E. Masters, *A new generation of epoxy composites for primary structural applications: materials and mechanics*, in *Toughened composites*. 1987, American Society for Testing and Materials Philadelphia, PA. p. 413-436.

284. Masters, J.E. *Correlation of impact and delamination resistance in interleafed laminates*. in *Sixth International Conference on Composite Materials and Second European Conference on Composite Materials(ICCM & ECCM).* 1987.

285. Yi, X.-S. and X.-F. An, *Effect of interleaf sequence on impact damage and residual strength in a graphite/epoxy laminate.* Journal of Materials Science, 2004. **39**(9): p. 3253-3255.

Appendix

Design of Pressurised Gas Gun System

In order for the objectives of this research project, as set out in Chapter 1, to be realised, a high-velocity pressurised gas gun system at the University of Nottingham was developed. The underlying philosophy of the design of the system was one of flexibility. The gas gun system had three primary functions:

1. Soft impact dynamic impact experiments on composite beam samples,
2. Ballistic impact experiments on composite beam and circular plate samples,
3. Dynamic compressive tests via the use of an instrumented direct-impact Kolsky bar apparatus.

It was necessary for the system to be able to alternate between these three functions with relative ease. This, combined with safety and ease of use, were the main design criteria.

Frame design

For expandability, the frame supporting the gas gun frame was a Machine Building Systems (MBS) modular construction. It utilised an aluminium alloy profile system, with the benefit of ease of expandability. The gas gun system consisted of two separate frames; one for supporting the sample holder and polycarbonate shield, and the other to support the pressure vessel and barrel. Figure.A.1 and Figure.A.2 presents sketches of the frame to support the sample holder and polycarbonate shield, and the frame to support gas gun barrel and pressure vessel, respectively. They were designed for the easy access to the equipment, and to transfer loading during dynamic impact events from the frame to the ground. The frames are securely bolted to the walls and floor to minimise vibrations within the system.

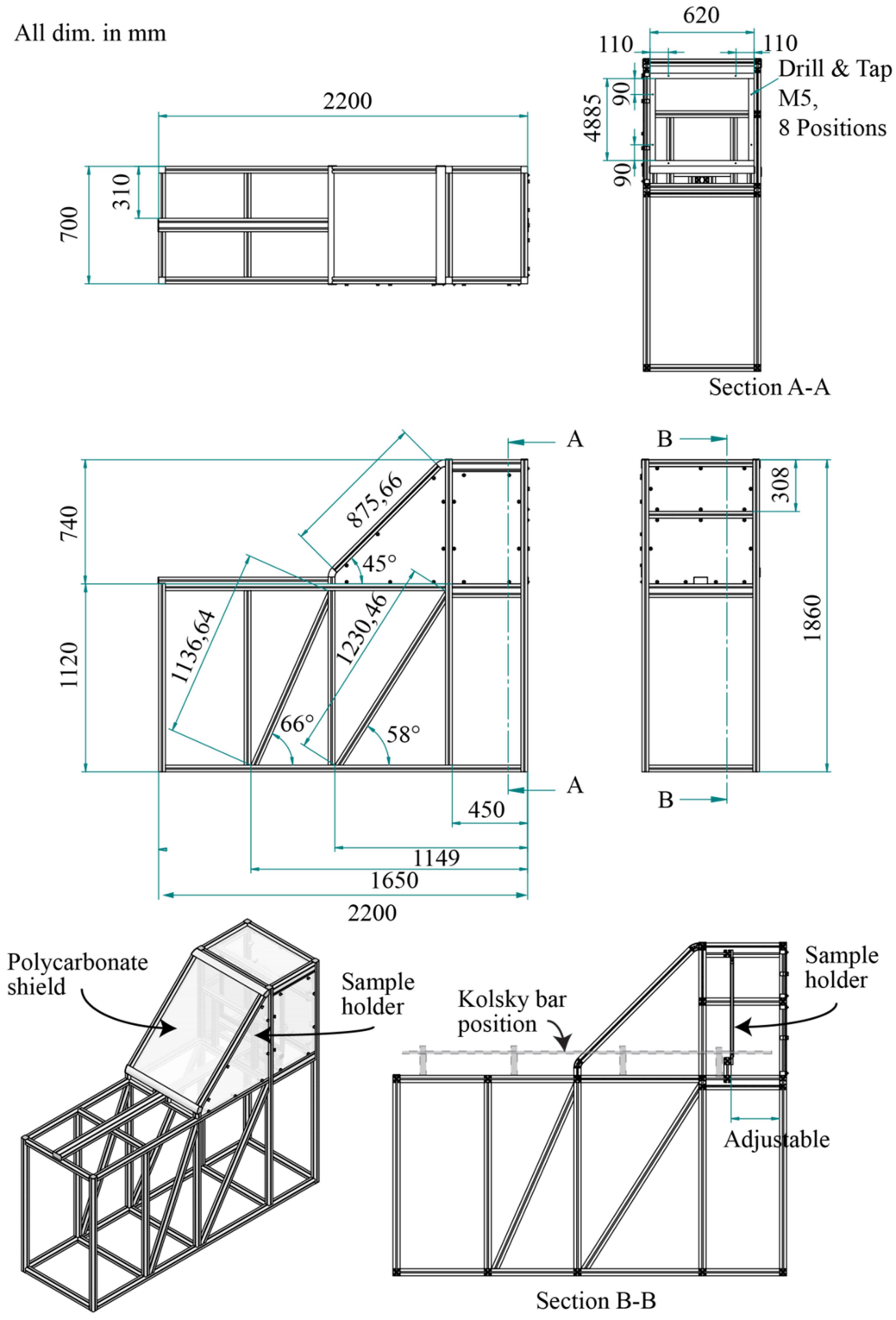


Figure.A.1. Sketch of frame to support the sample holder, polycarbonate shield / Kolsky bar.

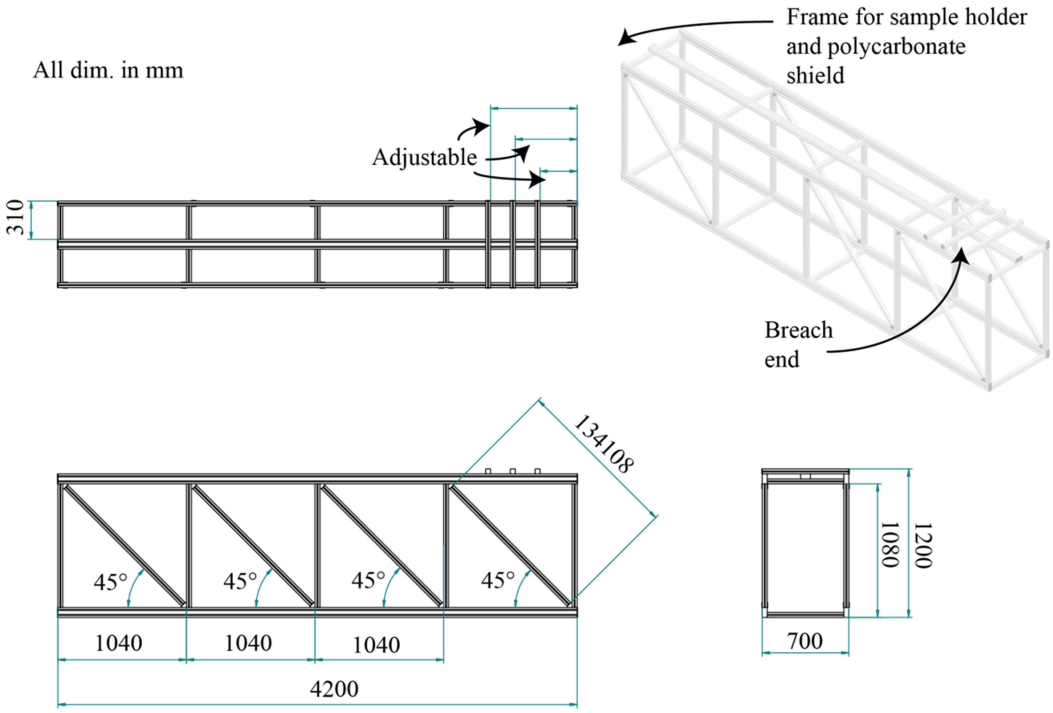


Figure.A.2 Sketch of frame to support gas gun barrel, pressure vessel, and velocity measurement system.

Sample supporters

Both beam samples and circular plate samples were to be accommodated for impact experiments. For beam samples, the two short edges were clamped within a custom-designed hardened steel sample fixture. This in turn was fixed onto the gas gun frame via 3 angle pieces by 6 M6 bolts. For circular plate impact experiments, square samples of 150 x 150 mm2 were cut from composite panels and fixed into place via a circular-ring clamp. Figure.A.3 and Figure.A.4 present sketches of the beam sample and plate sample clamping mechanisms, respectively.

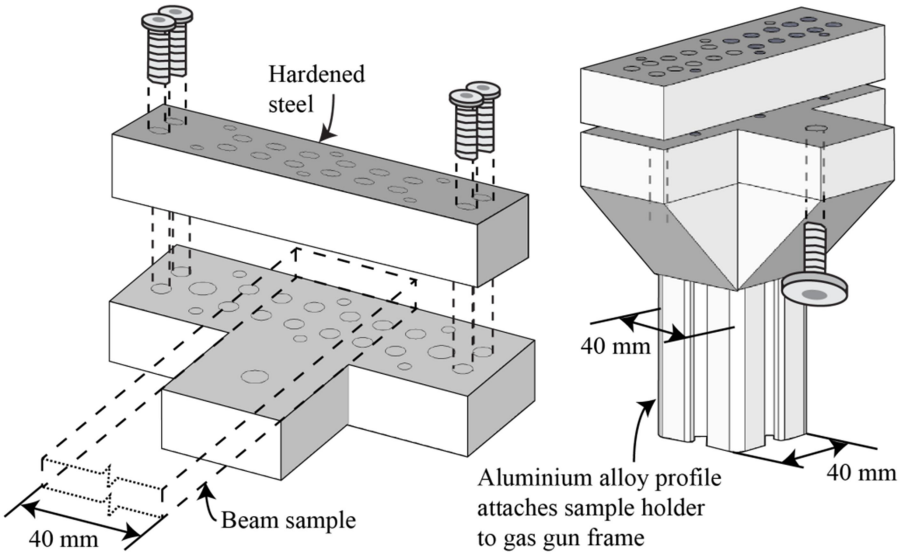


Figure.A.3. Sketch of sample holder for composite beam samples.

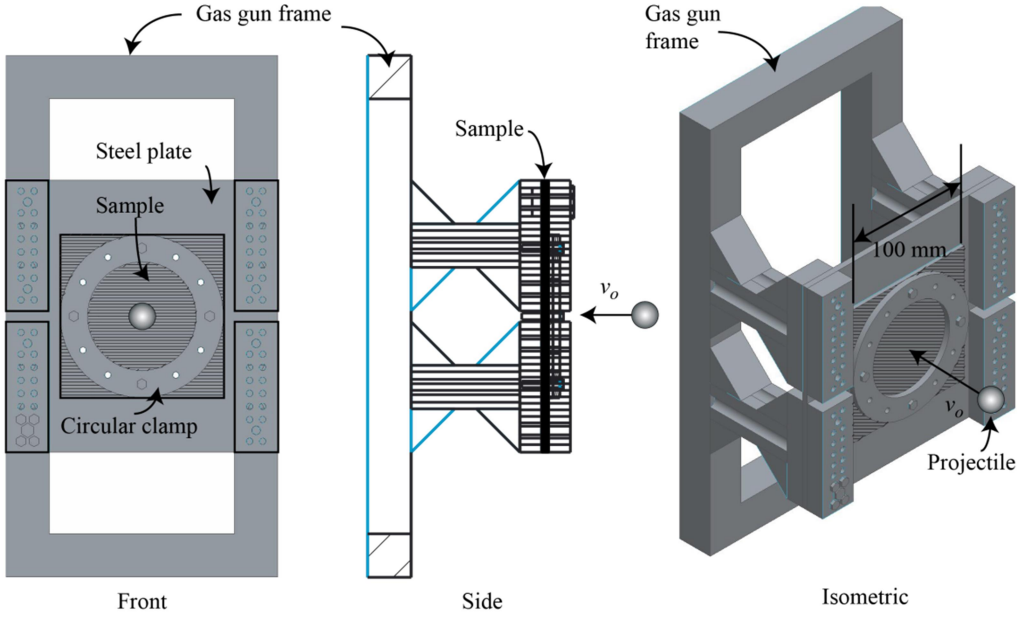


Figure.A.4. Sketch of sample holder for composite plates

Barrel design

A 3.5 m long barrel constructed from hardened steel was employed to accelerate aluminium foam projectiles for the soft impact experimental tests presented in

Chapter 4. The barrel had an external diameter of 40 mm and an internal diameter of 28 mm. Figure.A.5 presents a sketch of the barrel design employed for soft impact experiments. Figure.A.6 presents a sketch of the barrel supporters. Simply supported beam bending calculations revealed that 5 barrels supporters were sufficient.

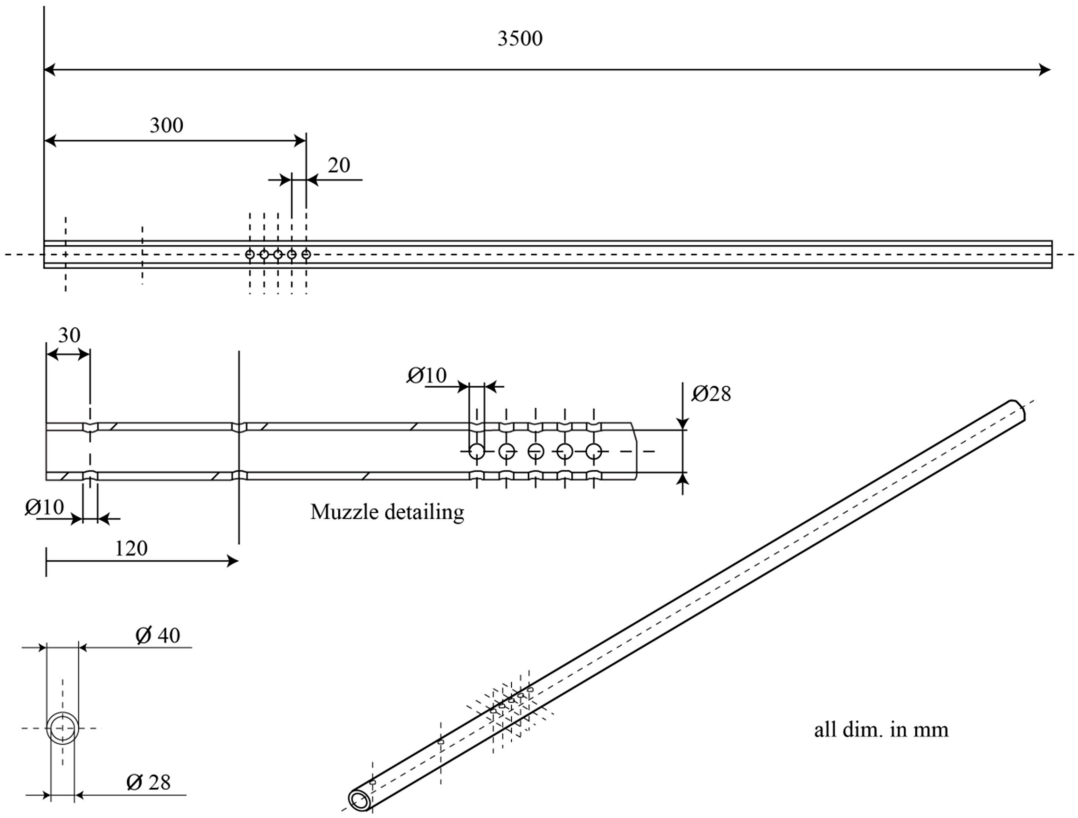


Figure.A.5. Sketch of barrel design for dynamic soft impact experiments.

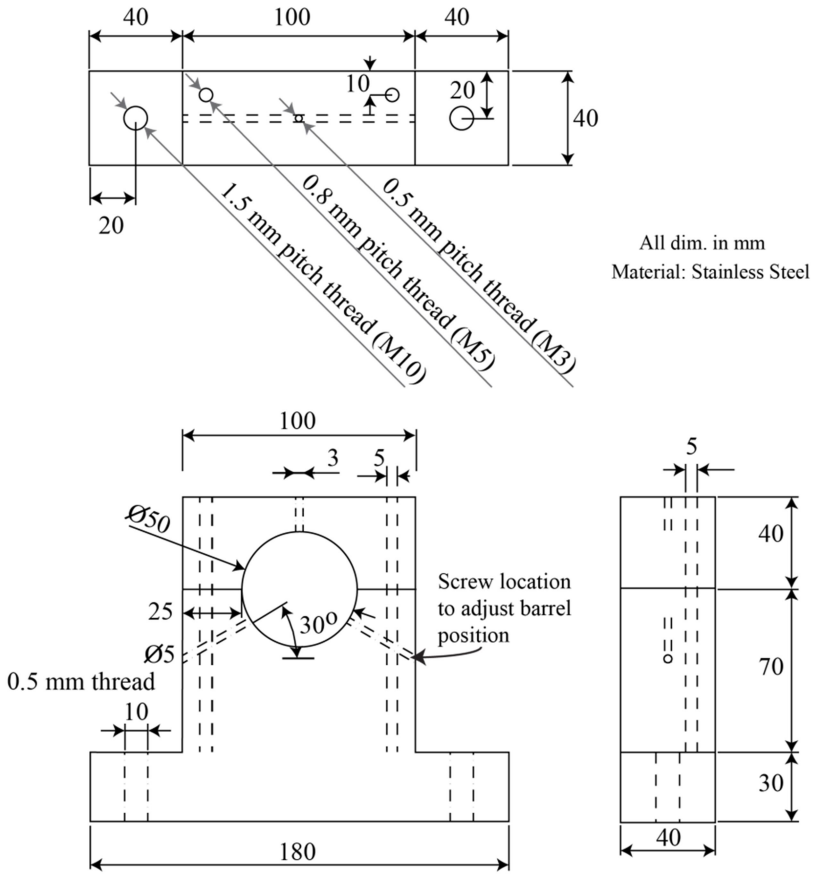


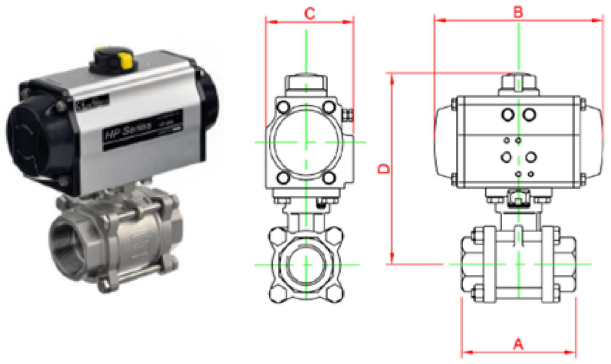
Figure.A.6. Barrel Supporter design

For ballistic impact testing, a stainless steel 3.5 m long barrel with a 13 mm internal diameter was used.

Pressure vessel, pressure release, and velocity measurement

The gas gun utilised two pressured gas systems: pressurised air for lower pressures (up to 6.5 bar), and pressurised nitrogen for higher pressures (up to 50 bar). An automatic pressure release valve was included within the pressure vessel in order to avoid over-pressurisation. The valve was set vent at a maximum pressure of 50 bars. The design of the pressure release system was governed by the need for minimal pressure release time, ensuing maximum acceleration of projectile, and reliability. To avoid the continual replacement of burst shims, a pressure-assisted fast-acting ball valve was chosen for pressure release. Pressure

was released via a solenoid-controlled fast acting pressure assisted spring-return ball valve actuator. Solenoid valve was ASCO pilot spool type single solenoid with aluminium body (serial number SC G551A001 MS). The solenoid was linked to a pressurised air-line, under a pressure of 6.5 bars. The solenoid was linked to a HP pneumatic spring return stainless steel ball valve actuator. presents the data sheet for the HP series fast-acting ball valve.



Description

A combination of HP pneumatic spring return or double acting actuator and 2 way 3-piece stainless steel full ball valve, giving reliability with economy. The HP range of penumatic actuators are manufactured from aluminium and have a hard anodised finish. Position indicator, end of stroke adjustment (+5) and Namur interface are fitted as standard.

The ball valves have stainless steel body and ball with PTFE seats. They are fully maintainable and have the option for screwed BSP parallel female ends, NPT Butt Weld or Socket weld ends.

The valve and actuator fit directly onto each other (valve gas an ISO mounting pad) so no mounting kits are required, thus making the package more compact and cost effective.

Standard Valve Specification		
Body Ends	:	316 Stainless Steel
Seat	:	PTFE
Stem seal	:	RPTFE
Pressure Rating	:	69 Bar
Ends	:	Screwed BSP
		NPT, Butt or Socket Weld

Figure.A.7. HP series fast-acting ball valve data sheet.

Velocity measurement was achieved via two laser-gates positioned at the muzzle end of the barrel. The lasers, when unbroken by the presence of the projectile, were directed upon visible light detectors. Imatronic gated cameo 650 nm, 0.8 mW lasers were used with Avago Technologies SFH551/1-1V 650 nm digital receiver diodes. As the laser gate becomes broken by the projectile travelling down the barrel, a 5V pulse is generated and recorded on an Instek 50 MHz 2 Channel Digital Oscilloscope. A sketch of the gas gun pressure vessel and setup of the velocity measurement laser gate system is presented in Figure.A.8. Figure.A.9 and Figure.A.10 present photographs of the completed gas gun system and gas gun pressure vessel, respectively. Figure.A.11 presents a photograph of the sample supporter and the polycarbonate shielding.

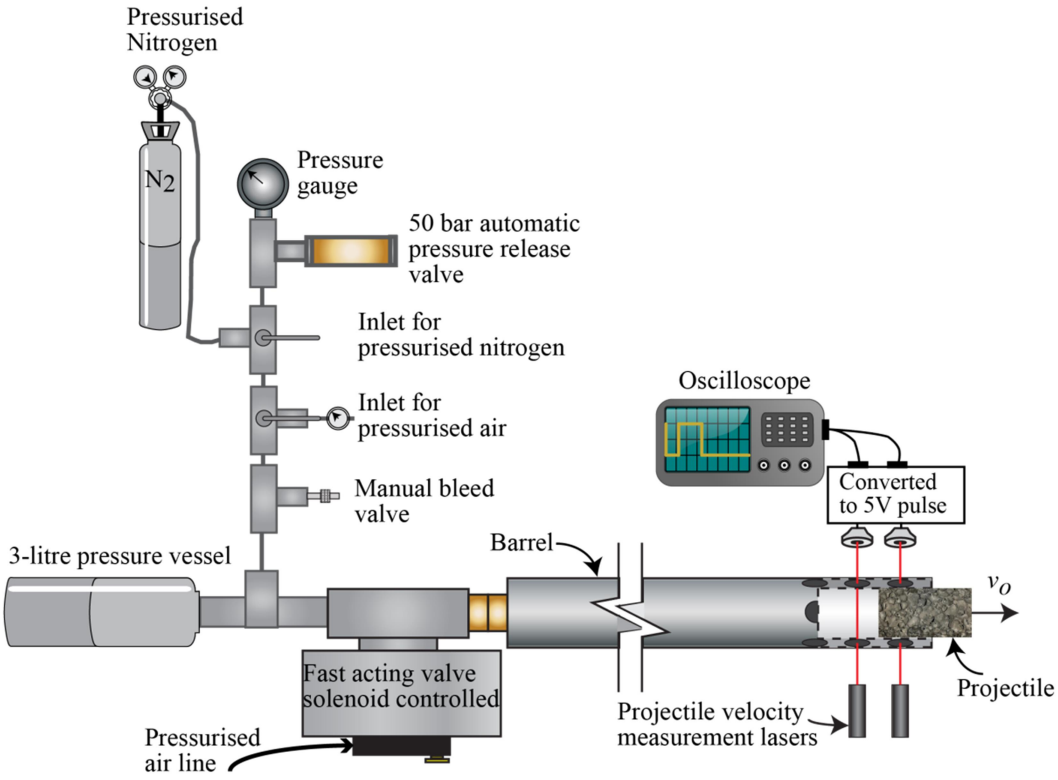


Figure.A.8. Sketch of the gas gun pressure vessel and projectile velocity measurement system.

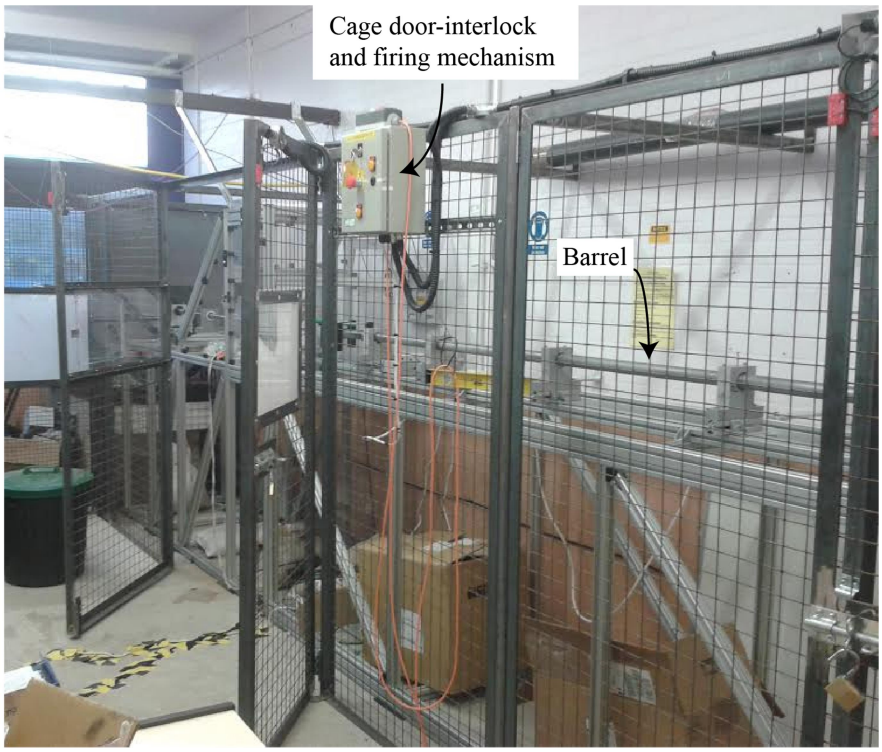


Figure.A.9. Photograph of completed gas gun system with cage and interlock system

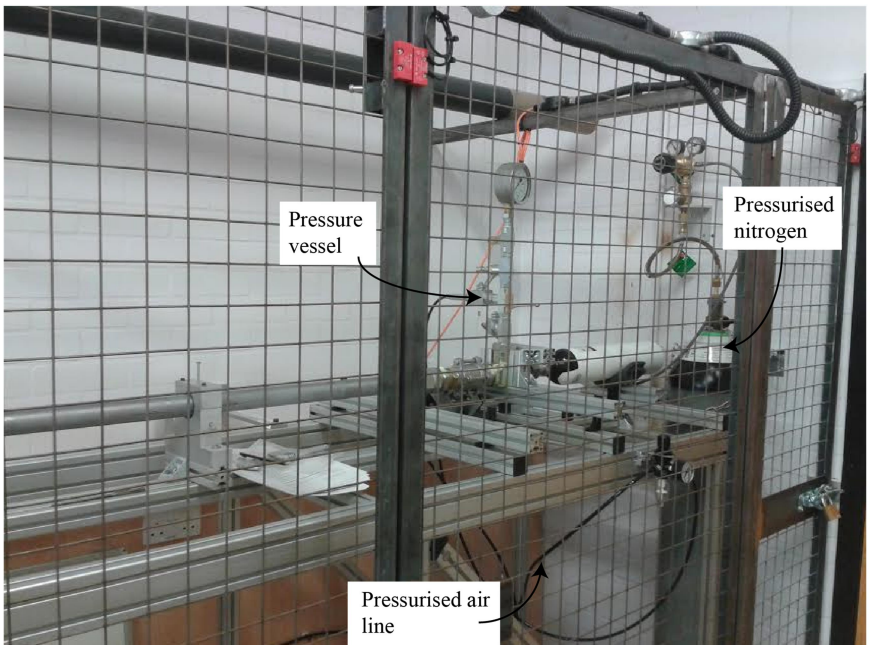


Figure.A.10.Photograph of breech end of gas gun barrel showing pressure vessel.

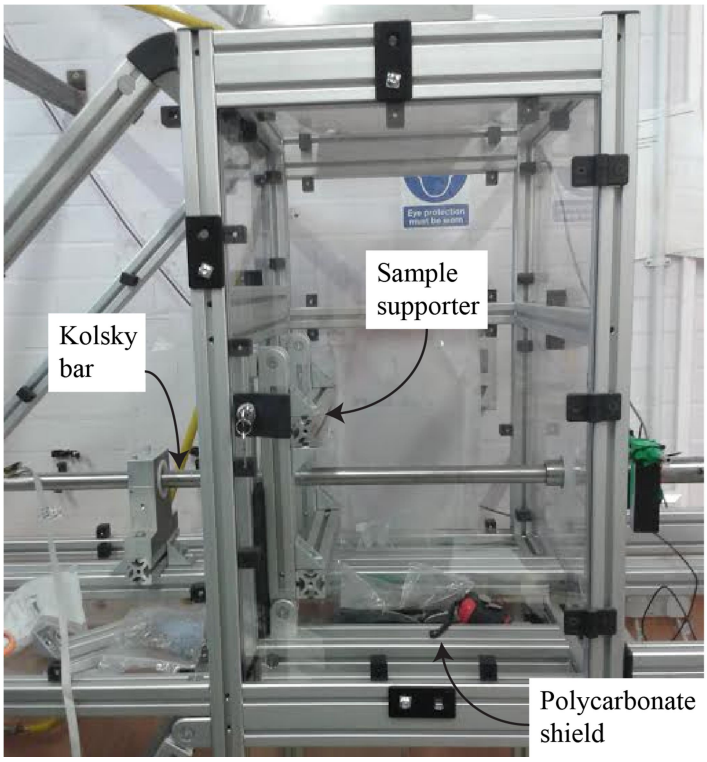


Figure.A.11. Photograph showing gas gun polycarbonate shield, sample supporter, Kolsky bar